Nano/Bio-Receiver Architectures and Detection Methods for Molecular Communications

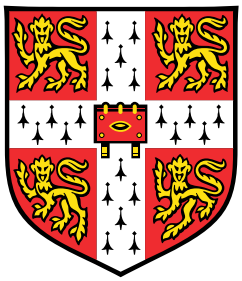

Murat Kuşcu

Department of Engineering
University of Cambridge

This dissertation is submitted for the degree of
Doctor of Philosophy

Girton College

January 2020

To my parents,
Fikriye Kuşcu and Süreyya Kuşcu.

Declaration

I hereby declare that this thesis is the result of my own work and includes nothing which is the outcome of work done in collaboration except as declared in the Preface and specified in the text. It is not substantially the same as any that I have submitted, or, is being concurrently submitted for a degree or diploma or other qualification at the University of Cambridge or any other University or similar institution except as declared in the Preface and specified in the text. I further state that no substantial part of my thesis has already been submitted, or, is being concurrently submitted for any such degree, diploma or other qualification at the University of Cambridge or any other University or similar institution except as declared in the Preface and specified in the text. This dissertation contains fewer than 65,000 words including appendices, bibliography, footnotes, tables and equations and has fewer than 150 figures, as prescribed by the Engineering Degree Committee.

Murat Kuşcu
January 2020

Nano/Bio-Receiver Architectures and Detection Methods for Molecular Communications

Murat Kuşcu

Abstract

Internet of Nano Things (IoNT) is an emerging technology, which aims at extending the connectivity into nanoscale and biological environments with collaborative networks of artificial nanomachines and biological entities integrated into the Internet. To enable the IoNT and its groundbreaking applications, such as real-time intrabody health monitoring, it is imperative to devise nanoscale communication techniques with low-complexity transceiver architectures. Bio-inspired molecular communications (MC), which uses molecules to transfer information, is the most promising technique to realise IoNT due to its inherent biocompatibility and reliability in physiologically-relevant environments.

Despite the substantial body of work concerning MC, the implications of an interface between MC channel and practical MC transceiver architectures are largely neglected, leading to a major gap between theory and practice. As the first step to remove this discrepancy, in this thesis, I develop a realistic analytical ICT model for microfluidic MC with surface-based receivers as a convection-diffusion-reaction system.

In the second part, I focus on biological MC receivers, which can be implemented in living cells using synthetic biology tools. In this direction, I theoretically develop low-complexity and reliable MC detection methods exploiting the various statistics of the stochastic ligand-receptor interactions at the membrane of biological MC receivers. The estimation and detection theoretical analysis of these detection methods demonstrate that even single type of receptors can provide sufficient statistics to overcome the receptor saturation problem, cope with the interference of non-cognate molecules, and simultaneously sense the concentration of multiple types of ligands. I also propose synthetic receptor designs for the transduction of decision statistics into a representation by concentration of intracellular molecules, and design chemical reaction networks performing decoding with intracellular reactions.

Finally, I fabricate a micro/nanoscale MC receiver based on graphene field-effect transistor biosensors and perform its ICT characterisation in a custom-designed microfluidic MC system with the information encoded into the concentration of DNAs. This experimental platform is the first practical demonstration of micro/nanoscale MC, and can serve as a testbed for developing realistic MC methods.

Acknowledgements

I express my sincere gratitude to my supervisor, Prof Özgür B. Akan, for leading the way from the very beginning of my research career. I am thankful to him for giving me the opportunity to join the Internet of Everything (IoE) Group as a research assistant. He has been a great role model and mentor for me, and I hope to continue learning from his guidance and wisdom, both extending far beyond the scope of scientific research.

I am also deeply grateful to Prof Andrea C. Ferrari for accepting me to the Cambridge Graphene Centre (CGC) as a CDT-aligned PhD student. It has been a great experience for me to be a member of this vibrant research community. I also thank my advisor Dr Antonio Lombardo for his crucial advice and insightful comments throughout the course, and also kindly providing lab space for the electrical measurements in Chapter 7.

I am particularly indebted to Dr Ergin Dinç and Dr Hamideh Ramezani, who trained me for most of the equipment and processes used in Chapter 7, and also extensively contributed to the optimisation of all the fabrication processes. I also acknowledge the contribution of Shahab Akhavan in Chapter 7 who performed the Raman spectroscopy, absorbance measurements and ALD for the final devices, and I thank him for devoting substantial time to help solve many problems during the tests. I also thank Dr Lorenzo Pedrazzetti and Muhammad Zulqurnain, who greatly helped me in my first year to plan the experiments, and Dr Eugene Alexeev, who helped with the Raman spectroscopy.

My gratitude extends to my colleagues: Dr Ergin Dinç, Çağlar Koca, Dr Oktay Çetinkaya, Dr Bilgesu A. Bilgin, Dr Hamideh Ramezani, Dr Shahab Akhavan, Adrees Arbab, Nathan Jay, and Giulia Muzio, whose moral support has been invaluable. I also acknowledge the warm friendship of Alessandro, Fred, Benoît and Chris from Girton College, who made my stay at the barren Swirles Court a pleasure, at least for a while.

I am indebted to Melis for her elegant presence in this journey with her unconventional friendship, love and joy.

I acknowledge the financial support of the European Research Council (Project MINERVA, ERC-2013-CoG #616922) and CAPE Acorn Post-graduate Research Award.

Finally, I am eternally grateful to my parents and sisters for their constant support, love and patience.

Publications

Journal Papers

1. **M. Kuscu**, H. Ramezani, E. Dinc, S. Akhavan, O. B. Akan, *"Graphene-based Molecular Communication Receiver: Fabrication and Microfluidic Analysis,"* in preparation.

2. **M. Kuscu**, O. B. Akan, *"Detection with Ligand Receptors under Molecular Interference in Molecular Communications,"* under review, 2020.

3. O. B. Akan, E. Dinc, **M. Kuscu**, B. A. Bilgin, *"Internet of Everything (IoE) - From Molecules to the Universe,"* under review, 2019.

4. **M. Kuscu**, O. B. Akan, *"Channel Sensing in Molecular Communications With Single Type of Ligand Receptors,"* **IEEE Transactions on Communications,** vol. 67, no. 10, pp. 6868-6884, October 2019.

5. **M. Kuscu**, E. Dinc, B. A. Bilgin, H. Ramezani, O. B. Akan, *"Transmitter and Receiver Architectures for Molecular Communications: A Survey on Physical Design with Modulation, Coding and Detection Techniques,"* **Proceedings of the IEEE,** vol. 107, no. 7, pp. 1302-1341, July 2019.

6. **M. Kuscu**, O. B. Akan, *"Maximum Likelihood Detection with Ligand Receptors for Diffusion-Based Molecular Communications in Internet of Bio-Nano Things,"* **IEEE Transactions on Nanobioscience,** vol. 17, no. 1, pp. 44-54, March 2018.

7. M. Aktas, **M. Kuscu**, E. Dinc, O. B. Akan, *"D-DSC: Decoding Delay-based Distributed Source Coding for Internet of Sensing Things,"* **PLOS One,** vol. 13, no. 3, p. e0193154, March 2018.

8. **M. Kuscu**, O. B. Akan, *"Modeling Convection-Diffusion-Reaction Systems for Microfluidic Molecular Communications with Surface-based Receivers in Internet of Bio-Nano Things,"* **PLOS One,** vol. 13, no. 2, p. e0192202, February 2018.

Book Chapters

9. E. Dinc, **M. Kuscu**, B. A. Bilgin, O. B. Akan, *"Internet of Everything - A Unifying Framework beyond Internet of Things,"* **Harnessing the Internet of Everything (IoE) for Accelerated Innovation Opportunities**, Edited by P. J. S. Cardoso, J. Monteiro, J. Semiao, and J. M. F. Rodrigues, IGI Global, January 2019.

Conference Papers

10. G. Muzio, **M. Kuscu**, O. B. Akan, *"Selective Signal Detection with Ligand Receptors under Interference in Molecular Communications,"* in **Proceedings of IEEE SPAWC 2018,** Kalamata, Greece, June 2018.

Table of Contents

List of Figures xvii

List of Tables xxiii

List of Acronyms xxv

1 Introduction 1
- 1.1 Internet of Everything . . . 1
- 1.2 Internet of Nano Things and Molecular Communications . . . 3
- 1.3 Main Contributions . . . 5
- 1.4 Structure of the Thesis . . . 6

2 Molecular Communications (MC) 9
- 2.1 Fundamentals of MC . . . 9
  - 2.1.1 Applications of MC . . . 11
- 2.2 Detection Methods for MC . . . 12
  - 2.2.1 MC Detection with Passive and Absorbing Receivers . . . 13
  - 2.2.2 MC Detection with Reactive Receivers . . . 22
- 2.3 MC Receiver Architectures . . . 29
  - 2.3.1 Receiver Architectures based on Nanomaterials . . . 30
  - 2.3.2 Receiver Architectures based on Engineered Bacteria . . . 38
  - 2.3.3 Macroscale MC Receiver Architectures . . . 39

3 Modelling Convection-Diffusion-Reaction Systems for Microfluidic Molecular Communications with Surface-based Nanoreceivers 41
- 3.1 Introduction . . . 41
- 3.2 Communication System Model . . . 43
- 3.3 Proposed Model . . . 46
  - 3.3.1 Two-Compartment Model . . . 47

3.3.2 Proposed Model . . . 49
3.4 Received Pulse Characteristics . . . 52
3.5 Results and Discussions . . . 53
3.6 Conclusion . . . 60

4 Maximum Likelihood Detection with Ligand Receptors Based on Receptor Unbound Time Intervals for Overcoming Receiver Saturation 63
4.1 Introduction . . . 63
4.2 Maximum Likelihood Estimation of Ligand Concentration . . . 65
4.2.1 Estimation based on Receptor Occupation Ratio . . . 65
4.2.2 Estimation based on Receptor Unbound Time . . . 66
4.2.3 Comparison of ML Estimators . . . 70
4.3 Communication System Model . . . 71
4.4 Maximum Likelihood Detection with Ligand Receptors . . . 72
4.4.1 Detection based on Receptor Occupation Ratio . . . 72
4.4.2 Detection Based on Receptor Unbound Time . . . 73
4.5 Performance Evaluation . . . 75
4.5.1 Effect of Number of Transmitted Molecules . . . 75
4.5.2 Effect of Signalling Interval . . . 76
4.5.3 Effect of Distance . . . 76
4.5.4 Effect of Number of Receptors . . . 78
4.5.5 Effect of Receiver Memory . . . 80
4.6 Discussion on Implementation . . . 80
4.7 Conclusion . . . 84

5 Channel Sensing in Molecular Communications with Ligand Receptors 85
5.1 Introduction . . . 85
5.2 Opportunities of Channel Sensing in MC . . . 88
5.3 Statistics of Ligand-Receptor Binding Reactions . . . 89
5.4 Channel Sensing based on Ligand-Receptor Binding Reaction . . . 93
5.4.1 System Model . . . 93
5.4.2 Optimal Estimation of Ligand Concentrations and Cramér-Rao Lower Bound . . . 94
5.4.3 Suboptimal Estimation of Ligand Concentrations . . . 97
5.5 Performance Evaluation . . . 103

5.5.1 Effect of Number of Ligand Types in the Mixture . . . 105
5.5.2 Effect of Similarity between Ligand Types . . . 106
5.5.3 Effect of Number of Unbound/Bound Duration Samples . . . 106
5.5.4 Effect of Concentration Ratios of Ligands . . . 108
5.5.5 Effect of Absence of Ligands . . . 108
5.5.6 Effect of Unknown Ligand Types . . . 111
5.6 Discussion on Implementation . . . 113
5.6.1 Acquisition of Receptor Unbound/Bound Time Duration Statistics 113
5.6.2 Estimation with Chemical Reaction Networks . . . 122
5.7 Conclusion . . . 123

6 Detection with Ligand Receptors under Molecular Interference in Molecular Communications 125
6.1 Introduction . . . 125
6.2 Statistics of Ligand-Receptor Binding Reactions . . . 127
6.3 Molecular Communication System . . . 128
6.4 Detection Methods . . . 129
6.4.1 Detection based on Number of Bound Receptors . . . 129
6.4.2 Detection based on Receptor Unbound Time Durations . . . 130
6.4.3 Detection based on Receptor Bound Time Durations . . . 132
6.4.4 Detection based on Receptor Unbound and Bound Time Durations 136
6.4.5 Decision Rule . . . 138
6.5 Performance Evaluation . . . 139
6.5.1 Effect of Interferer Concentration . . . 140
6.5.2 Effect of Similarity between Information and Interferer Molecules 141
6.5.3 Effect of Bit-0/Bit-1 Concentration Ratio . . . 143
6.5.4 Effect of Number of Receptors . . . 144
6.6 Discussion on Implementation . . . 145
6.7 Conclusion . . . 152

7 Graphene-based Molecular Communication Receiver 153
7.1 Introduction . . . 153
7.2 Fabrication of MC Receiver . . . 155
7.2.1 Fabrication of GFET . . . 155
7.2.2 Fabrication of Microfluidic Channels and Device Integration . . . 160
7.2.3 Functionalisation of GFET . . . 165
7.3 Characterisation of MC Receiver . . . 167

7.3.1 Optical Characterisation 167
7.3.2 Electrical Characterisation 169
7.4 Communication Performance 179
7.5 Conclusion 186

8 Conclusions and Future Work **189**
8.1 Conclusions 189
8.2 Future Work 191

Bibliography **195**

Appendix A Clarifications and Derivation Details **215**
A.1 Constraints on Signalling Interval for MC Detection Based on Receptor Unbound Time 215
A.2 Introducing Unknown Ligand Types for MC Channel Sensing 216

List of Figures

1.1 IoE framework integrating different ICT technologies. 2
1.2 Conceptual drawing of a real-time health monitoring application of IoNT. 3
1.3 IoNT as the core enabling technology of IoE. 5

2.1 Components of an MC system with biological and nanomaterial-based MC transmitter and receiver design approaches. 10
2.2 Hypothetical MC receiver models used for developing detection methods. 15
2.3 Different methods for sampling receptor states in reactive MC receivers. . 27
2.4 Main functional blocks of an MC receiver architecture. 29
2.5 Physical design of a graphene-based bioFET sensor acting as an MC receiver. 32
2.6 (a) Honeycomb lattice (left) and the corresponding Brillouin zone in the reciprocal space (right). (b) Electronic dispersion in the graphene's honeycomb lattice with a closer look into the energy bands near one of the Dirac points. Taken from Ref. [1]. 36

3.1 Microfluidic MC with surface-based receiver. 44
3.2 Conceptual drawing of the two-compartment model. 48
3.3 Optimal values of the free parameter k obtained with varying system parameters of microfluidic MC. 54
3.4 Time course of the number of bound receptors normalized by the total number of receptors for varying system parameters. 56
3.5 Received pulse delay t_{pd} with varying system parameters. 57
3.6 Normalized received pulse amplitude R_{pa}/R_{max} with varying system parameters. 58
3.7 Received pulse width τ_{pw} with varying system parameters. 59

4.1 Sampling for EROR and ERUT estimation schemes. 67
4.2 Fractional errors in concentration estimates based on EROR and ERUT schemes. 68

4.3 Effect of number of transmitted molecules on the detection performance of DROR and DRUT schemes. 77
4.4 Effect of symbol interval length on the detection performance of DROR and DRUT schemes. 78
4.5 Effect of transmitter-receiver distance on the detection performance of DROR and DRUT schemes. 79
4.6 Effect of number of receptors and receiver memory length on the detection performance of DROR and DRUT schemes. 81

5.1 Conceptual drawing of a biological MC device with ligand receptors on its surface exposed to a mixture of different ligand types of different affinities with the receptors, and example time course of binding and unbinding events occurring on the receptors. 92
5.2 Probability distribution of receptor bound time durations for a mixture of ligand types. 98
5.3 Average NMSE vs. varying number of ligand types. 106
5.4 Average NMSE vs. varying similarity between ligand types. 107
5.5 Average NMSE vs. varying number of unbound and bound time duration samples. 107
5.6 Average NMSE vs. varying concentration ratio of the highest-affinity ligand type. 109
5.7 MSE vs. varying number of samples for suboptimal unbiased estimator in the absence of different types of ligands. 110
5.8 Average NMSE in the presence of an unknown ligand. 112
5.9 State diagram of the proposed synthetic receptor design and demonstration of the activation and sampling cycles. 114
5.10 The kinetic scheme of an active receptor given as a Markov Process. . . 118
5.11 Steady-state distributions of second messengers produced by the proposed synthetic receptors. 120

6.1 Probability distributions of the bound time durations corresponding to interferer molecules, information molecules, and the mixture of them. The dashed line indicates the time threshold (see (6.20)) that helps discriminate between information and interferer molecules by separating the longer binding events from the shorter ones. 132

6.2 Gaussian approximation of decision statistics. Histograms are obtained via Monte Carlo simulations (50000 iterations) of stochastic ligand-receptor binding process under interference. Simulation parameters are set to the default values that are used in performance evaluation (see Table 6.2). Here it is assumed that bit-0 is transmitted, and thus, I use $c_0 = 4 \times K_{D,S}$. 134
6.3 Bit error probability as a function of mean interferer concentration μ_{C_I}/K_{D_I} for (a) non-saturation and (b) saturation conditions of the receiver. . . . 140
6.4 Bit error probability as a function of affinity ratio $\eta = k_S^-/k_I^-$ for the cases (a) when information molecules have more binding affinity, i.e., $\eta < 1$, and (b) when interferer molecules have more binding affinity, i.e., $\eta > 1$. . . . 142
6.5 (a) Bit error probability with varying ratio of the received concentrations corresponding to bit-0 and bit-1 transmissions, i.e., c_0/c_1. A magnified view is provided in (b). . . . 144
6.6 Bit error probability as a function of number of receptors. . . . 145
6.7 (a) Receptor design for DNBR. (b) Sampling of the number of bound receptors. (c) Receptor design for DRUT. (d) Sampling of the receptor unbound time intervals. . . . 147
6.8 (a) Receptor design for DRBT. (b) Sampling of the number of binding events of durations within specific time intervals. (c) Receptor design for DRUBT. (d) Sampling of the receptor unbound time intervals and the number of binding events of durations within specific time intervals. (e) Typical pathways in the kinetic proofreading mechanism of the DRBT and DRUBT receptors when information and interferer molecules bind an active unbound receptor. . . . 151

7.1 Computer-aided design for optical lithography of MC receiver. . . . 156
7.2 Process flow for the patterning of SLG channels. (a) SLG transferred on Si/SiO_2 substrate. (b) Coating of sample with photoresist layer. (c) SLG channel pattern defined by optical lithography. (d) SLG channel pattern after RIE etching. (e) Removal of residual photoresist layer from SLG surface, and the resulting SLG channel on the substrate. . . . 157
7.3 Process flow for the deposition of contacts. (a) Coating of sample with photoresist layer. (b) Contact pattern defined by optical lithography. (c) Deposition of Cr and Au metal films through thermal evaporation. (d) Patterned contacts after lift-off process. . . . 158

7.4 Process flow for the deposition of insulator. (a) Uniform Al_2O_3 film over the sample after ALD. (b) Coating of sample with photoresist layer. (c) Insulator pattern defined by optical lithography. (d) Exposed SLG channel and contacts after wet etching of Al_2O_3. (e) Patterned Al_2O_3 film after removal of excess photoresist. 159
7.5 (a) Optical micrograph of the fabricated GFET channels after Al_2O_3 etching process (only six of the seven channels are visible). (b) A closer look into one of the GFET channels. (c) Overall view of the fabricated 7-channel GFET before the bonding of microfluidic PDMS layer. 159
7.6 (a) Microfluidic PDMS layer bonded to the GFET surface after the inlets and outlet are defined, and the Pt gate electrode is placed on top. (b) Cross-sectional view of the MC receiver after PDMS layer bonding. . . . 160
7.7 (a) Computer-aided design for 3d printing of PDMS mould. (b) 3d-printed PDMS mould. (c) PDMS microfluidic channel with the Pt wire mounted on top as the gate electrode. 162
7.8 (a) Microfluidic measurement setup consisting of a 4-channel pressure regulator, a high-precision SMU, electrical probes and microfluidic accessories. (b) A closer look into the fabricated graphene-based MC receiver connected to the microfluidic setup. (c) Probe connections for electrical tests of the device. 163
7.9 Conceptual drawing of the microfluidic measurement setup with the practical implementation shown in Fig. 7.8 164
7.10 (a) Molecular structure of PBASE, and conceptual drawing of probe DNA (pDNA) and complementary target DNA (tDNA). (b) Noncovalent binding of PBASE to graphene via $\pi - \pi$ interaction. (c) Immobilisation of pDNA via conjugation reaction with the succinimide group of PBASE. (d) pDNA-tDNA hybridisation. 166
7.11 Raman spectra at 514 nm for the SLG on Si/SiO_2 substrate (black), after the application of the PBS electrolyte and drying (red), after the functionalisation with the PBASE linker (blue), and after the immobilisation of the pDNAs (purple). Raman spectrum of the pDNA molecules drop-cast on Si/SiO_2 substrate is also shown (green). All spectra except the one for pDNA on Si/SiO_2 (green) are normalised to the intensity of the G peak, I(G). 168
7.12 Absorbance spectrum of pDNA molecules 169

7.13 Transfer characteristics of four channels at different steps of functionalisation in terms of drain-source current I_{ds} as a function of varying gate voltage V_g with sweep rate 140 mV/s. In all measurements drain-source voltage is held constant at $V_{ds} = 0.1$ V. 170
7.14 Transfer characteristics of four channels at different steps of functionalisation in terms of drain-source current I_{ds} as a function of varying gate voltage V_g with sweep rate 140 mV/s. In all measurements drain-source voltage is held constant at $V_{ds} = 0.1$ V. 172
7.15 Leakage current analysis of the MC receiver 173
7.16 (a) Real-time sensing response of the MC receiver in terms of drain-source current I_{ds} with varying concentration of complementary target DNAs (tDNAs). (b) Equilibrium sensing response fitted by the Langmuir adsorption isotherm. Resulting dissociation constant for pDNA-tDNA hybridisation is $K_D = 730$ nM. 175
7.17 Specificity analysis of the MC receiver. (a) Real-time sensing response for complementary tDNA, non-complementary ntDNA_1 with single base-pair mismatch, and non-complementary ntDNA_2 with 7 base-pair mismatches (see Table 7.1). At $t \approx 1800$ s, the DNA solutions are replaced with 0.01xPBS solution to allow dissociation of the hybridised DNAs. (b) Real-time sensing response fitted by the Langmuir adsorption/desorption model, equations (7.7)-(7.8). 178
7.18 Normalised pulse response of the MC receiver in terms of drain-source current I_{ds} with constant operating voltages set to $V_g = 0$ V and $V_{ds} = 0.1$ V. (a, b) Three independent measurements taken from the same channel for 30-second-long and 60-second-long 1 μM tDNA pulses, respectively. (c, d) Pulse responses fitted by the normalised output of the transformed model given in (7.13). 180
7.19 Normalised receiver response for binary data transmission with fixed pulse length $T_p = 30$ s and varying bit intervals: (a) $T_s = 60$ s, (b) $T_s = 120$ s, (c) $T_s = 360$ s. The grey lines denote the received MC signals normalised by the baseline current, and the solid red lines are their low-pass filtered version by a moving average filter of 21-second length in MATLAB. Solid blue lines represent the normalised output of the model given in (7.17). Dashed orange lines indicate the time instants when bit-1 is transmitted, i.e., when the mechanical switch in the tDNA line is opened for 30 seconds. 184

7.20 Delay-shifted version of the receiver response for binary data transmission for varying bit intervals: (a) $T_s = 60$ s, (b) $T_s = 120$ s, (c) $T_s = 360$ s. Dashed orange line denotes the start time of the data transmission, and grey dashed lines demarcate the individual bit intervals. Green dots on the received MC signal indicates the sampled current values for difference-based detection method with the decoding rule formulated in (7.20). Transmitted/decoded bits are noted above each bit interval, with the red-coloured ones denoting the erroneously decoded bits. 185

List of Tables

2.1 Comparison matrix for MC detectors with passive and absorbing receivers 18
2.2 Design options, performance and applications of bioFETs 33

3.1 Default values of system parameters for simulation of microfluidic MC . . 54

4.1 Default values of simulation parameters for analysing detection based on receptor unbound time intervals 74

5.1 Comparison matrix for channel sensing methods 104

6.1 Comparison of detection methods under interference 138
6.2 Default values of system parameters for analysing detection performance under interference 139

7.1 Kinetic constants of DNA hybridisation measured by MC receiver 177

List of Acronyms

Acronyms / Abbreviations

2d Two dimensional

3d Three dimensional

ACF Auto-correlation function

ALD Atomic layer deposition

APS Ammonium persulphate

BEP Bit error probability

bioFET Field effect transistor-based biosensor

CIR Channel impulse response

CLT Central limit theorem

CME Chemical master equation

CMOS Complementary metal-oxide-semiconductor

CNT Carbon nanotube

CRLB Cramér-Rao lower bound

CRN Chemical Reaction Network

CSI Channel state information

CSK Concentration-shift keying

CTMP Continuous-Time Markov Process

CVD Chemical vapor deposition

DBMT Diffusion-based molecular timing

DI Deionized

DMF Dimethylformamide

DNA Deoxyribonucleic acid

DNBR Detection based on number of bound receptors

DRBT Detection based on receptor bound time durations

DROR Detection based on receptor occupation ratio

DRUBT Detection based on receptor unbound and bound time durations

DRUT Detection based on receptor unbound time

EDLC Electrical double layer capacitance

EDL Electrical double layer

EROR Estimation based on receptor occupation ratio

ERUT Estimation based on receptor unbound time

FA First arrival

FEA Finite element analysis

FET Field effect transistor

GFET Graphene field effect transistor

ICT Information and Communication Technology

IoBNT Internet of Bio-Nano Things

IoE Internet of Everything

IoMT Internet of Molecular Things

IoNT Internet of Nano Things

ISI Intersymbol interference

KPR Kinetic proofreading

LA Last arrival

LTI Linear time-invariant

MA Medium access

MAP Maximum a posteriori

MC Molecular communication

MDMA Molecular division multiple access

MIMO Molecular multiple-input multiple-output

ML Maximum likelihood

MN Magnetic nanoparticle

MoM Method of moments

MoS_2 Molybdenum disulfide

MoSK Molecule-shift keying

MSE Mean squared error

MUI Multi-user interference

NMSE Normalized mean squared error

NW Nanowire

OOK On-off keying

PA Passive receiver

PBASE 1-Pyrenebutyric acid N-hydroxysuccinimide ester

PBS Phosphate buffered saline

PDMS Polydimethylsiloxane

PLA Polylactic acid

PMMA Polymethyl methacrylate

PTFE Polytetrafluoroethylene

RDME Reaction-diffusion master equation

RD Reaction-diffusion

RNA Ribonucleic acid

RSK Ratio shift keying

Rx Receiver

SbS Symbol-by-Symbol

SINR Signal-to-interference-plus-noise-ratio

SiNW Silicon nanowire

SLG Single layer graphene

SNR Signal-to-noise-ratio

SPR Surface plasmon resonance

ssDNA Single-stranded deoxyribonucleic acid

SWCNT Single-walled carbon nanotubes

TMD Transition metal dichalcogenides

TxRx Transceiver

Tx Transmitter

Chapter 1

Introduction

1.1 Internet of Everything (IoE)

In this age of enlightenment, our understanding of the universe grows rapidly with an accelerating rate. We now understand that universe is a vast, but nevertheless connected, entity whose evolution is described by a set of rules, the laws of physics. These rules give rise to recurrent patterns within the universe, e.g., light, electrons, molecules, living creatures, planets, galaxies etc., that are persistent carriers of information. These laws of physics serve at the same time as protocols of communication between these information carrying entities. Thus, our description of the universe can be regarded as a theory for an **inter**connected **net**work of **everything** we perceive, i.e., *Internet of Everything (IoE)*. However, the quest for establishing a coherent understanding of this IoE requires probing it by our technology. In this regard, the technological term IoE, i.e., the concept of expanding the *Internet* to *Everything*, actually stands for the effort of expanding our knowledge and technology to match as much as possible to the universal IoE, and to gain control over it. This vision of IoE, therefore, is that of connecting our already developed infrastructure to all the various entities we observe within this universe, ranging from molecules and cells within human body to the people and planets [2]. This novel vision has an enormous potential to transform the way we connect with and understand the universe, by enabling new methods of interfering with the underlying processes at the single-molecular level, and extending the human consciousness and control with smart agents collaboratively sensing and acting upon environments never explored by any other paradigm before.

The IoE framework, as conceptually demonstrated in Fig. 1.1, is a set of different ICT technologies, such as Internet of Sense and Internet of Vehicles, which are seamlessly connected to each other to enable unprecedented applications. Each of these technologies

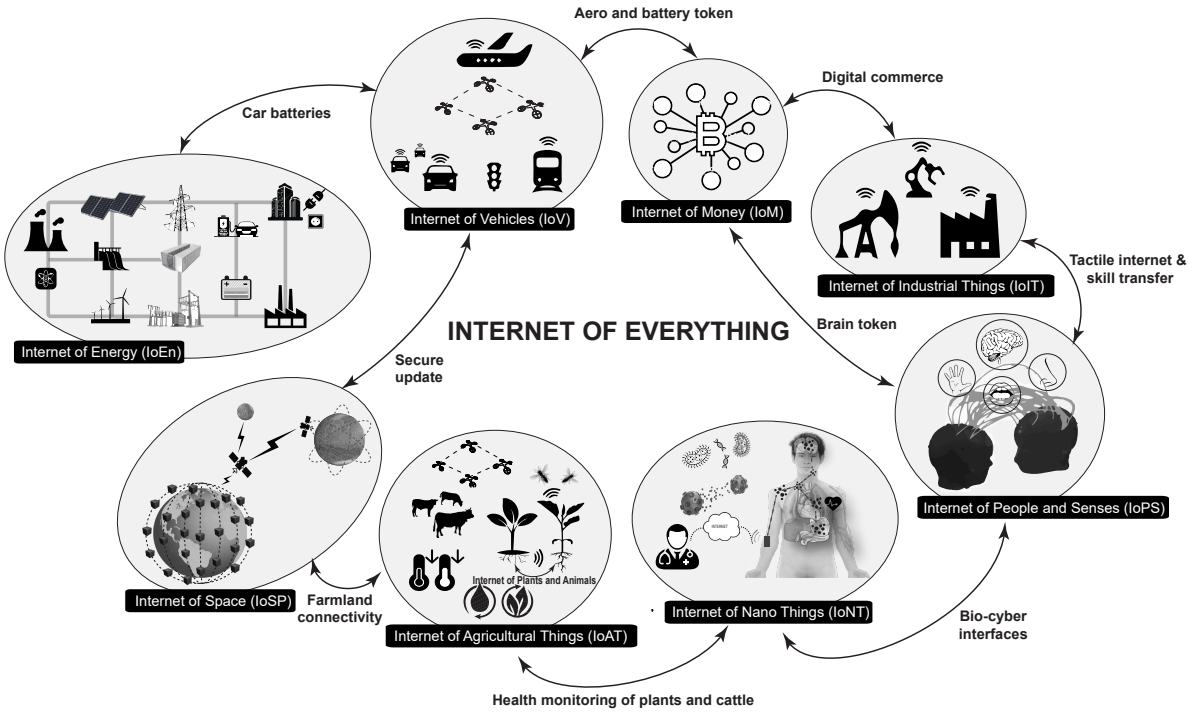

Fig. 1.1 IoE framework integrating different ICT technologies.

and applications feed into each other in this framework, and build up a broader network of heterogeneous technologies. Realization of the IoE framework demands highly interdisciplinary approaches to overcome unique connectivity and interoperability challenges mainly resulting from the close interaction between cyber and physical worlds and the enormous number of interconnected entities. The things, including nanoscale and biological entities, are interconnected anytime and everywhere within the IoE framework, implying a challenge for ubiquitous connectivity. Heterogeneous characteristics of technologies and services connected to each other require a high level of interoperability for seamless operation, which in turn calls for the design of novel interfaces, including those between biological and cyber domains. Miniaturization is another major challenge, which implies not only the requirement for scaling down the network nodes and transceivers, but also the communication links. This necessitates the design of novel communication techniques that can reliably operate at nanoscale and provide compatibility with biological entities.

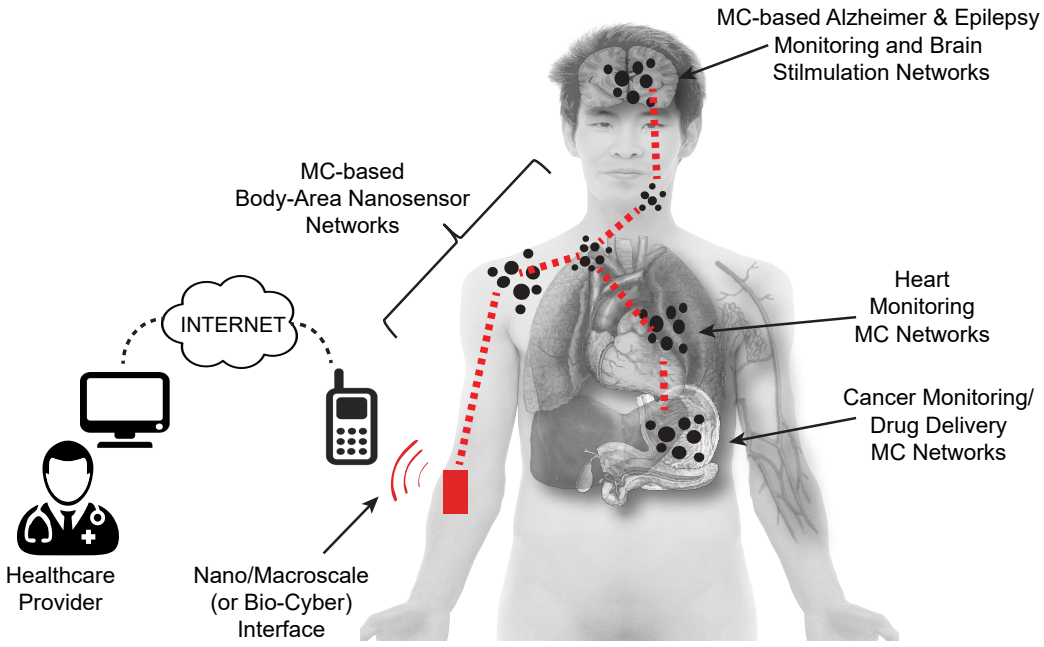

Fig. 1.2 Conceptual drawing of a real-time health monitoring application of IoNT.

1.2 Internet of Nano Things (IoNT) and Molecular Communications (MC)

One of the main building blocks of the IoE framework is IoNT, which defines artificial networks of nanoscale functional units, such as nano-biosensors and engineered bacteria, integrated into the Internet infrastructure [3]. IoNT concept is positioned to exploit the unusual interactions with the physical environment stemming from the nanoscale dimensions, and expected to greatly enhance the functionalities of individual nanomachines through cooperative nanonetworks, and enable groundbreaking applications based on new methods of monitoring intricate and dynamic physiological processes and interfering with them at unprecedented spatio-temporal resolutions.

The research in IoNT is fuelled by the advances in nanotechnology with the discovery of new nanomaterials, e.g., two dimensional (2d) layered materials such as graphene and MoS_2 with exceptional optoelectronic and biochemical properties [4], and the development of new fabrication processes resulting in novel nanoscale device architectures and processes transforming the conventional perception of sensing, actuating, computing and energy harvesting. Moreover, continuously extended understanding and control of living cells through the advances in synthetic biology research create new opportunities for IoNT.

Depending on the physical properties and the size of network nodes and communication mechanism, several technologies have been proposed within the larger IoNT scope. For example, Internet of Bio-Nano Things (IoBNT) has been coined to define the molecular communication networks of animate objects, such as engineered bacteria [5]. The optical networks of fluorophore-based single molecular devices have been termed the Internet of Molecular Things (IoMT) [6].

Envisaged applications of IoNT are mostly centred around the medical domain. For example, implantation of IoNT inside human body can enable continuous health monitoring with nanoscale sensing agents transferring real-time health status to remote healthcare providers for early-stage disease diagnosis [7], as demonstrated in Fig. 1.2. Moreover, actuation capabilities of nanomachines at single cellular and even at single molecular level can lead to paradigm-shifting ICT-based treatment techniques, such as smart drug delivery as well as single-cell prosthetics, e.g., artificial neurons, restoring the lost physiological functionalities of their biological counterparts [8, 9]. Furthermore, many environmental and military applications, such as toxic agent monitoring and covert military surveillance, are envisioned to be enabled by this emerging framework.

IoNT is key to the success in the quest to interact with the universal IoE at molecular resolution. It is an enabling technology for other technologies in the IoE framework, as demonstrated in Fig. 1.3. For example, it could provide high-resolution neural interfaces to enable the Internet of Senses, which necessitates seamlessly interfacing with the human brain. It could enable nanosensor networks for better control and optimisation of processes in Internet of Industrial Things applications. It also promises for continuous healthcare monitoring of cattle and plants for Internet of Agricultural Things. IoNT is, therefore, at the core of the IoE framework, and realising the IoNT could overcome the major challenges of the IoE.

Research in this field has so far focused on the theoretical investigation of the physical layer, as the associated challenges resulting from the peculiarities of nanoscale physics are the most pressing ones. Since implementing conventional EM communications among nanomachines is obstructed by the antenna size limitations and the severe attenuation of EM signals in the physiologically relevant media of IoNT applications, researchers have started a quest for alternative communication methods to extend the connectivity of the IoE down to nanoscale. Among the several paradigms proposed for use in nanonetworks, MC is the most promising one, because it exists in nature as the main communication mechanism of living cells and other microorganisms, and thus, its feasibility at these dimensions is already proved. Moreover, several of the aforementioned IoNT applications

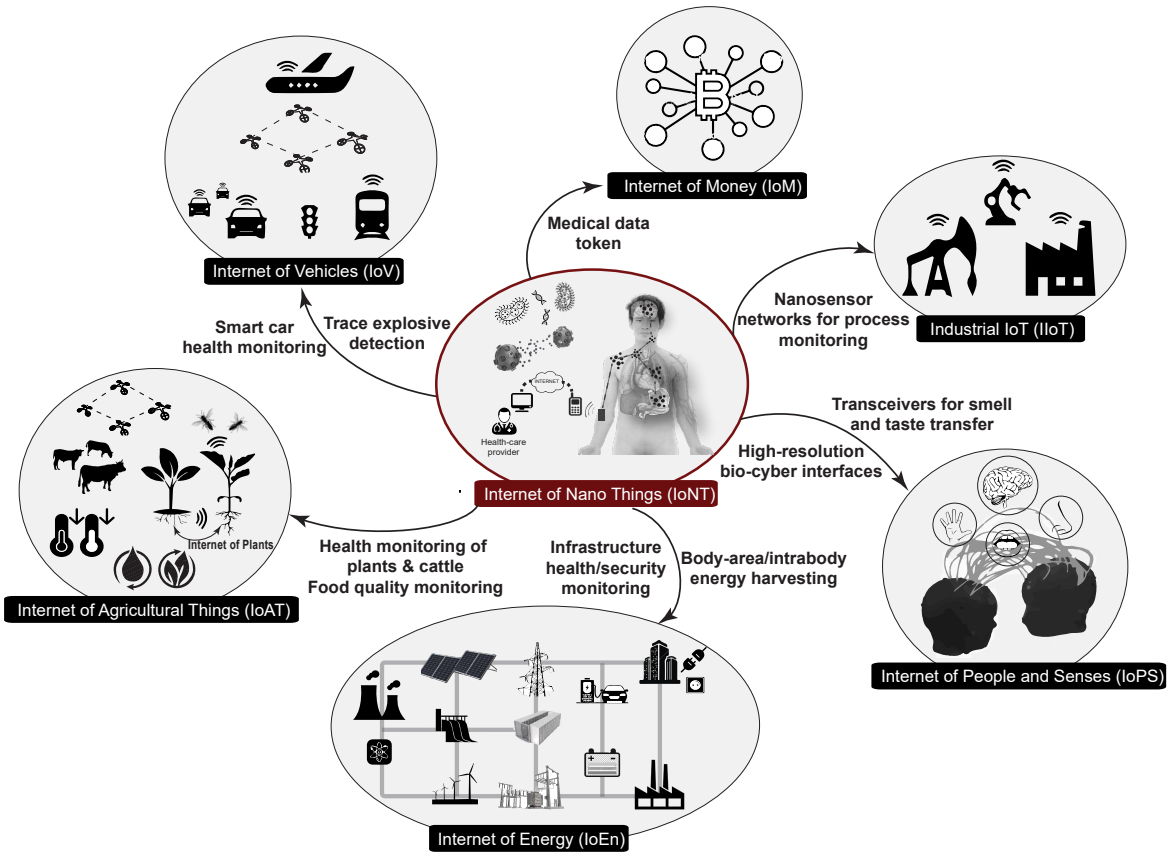

Fig. 1.3 IoNT as the core enabling technology of IoE.

require bio-compatibility, and thus, necessitate properties that are readily offered by natural molecular nanonetworks.

1.3 Main Contributions

The realisation of molecular nanonetworks demands novel engineering solutions, i.e., identification of the existing molecular communication mechanisms, such as those in human body systems, establishing foundations of molecular communication theory, development of networking techniques for nanomachines, and perhaps most importantly, the design and implementation of transceiver architectures suitable for MC applications.

The current literature, as reviewed in Chapter 2, mostly relies on unrealistic assumptions that isolate the MC channel from the processes regarding the transceiving operation. This causes a discrepancy between the theory and practice, as is clear from the initial experimental studies performed with commercially available biochemical sensors and molecular spray nozzles utilised as MC receiver and transmitter [10–12]. These studies

show that the nonlinearity and time-variance caused by the operation of transceivers do not match the theoretical results, invalidating a large number of communication and networking methods and protocols built upon these assumptions. Therefore, there is an urgent need for an intense research towards modelling and developing transceiver architectures for MC, and revisiting the previously established theoretical models by taking into account all the components of the transceiving operations.

This interdisciplinary PhD thesis work is one of the first research efforts that aim at developing realistic and practical micro/nanoscale receiver architectures and detection techniques for MC. In this direction, this dissertation addresses both nanomaterial-based and biological design approaches for MC receivers. For nanomaterial-based receiver designs, first, I develop an analytical model for a microfluidic MC system with a surface-based receiver, which is a highly nonlinear and time-varying convection-diffusion-reaction system and typically necessitates the use of computationally expensive numerical methods for extracting basic ICT performance metrics. Second, I fabricate a graphene field-effect transistor biosensor-based MC receiver integrated into a microfluidic MC system, and perform binary information transmission with single-stranded DNA molecules. This research stands as the first practical implementation of a micro/nano MC system in the literature. The experimental results obtained with the implemented microfluidic MC system are shown to be in good agreement with the developed analytical model.

For biological MC receiver designs, I develop multiple low-complexity MC detection methods, which exploit the stochastic ligand-receptor interactions taking place on the receiver surface to tackle the saturation problem resulting from finite number of receptors, and provide reliable detection under molecular interference. Following a similar approach, I also develop the first channel sensing method for MC, which enables simultaneous sensing of the concentrations of multiple types of ligands in the channel environment. This research is particularly important for developing multiple access and cognitive radio techniques for MC towards realising dense MC nanonetworks within IoNT and IoE frameworks.

1.4 Structure of the Thesis

This dissertation is organised as follows. Chapter 2 introduces the field of MC as an enabling technology for IoNT and IoE. I discuss about the fundamentals of MC along with a brief overview of its applications and challenges. I then present the operation principles of the MC receiver along with its essential requirements, and provide a detailed

review of the existing approaches to design MC receiver architectures and detection methods.

In Chapter 3, I develop an analytical model that can provide approximate solutions for the nonlinear and time-varying convection-diffusion-reaction equations to extract ICT performance metrics of a microfluidic MC system, where the information is encoded into the concentration of finite-duration molecular pulses.

In Chapter 4-6, I develop the detection and channel sensing methods for biological MC receivers with ligand receptors, and present their performance analysis from detection and estimation theoretical perspective. The maximum-likelihood (ML) detection method exploiting the unbound time intervals of ligand-receptor reactions to overcome the receptor saturation problem is presented in Chapter 4. The MC channel sensing method that can simultaneously sense the concentration of different types of ligands is introduced in Chapter 5. The design and performance evaluation of MC detection methods that can overcome the molecular interference problem is presented in Chapter 6.

In Chapter 7, I present the details about the fabrication and characterisation of a micro/nanoscale graphene-based MC receiver, and report on the results of the first MC data transmission using a microfluidic setup.

Lastly, Chapter 8 is dedicated to conclusions and future work.

Chapter 2

Molecular Communications (MC)

2.1 Fundamentals of MC

MC, the use of molecules to encode, transmit, receive and decode information, is radically different from conventional communication paradigms, e.g., EM communications, in various aspects such as the size and type of network entities, information transmission mechanisms, noise sources and fundamental performance limits including transmission delay, achievable data rates, coverage and power consumption.

Example MC scenarios between pairs of nanomachines are depicted in Fig. 2.1, where the messages are encoded into the concentration of molecules, and then transmitted to the receiver through molecular propagation in a fluid channel. The information can also be encoded into the type, release time, or the electronic state of the molecules [7].

Different kinds of propagation methods for molecular messages are investigated in the literature, such as passive diffusion, active transport with molecular motors [13], convection, and transport through gap junctions [14]. Among these, passive diffusion is the most promising, as it does not require energy consumption, and thus perfectly suits the energy limitations of the envisioned nanomachines.

MC channel has many peculiar characteristics. For example, the discrete nature of information carriers, i.e., molecules, results in molecular counting noise, which is of similar nature with the shot noise occurring in photonic devices [15]. The stochastic nature of the ligand-receptor binding process occurring at the receiver gives rise to coloured noise, also leading to a strong correlation between molecular propagation process and reception [16]. The slow nature of diffusion leads to a substantial amount of channel memory, which in turn, causes severe intersymbol interference (ISI), and limits the achievable data transmission rates [17]. The same reason also causes a significant delay in the transmission [18].

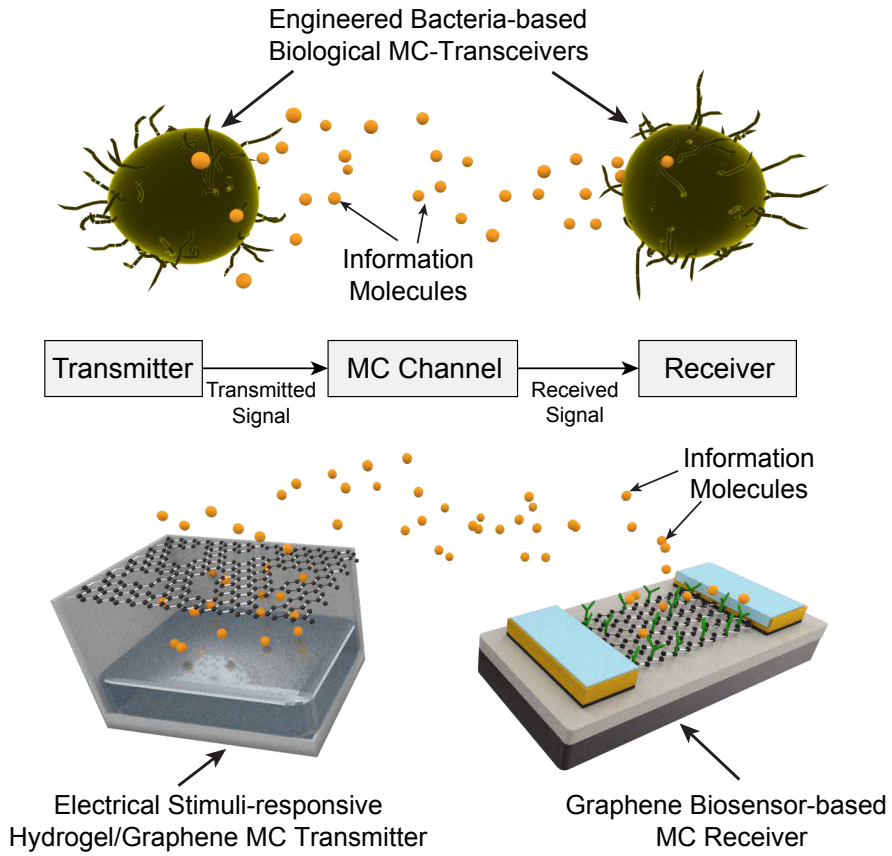

Fig. 2.1 Components of an MC system with biological and nanomaterial-based MC transmitter and receiver design approaches.

Modulation techniques in MC fundamentally differ from that in conventional EM communications, as the modulated entities, i.e., molecules, are discrete in nature, and the developed techniques should be robust against highly time-varying characteristics of the MC channel, as well as inherently slow nature of the propagation mechanisms [7]. Exploiting the observable characteristics of molecules, researchers have proposed to encode information into the concentration, type, or release time of the molecules [19, 20]. The simplest modulation method proposed for MC is on-off keying (OOK) modulation, where a binary symbol is represented by releasing a number of molecules or not releasing any [21]. Similarly, using a single type of molecule, concentration shift keying (CSK), that is analogous to amplitude shift keying (ASK) in traditional wireless channels, is introduced in order to increase the number of transmitted symbols by encoding information into the molecular concentration levels [22]. Molecular information can also be encoded into the type of molecules, i.e., molecule shift keying (MoSK) [20], or into the both type and

concentration of molecules to boost the data rate [23]. Additionally, the release order of different types of molecules [24], and the release time of single type of molecules [25] can be modulated to encode information in MC. Finally, in [26], authors propose the isomer-based ratio shift keying (IRSK), where the information is encoded into the ratio of different types of isomers in a molecule, i.e., molecule ratio-keying.

There are mainly two approaches considered for designing artificial nanomachines that can perform MC and build nanoscale networks. The first one is based on the use of novel nanomaterials, such as graphene, silicon nanowire (SiNW) and carbon nanotube (CNT), which manifest extraordinary characteristics at the interface of biology and electronics [27]. The other approach is based on synthetic biology, and envisions engineered, i.e., genetically modified, bacteria as artificial nanomachines with communication functionalities wired into their intracellular signalling networks [28]. The transmitter and receiver architectures are determined by the nature of the nanomachines. The receiver of a nanomachine is responsible for detecting the incoming molecular messages, transducing them into a processable signal, and processing the signal for extracting the encoded information. The decoded information can then be used by the nanomachine to realise a prespecified operation, e.g., modulation of gene expression or translocation. Therefore, the performance of the receiver is critical for the proper functioning of the nanomachine, and thus of the overall nanonetwork application.

2.1.1 Applications of MC

MC is not particularly positioned to increase the data rate beyond the level already provided by the state-of-the-art communication technologies, but to extend the connectivity to unprecedented environments where other techniques would perform poorly. In such environments, MC, as an enabling technology for IoNT, is promising for novel applications with high societal and economic impact. One of these environments is the human body, which is itself a large-scale heterogeneous molecular communication network of human body systems and living cells [29, 7]. Therefore, most of the envisioned MC applications are focused on the human healthcare. These range from smart drug delivery to continuous health monitoring, enabling the early diagnosis and treatment of human body diseases and maintaining the homeostasis [7, 8, 30]. In particular, molecular networks of mobile nanobiosensors circulating in the cardiovascular system and performing distributed sensing of biomarkers can enable the detection of human body disorders with single molecular resolution [8]. Molecular networks of collaborative active bionanomachines carrying drug molecules can deliver drugs to the targeted regions in human body without causing any side effect [31, 32]. Nanoactuators capable of establishing a molecular communication

link with natural cells can modulate the immune system response by amplifying or inhibiting it to preserve the homeostasis [8]. Based on the understanding of the molecular signalling pathways in cancer metastasis, molecular nanonetworks acting as molecular jammers can interfere with these natural pathways and inhibit the metastasis [7]. In a similar way, nanomachines, e.g., synthetic bacteria, capable of molecular communications can interfere with and modulate the molecular signalling in the gut-brain axis, which is connected with many diseases, such as depression and irritable bowel syndrome [33]. Moreover, implantable artificial organs and cells, e.g., artificial synapse, capable of mimicking the natural molecular communications can replace their impaired counterparts in the human body for the treatment of many irreversible disorders, e.g., spinal cord injury and Alzheimer's disease [7]. Again, synthetically modified human cells with new functionalities, e.g., logic-based sensing and actuation [34], can provide new opportunities for autonomous detection and treatment of many diseases.

Molecular communications, particularly in microfluidic channels, can also find a significant role in tissue engineering [8], and organ-on-chip technologies [35], providing realistic *in vitro* testbeds for drug tests obviating the need for animal testing, and in lab-on-chip technologies [36] by facilitating the efficient handling and processing of analytes.

Additionally, the use of mobile molecular nanonetworks of synthetic bacteria for localisation, targeting and inhibition of toxic chemical agents can find application in smart environmental monitoring [37]. Other applications of MC include the control of animal and plant behaviour through devices capable of pheromone-based MC [38], bacteria-based storage and transfer of high amount of digital data encoded into the base sequences of DNA molecules [39], molecular computers [40, 41], and infrastructure monitoring with molecular sensor networks in harsh environments, e.g., subterranean tunnels, or oil and gas pipelines, where EM communication is deemed unfeasible [42].

I believe that the practical realisation of nanoscale MC components, including the MC receiver, will greatly extend the application range of MC by revealing unique and unprecedented opportunities at the interface of nanotechnology, biology, and ICT.

2.2 Detection Methods for MC

Detection is one of the fundamental aspects of communications having tremendous impact over the overall communication performance. The detection of MC signals is particularly interesting due to the peculiarities of the MC channel and the communicating nanomachines, which impose severe constraints on the design of detection methods. For

example, the limited energy budget and computational capabilities of nanomachines due to their physical design restrict the complexity of the methods. The memory of the diffusion channel causes severe ISI and leads to time-varying channel characteristics with very short coherence time. The stochastic nature of the Brownian motion and the sampling of discrete message carriers bring about different types of noise, e.g., counting noise and receptor binding noise. The physiological conditions, in which most of the nanonetwork applications are envisioned to operate, imply the abundance of molecules with similar characteristics that can lead to strong molecular interference. These challenges have been addressed in MC to different extents. In this section, I provide an overview of the state-of-the-art MC detection approaches, along with a discussion on their performances and weaknesses.

Existing approaches to the MC detection problem can be classified according to the considered channel and received signal models, which reflect the envisioned device architectures that impose different constraints or allow different simplifications over the problem. Accordingly, detection methods are divided into two main categories: MC detection with passive and absorbing receivers, and MC detection with reactive receivers.

2.2.1 MC Detection with Passive and Absorbing Receivers

The nonlinearities and complexity of the MC systems often lead researchers to use simplifying assumptions to develop detection methods and analyse their performances. To this end, the intricate relationship between molecular propagation and sampling processes is often neglected.

Passive receiver (PA) concept is the most widely used simplifying assumption in the MC literature, as it takes the physical sampling process out of the equation, such that researchers can focus only on the transport of molecular messages to the receiver location. Accordingly, the passive receiver is often assumed to be a spherical entity whose membrane is transparent to all kinds of molecules, and it is a perfect observer of the number of molecules within its spherical *reception space*, as shown in Fig. 2.2 [15]. In the passive receiver approximation, the receiver has no impact on the propagation of molecules in the channel. Passive receivers can also be considered as if they include ligand receptors, which are homogeneously distributed within the reception space with very high concentration and infinitely high rate of binding with ligands, such that every single molecule in the reception space is effectively bound to a receptor at the time of sampling.

Another modelling approach, i.e., absorbing receiver (AB) concept [43], considers receiver as an hypothetical entity, often spherical, which absorbs and degrades every single

molecule that hits its surface, as demonstrated in Fig. 2.2. This approach improves the assumption of passive receiver one step further towards a more realistic scenario including a physical interaction between the receiver and the channel. In contrast to passive receiver, absorbing receiver can be considered to have receptors located on its surface. For a perfectly absorbing receiver, this means very high concentration of receptors with infinitely high absorption rate, such that every molecule that hits the surface is bound and consumed instantly.

Physical correspondence of both models is highly questionable. Nevertheless, they are widely utilized in the literature as they provide upper performance limits. However, ignoring the finite-rate receptor-ligand reactions, which often leads to further intricacies, e.g., receptor saturation, stands as a major drawback of these approaches.

Received Signal Models

When constructing the received signal models for diffusion-based MC, the transmitter geometry is usually neglected assuming that the it is a point source that does not occupy any space. This assumption is deemed valid when the distance between the transmitter and receiver is considerably larger than the physical sizes of the devices. Throughout this section, I will mostly focus on on-off keying (OOK) modulation, a particular type of concentration-shift keying (CSK) modulation, where the transmitter performs an impulsive release of a number of molecules to transmit bit-1, and does not send any molecule to transmit bit-0. This is the most widely used modulation scheme in MC detection studies, as it simplifies the problem while capturing the properties of the MC channel. However, I will also briefly review the detection schemes corresponding to other modulation methods, e.g., timing-based modulation and molecule-shift keying (MoSK) modulation, throughout this section.

Molecular propagation in the channel is usually assumed to be only through free diffusion, or through the combination of diffusion and uniform flow (or drift). In both cases, the channel geometry is often neglected and assumed to be unbounded, and molecules are assumed to propagate independently from each other. In some studies addressing passive receivers, researchers consider the existence of enzymes in the channel, which reduce the impact of the ISI by degrading the residual messenger molecules through first-order reaction [44]. For a three dimensional free diffusion channel with uniform flow in the presence of degrading enzymes, the number of molecules observed in the spherical reception space of a passive receiver follows non-stationary Poisson process [45, 46], i.e.,

$$N_{\mathrm{RX|PA}}(t) \sim \mathrm{Poisson}\left(\lambda_{\mathrm{RX}}(t)\right), \tag{2.1}$$

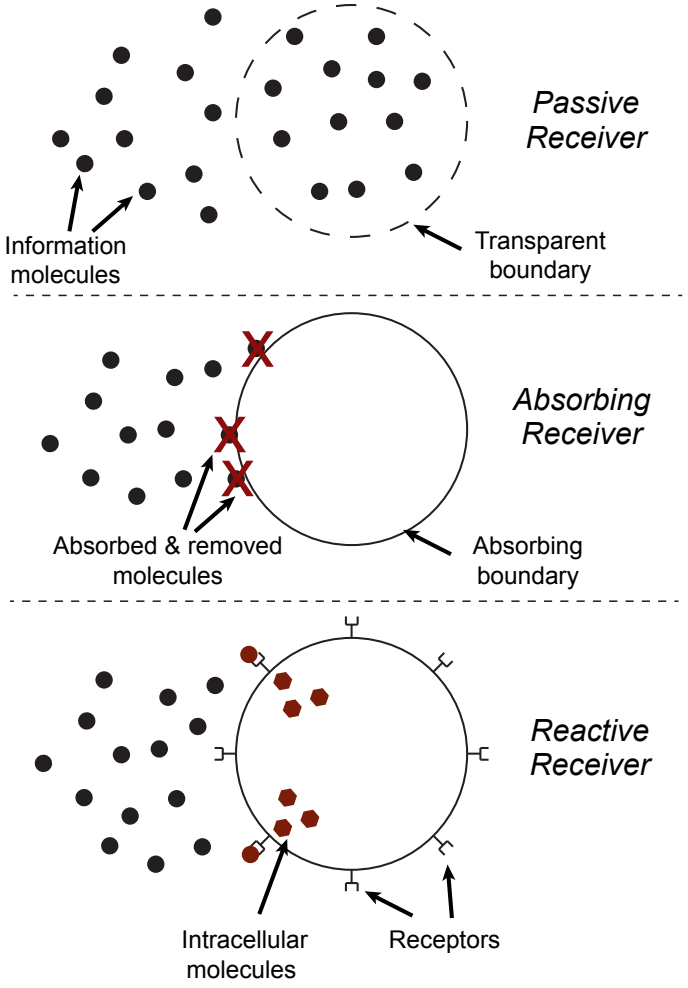

Fig. 2.2 Hypothetical MC receiver models used for developing detection methods.

where the time-varying mean of this process $\lambda_{\mathrm{RX}}(t)$ can be given by

$$\lambda_{\mathrm{RX}}(t) = \lambda_{\mathrm{noise}} + Q \sum_{j=1}^{\left\lfloor \frac{t}{T_s}+1 \right\rfloor} s[i] P_{\mathrm{obs}}\Big(t - (j-i)T_s\Big). \tag{2.2}$$

The mean depends on the number of transmitted molecules Q to represent bit 1, the symbols transmitted in the current symbol interval as well as in the previous symbol intervals, i.e., $s[i]$, and the length of a symbol interval T_s. Most MC studies include an additive stationary noise in their models representing the interfering molecules available in the channel as a result of an independent process in the application environment. These molecules are assumed to be of the same kind with the messenger molecules and their number is represented by a Poisson process and captured by λ_{noise}. Channel response

is integrated into the model through the function $P_{\text{obs}}(t)$, which is the probability of a molecule transmitted at time $t = 0$ to be within the sampling space at time t. When the transmitter-receiver distance is considerably large, ligands are typically assumed to be uniformly distributed within the reception space. As a result, the channel response can be written as

$$P_{\text{obs}}(t) = \frac{V_{\text{RX}}}{(4\pi Dt)^{3/2}} \exp\left(-kC_E t - \frac{|\vec{r}_{\text{eff}}|^2}{4Dt}\right), \tag{2.3}$$

where $V_{\text{RX}} = \frac{4}{3}\pi d_{\text{RX}}^3$ is the volume of the spherical receiver with radius d_{RX}, D is the diffusion coefficient, C_E is the uniform concentration of the degrading enzymes in the channel, k is the rate of enzymatic reaction, and $\vec{r}_{\text{eff}}$ is the effective transmitter-receiver distance vector, which captures the effect of uniform flow [45]. Assuming that the transmitter and receiver are located at $\vec{r}_{\text{TX}} = (0, 0, 0)$, $\vec{r}_{\text{RX}} = (x_0, 0, 0)$, respectively, and the flow velocity is given by v_x, v_y, v_z in 3D Cartesian coordinates, the magnitude of the effective distance vector can be written as follows

$$|\vec{r}_{\text{eff}}| = \sqrt{(x_0 - v_x t)^2 + (v_y t)^2 + (v_z t)^2}. \tag{2.4}$$

For an absorbing receiver, the received signal is usually taken as the number of molecules absorbed by the receiver within a time interval [43]. For a diffusion channel without flow, the probability density for a molecule emitted at $t = 0$ to be absorbed by a perfectly absorbing receiver of radius r_r and located at a distance r from the transmitter at time t is given by

$$f_{\text{hit}}(t) = \frac{r_r}{r} \frac{1}{\sqrt{4\pi Dt}} \frac{r - r_r}{t} \exp\left(-\frac{(r - r_r)^2}{4Dt}\right), \tag{2.5}$$

and the cumulative distribution function (CDF) becomes

$$F_{\text{hit}}(t) = \int_0^t f_{\text{hit}}(t')dt' = \frac{r_r}{r} \operatorname{erfc}\left[\frac{r - r_r}{\sqrt{4Dt}}\right], \tag{2.6}$$

where erfc is the complementary error function [43]. The CDF can be used to calculate the probability of a molecule transmitted at time $t = 0$ to be absorbed within the k^{th} signalling interval, i.e.,

$$P_k = F_{\text{hit}}(kT_s) - F_{\text{hit}}([k - 1]T_s). \tag{2.7}$$

When considering multiple independent molecules emitted at the same time, the number of molecules absorbed at the k^{th} interval becomes Bernoulli random variable with the success probability of P_k. Assuming that the success probability is low enough, Gaussian approximation of the Bernoulli random process can be used to write

$$N_{\mathrm{RX|AB}}[i] \sim \mathcal{N}\left(\mu[i], \sigma^2[i]\right), \tag{2.8}$$

where its signal-dependent mean and variance can be written as a function of current and previously transmitted bits $s[i]$, i.e.,

$$\mu[i] = Q \sum_{i}^{k} P_k s[i-k+1], \tag{2.9}$$

$$\sigma^2[i] = \sigma^2_{\mathrm{noise}} + Q \sum_{i}^{k} P_k(1-P_k) s[i-k+1]. \tag{2.10}$$

Note that as in the case of passive receiver, the received signal model includes the contribution of a stationary noise through its variance $\sigma^2_{\mathrm{noise}}$. Unfortunately, in the literature, there is no analytical model for absorbing receivers in diffusion-based MC channels with uniform flow and degrading enzymes.

Detection Methods

Detection methods for MC with passive and absorbing receivers in general can be divided into two main categories depending on the method of concentration measurement: sampling-based and energy-based detection. Passive receivers are usually assumed to perform sampling-based detection, which is based on sampling the instantaneous number of molecules inside the reception space at a specific sampling time [56]. Absorbing receivers, on the other hand, are typically assumed to utilize energy-based detection, which uses the total number of molecules absorbed by the receiver during a prespecified time interval, that is usually the symbol interval [55]. In some studies, passive receivers are also considered to perform energy-based detection through taking multiple independent samples of number of molecules inside the reception space at different time instants during a single symbol interval, and passing them through a linear filter which outputs their weighted sum as the energy of the received molecular signal [49, 45].

As in conventional wireless communications, detection can be done on symbol-by-symbol or sequential basis. The symbol-by-symbol detection tends to be more practical in terms of complexity, whereas the sequence detectors require the receiver to have a memory to store the previously decoded symbols. Due to the MC channel memory

Table 2.1 Comparison Matrix for MC Detectors with Passive and Absorbing Receivers

Description	**Channel Characteristics**	**Modulation & Transmit Waveform**	**Detector Type**	**Rx Type**	**Measurement Method**	**CSI Req.**	**Complex.**	**Perf.**
One-shot fixed-threshold detector [47]	Diffusion	CSK/OOK-Impulse	SbS	PA	Sampling	Ins. CSI	Low	Sub.
Weighted sum detector [48]	Diff./Flow/En./EI	CSK/OOK-Impulse	SbS	PA	Sampling	Ins. CSI	Low	Opt.
Weighted sum detector [49, 45]	Diff./Flow/En./EI	CSK/OOK-Impulse	SbS	PA	Sampling	Ins. CSI	Low	Sub.
Adaptive-threshold detector [50]	Diff./EI	CSK/OOK-Impulse	SbS	PA	Sampling	No CSI	Moderate	Sub.
Adaptive-threshold detector [51–53]	Diffusion	CSK/OOK-Impulse	SbS	AB	Energy	No CSI	Low	Sub.
Linear equalizer (MMSE) [46]	Diffusion	CSK/OOK-Pulse	Seq.	PA	Sampling	Ins. CSI	Very High	Sub.
Nonlinear equalizer (DFE) [46]	Diffusion	CSK/OOK-Pulse	Seq.	PA	Sampling	Ins. CSI	Very High	Sub.
ML sequence detector with Viterbi [46]	Diffusion	CSK/OOK-Pulse	Seq.	PA	Sampling	Ins. CSI	Very High	Opt.
ML sequence detector with Viterbi [49]	Diff./Flow/En./EI	CSK/OOK-Impulse	Seq.	PA	Sampling	Ins. CSI	Very High	Opt.
ML sequence detector with Viterbi [54]	Diffusion	MoSK-Impulse	Seq.	PA	Sampling	Ins. CSI	Very High	Opt.
Near ML sequence det. with RS Viterbi [47]	Diffusion	CSK/OOK-Impulse	Seq.	PA	Sampling	Ins. CSI	High	Sub.
Strength-based ML detector [55]	Diffusion	CSK/ASK-Impulse	SbS	PA	Energy	Ins. CSI	High	Opt.
Sampling-based ML detector [56]	Diffusion	CSK/ASK-Impulse	SbS	PA	Sampling	Ins. CSI	High	Opt.
Derivative-based detector [57]	Diffusion	CSK/OOK-Impulse	SbS	AB	Energy	Ins. CSI	Moderate	Sub.
Noncoherent detector [58]	Diffusion	CSK/B-CSK-Pulse	SbS	PA	Sampling	No CSI	Low	Sub.
Local convexity-based noncoherent det. [59]	Diffusion	CSK/OOK-Pulse	SbS	PA	Sampling	No CSI	Moderate	Sub.
Noncoherent ML threshold-based det. [60]	Diff./EI	CSK/OOK-Impulse	SbS	PA&AB	Sampling	Stat. CSI	Low	Opt.
Noncoherent ML sequence detector [60]	Diff./EI	CSK/OOK-Impulse	Seq.	PA&AB	Sampling	Stat. CSI	High	Opt.
Noncoherent decision-feedback detector [60]	Diff./EI	CSK/OOK-Impulse	Seq.	PA&AB	Sampling	Stat. CSI	Very High	Sub.
Noncoherent blind detector [60]	Diff./EI	CSK/OOK-Impulse	SbS	PA&AB	Sampling	No CSI	Low	Sub.
ML sequence detector with CC codes [61]	Diff./EI	CSK/ASK-Impulse	Seq.	PA	Sampling	No CSI	Very High	Opt.
Asynchronous fixed-threshold detector [62]	Diffusion	CSK/OOK-Impulse	SbS	PA	Sampling	Ins. CSI	Moderate	Sub.
Asynchronous adaptive-th. det. with DF [62]	Diffusion	CSK/OOK-Impulse	SbS	PA	Sampling	Ins. CSI	High	Sub.
Adaptive-threshold detector (Mobile MC) [63]	Diff./TV	CSK/OOK-Impulse	SbS	PA	Sampling	Ins. CSI	Very High	Sub.
Single-sample th. det. (Mobile MC) [64]	Diff./Flow/TV	CSK/OOK-Impulse	SbS	PA	Sampling	Out. CSI	High	Sub.
ML sequence detector (Timing Channel) [65]	Diffusion	Release time-Impulse	Seq.	AB	Arrival time	Ins. CSI	Very High	Opt.
Sequence detector with modified Viterbi [65]	Diffusion	Release time-Impulse	Seq.	AB	Arrival time	Ins. CSI	High	Sub.
Symbol by symbol timing detector [65]	Diffusion	Release time-Impulse	SbS	AB	Arrival time	No CSI	Low	Sub.
ML detector with FA & LA times [66, 67]	Diffusion	Release time-Impulse	SbS	AB	Arrival time	Ins. CSI	Moderate	Opt.

Abbreviations | Diff.: Diffusion – En.: Enzyme – EI: External Interference – TV: Time-varying – SbS: Symbol-by-symbol detector – Seq.: Sequential detector – PA: Passive receiver – AB: Absorbing receiver – Ins. CSI: Instantaneous CSI – Stat. CSI: Statistical CSI – Out. CSI: Outdated CSI – Sub.: Sub-optimal – Opt. Optimal – Complex.: Complexity – Perf.: Performance – DF: Decision-Feedback – FA: First Arrival – LA: Last Arrival – CC codes: Constant Composition codes – RS: Reduced-State

causing a considerable amount of ISI for high data rate communication, the sequence detectors are more frequently studied in the literature.

Next, I review the existing MC detection techniques developed for passive and absorbing receivers by categorizing them into different areas depending on their most salient characteristics. A comparison matrix for these methods can also be seen in Table 2.1.

Symbol-by-Symbol (SbS) Detection: SbS MC detectors in the literature are usually proposed for very low-rate communication scenarios, where the ISI can be neglected, asymptotically included into the received signal model with a stationary mean and variance, or approximated by the weighted sum of ISI contributions of a few previously transmitted symbols. In [47], a one-shot detector is proposed based on the asymptotic approximation of the ISI assuming that the sum of decreasing ISI contributions of the previously transmitted symbols can be represented by a Gaussian distribution through central limit theorem (CLT) based on Lindeberg's condition. A fixed-threshold detector is proposed with a threshold maximizing the mutual information between transmitted and decoded symbols. Similarly, in [45, 49], a matched filter in the form of a weighted sum detector is proposed using a different asymptotic ISI approximation as though it results from a continuously emitting source leading to a stationary Poisson distribution of interference molecules inside the reception space. In this scheme, a passive receiver performs energy-based detection taking multiple samples at equally spaced sampling times during a single symbol transmission, and the weights of the samples are adjusted according to the number of molecules expected at the corresponding sampling times. This matched filter is proved to be optimal in the sense that it maximises SNR at the receiver. However, the optimal threshold of this detector does not lend itself to a closed-form expression, and thus, it should be numerically obtained through resource-intensive search algorithms. Similarly, in [48], considering also the external sources of interference, another linear matched filter is designed maximizing the expected signal-to-interference-plus-noise-ratio (SINR) for SbS detection, and shown to outperform previous schemes especially when the ISI is severe. There are also adaptive-threshold-based SbS detection methods relying on receivers with memory of varying length taking into account only the ISI contribution of a finite number of previously transmitted symbols [50–53, 55, 56]. In these schemes, the adaptive threshold is updated for each symbol interval using the ISI estimation based on the previously decoded symbols. SbS detection is also considered in [60, 62], which will be discussed next in the context of noncoherent and asynchronous detection.

Sequence Detection and ISI Mitigation: Optimal sequence detection methods based on Maximum a Posteriori (MAP) and Maximum Likelihood (ML) criteria are proposed in [46] for MC with passive receivers. Even though the complexity of the sequence detectors are reduced by applying Viterbi algorithm, it still grows exponentially with increasing channel memory length. To reduce the complexity further, a sub-optimal linear equalizer based on Minimum Mean-Square Error (MMSE) criterion is proposed. To improve the performance of the sub-optimal detection, a nonlinear equalizer, i.e., Decision-Feedback Equalizer (DFE), is also proposed in the same study. DFE is shown to outperform linear equalizers with significantly less complexity than optimal ML and MAP sequence detection methods. Similarly, a near-optimal ML sequence detector employing Viterbi algorithm is proposed in [47]. Another optimal ML sequence detector is introduced in [49] for MC with uniform flow and enzymes that degrade information molecules.

In addition to the sequence detection methods and equalizers, there are other approaches proposed to overcome the effects of the ISI on detection. For example, in [68], the authors propose to shift the sampling time by increasing the reception delay to reduce the effect of ISI. In [57], a derivative-based signal detection method is proposed to enable high data rate transmission. The method is based on detecting the incoming messages relying on the derivative of the channel impulse response (CIR).

Noncoherent Detection: Most of the MC detection methods requires the knowledge of the instantaneous CSI in terms of CIR. However, CIR in MC, especially in physiologically relevant conditions, tends to change frequently, rendering the detection methods relying on the exact CIR knowledge ineffective. Estimating the instantaneous CIR is difficult and requires high computational power. To overcome this problem, researchers propose low-complexity noncoherent detection techniques. For example, in [53], the authors develop a simple detection method for absorbing receivers, which does not require the channel knowledge. In this scheme, the receiver performs a threshold-based detection by comparing the number of absorbed molecules in the current interval to that of the previous symbol interval. The adaptive threshold is updated in every step of detection with the number of molecules absorbed. However, this method performs poorly when a sequence of consecutive bit-1's arrives. Similarly, in [58], the difference of the accumulated concentration between two adjacent time intervals is exploited for noncoherent detection. In [59], the local convexity of the diffusion-based channel response is exploited to detect MC signals in a noncoherent manner. A convexity metric is defined as the test statistics, and the corresponding threshold is derived. There are also methods requiring only the statistical CSI rather than the instantaneous CSI [60]. Additionally,

constant-composition codes are proposed to enable ML detection without statistical or instantaneous CSI, and shown to outperform uncoded transmission with optimal coherent and noncoherent detection, when the ISI is neglected [61].

Asynchronous Detection: The synchronization between the communicating devices is another major challenge. However, in the previously discussed studies, synchronization is assumed to be perfect. To overcome this limitation, an asynchronous peak detection method is developed in [62] for the demodulation of MC signals. Two variants has been proposed. First method is based on measuring the largest observation within a sampling interval. This SbS detection method is of moderate complexity and non-adaptive, comparing the maximum observation to a fixed threshold. The second method is adaptive and equipped with decision feedback to remove the ISI contribution. In this scheme, the receiver takes multiple samples per bit and adjusts the threshold for each observation based on the expected ISI.

Detection for Mobile MC: The majority of MC studies assumes that the positions of transmitter and receiver are static during communication. The mobility problem of MC devices has just recently started to attract researchers' attention. For example, MC between a static transmitter and a mobile receiver is considered in [63], where the authors propose to reconstruct the CIR in each symbol interval using the time-varying transmitter-receiver distance estimated based on the peak value of the sampled concentration. Two adaptive schemes, i.e., concentration-based adaptive threshold detection and peak-time-based adaptive detection, are developed based on the reconstructed CIR. In [64], different mobility cases including mobile transmitter and receiver, mobile transmitter and fixed receiver, and mobile receiver and fixed transmitter are considered to develop a stochastic channel model for diffusive mobile MC systems. The authors derive analytical expressions for the mean, PDF, and auto-correlation function (ACF) of the time-varying CIR, through an approximation of the CIR with a log-normal distribution. Based on this approximation, a simple model for outdated CSI is derived, and the detection performance of a single-sample threshold detector relying on the outdated CSI is evaluated.

Other Detection Techniques: MC detection problem is also addressed for molecule shift keying (MoSK) modulation. In [54], an optimal ML sequence detector employing Viterbi algorithm is proposed assuming that a passive receiver can independently observe MC signals carried by different types of molecules. This assumption greatly simplifies the problem and enable the application of detection methods developed for CSK-modulated MC signals for MoSK signals as well.

Diffusion-based molecular timing (DBMT) channels are also addressed from detection theoretical perspective. DBMT channels without flow are accompanied by a Lévy

distributed additive noise having a heavy algebraic tail in contrast to the exponential tail of inverse Gaussian distribution, which DBMT channel with flow follows [66]. In [65], an optimal ML detector is derived for DBMT channels without flow; however, the complexity of the detector is shown to have exponential computational complexity. Therefore, they propose sub-optimal yet practical SbS and sequence detectors based on the random time of arrivals of the simultaneously released information molecules, and show that the performance of the sequence detector is close to the one of computationally expensive optimal ML detector.

In DBMT channels without flow, linear filtering at the receiver results in a dispersion larger or equal to the dispersion of the original, i.e., unfiltered, sample, rendering the performance of releasing multiple particles worse than releasing a single particle. Based on this finding, the authors in [66] develop a low-complexity detector, which is based on the first arrival (FA) time of simultaneously released particles by the transmitter. The method is based on the observation that the probability density of the FA gets concentrated around the transmission time when the number of released molecules M increases. Neglecting ISI, it is shown in the same paper that the proposed FA-based detector performs very close to the optimal ML detectors for small values of M. However, the ML detection still performs significantly better than the FA for high values of M. The detection based on the order statistics has been extended in the same authors' later work [67], where they consider also the detection based on the last arrival (LA) time. Defining a system diversity gain as the asymptotic exponential decrease rate of error probability with the increased number of released particles, they showed that the diversity gain of LA detector approaches to that of computationally expensive ML detector.

2.2.2 MC Detection with Reactive Receivers

This type of receiver samples the molecular concentration of incoming messages through a set of reactions it performs via specialized receptors or enzymes, as shown in Fig. 2.2. The reactive receiver approach is more realistic in the sense that natural cells, e.g., bacteria and neurons, sense molecular communication signals through their receptors on the cell membrane, and many types of artificial biosensors, e.g., bioFETs, are functionalised with biological receptors for higher selectivity. Since synthetic biology, focusing on using and extending natural cell functionalities, and artificial biosensing are the two phenomena that are considered for practical implementation of MC receivers, studying MC detection with reactive receivers has more physical correspondence. Therefore, this thesis work is focused on reactive MC receiver architectures and detection techniques.

Diffusion-based MC systems with reactive receivers, in most cases, can be considered as reaction-diffusion (RD) systems with finite reaction rates. Although RD systems, which are typically highly nonlinear, have been studied in the literature for a long time, they do not usually lend themselves to analytical solutions, especially when the spatio-temporal dynamics and correlations are not negligible. To be able to devise detection methods and evaluate their performance in the MC framework, researchers have come up with different modelling approaches, which will be reviewed next. For the sake of brevity, I focus this review on detection with receivers equipped with ligand receptors which have only one binding site.

Ligand-receptor binding reaction for a single receptor exposed to time-varying ligand concentration $c_L(t)$ can be schematically demonstrated as follows

$$\mathrm{U} \underset{\mathrm{k_-}}{\overset{\mathrm{c_L(t)\ k_+}}{\rightleftharpoons}} \mathrm{B}, \tag{2.11}$$

where k_+ and k_- are the ligand-receptor binding and unbinding rates, respectively; U and B denote the unbound and bound states of the receptor, respectively. When there are N_R receptors, assuming that all of them are exposed to the same concentration of ligands, reaction rate equation (RRE) for the number of bound receptors can be written as [16]

$$\frac{dn_B(t)}{dt} = k_+ c_L(t)\left(N_R - n_B(t)\right) - k_- n_B(t). \tag{2.12}$$

As is clear, while the binding reaction is second-order depending on the concentrations of both ligands and available receptors, unbinding reaction is first-order and only depends on the number of bound receptors.

Most of the time, the bandwidth of MC signals can be assumed to be low enough to drive the binding reaction to near equilibrium and allow applying quasi steady-state assumption for the overall system. In this case, time-varying concentration $c_L(t)$ can be treated constant, i.e., $c_L(t) = c_L$, and $dn_B(t)/dt = 0$, which results in the following expression for the mean number of bound receptors

$$\mathrm{E}[n_B] = \frac{c_L}{c_L + K_D} N_R, \tag{2.13}$$

where $K_D = k_-/k_+$ is the dissociation constant, which is a measure of affinity between the specific type of ligand and receptor. Even at equilibrium, the receptors randomly fluctuate between the bound and unbound state. The number of bound receptors n_B, at equilibrium, is a Binomial random variable with success probability $p_B = c_L/(c_L + K_D)$,

and its variance can be given accordingly by

$$\mathrm{Var}[n_B] = p_B(1 - p_B)N_R. \tag{2.14}$$

More insight can be gained by examining the continuous history of binding and unbinding events over receptors. The likelihood of observing a series of n binding-unbinding events at equilibrium can be given by

$$\mathrm{p}(\{\tau^B, \tau^U\}_n) = \frac{1}{Z} e^{-\sum_{j=1}^{n} \tau_j^U \left(\sum_{i=1}^{M} k_i^+ c_i\right)} \prod_{j=1}^{n} \sum_{i=1}^{M} k_i^+ c_i k_i^- e^{-k_i^- \tau_j^B}, \tag{2.15}$$

where Z is the normalization factor, τ_j^U and τ_j^B are the j^{th} unbound and bound time intervals, respectively, c_i, k_i^+ and k_i^- are the concentration, binding rate, and unbinding rate of i^{th} type of ligand, respectively, M is the number of ligand types present in the channel [69, 70]. Note that the likelihood is equally valid for the cases of single receptor and multiple receptors, as long as the collected n samples of unbound and bound time intervals are independent. These observable characteristics of the ligand-receptor binding reactions have been exploited to infer the incoming messages to different extents, as will be reviewed next.

Received Signal Models

The nonlinearities arising from the interaction of time-varying MC signals with receptors have led to different approaches for modeling MC systems with reactive receivers compromising on different aspects to develop detection techniques and make the performance analyses tractable. A brief review of these modelling approaches are provided as follows.

Reaction-Diffusion Models with Time-varying Input: One of the first attempts to model the ligand-receptor binding reactions from an MC theoretical perspective is provided in [16], where the authors develop a noise model for the fluctuations in the number of bound receptors of a receiver exposed to time-varying ligand concentrations as MC signals. The model is based on the assumption of a spherical receiver, in which ligand receptors and information-carrying ligands are homogeneously distributed. For an analytically tractable analysis, the concentration of incoming ligands is assumed to be constant between two sampling times, i.e., during a sampling interval, and the ligand-receptor binding reaction is assumed to be at equilibrium at the beginning of each sampling interval. In light of these assumptions, the authors obtain the time-varying variance and mean of the number of bound receptors, which are valid only for the corresponding sampling interval. A more general approach without the equilibrium

assumption to obtain the mean number of bound receptors with time-varying input signals, i.e., ligand concentration, is contributed by [71] and [72], through solving the system of differential equations governing the overall diffusion-reaction MC system. The authors of the both studies consider a spherical receiver with ligand receptors on its surface and a point transmitter, which can be anywhere on a virtual sphere centred at the same point as the receiver but larger than that, to obtain a spherical symmetry to simplify the overall problem. As a result, the transmitter location cannot be exactly specified in the problem. In [72], the authors consider that the spherical receiver is capable of binding ligands at any point on its surface, which is exactly equal to the assumption of infinite number of receptors. On the other hand, [71] considers finite number of receptors uniformly distributed on the receiver surface, and addresses this challenge through boundary homogenization. However, boundary homogenization for finite number of receptors does not take into account the negative feedback of the bound receptors on the second-order binding reaction (see (2.12)), and thus, the developed analytical model is not able to capture the indirect effects of finite number of receptors, e.g., receptor saturation. This is clear from their analysis, such that the discrepancy between the analytical model and the particle-based simulation results is getting larger with increasing ligand concentration.

Frequency Domain Model: Another modelling approach is provided in [73], where the authors, assuming that the probability of a receptor to be in the bound state is very low, take the number of available, i.e., unbound, receptors equal to the total number of receptors at all time points. The completely first order characteristics of the resulting RRE enables them to carry out a frequency domain analysis, through which they show the ligand-receptor binding reaction manifests low-pass filter characteristics. However, this approximate model is relevant only when the probability of receptor-ligand binding is very low.

Discrete Model based on Reaction-Diffusion Master Equation (RDME): To capture the stochasticity of the reaction-diffusion MC, another approach is introduced in [74], where the authors develop a voxel-based model based on RDME, with the diffusion and reactions at the receiver modelled as Markov processes. The three-dimensional MC system is discretized and divided into equal-size cubic voxels, in each of which molecules are assumed to be uniformly distributed, and allowed to move only to the neighbouring voxels. In the voxel accommodating the transmitter, the molecules are generated according to a modulation scheme, and the receiver voxel hosts the receptor molecules, where the ligands diffusing into the Rx voxel can react based on law of mass action. The jump of a ligand from one voxel to another is governed by a diffusion rate parameter, which is a

function of the voxel size and the ligand diffusion coefficient. The number of ligands and bound receptors are stored in a system state vector, which is progressed with a given state transition rate vector storing the reaction, diffusion, and molecule generation rates. In the continuum limit, the model is able to provide closed-form analytical expressions for the mean and variance of the number of bound receptors for small-scale systems. However, for larger systems, with a high number of voxels, the efficiency of the model is highly questionable.

Steady-State Model: In addition to the above approaches considering time-varying signals, some researchers prefer using the assumption of steady-state ligand-receptor binding reaction with stationary input signals at the time of sampling, based on fact that the bandwidth of incoming MC signals is typically low because the diffusion channel shows low-pass filter characteristics and the reaction rates are generally higher than the diffusion rate of molecules. This assumption enables the separation of the overall system into two; a deterministic microscale diffusion channel and the stochastic ligand-receptor binding reaction at the interface between the receiver and the channel. Accordingly, at the sampling time, the ligand concentration around the receptors assumes different constant values corresponding to different symbols. The only fluctuations are resulting from the binding reaction, where the random number of bound receptors follows Binomial distribution, whose mean and variance are given in (2.13) and (2.14), respectively. The steady-state assumption is applied in [75], where the authors derive reaction-diffusion channel capacity for different settings. I also adopt this model in developing detection techniques for biological MC receivers in Chapters 4-6.

Detection Methods

The literature on detection methods for MC with reactive receivers is relatively scarce, and the reason can be attributed partly to the lack of analytical models that can capture the nonlinear ligand-receptor binding reaction kinetics and resulting noise and ISI. Nevertheless, the existing methods can be divided into three categories depending on the type of assumptions made and considered receiver architectures.

Detection based on Instantaneous Receptor States: The first detection approach is based on sampling the instantaneous number of bound receptors at a prespecified time, as shown in Fig. 2.3, and comparing it to a threshold. In [72], the authors study a threshold-based detection for OOK modulated ligand concentrations, using the difference between the number of bound molecules at the start and end of a bit interval. In [73], converting the ligand-receptor binding reaction to a completely first-order reaction with the assumption that all of the receptors are always available for binding, the authors

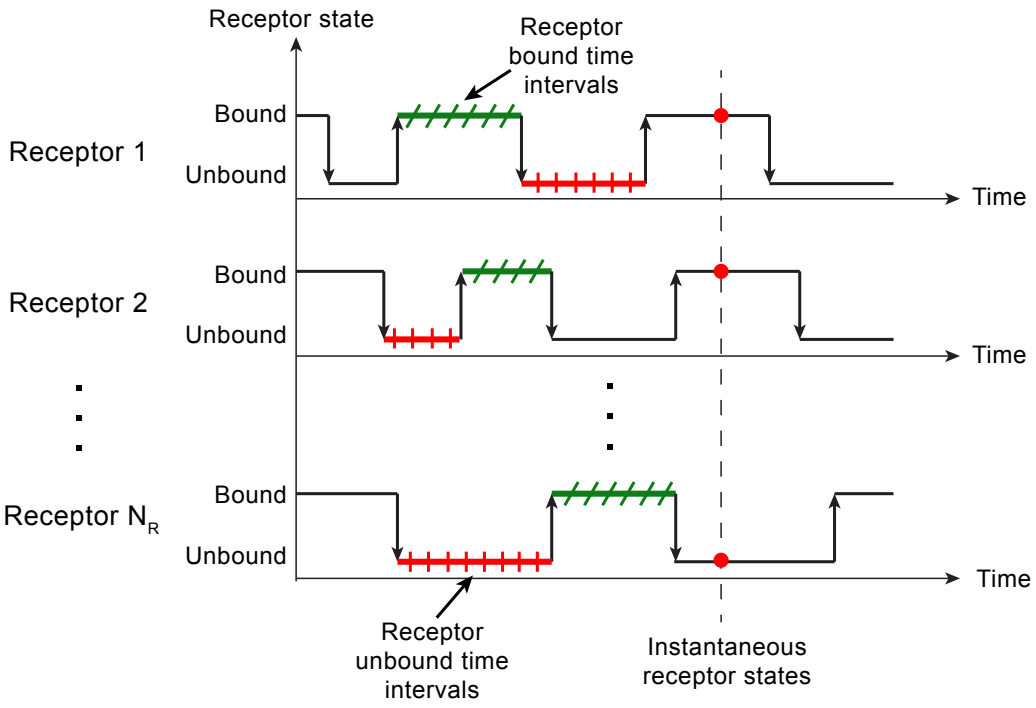

Fig. 2.3 Different methods for sampling receptor states in reactive MC receivers.

manage to transform the problem into the frequency domain. For the modulation, they consider MoSK with different receptors corresponding to different ligands; therefore, the problem basically reduces to a detection problem of the concentration-encoded signals for each ligand-receptor pair. To reduce the amount of noise, they propose to apply a whitening filter to the sensed signal in the form of number of bound receptors, and then utilize the same detection technique they proposed in [54]. An energy-based detection scheme is proposed in [76], where the test statistics is the total number of binding events that occur within a symbol duration. They propose a variable threshold-detection scheme with varying memory length. The article also takes into account the ISI; however, the model assumes that all the receptors are always available for binding, and completely neglects the unbinding of ligands from the receptors, making the reaction irreversible.

Detection based on Continuous History of Receptor States: The second detection approach is based on exploiting the continuous history of binding and unbinding events occurring at receptors, or the independent samples of time intervals that the receptors stay bound and unbound, as demonstrated in Fig. 2.3. As we see in the likelihood function in (2.15), the unbound time intervals are informative of the total ligand concentration, whereas the bound time intervals are informative of the type of bound molecules. In [77, 78], using a voxel-based MC system model introduced in [74], and

by neglecting the ISI, the authors develop an optimal MAP demodulator scheme based on the continuous history of receptor binding events. The authors assume time-varying input signal. The resulting demodulator is an analogue filter, which requires the biochemical implementation of mathematical operations, such as logarithm, multiplication, and integration. The demodulator also needs to count the number of binding events. In [77], they provide an extension of the demodulator for the ISI case by incorporating a decision feedback, and show the performance improvement with increasing receiver memory. The continuous history of receptor unbound states is exploited in Chapter 4, to overcome the saturation problem in reactive receivers with finite number of receptors.

One of the challenges of reactive receivers is their selectivity towards the messenger molecules, which is not perfect in practice. It is highly probable, especially in physiologically relevant environments, that there are similar ligands in the channel, which can also bind the same receptors, even though their unbinding rate is higher than that of the correct, i.e., messenger, ligands. This causes a molecular interference, which impedes the detection performance of the receiver especially when the concentration of interferer molecules is not known to the receiver. This problem is addressed in Chapter 5 and Chapter 6.

Detection for Biosensor-based MC Receivers: The third set of detection methods deals with the biosensor-based receivers, where the binding events are transduced into electrical signals (see Chapter 2). In bioFET-based receivers the concentration of bound charge-carrying ligands are converted into electrical signals that are contaminated with additional noise. It is not possible to observe individual receptors states; therefore, the detection based on continuous history of binding events is not applicable for these receivers. Accounting for the 1/f noise and binding fluctuations at steady-state conditions, in [79], authors develop an optimal ML detection scheme for CSK in the absence of ISI considering a SiNW bioFET-based MC receiver. Approximating the binding and 1/f noise with a Gaussian distribution, they reduce the overall problem to a fixed-threshold detection problem and provide closed-form analytical expressions for the optimal thresholds and corresponding symbol error rates. The performance evaluation reveals that the 1/f noise, which is resulting from the defects of the semiconductor FET channel, surpasses binding noise resulting from the fluctuations of the receptor states, especially at low frequencies, and severely degrades the detection performance.

In Chapter 7, where I report on the fabrication of a micro/nanoscale graphene bioFET-based MC receiver, I adopt a simpler detection approach considering the resource limitations of the envisioned nanomachines. Accordingly, I apply a difference-based detection method for binary OOK-modulated information transmission, which simply

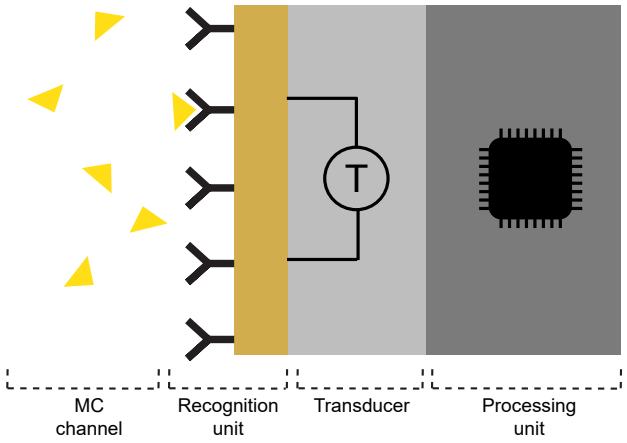

Fig. 2.4 Main functional blocks of an MC receiver architecture.

compares the electrical output sampled at the beginning and end of a bit interval to decode the incoming information. This method is shown to provide acceptable detection performance for the fabricated MC receiver.

2.3 MC Receiver Architectures

MC receiver fundamentally differs from a conventional EM communication receiver. As demonstrated in Fig. 2.4, it basically consists of three subunits. (i) The recognition unit is the interface between the MC channel and the receiver, with the function of selectively interacting with the target molecules that carry the MC information, and thus providing the required molecular selectivity to suppress the interference of other molecular sources in the environment. (ii) The transducer unit converts the molecular recognition events, i.e., ligand-receptor binding, into a processable signal, e.g., electrical or biochemical signal. Transduced signals are collected by (iii) the processing unit (molecular signalling networks within the cell for the case of engineered bacteria), which then filter, amplify and demodulate the signal to recover the transmitted information based on a preset modulation/detection scheme.

In the design of MC receiver, its integrability into nanomachines with limited computation, memory and energy resources must be taken into consideration. This dictates the following requirements for the functionality and physical design of the receiver [27]:

- ***In situ* operation and in-device processing:** For the stand-alone operation of nanonetworks in an IoNT application, the receiver should not rely on post-

processing of the transduced signals by an external macroscale device or a human controller.

- **Label-free detection:** Detection of information carrying molecules must be performed based on their intrinsic characteristics, i.e., the detection should not require additional molecular labelling procedure or any other preparation stage.
- **Continuous operation:** The MC receiver should be reversibly responsive to the incoming molecular signals, i.e., it should return to the initial state after signal detection to be ready for the next channel use. This requires *reversible* recognition, e.g., ligand-receptor binding, and transducing processes.
- **Energy efficiency:** Due to the size and energy limitations of nanomachines and the energy-harvesting constraints imposed by the application environments, the energy consumption of the receiver must be optimised. This primarily requires the development of low-complexity receiver architectures and detection methods.
- **Miniaturization:** To be integrated into a micro/nanomachine, the MC receiver must be built on micro/nanoscale components.

2.3.1 Receiver Architectures based on Nanomaterials

Functionality of an MC receiver is very similar to the one of biosensors, which are also designed for the aim of detecting analyte concentrations in an analyte solution [80]. Hence, the first theoretical studies on MC receiver design are focused on analysing the feasibility and performance of existing biosensing options for detecting MC signals [10–12, 27, 79].

Although a biosensor and an MC receiver have common design principles, there are also fundamental differences between them, which mainly arise from their distinct application areas, as stated below.

- Biosensors are designed to perform typically in equilibrium conditions. However, MC receivers must continuously observe the environment and detect the information encoded into a dynamically changing property related to the molecules, such as concentration, type/ratio/order, or arrival time.
- Biosensors are mostly designed for laboratory applications with macroscale readout devices and human observers to compensate the lack of an integrated processor. Such scheme is not applicable for an MC receiver.

Thus, while the biosensing methods and biosensor architectures provide important insights into the MC receiver design, ICT requirements imposed by the MC paradigm must be considered to reach appropriate technological solutions.

Among existing biosensing options, the electronic biosensors are mainly under the focus for MC receiver design [27]. The remaining options, i.e., optical and mechanical sensing, typically need macroscale excitation and detection units [81–83], making them inappropriate for an MC receiver that requires *in situ* operation and in-device processing. Biocatalytic [84] and affinity-based [85] sensors are the two types of electrical biosensors differing in their molecular recognition methods. *Biocatalytic recognition* is based on two steps. First, an enzyme, immobilized on the device, binds target molecules producing electroactive species, such as hydrogen ion. Diffusion of these species to the vicinity of the working electrode of the transducer is then being sensed, as it modulates one of electrical characteristics of the device, such as conductance. Widely studied glucose and glutamate sensors are examples of the biocatalytic electronic sensors [84, 86].

Alternatively, *affinity-based sensing* is based on reversible receptor-ligand interactions on the recognition layer of the sensor [85], and can be utilised for a wider range of target molecules, such as proteins, nucleotides, and antigens [85, 87]. Also, it does not necessitate the production of additional species that may adversely affect the biocompatibility. Hence, affinity-based recognition has been considered more appropriate for the design of MC receiver in the literature [27].

Recent advances in nanotechnology have led to the design of field-effect transistor-based biosensors (bioFETs) providing affinity-based electronic sensing with use of nanowires, nanotubes, organic polymers, graphene and related two-dimensional materials as the transducer unit [86, 88–94]. Detection of target molecules by bioFETs is based on the modulation of transducer channel conductivity as a result of affinity-based sensing. Simple operation principles together with the extensive literature on FETs established through many years, electrical controllability of the main device parameters, high-level integrability, and plethora of optimization options for varying applications make FET-based biosensing technology a quite promising approach for the design of electronic MC receiver. Moreover, this sensing method provides label-free, continuous and *in situ* operation at nanoscale. Thus, the design of an MC receiver based on the principles of affinity-based bioFETs has been the main approach considered in the MC literature [27, 79], which will be overviewed in the rest of this section.

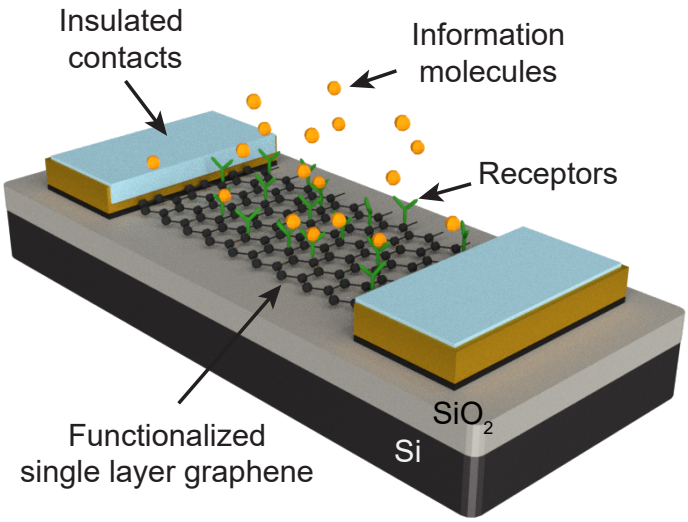

Fig. 2.5 Physical design of a graphene-based bioFET sensor acting as an MC receiver.

BioFET-based MC Receiver Architectures

As shown in Fig. 2.5, a bioFET is similar to conventional FETs, with the exception of a non-existent gate dielectric. Here, the transducer channel is directly exposed to an electrolyte solution. The ionic redistribution of the solution ions in the vicinity of the transducer channel surface creates a thin ionic layer which is called the electrical double layer (EDL). EDL acts as the gate dielectric, whose thickness, and thus the capacitance, is determined by the ionic composition of the electrolyte solution. In the top-gated operation of bioFETs, a remote solution gate is placed in the electrolyte solution. This solution gate helps stabilize the surface potential over the transducer channel, and as a result, enables a stable EDL structure, which is crucial for reliable sensing.

Depending on the type of the target analyte, the transducer channel is functionalised with ligand receptors either chemically or electrostatically. Functionalisation is necessary for providing the required level of selectivity, i.e., specificity, against the target molecules, and also for preventing non-specific adsorption of target molecules directly onto the transducer surface. Binding of target analytes with intrinsic charges leads to the alteration of surface potential, which, in turn, modulates the density of charge carriers in the transducer channel through the field-effect over the electrical double layer capacitance (EDLC).

One of the significant advantages of bioFETs over other electronic sensors is their wide range of design parameters. A list of FET-based biosensors with varying design parameters and applications is provided in Table 2.2. In the following, these design

Table 2.2 Design Options, Performance and Applications of bioFETs

Transducer channel	**Bioreceptor**	**Limit of detection**	**Application**	**Ref.**
SWCNT	Acetylcholine(Ach) receptor	100 pM	ACh detection	[94]
SWCNT	Receptor protein (antibody)	1 ng/ml	Prostate cancer detection	[93]
SWCNT	Anti Carcinoembryonic antigen (CEA)	∼55 pM	CEA detection	[95]
SiNW	Receptor protein (antibody)	∼2 fM	Prostate cancer detection	[92]
SiNW	Estrogen receptors	10 fM	dsDNA detection	[96]
ZnO NW	Anti-Immunoglobulin G(IgG) antibodies	∼0.3 nM	IgG antibodies sensing	[91]
Graphene	Glucose oxidase (enzyme)	0.1 mM	Glucose sensor	[86]
Graphene	Glutamic dehydrogenase (enzyme)	5 μM	Glutamate sensor	[86]
Graphene	Pyrene-linked peptide nucleic acid (pPNA)	2 pM	DNA sensor	[90]
Graphene	Single-stranded DNA	25 aM	DNA sensor	[97]
Graphene	Immunoglobulin E (IgE) aptamers	0.3 nM	IgE protein detection	[98]
MoS_2	Glucose oxidase (enzyme)	300 nM	Glucose sensor	[88]
MoS_2	Single-stranded DNA	1 fM	DNA sensor	[99]

options are further explained.

Receptors: First important design parameter arises from the type of receptors used in the Biorecognition Unit, which causes the selectivity of the receiver for a certain type of molecules that will be used as information carrier in MC paradigm. Among possible receptor types for affinity-based bioFETs, natural receptor proteins and aptamer/DNAs are appropriate ones for an MC receiver, since their binding to the target molecule is reversible and their size is small enough for the binding event to be detected in the presence of ionic screening [85, 87]. As an example, the FET transducer channel is functionalised with natural receptors, e.g., neuroreceptors, to detect taste in bioelectronic tongues [100] and odorants in olfactory biosensors [101]. An advantage of these type of receptors is their biocompatibility that makes them suitable for *in vivo* applications. In addition, the use of aptamers, i.e., artificial single-stranded DNAs and RNAs, in the recognition unit of bioFETs provides detectors for a wide range of targets, such as small molecules, proteins, ions, amino acids and other oligonucleotides [89, 98, 102]. Since an immense number of aptamer-ligand combinations with different affinities exist, it provides a powerful design option to control the selectivity of the MC receiver.

Transducer channel: Another important design parameter is the material used as the transducer channel between source and drain electrodes, which determines the receiver geometry and affects the electrical noise characteristics of the device. Nanowires (NWs) [92, 103], single-walled carbon nanotubes (SWCNTs), graphene [104], transition metal dichalcogenides (TMDs), e.g., molybdenum disulfide (MoS_2) [105], and organic materials such as conducting polymers [106] are some examples of nanomaterials suitable for use in a bioFET transducer channel. In the first generation of bioFETs, one dimensional

materials, such as SWCNT and NW, have been widely utilized as the channel in a bulk form. However, use in the form of single material or aligned arrays outperforms the bulk channels in terms of sensitivity and reduced noise [107]. Among possible NW materials, such as SnO_2, ZnO and In_2O_3 [108], silicon NW (SiNW) bioFETs have shown high sensitivity, high integration density, high speed sampling and low power consumption [109–114]. However, their reliable and cost-efficient fabrication is still an important research challenge [89, 115]. Comprehensive reviews exist on the performance of SiNW bioFETs, their functionality in biomedical applications such as disease diagnostic, their top-down and bottom-up fabrication processes and integration within complementary metal-oxide-semiconductor (CMOS) technology [107, 114, 116–118]. SWCNT-based bioFETs offer higher detection sensitivity due to their electrical characteristic; however, these devices also face fabrication challenges, such that their defect-free fabrication is the most challenging among all candidates [119].

While both NWs and CNTs have one-dimensional structure, use of two-dimensional materials as the transducer channel leads to higher sensitivity, since a planar structure provides higher spatial coverage, more bioreceptors can be functionalised to its surface, and all of its surface atoms can closely interact with the bond molecules. Besides, their fabrication is compatible with planar nanofabrication processes. Thus, graphene, with its extraordinary electrical, mechanical and chemical characteristics, is a promising alternative for the transducer channel of bioFETs [115, 120]. Intrinsic flexibility of graphene provides higher compatibility in terms of integration into devices with non-planar surfaces which can be more suitable for the design of nanomachines in an MC application [104]. There is currently tremendous amount of interest in building different configurations of graphene bioFETs, e.g., back-gated [121] or solution-gated [120], with research showing its superior sensing performance for various analytes, e.g., antigens [122], DNA [123], bacteria [124], odorant compounds [120], and glucose [125].

While the existing biosensing literature can provide insight for the MC receiver design, there is a need for investigation of design options according to the ICT requirements of an MC receiver. Few studies have focused on evaluating the performance of bioFETs in an MC paradigm. A SiNW bioFET-based MC receiver is modelled in [27] based on equilibrium assumption for the receptor-ligand reaction at the receiver surface. The study provides a circuit model for the transducer unit of the receiver. This work is further extended in [79], where the spatial and temporal correlation effects resulting from finite-rate transport of ligands to the stochastic ligand-receptor binding process are considered to derive the receiver model and its noise statistics. In [126], an MC receiver consisting of an aerosol sampler and an antibody-functionalised SiNW bioFET

is theoretically studied for virus detection. The performance of the receiver is studied by considering the system in steady state. While the receiver model in [126] takes into account the flicker noise and thermal noise, it neglects the interference effects assuming that the MC receiver operates in a perfectly sanitized environment. The models used in all of these studies consider the ligand-receptor binding process in thermal equilibrium, and thus, they do not capture the correlations resulting from the time-varying ligand concentration occurring in the case of MC. More importantly, these studies only cover SiNW bioFET-based MC receivers, and do not provide much insight into the performance of other nanomaterials as the transducer channel, such as graphene that promises for higher detection sensitivity due to its two-dimensional structure.

Graphene, and Graphene bioFET-based DNA Sensors: Graphene, an allotrope of carbon, is a single atom thick material consisting of a two-dimensional honeycomb lattice of carbon atoms (see Fig. 2.6(a)), which are sp^2 hybridized such that each carbon atom is connected to the three adjacent carbon atoms via strong in-plane sp^2 (or σ-) bonds with 120-degree bond angles and 1.42 Å bond length [127]. The remaining half-filled π-orbital extends perpendicularly out of plane, and merges with the other neighbouring π-orbitals, such that they together form a very large orbital, where electrons can move easily giving rise to the graphene's very high conductivity [1].

The electronic band structure of graphene is plotted in Fig. 2.6(b), which shows the crossing of the conduction and valence bands at the Fermi energy (E_F) where the density of states (DoS) is zero [1]. In contrast to conventional semiconductor materials, graphene has zero band gap, which leads to extraordinary properties, such as ambipolarity, enabling to alter the conduction between electrons and holes with electric field [128]. The band crossing point, known as the graphene's Dirac point, is where the graphene attains the maximum resistivity as a result of zero DoS. The electronic energy dispersion near the Brillouin zone corners, i.e., close to the Dirac points, is linear in contrast with the parabolic dispersion observed in other semiconductors. The linear dispersion gives rise to the behaviour of electrons like massless Dirac fermions with the velocity of 1/300 of the speed of light [1]. The charge carrier mobility in single layer graphene can theoretically reach to the values >200,000 $cm^2/V{\cdot}s$ at room temperature [129, 130]. On the other hand, the experimentally measured mobility values at room temperature exceed 150,000 $cm^2/V{\cdot}s$ for mechanically exfoliated samples [131], and reach up to 70,000 $cm^2/V{\cdot}s$ for wet-transferred graphene grown with chemical vapour deposition (CVD), through encapsulation with hexagonal boron nitride (hBN) [130]. These extremely high

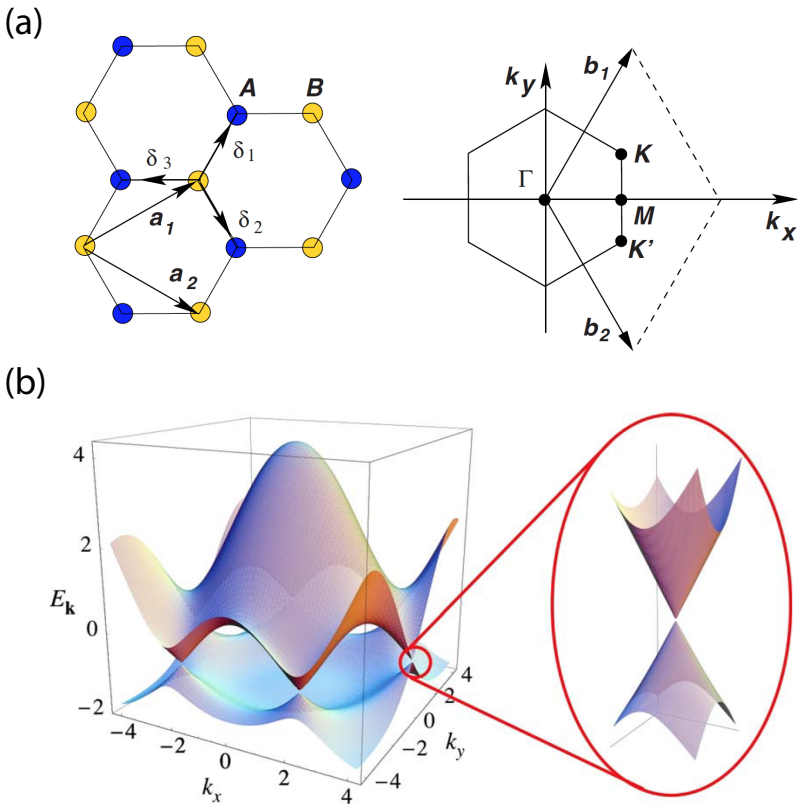

Fig. 2.6 (a) Honeycomb lattice (left) and the corresponding Brillouin zone in the reciprocal space (right). (b) Electronic dispersion in the graphene's honeycomb lattice with a closer look into the energy bands near one of the Dirac points. Taken from Ref. [1].

carrier mobilities at room temperature make the graphene one of the most promising nanomaterials for novel high-speed electronic applications [4].

Graphene can be produced through several methods differing in scalability and quality of the resulting samples. The simplest method is mechanical exfoliation, which relies on the use of an adhesive tape to exfoliate graphite into thin graphene flakes [132]. The method yields very high quality graphene. However, the size of the resulting graphene flakes is usually limited to hundreds of μm, and due to the requirement of optical microscopy-based inspection to determine quality flakes, it is not scalable. Nonetheless, the technique is frequently used in laboratory scale to fabricate proof-of-concept devices [133]. Another commonly employed technique is based on CVD growth of graphene on metal substrates, e.g., Cu [134]. The method is more scalable than mechanical exfoliation, consistently providing cm-scale poly-crystalline graphene layers and mm-scale single crystalline graphene domains [135, 136]. On the other hand, the need for transfer of

graphene from metal surface to an insulating substrate, which usually involves wet chemical treatments, may degrade the quality of the resulting CVD graphene-based devices. Still, the consistent achievement of high quality graphene makes this technique the most widely utilised for research purposes and industrial applications [4]. Other production techniques include growth on silicon carbide (SiC), molecular beam epitaxy (MBE), and chemical synthesis [133, 137]. In this thesis, I use CVD-grown poly-crystalline graphene (obtained externally) in the fabrication of graphene-based MC receiver.

Regarding bio/chemical sensing applications, graphene's most important advantage is its high sensitivity to the electric field and charged analytes, e.g., ions, DNAs, which is enabled by many factors. First, all of the carbon atoms in one-atom-thick graphene are exposed to the environment [138]. Second, the extremely high carrier mobility of graphene results in very high transconductance in a bioFET configuration. Also, the oxide layer present in more conventional Si-based bioFETs, is replaced by an EDL forming in the graphene-electrolyte interface, which can attain very small thicknesses increasing the gate capacitance, and thus the transconductance to very high values [97]. Other advantages include the bio-inertness and chemical robustness of graphene, the flexibility promising for wearable biosensor applications, and the compatibility with standard planar technologies [4]. On the other hand, one should note that the lack of band gap resulting in increased off-state leakage current can lead to a lower sensitivity compared to other 2d nanomaterials with nonzero band gap, such as MoS_2 [105].

The ambipolar nature of graphene results in both p-type and n-type doping due to the local gating effect, which is reflected to a shift in its charge neutrality point (CNP, which is equal to Dirac point when no doping exists). Therefore, while positively charged analytes close to the graphene surface accumulate negative charge in graphene through gating effect resulting in n-type doping and giving rise to a negative shift in the CNP, negatively charged analytes, e.g., DNA, cause p-type doping and positive shift of the CNP [139].

The high sensitivity of graphene can also be a limiting factor, as it makes graphene highly responsive to local environmental perturbations, e.g., ionic density fluctuations in the exposed electrolyte, increasing the noise power at the electrical output [140]. Also, biomolecules, e.g., DNA and proteins, can nonspecifically bind to the graphene surface through hydrophobic interactions, preventing the pristine graphene from providing specificity against a particular target analyte [139]. This necessitates the biofunctionalisation of graphene surface with specific receptor probes that can selectively bind the target analytes. However, in most cases, the receptor molecules have no available groups to

directly and strongly bind to the graphene; therefore, linker molecules are generally employed between the receptor molecules and the graphene surface [139].

The attachment of receptors or linker molecules to the graphene surface can be made through covalent or noncovalent functionalisation. Covalent functionalisation is usually avoided as it disrupts the sp^2 structure resulting in significant changes in the electronic and physical properties of graphene [141]. On the other hand, noncovalent functionalisation is based on the physisorption of pyrene-based molecules on the basal plane of graphene through π-π stacking, and does not cause any change in the graphene's electronic structure and physical properties. The most widely used linker molecule in graphene bioFET applications is 1-pyrenebutyric acid N-hydroxy succinimide ester (PBASE), which is an small aromatic molecule with a pyrene group that can be strongly attached to the graphene surface through noncovalent π-πstacking. Its self-limiting nature results in a thin self-assembled monolayer on graphene [139]. However, currently there is not any method to quantitatively determine the surface coverage of PBASE linkers on graphene surfaces; therefore, arriving at conclusions about the absence of nonspecific bindings in sensing experiments is usually difficult.

DNA molecules can directly adsorb onto the graphene surface through noncovalent interaction with its basal plane, which has been widely used for developing simple DNA hybridisation sensors with graphene [123, 142–144]. However, this technique is highly prone to non-specific binding and desorption of probe DNA molecules from surface upon hybridisation. Therefore, this strategy used in the initial graphene bioFET-based DNA sensing studies has been replaced by a more specific functionalisation technique that uses PBASE linker molecules, which immobilise the probe DNAs on graphene surface through conjugation reaction [89, 145]. Using this immobilisation technique, attomolar detection limits for target DNA detection have been reported in the literature [97, 146]. Integration of the graphene bioFET-based DNA sensors into microfluidic channels is also widely adopted in the literature for real-time hybridisation monitoring [89, 147, 148]. In this thesis, I follow one of these works [89], in developing the graphene bioFET DNA sensor as an MC receiver integrated with a microfluidic chip.

2.3.2 Receiver Architectures based on Engineered Bacteria

Synthetic biology, i.e., engineering of biological networks inside living cells, has seen remarkable advancements in the last decade, such that it becomes possible to device engineered cells, e.g., bacteria, for use as biological machines, such as sensors and actuators, for various applications. Synthetic biology also stands as a promising means of devising nanoscale biotransceivers for IoNT applications, by implementing transmission

and reception functionalities within living cells by modifying the natural gene circuits or creating new synthetic ones [28]. The technology is already mature enough to allow performing complex digital computations, e.g., with networks of genetic NAND and NOR gates, as well as analogue computations, such as logarithmically linear addition, ratiometric and power-law computations, in synthetic cells [149]. Synthetic gene networks integrating computation and memory is also proven feasible [150]. More importantly in this context, the technology enables implementing bio-nanomachines capable of observing individual receptors, as naturally done by living cells; thus, stands as a suitable domain for practically implementing more information-efficient MC detectors based on the binding state history of individual receptors.

The literature in applying synthetic biology tools to design bacteria-based MC transceivers is scarce, although there are many studies proposing the use of bacteria as carriers of DNA-encoded molecular messages [151–153]. An MC biotransceiver architecture integrating molecular sensing, transmitting, receiving and processing functions through genetic circuits is introduced in [28]. However, the analysis is based on the assumption of linearity and time-invariance of the gene translation networks, and does not provide any insight into the associated noise sources. An overview of biological circuit elements necessary for molecular communications is given in [154], and a system theoretic model for those biological circuits is developed in [155]. Other studies include the design of MC functional units based on biological circuits, such as modulated parity-check encoding circuit [156], parity-check analogue decoder circuit [157], and a signalling kinase cascade for biochemically filtering frequency-domain encoded molecular signals [158].

2.3.3 Macroscale MC Receiver Architectures

Few studies in MC literature have focused on macroscale implementation of MC systems taking into account the physical limitations of a receiver, although the utilized receivers are made of off-the-shelf macroscale components. In [10], the isopropyl alcohol (IPA) is used as information carrier, and commercially available metal oxide semiconductor alcohol sensors are used as MC receiver. This study provides a testbed for MC with macroscale dimensions, which is later on utilised in [159] to estimate its combined channel and receiver model. This testbed is extended to a molecular multiple-input multiple-output (MIMO) system in [160] to improve the achievable data rate. In [11], the information is encoded in pH level of the transmitted fluid, and a pH probe sensor is used as the MC receiver. On the grounds that the use of acids and bases for information transmission can adversely affect the other processes in the application environment, such as in the human body, magnetic nanoparticles (MNs) are employed as information-carrying molecules in

microfluidic channels in [12]. In this study, a bulky susceptometer is used to detect the concentration of MNs and decode the transmitted messages. In addition, the performance of MN-based MC, where an external magnetic field is employed to attract the MNs to a passive receiver, is analysed in [161].

However, as explained, the focus of the aforementioned studies is on macroscale MC using commercially available sensors as receiver. Therefore, these studies do not contribute to the development of a design and optimisation framework for practical nanoscale MC receivers that can be integrated into micro/nanoscale devices.

Chapter 3

Modelling Convection-Diffusion-Reaction Systems for Microfluidic Molecular Communications with Surface-based Nanoreceivers

3.1 Introduction

In this chapter, I investigate a particular type of MC system, i.e., microfluidic MC, where the concentration-encoded molecular information is conveyed via diffusion and convection induced by fluid flow to a surface-based reactive receiver in a microfluidic channel. The receiver containing ligand receptors on its surface is placed at the bottom of the channel, and it samples the propagating information molecules, i.e., ligands, based on ligand-receptor binding reaction. The concentration of bound receptors is informative of the transmitted ligand concentration, thus, used to decode the transmitted message. After the passage of the finite-length ligand concentration pulse through the microfluidic channel, the channel and receiver return to their initial states due to the clearance by the continuous fluid flow. End-to-end system can be defined as a *convection-diffusion-reaction system*, which is highly nonlinear; and the finite duration of transmitted pulses makes the problem even more nonlinear and complex.

Convection-diffusion-reaction systems are especially prominent in microfluidic sensing and chromatography applications, such as affinity chromatography [162], microfluidic

surface plasmon resonance (SPR) sensing [163], where analytes are propagated over ligand-specific receptor assays. In addition to the studies targeting microfluidic surface-based biosensing technologies, such as planar thin gold film SPR sensors [164], semiconductor bioFETs [165], a considerable amount of efforts has been devoted to modeling and control of the complex interplay between convection, diffusion and reaction to optimize the efficiency of analyte transport [166, 167].

Molecular transport in microfluidic channels has been recently addressed from communication theoretical perspective in [168, 169], which develop end-to-end channel models for the linear time-invariant systems consisting of biological transmitters and receivers placed in chambers along the microfluidic channel. Moreover, the response of the bacterial receivers within microfluidic channels are experimentally reported in [170], where empirical models based on linear approximations are developed for the transient response of bacteria to pulse-amplitude-modulated molecular messages. Additionally, digital microfluidic MC networks based on droplets have been studied in [171]. Considering the surface-based receivers, this chapter targets more complicated systems that are neither linear nor time-invariant.

Microfluidic MC systems integrated with surface-based molecular receivers are promising for groundbreaking applications within the IoNT framework. For example, in an *in vivo* continuous health monitoring application, mobile nanosensors circulating within the cardiovascular system can inform a bio-cyber gateway placed at the interior surface of blood vessels about their sensing operations through molecular signals in blood flow, where convection and diffusion act simultaneously on the transport of molecules [5]. Furthermore, it can also find use in microfluidic networked lab-on-a-chip devices, which is an emerging technology to diversify the point-of-care medical applications and increase the efficiency of on-chip diagnostics [172]. Moreover, imitating the transport of molecules with convection and diffusion in confined geometries like vascular and neuro-synaptic channels, similar microfluidic configurations can find application in organs-on-chips and artificial synapses relying on molecular information and communication technologies [7, 173, 35, 174].

The overall process, which covers the release of ligands by the transmitter in the form of a finite-duration concentration pulse, the propagation of molecules in laminar flow through the microfluidic channel, and the molecular detection by the surface receiver equipped with finite number of ligand receptors is a highly nonlinear and time-varying process, and does not yield an analytical solution for the ligand and bound receptor concentration fields. Therefore, it necessitates the application of computationally-expensive numerical methods, such as finite element analysis (FEA). In this chapter, I develop an end-to-end analytical

model that can capture the expected time course of the received signal in terms of number of bound receptors. The model is based on the quasi-steady state two-compartment model, which is tailored to incorporate the time-varying characteristics of the microfluidic MC system. The resulting model captures the effect of the channel and receiver geometry, and the system parameters regarding the fluid flow and ligand-receptor reaction. It takes into account the nonlinearities caused by laminar flow resulting in parabolic velocity profile and finite number of receptors resulting in saturation of the receiver. The effect of interplay between reaction and transport rates, which can lead to a depletion layer over the receiver surface is also covered. Based on the developed model, approximate analytical expressions are derived for the received pulse delay, pulse amplitude and pulse width to help characterize and optimize the system from communication theoretical perspective. The analytical results are compared to the numerical solutions obtained using COMSOL Multiphysics, which is a FEA simulation software.

3.2 Communication System Model

In this section, the end-to-end model of the microfluidic communication channel is represented as a system of partial differential equations. I utilise a 2d model considering a microfluidic channel with rectangular cross section as shown in Fig. 3.1(a). 2d models are proved effective in modelling the molecular transport, especially when there is an obvious interplay between convection, diffusion and surface reaction, as the uniformity of the molecular concentration along y-direction is disturbed above the reactive surface [175]. On the other hand, for the cases where there is no reactive surface, 1d models can successfully capture the effect of convection and diffusion [176].

Using a similar notation to that of [175], three orthogonal domains are defined: (i) bulk domain $\boldsymbol{\Omega_b}$, where the convection and diffusion of ligands occur, (ii) reacting surface domain $\boldsymbol{\Omega_{rx}}$ denoting the biorecognition layer of the receiver, where the ligand-receptor reaction occurs, and (iii) non-reacting surface domains $\boldsymbol{\Omega_{nr}}$ defining the walls of the microfluidic channel excluding the receiver surface, as demonstrated in Fig. 3.1(b). I also define two dependent variables $c = c(x, y, t)$ denoting the ligand concentration in space and time domain, and $R = R(x, t)$ denoting the bound receptor concentration at the receiver surface.

Hence, in a 2d convection-diffusion system the propagation of ligands is governed by

$$\frac{\partial c}{\partial t} = D\nabla^2 c - u_x(y)\frac{\partial c}{\partial x}, \quad (x, y) \in \boldsymbol{\Omega_b}, \tag{3.1}$$

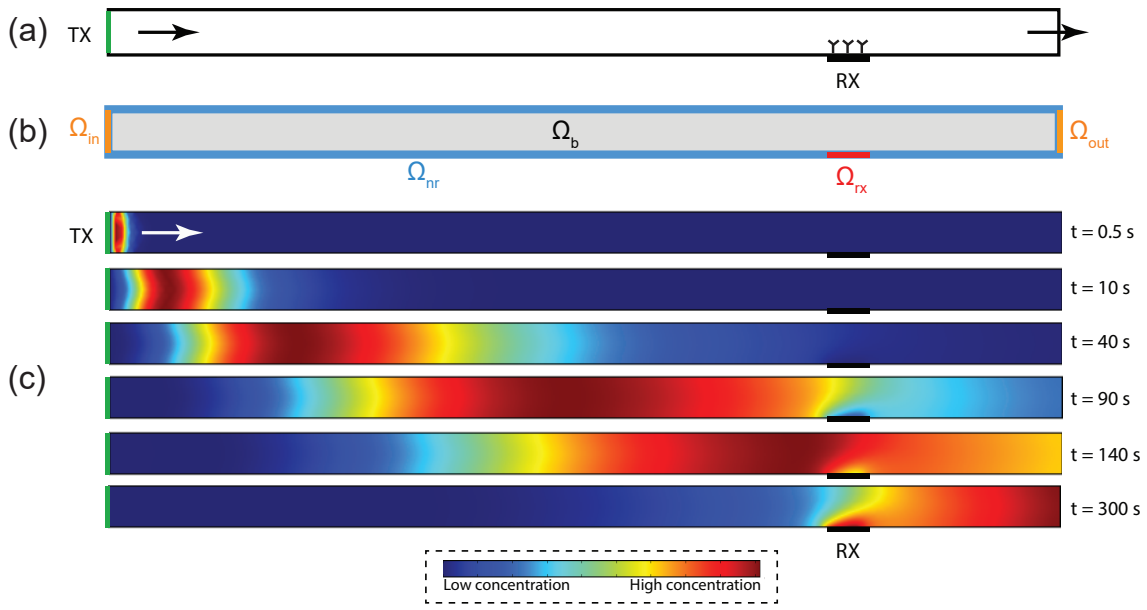

Fig. 3.1 Microfluidic MC with surface-based receiver. (a) Conceptual drawing of the system. (b) Domains and boundaries used in the system model. (c) Demonstration of concentration-encoded molecular message propagation over the reactive surface of the receiver in convection-diffusion channel. Finite element simulations are carried out in COMSOL Multiphysics.

where $\nabla^2 = \frac{\partial^2}{\partial x^2} + \frac{\partial^2}{\partial y^2}$ is the two dimensional Laplace operator, $u_x(y)$ is the flow velocity as a function of distance to the surrounding walls. Assuming a fully developed laminar flow in the microfluidic channel yields a parabolic flow velocity profile, i.e.,

$$u_x(y) = 4u(y/h)(1 - y/h), \quad (x, y) \in \boldsymbol{\Omega_b}, \tag{3.2}$$

where u is the maximum flow velocity. D is the effective diffusion coefficient taking into account the effect of Taylor-Aris-type dispersion [168]. For a channel with rectangular cross-section, it is given by

$$D = \left(1 + \frac{8.5u^2 h_{ch}^2 w_{ch}^2}{210 D_0^2 (h_{ch}^2 + 2.4 h_{ch} w_{ch} + w_{ch}^2)}\right) D_0, \tag{3.3}$$

where the intrinsic diffusion coefficient is denoted by D_0 [168]. Here, h_{ch} and w_{ch} denote the height and width of the microfluidic channel, respectively.

No-flux boundary condition is assigned to the non-reacting walls of the channel, i.e.,

$$\frac{\partial c}{\partial y} = 0, \quad y \in \boldsymbol{\Omega_{nr}}. \tag{3.4}$$

On the other hand, the flux condition at the reactive boundary, where ligand-receptor reaction occurs, is given by

$$-D\frac{\partial c}{\partial y} = \mathcal{R}(R,c), \quad y \in \boldsymbol{\Omega_{rx}}, \tag{3.5}$$

where R is the bound receptor concentration, and $\mathcal{R}$ denotes the reactive flux.

The inlet and outlet boundary conditions are defined as follows

$$c(x=0,y,t) = c_{in}(t), \tag{3.6}$$

$$\frac{\partial c(x=L,y,t)}{\partial x} = 0, \tag{3.7}$$

where $c_{in}(t)$ is the transmitted signal.

Assuming no surface diffusion for receptors at the receiver surface, bound receptor concentration can be written as a function of time:

$$\frac{\partial R}{\partial t} = \mathcal{R}(R,c), \quad (x,y=0) \in \boldsymbol{\Omega_{rx}}. \tag{3.8}$$

Given the finite receptor concentration at the receiver, ligand-receptor binding reaction can be described by the first-order Langmuir kinetics giving the reactive flux as

$$\mathcal{R}(R,c) = k_1 c|_{y=0}(R_{max} - R) - k_{-1}R, \quad (x,y=0) \in \boldsymbol{\Omega_{rx}}. \tag{3.9}$$

Lastly, the initial conditions for the system are defined as

$$R(x,0) = 0, \quad (x,y=0) \in \boldsymbol{\Omega_{rx}}. \tag{3.10}$$

$$c(x,y,0) = 0, \quad (x,y) \in \boldsymbol{\Omega_b}. \tag{3.11}$$

The system model presented above is not analytically tractable and necessitates numerical methods to compute the ligand and bound receptor concentration. A numerical solution of the system model obtained in COMSOL for a representative scenario is demonstrated in Fig. 3.1(c) for the time-varying concentration of a propagating ligand pulse transmitted in the form of a rectangular pulse. In the FEA simulation, the COMSOL Multiphysics modules of the transport of diluted species, laminar flow, and general form boundary partial differential equations are employed. A coarse mesh is used with a maximum finite element size of 2 μm, and the microfluidic liquid is assumed to be water undergoing incompressible laminar flow at 293.15 K with a viscosity of 0.001 Pa·s. The maximum flow velocity is set to $u = 5$ μm/s. Microfluidic channel width and height are

$w_{ch} = 20$ μm and $h_{ch} = 20$ μm, respectively. The length of the receiver along the flow axis is $l_{rx} = 20$ μm, and the distance of the receiver to the channel entrance is $d_{rx} = 350$ μm. The rate of ligand transmission is $N_m = 2$ fmol/s, and the transmitted pulse length is $T_p = 0.5$ s. The surface concentration of receptors on the receiver is $\rho_{SR} = 1 \times 10^{-8}$ mol/m^2. Binding and unbinding rates of the ligand-receptor pair are 1×10^2 m^3/mol·s and 1×10^{-2} s^{-1}, respectively. Intrinsic diffusion coefficient of ligands is $D_0 = 1 \times 10^{-10}$ m^2/s. The same physics and the same parameter values except for the distance of the receiver and the maximum flow velocity will be used as the default setting in evaluating the accuracy of the proposed approximate analytical model for the received signal in Section 3.5.

3.3 Proposed Model

I develop an analytical model that approximates the time course of the mean number of bound receptors on the receiver surface for a rectangular ligand concentration pulse transmitted at the channel inlet, as shown in Fig. 3.1(c). Prior to modelling, it is worth elaborating briefly on the impact of conditions resulting from the competition between ligand transport and ligand-receptor reaction.

In convection-diffusion-reaction systems, if the convective/diffusive transport in the channel supplies ligands much more quickly than the receptors can bind them, then the system becomes reaction-limited, implying that transport dynamics has negligible effect on the resulting waveform for the bound receptor concentration. In such cases, ligand concentration near the receiver surface can be assumed equal to the concentration of ligands supplied at the channel inlet, and the well-mixed condition can be assumed for modelling the ligand-receptor reaction [175].

In practical systems, however, the reaction-limited condition often does not hold, because the concentration of supplied ligands is not continuous, giving rise to a concentration gradient between the channel inlet and the reactive surface [177, 178]. Furthermore, in microfluidic channels, the fluid flow is usually laminar leading to a parabolic flow velocity profile above the reactive surface, implying a concentration gradient from the center of the channel toward the reactive surface [175]. More importantly, when the system is utilised for communication purposes, reaction rates at the receiver surface should be kept large enough compared to the transport rate in order not to cause intersymbol interference (ISI). Because of these reasons, it is considered that the system would be operating either in transport-limited regime, where the reaction rates are much larger than the ligand transport rate, or under partial mass transport limitations, caused by

similar transport and reaction rates. In such cases, mass transport limitations could have substantial impact on the time course of bound receptor concentration, and well-mixed condition for the surface reactions often does not hold.

A compartmental approach is developed in [179] to model the ligand-receptor kinetics affected by mass transport limitation. It is based on dividing the space domain into two compartments, in each of which the ligand concentration can be assumed steady. This steady-state assumption proved to be effective in describing the isolated association and dissociation phases (two-stage process). The two-compartment model is widely employed in BIAcore analyses to determine the affinity of various ligand-receptor pairs [177].

I make use of the two-compartment model by tailoring it to capture the peculiarities of the MC system under investigation. I will demonstrate that this simple yet effective strategy can be used to reveal the characteristics of the microfluidic MC channel by means of analytical expressions.

3.3.1 Two-Compartment Model

Here, I review the fundamentals of two-compartment model that is modified to propose an approximate model for the microfluidic MC channel.

In the two-compartment model, ligand concentration of the first compartment is assumed to be equal to the concentration at the channel inlet $c = c_0$ [179], as shown in Fig. 3.2. The concentration in the second compartment covering the receptors $c|_{y=0}$ could be different than the bulk concentration due to the binding reactions occurring at the receiver surface. Concentration gradient between the two compartments results in a flux of ligands expressed by

$$\mathcal{J} = k_T(c_0 - c|_{y=0}), \tag{3.12}$$

where k_T is the mass transport parameter, which is a function of the channel and receiver geometries, and the system parameters regarding diffusion and convection of ligands [178], i.e.,

$$k_T = C_T A_{rx} \sqrt[3]{\frac{D^2 F}{h_{ch}^2 w_{ch}(d_{rx} + l_{rx})}}, \tag{3.13}$$

where $A_{rx} = l_{rx} w_{rx}$ is the receiver surface area with the receiver width $w_{rx} = w_{ch}$. Here, C_T is defined as

$$C_T = 1.47 \left(\frac{1 - (d_{rx}/(d_{rx} + l_{rx}))^{2/3}}{1 - d_{rx}/(d_{rx} + l_{rx})} \right), \tag{3.14}$$

where d_{rx} is the minimum distance of the channel inlet to the receiver, l_{rx} is the length of receiver along the x-axis, and $F = h_{ch} \times w_{ch} \times u$ is the maximum flow rate.

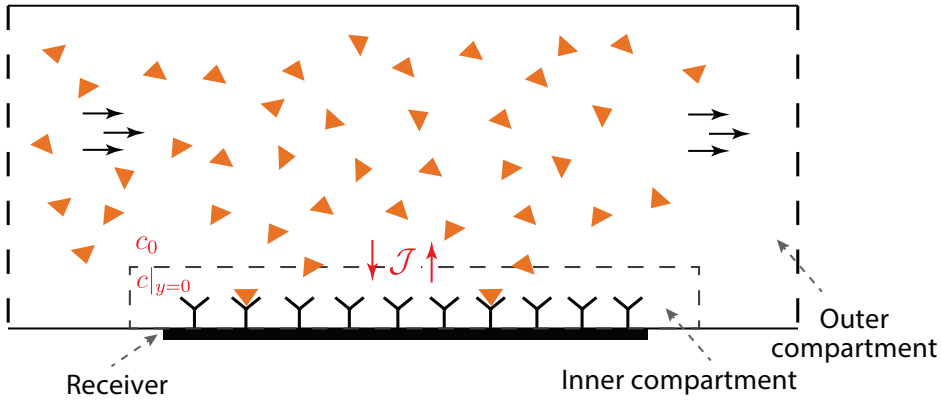

Fig. 3.2 Conceptual drawing of the two-compartment model.

The steady-state solution of this two-compartment model for ligand concentration near the receiver surface is obtained by equating the ligand flux to the surface, $\mathcal{J}$ given in equation (3.12), to the reactive flux $\mathcal{R}$ given by equation (3.9), i.e.,

$$c|_{y=0} = \frac{k_T c_0 + k_{-1} N_R}{k_1 (N_{R,max} - N_R) + k_T}, \tag{3.15}$$

where the position-dependent surface receptor concentrations in equation (3.9) are integrated over the receiver surface to obtain the number of receptors in units of *mole*, i.e., $N_{R,max} = R_{max} A_{rx}$, $N_R = \int_S R \, dA_{rx}$.

Substituting this expression into equation (3.9) yields a nonlinear differential equation representing the evolution of the number of bound receptors, i.e.,

$$\frac{dN_R}{dt} = \frac{k_1 k_T c_0 (N_{R,max} - N_R) - k_{-1} k_T N_R}{k_1 (N_{R,max} - N_R) + k_T} \tag{3.16}$$

The solution of equation (3.16) for the association phase is then obtained by setting the initial conditions as $c(x, y, 0) = c_0$ and $R(0) = 0$ [178, 180], i.e.,

$$N_{R,a}(t) = N_{R,eq} \left(1 - \frac{\mathcal{W}_0[\alpha - \beta t]}{\alpha} \right), \tag{3.17}$$

where $\mathcal{W}_0[.]$ is the principal branch of the Lambert $\mathcal{W}$ function, and

$$N_{R,eq} = \frac{c_0}{c_0 + K_D} N_{R,max}, \tag{3.18}$$

$$\alpha = \frac{k_1 c_0 N_{R,max}}{k_{-1} N_{R,max} + k_T (c_0 + K_D)}, \tag{3.19}$$

$$\beta = \frac{k_1 c_0 + k_{-1}}{1 + \frac{k_{-1} N_{R,max}}{k_T (c_0 + K_D)}}. \tag{3.20}$$

The solution of equation (3.16) for the dissociation phase can then be found by setting the initial conditions as $c(x, y, 0) = 0$ and $N_R(0) = N_{R,0}$, with $N_{R,0}$ being the number of bound receptors at the start of the dissociation phase [178, 180], i.e.,

$$N_{R,d}(t) = \gamma \mathcal{W}_0 \left[-\frac{N_{R,0}}{\gamma} \exp \left[\frac{-k_1 N_{R,0} - k_T k_{-1} (t - t_0)}{k_1 \gamma} \right] \right], \tag{3.21}$$

with

$$\gamma = \frac{k_1 N_{R,max} + k_T}{k_1}. \tag{3.22}$$

3.3.2 Proposed Model

I propose an approximate model built upon the two-compartment model described above. In the two-compartment model, for each of the phases, e.g., association and dissociation phases, the bulk concentration in the first compartment is assumed constant and equal to its initial value. However, in the MC system, the finite-length input results in finite-duration interaction between the transmitted ligands and the receptors on the receiver surface as shown in Fig. 3.1(c), making it impractical to directly apply the two-compartment model.

The strategy here is to consider the whole process again as a two-phase process consisting of association and dissociation phases, and then, set the start time instances of the association and dissociation phases to reflect the effects of the finite-duration passage of the ligands. I also define an effective ligand pulse length and effective ligand pulse concentration in order to analyse the system within the framework of the two-compartment model. I start with modelling the propagation in the microfluidic convection-diffusion channel. After this step, the receiver reactions will be incorporated into the model with a modified two-compartment model.

First, the distance between transmitter and receiver d is taken as the distance of the centre of the receiver to the entrance of the channel where transmission occurs:

$$d = d_{rx} + l_{rx}/2. \tag{3.23}$$

When the transmitter sends an impulse signal in the form of surface concentration, i.e., $N/(A_{ch}N_A) = 1(mol/m^2)$, neglecting the reaction at the receiver for the moment, the ligand concentration anywhere in the channel at any time can be written as [168]

$$c_{imp}(x,t) = \frac{1}{\sqrt{4\pi Dt}} \exp\left[-\frac{(x-ut)^2}{4Dt}\right]. \tag{3.24}$$

The concentration function is Gaussian with variance $\sigma^2_{imp} = 2Dt$, which is varying with time, making the subsequent calculations analytically untractable. Therefore, during the passage of the resulting ligand pulse, the dispersion is neglected, and it assumed that the variance is constant at the receiver location, rendering the shape of the ligand pulse a Gaussian function with the variance $\sigma^2_R = 2Dd/u$, moving at the flow velocity. Hence, the end-to-end impulse response of the communication channel from the transmitter to the receiver location becomes

$$c_R^{imp}(t) = \frac{1}{\sqrt{4\pi Dd/u}} \exp\left[-\frac{(d-ut)^2}{4Dd/u}\right]. \tag{3.25}$$

In this study, a more practical signal, i.e., finite-length rectangular pulse, is considered as the input. Accordingly, transmitter releases a total of N molecules at a constant rate μ_T for a specified pulse duration T_p uniformly through the entire surface of the channel inlet; thus, the transmitted signal can be written as

$$s(t) = \frac{\mu_T}{A_{ch}N_A} \operatorname{rect}\left[\frac{t}{T_p} - 0.5\right], \tag{3.26}$$

where $\operatorname{rect}[t] = 1$ for $-0.5 < t < 0.5$ is the rectangular function, and $\mu_T = N/T_p$ is the transmission rate in $molecules/s$.

The convection-diffusion channel excluding the ligand-receptor reactions is a linear time-invariant (LTI) system [169]; thus, the response to a rectangular pulse can be found via convolution, i.e.,

$$c_R^{rect}(t) = s(t) * c_R^{imp}(t) = \frac{\mu_T}{2uA_{ch}N_A}\left(\operatorname{erf}\left[\frac{ut-d}{2\sqrt{Dd/u}}\right] - \operatorname{erf}\left[\frac{ut-uT_p-d}{2\sqrt{Dd/u}}\right]\right), \tag{3.27}$$

where N_A is the Avogadro's number.

The ligand pulse delay is defined as the time it takes for the peak ligand concentration to reach the centre of the receiver, i.e.,

$$t_D = d/u + T_p/2. \tag{3.28}$$

To utilise the two-compartment model, the Gaussian-shaped ligand concentration pulse propagating over the receiver is approximated as a finite duration pulse with a pulse length set to cover approximately $95-96\%$ of the ligands, as done in [181]. This effective ligand pulse length is computed as

$$w_p^{rect} = 4\sigma_R + T_p u, \tag{3.29}$$

where $\sigma_R = \sqrt{2Dd/u}$. Then the effective ligand pulse passage duration is given by

$$\tau_p^{rect} = \frac{w_p^{rect}}{u}. \tag{3.30}$$

Every point along the receiver surface is assumed to be exposed to a stationary concentration within a time window, whose end-points are marked by association and dissociation times. Taking the pulse delay as the central point in time, the association time can be set as

$$t_a = t_D - \frac{\tau_p^{rect}}{2}, \tag{3.31}$$

and the dissociation time is set to

$$t_d = t_D + \frac{\tau_p^{rect}}{2}. \tag{3.32}$$

Then, the effective ligand pulse concentration is calculated as the time-average of the concentration passing over the receiver surface between t_a and t_d, i.e.,

$$c_{avg} = \frac{1}{\tau_p^{rect}} \int_{t_a}^{t_d} c_R^{rect}(t)dt = \frac{1}{\tau_p^{rect}} \Big(Q(t_d) - Q(t_a) \Big), \tag{3.33}$$

where $Q(t)$ is given by

$$\begin{aligned} Q(t) =& \frac{1}{2u^2} \left((ut-d)\,\mathrm{erf}\left[\frac{ut-d}{2\sqrt{Dd/u}} \right] - (ut-uT_p-d)\,\mathrm{erf}\left[\frac{ut-uT_p-d}{2\sqrt{Dd/u}} \right] \right) \\ &+ \sqrt{\frac{Dd}{\pi u^5}} \left(\frac{N_m}{A_{ch}} \right) \left(\exp\left[-\frac{(ut-d)^2}{4Dd/u} \right] - \exp\left[-\frac{(ut-uT_p-d)^2}{4Dd/u} \right] \right). \end{aligned} \tag{3.34}$$

Given the definitions regarding the effective ligand pulse concept, the time course of the mean number of bound receptors for a system, where the transmission starts at $t = 0$, obtained by the two-compartment model can be given by

$$N_R(t) = N_{R,eq}\left(1 - \frac{\mathcal{W}_0\left[\alpha^* \exp\left[\alpha^* - \beta^*(t - t_a)\right]\right]}{\alpha^*}\right)\Big(\Theta\left[t - t_a\right] - \Theta\left[t - t_d - \epsilon\right]\Big) \tag{3.35}$$
$$- \gamma^* \mathcal{W}_0\left[-\frac{N_{R,0}}{\gamma^*} \exp\left[\frac{-k_1 N_{R,0} - k_T^* k_{-1}(t - t_d)}{k_1 \gamma^*}\right]\right]\Theta\left[t - t_d - \epsilon\right],$$

where $\Theta[.]$ denotes the Heaviside step function, and ϵ is an infinitesimal number. The modified parameters are given as follows

$$N_{R,eq}^* = \frac{c_{avg}}{c_{avg} + K_D} N_{R,max}, \tag{3.36}$$

$$\alpha^* = \frac{k_1 c_{avg} N_{R,max}}{k_{-1} N_{R,max} + k_T^*(c_{avg} + K_D)}, \tag{3.37}$$

$$\beta^* = \frac{k_1 c_{avg} + k_{-1}}{1 + \frac{k_{-1} N_{R,max}}{k_T^*(c_{avg} + K_D)}}, \tag{3.38}$$

$$\gamma^* = \frac{k_1 N_{R,max} + k_T^*}{k_1}, \tag{3.39}$$

where the transport parameter is set to $k_T^* = k_T \times k$ to be optimized for the MC system. Note that $N_{R,0}$ in (3.35) is the number of bound receptors at the beginning of the dissociation phase, i.e., at time t_d, and can be obtained as follows

$$N_{R,0} = N_R^*(t_d) = N_{R,eq}^*\left(1 - \frac{\mathcal{W}_0\left[\alpha^* \exp\left(\alpha^* - \beta^*(t_d - t_a)\right)\right]}{\alpha^*}\right). \tag{3.40}$$

3.4 Received Pulse Characteristics

In this section, based on the proposed model, analytical expressions for the pulse delay, pulse amplitude and pulse width are derived for the characterisation of the microfluidic MC system. A similar approach has been previously taken for the diffusion-based MC channels in [182]. In the next section, the results will be compared to that obtained via numerical FEA in COMSOL Multiphysics for different system settings.

Pulse delay, different from the ligand pulse delay given in equation (3.28), is defined as the time instant, at which the number of bound receptors reaches its peak value. In

this model, the number of bound receptors given by equation (3.35) is monotonically increasing for $t \leq t_d$, and monotonically decreasing for $t > t_d$. Therefore, the pulse delay can be simply obtained as follows

$$t_{pd} = t_d = t_D + \frac{\tau_p^{rect}}{2} = \frac{d}{u} + \frac{T_p + \tau_p^{rect}}{2} = \frac{d}{u}\left(1 + \sqrt{\frac{8D}{ud}}\right) + T_p. \tag{3.41}$$

Then, the **pulse amplitude**, as the peak value of the received signal, is given by

$$N_{R,pa} = N_R^*(t_{pd}). \tag{3.42}$$

Another important metric is the **pulse width**. As done in [182] for MC, it is defined as the time interval, at which the pulse magnitude is greater than the half of its peak value. The pulse width has implications for the achievable bandwidth as it determines the extent of ISI. Based on the model, pulse width is calculated as

$$\tau_{pw} = \tau_p^{rect} - \frac{k_1\gamma^*\left(\ln[\frac{1}{2}] - \frac{N_{R,pa}}{2\gamma^*}\right) + k_1 N_{R,pa}}{k_T k_{-1}} - \frac{1}{\beta^*}\left(\frac{\alpha^* N_{R,pa}}{2N_{R,eq}^*} - \ln\left[1 - \frac{N_{R,pa}}{2N_{R,eq}^*}\right]\right), \tag{3.43}$$

where $N_{R,eq}^*$, α^*, β^*, and γ^* are given in equations (3.36)-(3.39).

The above analytical expressions for the received pulse delay, pulse amplitude and pulse width are of paramount importance for MC engineering, as they enable an optimisation framework that can be utilised to optimise the overall system from ICT perspective, and help develop advanced communication schemes, such as optimal detection methods and modulation techniques.

3.5 Results and Discussions

In this section, I first estimate the transport parameter $k_T^* = k \times k_T$, and then, evaluate the accuracy of the proposed analytical model by comparing the calculations under different conditions to the results obtained via FEA in COMSOL Multiphysics. The default values of the system parameters used in the analyses are listed in Table 3.1.

To find the optimal value of the free parameter k, nonlinear least square estimation is performed in MATLAB using Levenberg-Marquardt optimisation algorithm. The curve fitting is conducted on the numerical results obtained via COMSOL for 35 different scenarios, in each of which only one parameter is changed from its default setting at

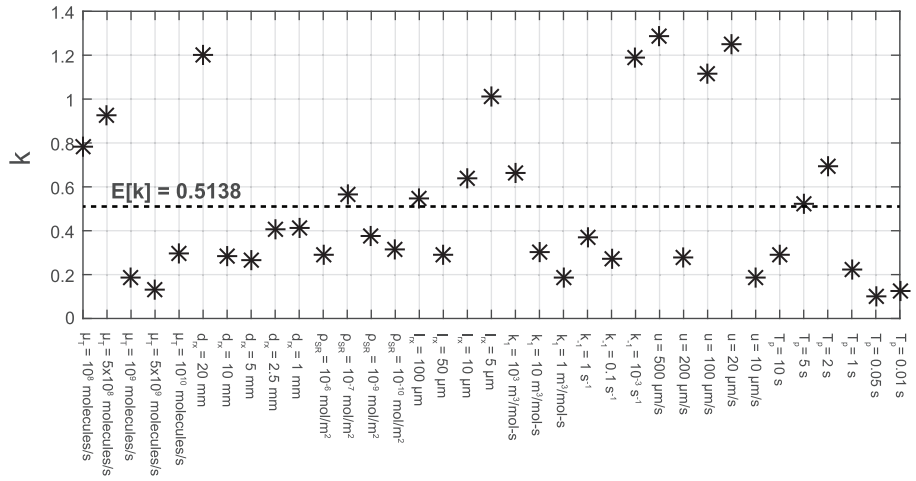

Fig. 3.3 Optimal values of free parameter k obtained with varying system parameters.

a time. The results of the optimisation with the corresponding system parameters are presented in Fig. 3.3. The mean and the standard deviation of the obtained data are 0.5138 and 0.3616, respectively. Setting k to its mean, I rewrite the transport parameter optimised for the communication scenario as

$$k_T^* = 0.5138 \times k_T = 0.7553 \left(\frac{1 - (d_{rx}/(d_{rx} + l_{rx}))^{2/3}}{1 - d_{rx}/(d_{rx} + l_{rx})} \right) \sqrt[3]{\frac{D^2 F}{h_{ch}^2 w_{ch} (d_{rx} + l_{rx})}}. \tag{3.44}$$

Using the optimised transport parameter, the time course of the normalized number of bound receptors obtained via equation (3.35) is compared to the numerical results of COMSOL experiments under different scenarios. The results are presented in Fig. 3.4.

Table 3.1 Default values of system parameters for simulation of microfluidic MC

Microfluidic channel height (h_{ch})	20 μm
Microfluidic channel width (w_{ch})	20 μm
Rete of ligand transmission (N_m)	1×10^9 1/s
Transmitted pulse length (T_p)	0.5 s
Distance to the front-end of the receiver (d_{rx})	15 mm
Max flow velocity (u)	50 μm/s
Intrinsic diffusion coefficient of ligands (D_0)	1×10^{-10} m^2/s
Binding rate (k_1)	1×10^2 m^3/(mol·s)
Unbinding rate (k_{-1})	1×10^{-2} 1/s
Surface concentration of receptors at the receiver (ρ_{SR})	1×10^{-8} mol/m^2
Receiver length along the x-axis (l_{rx})	20 μm

It is clear that the proposed analytical model well approximates the numerical solution, justifying the accuracy of the model.

In the second part, the capability of the proposed model to reflect the characteristics of the received signal is examined under various conditions, this time, using the metrics defined in the previous section. Accordingly, the pulse delay obtained via equation (3.41) is compared to the numerically computed results in Fig. 3.5. As is seen, the simple expression given in equation (3.41) is quite accurate in approximating the numerical results and following the trends with varying parameter values. It is worth noting that the received pulse delay is not affected by the molecular transmission rate, the surface receptor concentration, and the binding/unbinding rates of the ligand-receptor pairs. As expected, it is most effectively influenced by the minimum transmitter-receiver distance d_{rx} and the flow velocity u.

The analyses are repeated for the normalized pulse amplitude, which is the ratio of the peak number of bound receptors to the total number of receptors. The pulse amplitude is quite important for communication system design, as it directly influences the signal-to-noise ratio of the received signal. The results obtained via equation (3.42) are compared to the numerical results in Fig. 3.6. The parameters range between values corresponding to sparsely occupied and saturated receiver. The results reveal that almost all parameters have substantial effect on the pulse amplitude, and the numerical results and the corresponding trends are well approximated by the proposed analytical model, regardless of whether the receiver is saturated or sparsely occupied.

One interesting observation can be made for the effect of varying flow velocity on the received pulse amplitude. As shown in Fig. 3.5(g), for a fixed molecular transmission rate, the pulse amplitude decreases when the flow velocity becomes higher or lower than a certain optimal value. The reason can be explained as follows. For very low flow velocities, the degree of the attenuation through dispersion in the channel increases leading to a lower ligand pulse amplitude passing over the receiver. Also, for lower flow velocities, the effect of transport limitation is more pronounced. These effects are overcome with the increasing flow velocity. However, as the flow velocity increases, the duration of contact between the propagating ligand pulse and the receiver surface decreases such that a smaller number of ligands can find enough time to diffuse vertically on to the receiver surface for reaction, resulting in a decrease in the received pulse amplitude. The latter effect starts to dominate over the former one as the flow velocity increases further beyond a certain threshold, such that we observe the concave dependence of the received pulse amplitude on the flow velocity. A similar trend was also observed and discussed in detail in [79, 183, 184].

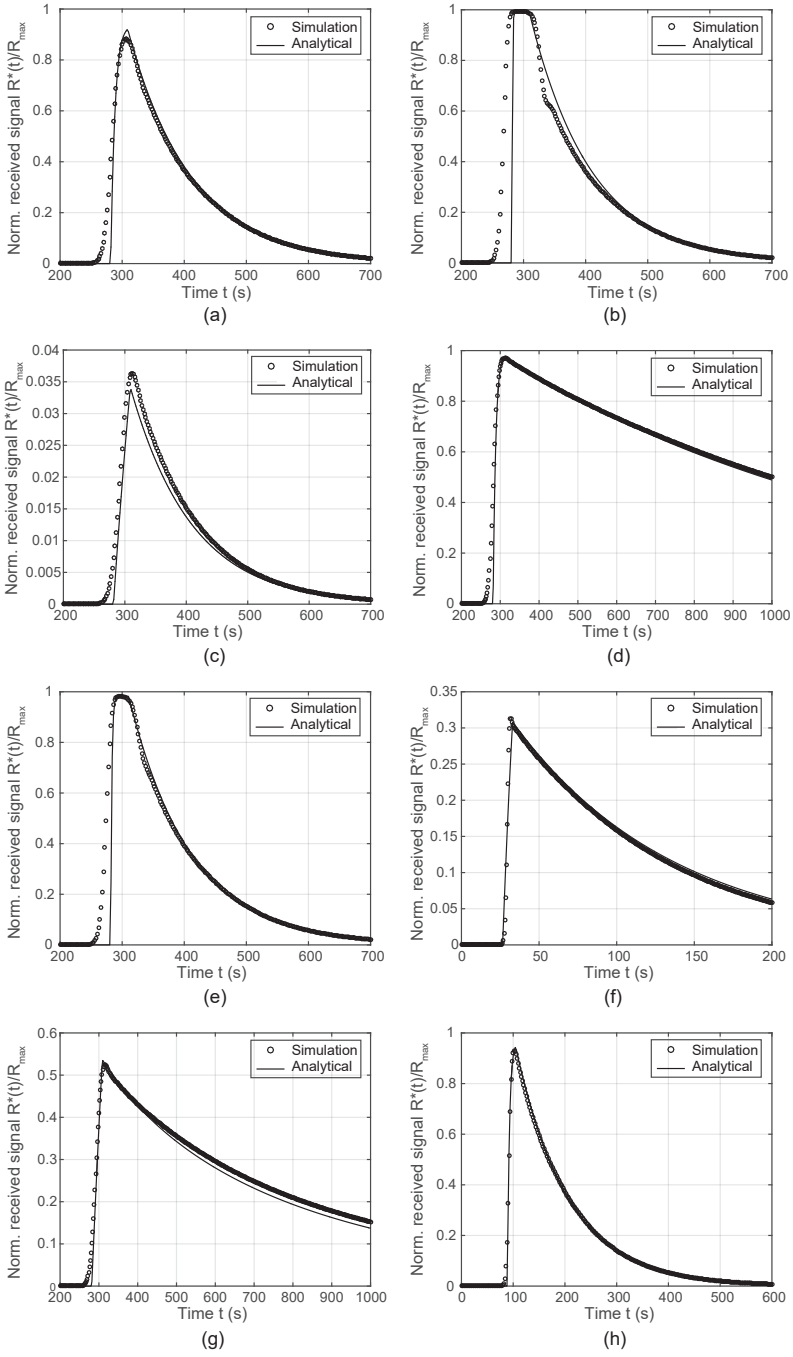

Fig. 3.4 Time course of the number of bound receptors normalized by the total number of receptors for varying system parameters. In each analysis, only one parameter is changed from its default value given in Table 3.1. (a) Default setting. (b) $\mu_T = 10^{10}$ molecules/s. (c) $k_1 = 1$ m^3/mol·s. (d) $k_{-1} = 10^{-3}$ s^{-1}. (e) $T_p = 5$ s. (f) $u = 500$ μs. (g) $\rho_{SR} = 10^{-6}$ mol/m^2. (h) $d_{rx} = 5$ mm.

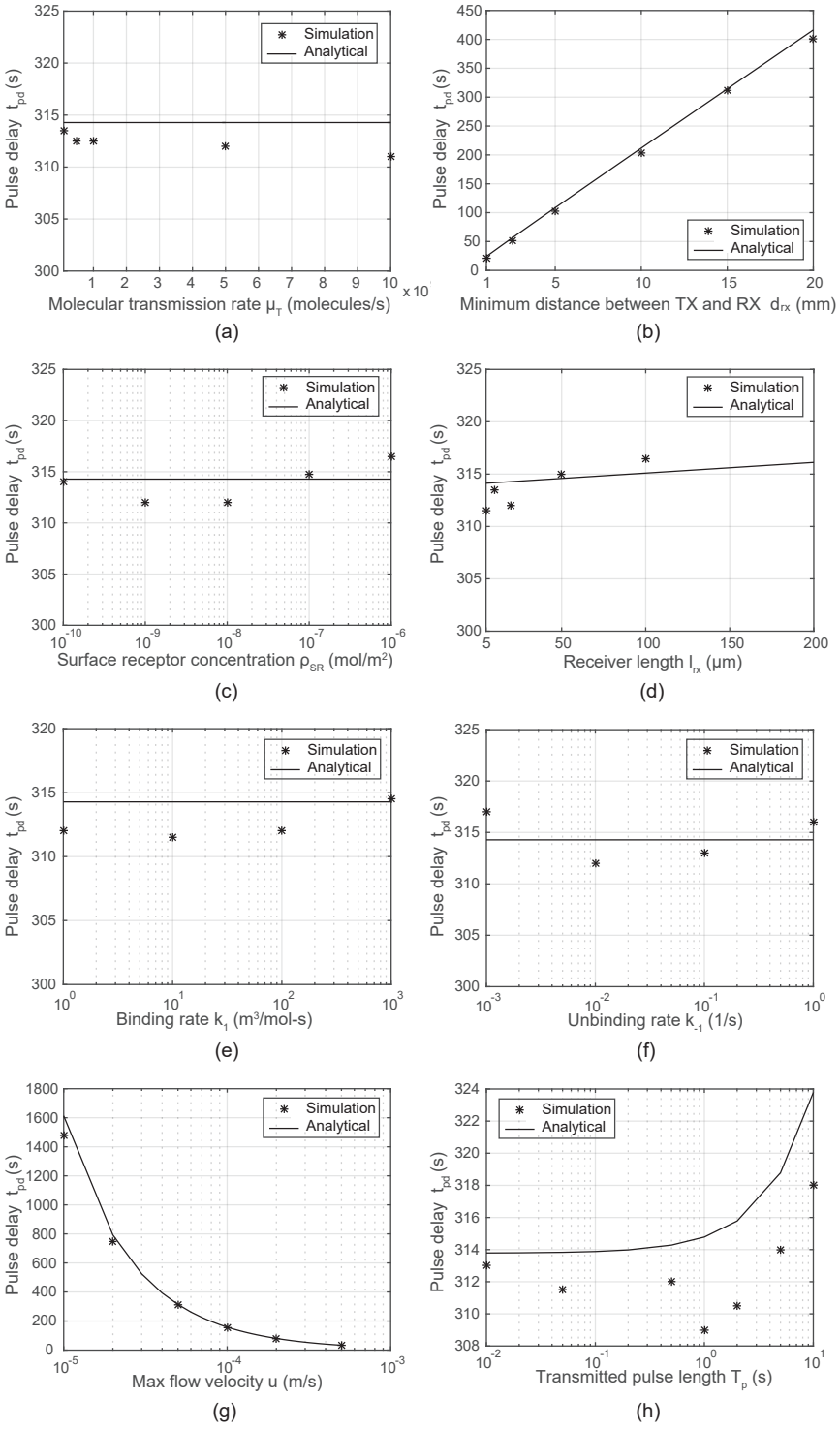

Fig. 3.5 Received pulse delay t_{pd} with varying system parameters.

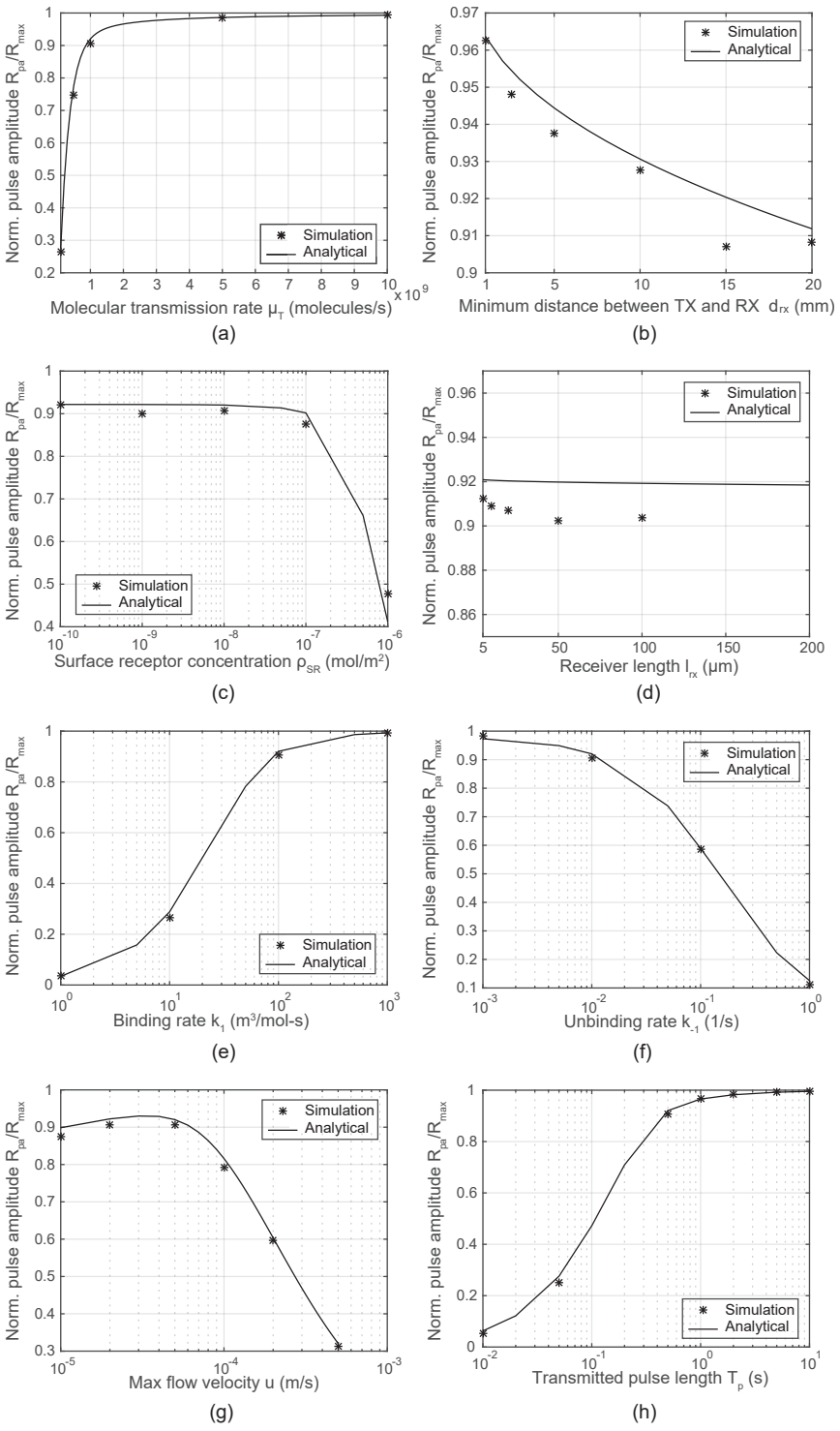

Fig. 3.6 Normalized received pulse amplitude R_{pa}/R_{max} with varying system parameters.

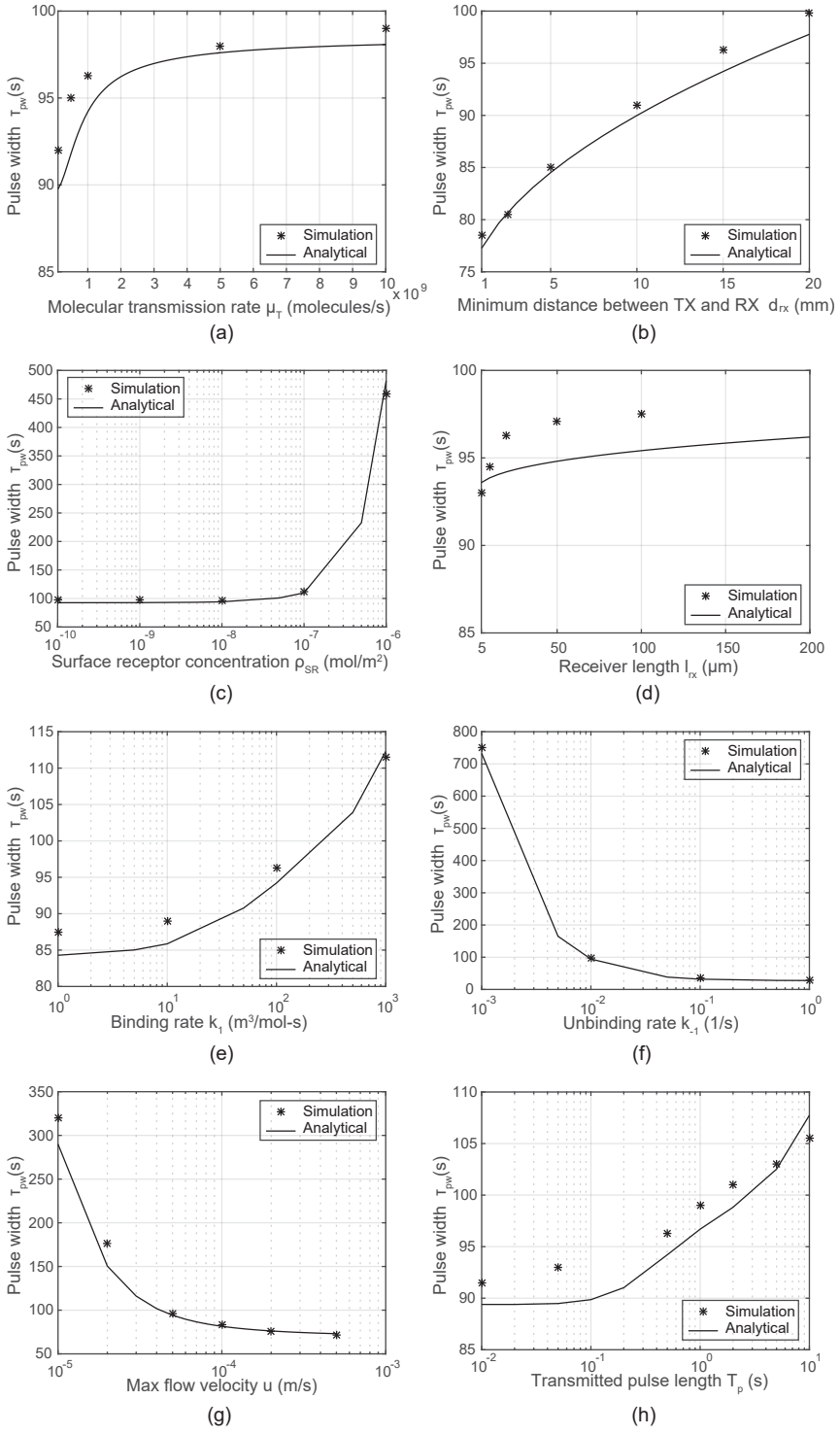

Fig. 3.7 Received pulse width τ_{pw} with varying system parameters.

The third set of analyses are conducted for the pulse width, which is an important parameter since it is directly linked to the extent of ISI and achievable bandwidth. For a fixed symbol duration, ISI increases with pulse width. The analytical results compared to the numerical calculations are presented in Fig. 3.7. The proposed model well approximates the characteristic trends observed under varying conditions. The results reveal that the unbinding rate of the utilized ligand-receptor pair is the most critical parameter that influences the pulse width of the received signal.

The proposed model in this study, which is quite simple and practical by not requiring the computationally expensive numerical methods, is able to accurately capture the design trade-offs, and could be used to design efficient and reliable microfluidic MC systems before their final implementation.

Finally, I would like to discuss about an alternative communication scheme that can be targeted to improve the performance of the microfluidic MC with surface-based receivers. The performance could be substantially improved if multiple types of ligand-receptor pairs with different binding characteristics are employed in the communication system [27]. This way, the transmitter can employ molecular division multiplexing, similar to the code division multiplexing in conventional EM communication systems, to boost the communication rate by simultaneously transferring multiple messages in the same channel without causing significant interference. This can be realised in two ways: (i) Employing multiple receiver antennas, e.g., surface-based biosensors, each having a different type of receptors that bears affinity to a different type of ligands. In this scheme, the receiver can process the output of each antenna separately with minimum interference. (ii) Employing multiple types of receptors corresponding to different types of ligands on the same receiver antenna. In this scheme, the states of different receptors are superposed at the receiver output; therefore, it requires more complex signal processing to discriminate the contributions of different messages conveyed through different ligands. Fortunately, there are a few studies proposing frequency domain detection techniques to exploit the diversity in the critical frequency of ligand-receptor binding noise [27, 185].

3.6 Conclusion

In this chapter, I develop an analytical model that can approximate the time course of the number of bound receptors in microfluidic MC systems with surface-based receivers equipped with ligand receptors. The model is based on the two-compartment model of convection-diffusion-reaction systems, which is tailored to capture the characteristics of the MC system. The comparison of the analytical model-based results with the numerical

results obtained by solving the system model in COMSOL proves the accuracy of the developed model, which is quite successful in capturing the nonlinearities of the system. I also provide closed-form analytical expressions for the pulse width, pulse amplitude and pulse delay of the received signals to provide a framework that would help optimize the microfluidic systems from ICT perspective.

Chapter 4

Maximum Likelihood Detection with Ligand Receptors Based on Receptor Unbound Time Intervals for Overcoming Receiver Saturation

4.1 Introduction

Detection of concentration-encoded messages is a fundamental problem in MC, which has increasingly attracted the attention of researchers in recent years [46, 47]. Living cells, e.g., engineered bacteria, sense molecular concentrations through their receptor proteins, called ligand receptors, which can be located at the cell surface or inside the cell and chemically interact with the ligands in their vicinity [186]. In this regard, the receptors constitute an interface between the external environment and internal molecular networks of living cells. On the other hand, current studies focusing on synthetic MC mostly neglect the stochastic dynamics of receptors, by assuming that the receiver is a perfect observer capable of counting every single information molecule inside a virtually-defined receiver volume. However, the idealisation of the receiver renders all of these approaches impractical; thus, leaves a substantial gap between the theory and practice in every aspects of MC.

This study focuses on the detection problem for MC receivers with ligand receptors. Ligands, referring to information molecules in this context, interact with receptors by randomly and reversibly binding them. The receptor-ligand interaction can be described by a two-state Markov process governed by the binding and unbinding rates of the

ligand-receptor pair [16]. Binding rate is proportional to the ligand concentration in the vicinity of the receptors, while the unbinding rate is invariant to the concentration of ligands. For receptors with a single binding unit, the states of the MC process correspond to the bound and unbound states of the receptors. Finite number of receptors makes the overall interaction nonlinear, which leads to receiver saturation problem when the receptors are exposed to a high concentration of ligands, degrading the sensitivity of the receptors. The existence of receptors complicates the MC detection problem, but at the same time, it unveils a whole new set of observable parameters that are informative of the transmitted symbols.

Here, I investigate the feasibility of Maximum Likelihood (ML) detection based on ligand-receptor interaction, and analyse two different detection techniques varying in its practicality and performance. The first method relies on the instantaneous receptor occupation states and uses the ratio of bound receptors to decide on the transmitted symbol. This method is quite aligned with the MC studies that utilise ligand receptors at the receiver [16, 75]. The second detection method, on the other hand, takes a radically different approach and infers the transmitted symbol from the amount of time the receptors stay unbound.

The likelihood ratio tests are formulated for both type of ML detectors by taking into account the ISI resulting from the memory of the diffusion channel. A comprehensive numerical analysis is conducted to compare their performances in different conditions in terms of resulting bit error probability (BEP). For the first time in the MC literature, the receptor saturation problem is addressed, and the results show that detection based on receptor unbound times is quite reliable in the saturation regime of the receiver. I also discuss the practicality of the detectors in light of state-of-the-art approaches to devise bio-nanomachines.

The remainder of this chapter is organised as follows. In Section 4.2, two different ML estimation schemes are introduced based on receptor occupation ratio and total receptor unbound time. Details of the considered MC scenario are presented in Section 4.3. I introduce the ML detectors in Section 4.4. Performance evaluation results are provided in Section 4.5. A brief discussion on the implementation of the detectors is presented in Section 4.6. Finally, the concluding remarks are given in Section 4.7.

4.2 Maximum Likelihood Estimation of Ligand Concentration

In this section, I investigate two different ML estimators, which constitute the bases for the detectors introduced in Section 4.4. I consider a scenario, where a sensory system comprising of ligand receptors estimates the ligand concentration based on the observable parameters of ligand-receptor interaction. The receptors are assumed to be exposed to a single type of ligands with a stationary concentration.

In ligand-receptor binding reaction, receptors randomly bind to ligands in their vicinity. A receptor can be either in the Bound (B) or Unbound (U) state. Neglecting the ligand diffusion effects on the reaction with the assumption that the diffusion kinetics of ligands to the receptors are comparably faster than the ligand-receptor binding kinetics, and assuming that there is no interaction, e.g., cooperativity, between receptors, which are exposed to the same concentration of ligands, the state of a single receptor is governed by the following two state Continuous-Time Markov Process (CTMP), i.e.,

$$\mathrm{U} \underset{\mathrm{k_-}}{\overset{\mathrm{c\ k_+}}{\rightleftharpoons}} \mathrm{B}, \tag{4.1}$$

where c denotes ligand concentration in the vicinity of receptors, k_+ and k_- are the binding and unbinding rates for the ligand-receptor pair [187]. Note that the overall binding rate, i.e., transition rate from unbound to bound state, is modulated by the ligand concentration c.

4.2.1 Estimation based on Receptor Occupation Ratio (EROR)

Assuming steady-state conditions for the ligand-receptor binding reaction, the probability of finding a receptor in the bound state at any time is given by

$$p_B = \frac{c}{c + K_D}, \tag{4.2}$$

where $K_D = k_-/k_+$ is the dissociation constant, which governs the affinity between the ligand-receptor pair [188]. The state of a single receptor at steady-state can be considered as a Bernoulli random variable with probability of success p_B. When the sensory system is composed of N_R receptors, the random number of bound receptors N follows Binomial

distribution, i.e.,

$$P(N|p_B) = \binom{N_R}{N} p_B^N (1-p_B)^{N_R-N}, \tag{4.3}$$

and the mean number of bound receptors becomes $\mathrm{E}[N] = p_B N_R$. Equation (4.3) and the deterministic relation between p_B and c, given in (4.2), can be exploited to estimate the concentration c from the observed number of bound receptors N. Accordingly, the system can acquire the state of each receptor at once at a specific sampling time, as illustrated in Fig. 4.1, and use only this information to estimate the concentration. An unbiased estimator for p_B can be given by

$$\hat{p}_B = \frac{N}{N_R}, \tag{4.4}$$

and the variance of this estimator is

$$\sigma^2_{\hat{p}_B} = \frac{\mathrm{Var}[N]}{N_R^2} = \frac{p_B(1-p_B)}{N_R}. \tag{4.5}$$

An estimator for the concentration can then be given by inverting the input-output relation between c and p_B in (4.2), i.e.,

$$\hat{c}_N = K_D \frac{\hat{p}_B}{1-\hat{p}_B}. \tag{4.6}$$

Finally, using the rules of error propagation [189], one can write the fractional error in the estimate of concentration as

$$\left(\frac{\delta \hat{c}_N}{c}\right)^2 = \frac{1}{c^2}\left(\frac{dc}{dp_B}\right)^2 \sigma^2_{\hat{p}_B} = \frac{1}{p_B(1-p_B)N_R}. \tag{4.7}$$

Note that the estimation error approaches infinity as occupation ratio p_B nears 0 or 1, corresponding to sparsely occupied and saturation regimes of the sensory system, respectively.

4.2.2 Estimation based on Receptor Unbound Time (ERUT)

Receptors undergo a series of binding and unbinding events when exposed to a ligand concentration, and thus a series of independent bound and unbound time intervals can be observed. The durations of bound and unbound intervals follow exponential distributions with the corresponding rate parameters $\lambda_b = k_-$ and $\lambda_u = ck_+$, respectively. This implies

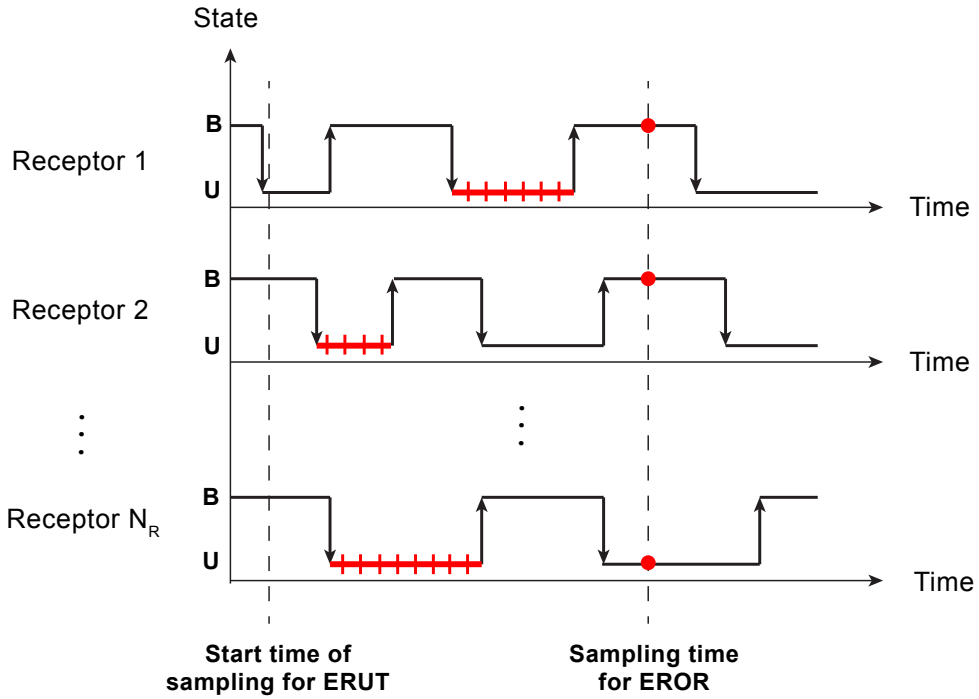

Fig. 4.1 Sampling for EROR and ERUT schemes, demonstrated over a typical binding sequence of N_R receptors.

that the receptors at the bound state are insensitive to the ligand concentration c, and only the unbound time intervals are informative of the concentration.

For the concentration estimation, it is considered that the receiver takes a single sample of unbound time interval from each receptor. From practical point of view, this corresponds to a scenario, where the receiver triggers its receptors at a predefined time, highlighted as the start time of sampling in Fig. 4.1, to inform about the length of the first unbound interval just after the next unbinding event. The corresponding unbound time intervals are also demonstrated in Fig. 4.1. Hence, the receiver is assumed to collect N_R number of independent samples for the length of receptor unbound times from N_R number of receptors. The time necessary for collecting this information can be approximated by considering the worst-case scenario, where a receptor is triggered just after it gets into the unbound state, as demonstrated in the trajectory of Receptor 1 in Fig. 4.1. In this case, it takes an amount of time corresponding to two unbound and one bound intervals for the sampling to be completed. Therefore, the average of maximum sampling time τ_s can be given by

$$\mu_{\tau_s} = 2\mu_{\tau_u} + \mu_{\tau_b}, \tag{4.8}$$

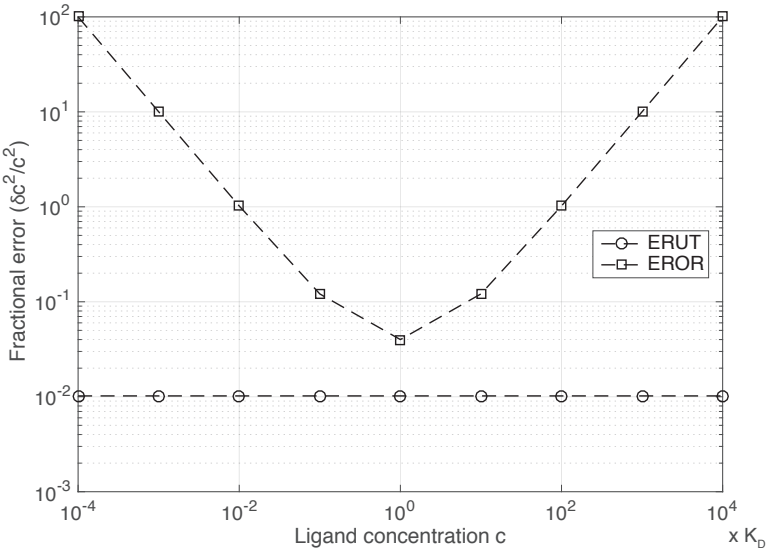

(a)

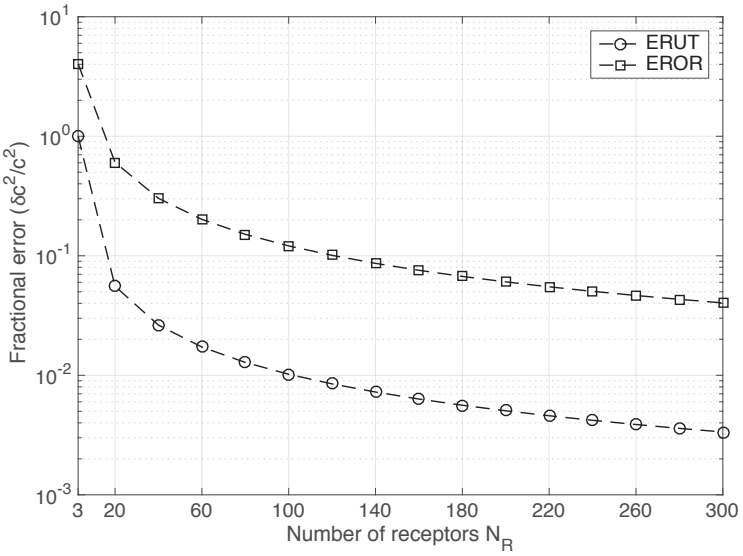

(b)

Fig. 4.2 Fractional errors in concentration estimates based on EROR and ERUT schemes (a) with varying concentration c, and (b) with varying number of receptors N_R.

where $\mu_{\tau_u} = 1/\lambda_u = 1/(k_+ c)$ and $\mu_{\tau_b} = 1/\lambda_b = 1/k_-$ are the mean unbound and bound time intervals, respectively.

In light of above assumption, the likelihood of observing a particular set of N_R unbound time intervals is given by

$$f(\{\tau_u\}|c) = \prod_{i=1}^{N_R} k_+ c e^{-k_+ c\tau_{u,i}} = e^{-k_+ cT_U}(k_+c)^{N_R}, \tag{4.9}$$

where $\{\tau_u\} = \{\tau_{u,1}, \ldots \tau_{u,i}, \ldots \tau_{u,N_R}\}$ is the set of unbound time intervals observed on N_R receptors with $\tau_{u,i}$ denoting the length of i^{th} unbound time interval, and $T_U = \sum_{i=1}^{N_R} \tau_{u,i}$ is the total length of stay in the unbound state. The log-likelihood of observing a set of unbound time intervals is then written as

$$\mathcal{L}_T\left(c;\ \{\tau_u\}\right) = \ln f\left(\{\tau_u\}|c\right) = N_R \ln(k_+c) - k_+ cT_U. \tag{4.10}$$

If the derivative of the log-likelihood function in (4.10) with respect to c is taken equal to zero, one obtains an expression for the ML estimate of ligand concentration, i.e., c_T^*,

$$\frac{\partial \mathcal{L}_T}{\partial c} = \frac{N_R}{c} - k_+ T_U = 0, \tag{4.11}$$

$$\hat{c}_T^* = \frac{N_R}{k_+ T_U}. \tag{4.12}$$

As being the sum of N_R independent and identically distributed (i.i.d.) exponential random variables τ_u, mean of which is $1/(k_+c)$, T_U becomes a *gamma distributed random variable*, i.e., $f(T_U|c) = Gamma(N_R, k_+c)$, with the mean and variance given by

$$\mathrm{E}(T_U|c) = \frac{N_R}{k_+ c}, \tag{4.13}$$

$$\mathrm{Var}(T_U|c) = \frac{N_R}{(k_+c)^2}. \tag{4.14}$$

On the other hand, the reciprocal of the total unbound time of receptors, i.e., $1/T_U$, follows *inverse gamma distribution*, with mean $(k_+c)/(N_R - 1)$. Therefore, the mean of the estimator $\hat{c}_T^*$ is given as follows

$$\mathrm{E}[\hat{c}_T^*] = \frac{cN_R}{N_R - 1}, \tag{4.15}$$

which suggests that the estimator is biased. As hinted by (4.15), an unbiased estimator can be given by

$$\hat{c}_T = \frac{N_R - 1}{k_+ T_U}, \tag{4.16}$$

and the fractional error of this unbiased estimator can be written as

$$\begin{aligned} \left(\frac{\delta \hat{c}_T}{c}\right)^2 &= \frac{1}{c^2}\left(\frac{N_R - 1}{k_+}\right)^2 \mathrm{Var}\left(\frac{1}{T_U}\right) \\ &= \frac{1}{N_R - 2} \quad \text{for} \quad N_R > 2. \end{aligned} \tag{4.17}$$

In the second line of (4.17), I use the fact that $1/T_U$ is inverse gamma distributed, and its variance is given by $\mathrm{Var}(1/T_U) = (k_+ c)^2 / \left((N_R - 1)^2 (N_R - 2)\right)$ for $N > 2$.

Comparing ERUT and EROR schemes in terms of fractional errors in their estimation, i.e., comparing (4.7) and (4.17), one can see that while the error in EROR estimate approaches infinity as the mean occupation ratio p_B gets close to 0 or 1, the extent of error for ERUT is invariant to this ratio, hinting at a substantial performance improvement in saturated and sparsely occupied regimes of the sensory system.

4.2.3 Comparison of ML Estimators

Here, the performances of the estimators are numerically compared in terms of lower bounds on the estimation errors in Fig. 4.2. The results, when $N_R = 100$, and c varies between $10^{-4} K_D$ and $10^4 K_D$, are presented in Fig. 4.2(a). As is seen, the performance of the first estimator substantially degrades when the system is exposed to a very low or very high concentration, i.e., when it is sparsely occupied or almost saturated. On the other hand, the second estimator based on total unbound time is invariant to ligand concentration, and always performs better than the first estimator.

In the second analysis, the ligand concentration is kept constant at $c = 10 K_D$, while the number of observations is varied. As is seen in Fig. 4.2(b), the estimation error decreases with increasing number of observations, and the ERUT-based estimator surpasses the EROR-based estimator by a factor of $1/\Big(p_B(1-p_B)\Big)$, which goes to infinity as the occupation ratio approaches 0 or 1.

In summary, the ERUT-based estimator has a substantial advantage over the EROR-based estimator especially when the system is sparsely occupied ($p_B \simeq 0$) or saturated ($p_B \simeq 1$). In the following, I introduce the ML detectors for MC built upon these estimators, and compare their performances in terms of bit error probability.

4.3 Communication System Model

I consider a time-slotted molecular communication system between a single transmitter nanomachine (Tx) and a single receiver nanomachine (Rx) in a three dimensional fluid environment, which has infinite extent in all dimensions. Tx and Rx are assumed to be synchronized with each other in terms of time. The system utilizes ON/OFF keying (OOK) modulation such that the point source Tx transmits Q molecules as an impulse at the beginning of a time slot to represent the input symbol $s = 1$, and does not transmit any molecule during the time slot to represent $s = 0$.

Transmitted molecules freely propagate in the channel through diffusion, and a fraction of them reaches the Rx location. For the reception process, I follow the same assumptions as in [16]. Accordingly, it is assumed that the receptors are homogeneously distributed inside the receiver volume, and the boundaries of the receiver has negligible effect on the transport dynamics of ligands. Considering that the distance between the Tx and Rx is expected to be very large compared to the dimensions of the nanomachines, one can assume that ligand concentration is also homogeneous inside the receiver volume and equal to its value at the receiver location. Solving the Fick's second law of diffusion for free propagation of ligands, the channel impulse response is obtained as [47]

$$h(t) = (4\pi Dt)^{-3/2} \exp\left(- \frac{d^2}{4Dt} \right), \tag{4.18}$$

where d is the Tx-Rx distance, and D is the diffusion coefficient. Then, the concentration at the receiver location during the i^{th} signalling interval becomes

$$c_{[i]}(t) = \sum_{j=i-I}^{i} s_{[j]} Q h\Big(t + (i-j)T_s\Big) \quad \text{for} \quad t \in [0, T_s), \tag{4.19}$$

where Q is the number of transmitted molecules, T_s is the symbol interval, $s_{[j]} \in \{0, 1\}$ is the transmitted symbol in the j^{th} signalling interval, and I is the channel memory length, i.e., number of interfering symbols. In fact, I goes to infinity in a molecular communication channel, as there is always nonzero probability to find a previously transmitted molecule in the receiver volume. However, this probability quickly decreases with time; thus, the problem here is simplified by considering a finite I.

4.4 Maximum Likelihood Detection with Ligand Receptors

Given the system model in Section 4.3, the detection problem can be cast as a binary hypothesis testing problem, which is formulated for the ith signalling interval as follows

$$\begin{aligned} H_1 &: \ Q \text{ molecules emitted at } t = (i-1)T_s, \text{ i.e., } s_{[i]} = 1 \\ H_0 &: \ \text{No molecule emitted at } t = (i-1)T_s, \text{ i.e., } s_{[i]} = 0 \end{aligned} \tag{4.20}$$

The ML detection methods introduced in the sequel aim at solving the above binary hypothesis testing problem based on the ligand-receptor interaction parameters observable by the receiver.

In developing the detection methods, following the work in [190], I assume that the receiver has a finite memory, and it keeps M number of previously decoded bits in its memory to make use of them along with the channel impulse response function (4.18) to estimate the interference resulting from previous transmissions. Given that the sampling time is fixed and equal to t_s for any signalling interval, one can write the ISI estimate of receiver in the i^{th} signalling interval as

$$\Omega_{[i]} = \sum_{j=i-M}^{i-1} \hat{s}_{[j]} Q h\left(t_s + (i-j)T_s\right) + p_1 Q \sum_{j=i-I}^{i-M-1} h\left(t_s + (i-j)T_s\right), \tag{4.21}$$

where $\hat{s}_{[i]}$ is the i^{th} decoded bit, and $p_1 = P\{s_{[i]} = 1\}$ is the probability for the transmitter to transmit bit-1, which is taken as equal to 0.5, i.e., events $s_{[i]} = 1$ and $s_{[i]} = 0$ are equiprobable. Here, the first summand in the RHS of (4.21) is the estimated value of ISI resulting from M most recent bits decoded by the receiver. The last summand of (4.21) is the ISI resulting from the $(I - M)$ number of bits transmitted prior to the M most recent ones, which is taken as equal to its mean.

4.4.1 Detection based on Receptor Occupation Ratio (DROR)

Using the estimation method described in Section 4.2.1, I now develop a detection technique based on the instantaneous occupation ratio of the receptors. As discussed earlier, the receiver makes use of the number of bound receptors at the sampling time together with its channel impulse response and previously decoded bits stored in its memory to decide between the hypotheses H_0 and H_1.

The estimated likelihood of observing N bound receptors at the sampling time, conditioned on the current transmitted symbol $s_{[i]} = \{0, 1\}$ and receiver's ISI estimate $\Omega_{[i]}$ can be written by using (4.2), (4.3) and (4.21), i.e.,

$$P^*(N|s_{[i]}, \Omega_{[i]}) = \binom{N_R}{N} \left(\frac{\Omega_{[i]} + s_{[i]}\Phi}{\Omega_{[i]} + s_{[i]}\Phi + K_D} \right)^N \left(\frac{K_D}{\Omega_{[i]} + s_{[i]}\Phi + K_D} \right)^{N_R - N}, \tag{4.22}$$

where $\Phi = Qh(t_s)$, and superscript * denotes that this is an estimated likelihood function. Based on (4.22), the hypothesis testing problem can be simplified to a likelihood ratio test (LRT), i.e.,

$$\frac{P^*(N|s_{[i]} = 1, \Omega_{[i]})}{P^*(N|s_{[i]} = 0, \Omega_{[i]})} \underset{H_0}{\overset{H_1}{\gtrless}} 1. \tag{4.23}$$

The LRT can be further simplified by introducing a detection threshold $\lambda_{DROR,[i]}$, i.e.,

$$N \underset{H_0}{\overset{H_1}{\gtrless}} \lambda_{DROR,[i]} = N_R \frac{\ln\left(\frac{\Omega_{[i]}+\Phi+K_D}{\Omega_{[i]}+K_D}\right)}{\ln\left(\frac{\Omega_{[i]}+\Phi}{\Omega_{[i]}}\right)}, \tag{4.24}$$

where the receiver decides H_1 when $N = \lambda_{DROR,[i]}$.

4.4.2 Detection Based on Receptor Unbound Time (DRUT)

As revealed in Section 4.2.2, ligand concentration at the receiver location can be inferred from the total unbound time of receptors T_U, when the number of observed unbound intervals are known to the receiver. Here, I propose a novel detection method based on this estimation scheme. The receiver is assumed to acquire the knowledge of N_R unbound time intervals from its receptors, and use this observation to decode the transmitted symbol s. I also assume that during the observation time window, the ligand concentration at the receiver location remains stationary. This assumption is frequently utilised in MC literature [16, 75], and largely holds true because the transmitted signals are low-pass filtered by the diffusion process, making the time-scale of biologically-relevant ligand-receptor binding reactions is very low compared to the timescale of deviations in the ligand concentration. Additionally, the amount of time required for obtaining N_R samples is on the scale of time required for just two successive unbinding-binding events in a single receptor (see (4.8), and Appendix A.1. for further discussion). Under this assumption, the estimated probability density of the total unbound time of receptors conditioned on

the current transmitted bit $s_{[i]}$ and estimated ISI $\Omega_{[i]}$ can be written as

$$f^*(T_U|s_{[i]},\Omega_{[i]}) = \frac{\left(k_+(\Omega_{[i]}+s_{[i]}\Phi)\right)^{N_R}}{\Gamma(N_R)} T_U^{N_R-1} e^{-k_+(\Omega_{[i]}+s_{[i]}\Phi)T_U} \tag{4.25}$$

where $\Gamma(.)$ is the complete gamma function. The log-likelihood is then given by

$$\begin{aligned}\mathcal{L}_U^*(T_U;s_{[i]},\Omega_{[i]}) &= \ln f^*(T_U|s_{[i]},\Omega_{[i]}) \\ &= N_R \ln\left[k_+(\Omega_{[i]}+s_{[i]}\Phi)\right] - k_+T_U(\Omega_{[i]}+s_{[i]}\Phi) + C,\end{aligned} \tag{4.26}$$

where C is a constant term representing the summands that are invariant to $s_{[i]}$ and cancelled out in the likelihood-ratio test, which is formulated as follows

$$\mathcal{L}_U^*(T_U;s_{[i]}=0,\Omega_{[i]}) \underset{H_1}{\overset{H_0}{\gtrless}} \mathcal{L}_U^*(T_U;s_{[i]}=1,\Omega_{[i]}) \tag{4.27}$$

The test is further simplified by introducing a time-varying threshold variable $\lambda_{DRUT,[i]}$, i.e.,

$$T_U \underset{H_1}{\overset{H_0}{\gtrless}} \lambda_{DRUT,[i]} = \frac{N_R}{k_+\Phi} \ln\left(\frac{\Omega_{[i]}+\Phi}{\Omega_{[i]}}\right) \tag{4.28}$$

It can be inferred from the detection rule (4.28) that higher unbound times are more likely to result from $s = 0$ transmission, i.e., implying less amount of ligands at the receiver. When the concentration becomes higher, there is a higher chance that an unbound receptor quickly rebinds to another ligand.

Table 4.1 Default values of simulation parameters for analysing detection based on receptor unbound time intervals

Number of transmitted ligands for $s = 1$ (Q)	5×10^7
Transmitter-receiver distance (d)	10 μm
Diffusion coefficient of ligands (D)	1×10^{-10} m^2/s
Binding rate (k_+)	2×10^{-19} m^3/s
Unbinding rate (k_-)	20 s^{-1}
Number of receptors on the receiver surface (N_R)	100
ISI length (I)	25
Receiver memory length (M)	2
Symbol interval (T_S)	$4 \times t_{peak}$
Sampling time (t_s)	t_{peak}

4.5 Performance Evaluation

I carry out a comparative analysis to evaluate the performance of the introduced detection schemes in terms of resulting bit error probabilities (BEPs) under different system settings with varying parameters, such as memory length M, number of transmitted molecules Q, Tx-Rx distance d. The default values of system parameters used in the analysis are given in Table 6.2, and the selection criteria for them are discussed in Appendix A.1. I apply Monte Carlo method to estimate the corresponding BEPs as the average value resulting from 1000 runs of simulation of transmitting a pseudorandom sequence of 1000 bits for each different system setting. In each run of the Monte Carlo simulation, BEP values are computed recursively using the detection thresholds given in (4.24) and (4.28).

To increase the signal-to-interference ratio (SIR), I assume that the receiver samples the receptor states or triggers the receptors to inform about the unbound time when the ligand concentration at the receiver location attains its maximum for $s = 1$ transmission, i.e. $t_s = t_{peak}$. Peak time can be derived from the impulse response (4.18), and depends only on the Tx-Rx distance and diffusion coefficient, i.e., $t_{peak} = \frac{d^2}{6D}$. Additionally, I set the default signalling interval to $T_S = 4 \times t_{peak}$, which leads to a moderate ISI in default setting.

Throughout the analysis, along with the results in terms of BEP, I also provide plots for typical occupation ratio p_B^* as function of the system parameter under evaluation to show the degree of saturation and sparsity, and its effect on the detector performance. It is calculated as the mean receptor occupation ratio corresponding to the expected value of concentration at the receiver volume, i.e.,

$$p_B^*(s) = \frac{\mathrm{E}[c|s]}{\mathrm{E}[c|s] + K_D}, \tag{4.29}$$

where $\mathrm{E}[c|s] = sQh(t_s) + p_1 Q \sum_{j=1}^{I} h(t_s + jT_S)$ is the mean ligand concentration at the receiver volume conditioned on the transmitted bit in the current signalling interval, with $s = \{0, 1\}$ denoting the bit 0 or bit 1 transmission.

4.5.1 Effect of Number of Transmitted Molecules

I first investigate the effect of number of transmitted molecules Q on the detection performance. As Q increases, more ligands reach the receiver, making the receptors approach the saturation, as is evident from the varying typical receptor occupation ratio plotted in Fig. 4.3(b). As the receptors get saturated, the performance of the DROR-type detector is severely degraded. BEP increases to almost 0.5, implying that

the detector becomes unable to discriminate the transmitted binary symbols from each other. On the other hand, as seen in Fig. 4.3(a), the performance of the DRUT-type detector is not affected by this parameter. The reason may not be obvious at first sight. As we see in (6.14) and (6.15), the mean and standard deviation of the total unbound time of receptors are scaled with the same factor as the concentration is varied. Therefore, DRUT-type detector, which is based on receptor unbound time, has the same performance regardless of the received concentration and the number of transmitted molecules. Furthermore, note that the DRUT-type detector always outperforms the DROR-type detector, independent of Q.

4.5.2 Effect of Signalling Interval

In the second analysis, I study the relation between the length of the signalling intervals T_S, i.e., the reciprocal of the transmission rate, and the detection performance. Decreasing the length of the signalling interval, i.e., increasing the transmission rate, leads to the saturation of the receptors by increasing the ISI and the ligand concentration at the receiver. However, the increase in the concentration with decreasing T_S does not occur at the same rate for $s = 0$ and $s = 1$ transmission as captured in (4.19) and evident from Fig. 4.4(b). Therefore, different from the first analysis, both type of detectors are significantly affected by the length of the signalling intervals, as seen in Fig. 4.4(a). The improvement of the detection performance with the increasing signalling interval is more pronounced for the DRUT scheme. This is because the ratio of the likelihoods corresponding to $s = 1$ and $s = 0$ transmissions for the DRUT scheme given in Eq. 4.26 is much more sensitive to the decreasing ISI level, that is estimated based on the receiver memory, when compared to the DROR scheme.

4.5.3 Effect of Distance

Next, I investigate the detection performance with varying Tx-Rx distance d. For fixed Q, as the distance increases, concentration at the receiver decreases for both $s = 0$ and $s = 1$ transmissions. As seen in Fig. 4.5(b), the typical occupation ratio ranges between values corresponding to sparsely occupied and saturated receiver, while the distance increases from 10 μm to hundred 100 μm. The DROR scheme performs poorly under both saturation and sparsity conditions, when the typical occupation ratios for $s = 0$ and $s = 1$ approach to each other, and it becomes harder for the receiver to discriminate the two symbols. However, the performance of DRUT-type detector is not affected by

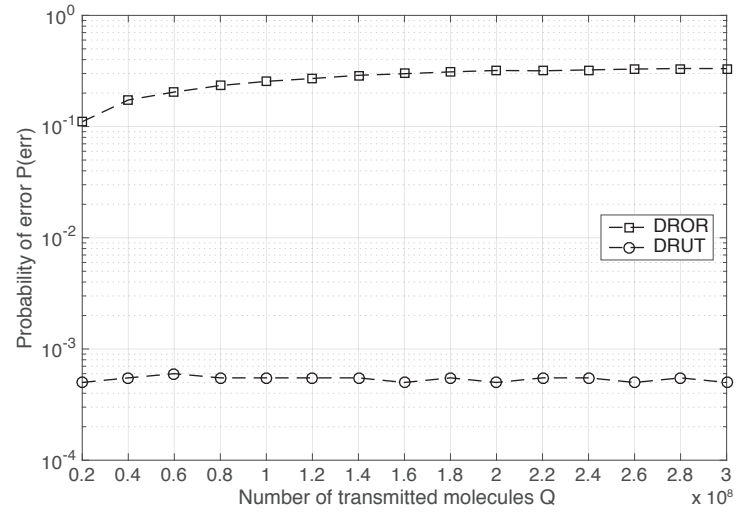

(a)

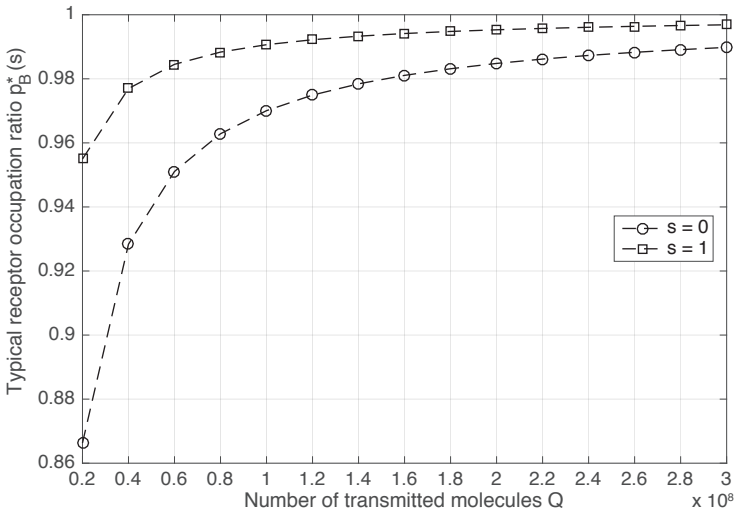

(b)

Fig. 4.3 Effect of number of transmitted molecules Q on the detection performance: (a) bit error probability $P(err)$ with varying Q, (b) corresponding typical receptor occupation ratio p_B^*.

the distance, due to exactly the same reasons as I explain in the first analysis in Section 4.5.1.

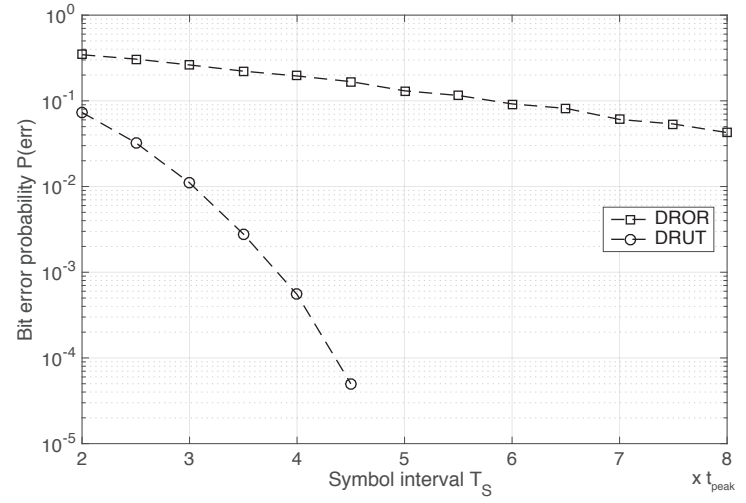

(a)

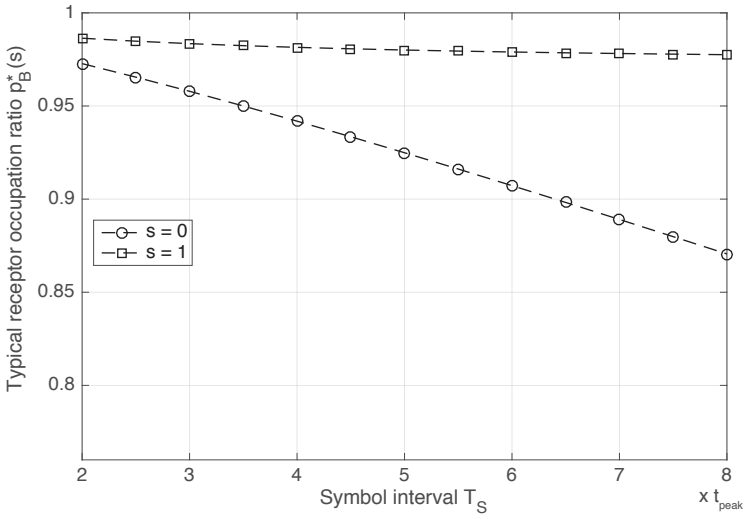

(b)

Fig. 4.4 Effect of symbol interval length T_S on the detection performance: (a) bit error probability $P(err)$ with varying T_S, (b) corresponding typical receptor occupation ratio p_B^*.

4.5.4 Effect of Number of Receptors

I perform another analysis to evaluate the effect of varying number of receptors N_R available in the reception space, which is equal to the number of samples used for detection. Default parameter values given in Table 4.1 are set to make the receptors almost saturate for both $s = 1$ and $s = 0$. Under these conditions, the result of the analysis is shown in

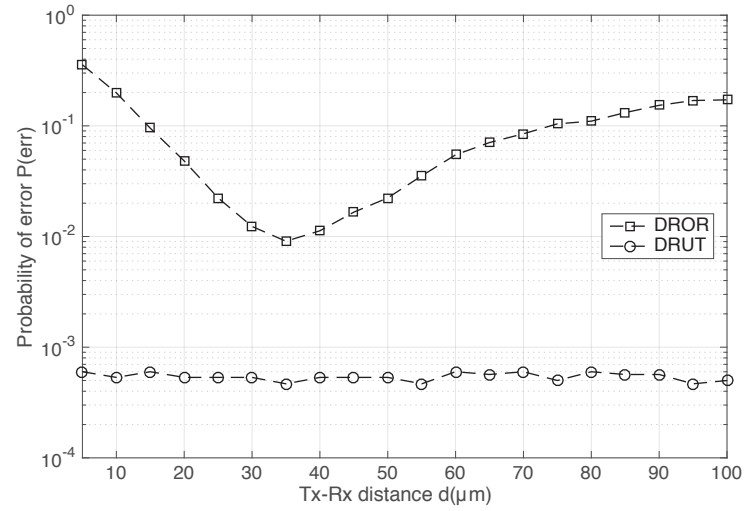

(a)

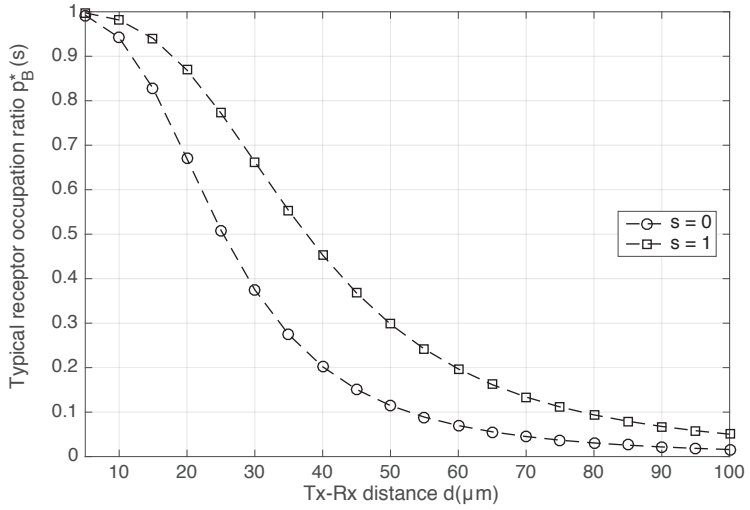

(b)

Fig. 4.5 Effect of Tx-Rx distance d on the detection performance: (a) bit error probability $P(err)$ with varying d, (b) corresponding typical receptor occupation ratio p_B^*.

Fig. 4.6(a). As is seen, the performance of both type of detectors improves with increasing number of receptors. However, the performance improvement in the DRUT-type detector is more evident than the DROR-type detector. The difference can be attributed to the significantly different extent of errors resulting from the underlying estimation methods especially under saturation conditions, which has been covered in Section 4.2.

Note that the model used in this study does not capture the effect of spatial dimensions of the reception space and thus the receptor concentration, and it is based on the assumption that the receptors operate independently of each other. However, high concentration of receptors on a sensory system can give rise to correlations between receptors, due to the correlated transport of ligands to the closely located receptors. The resulting correlation between receptors is found to have a small and negative effect on the ability of sensory system to estimate the ligand concentration [191]. However, it is not included in this study for the sake of mathematical tractability.

4.5.5 Effect of Receiver Memory

The last analysis is performed to reveal the effect of varying length of receiver memory M on the detection performance. As is seen in Fig. 4.6(b), increasing the memory length significantly improves the performance of the DRUT-type detector, whereas only a slight decrease in the probability of error is observed for DROR-type detector. This analysis once again signifies that DRUT-type detector substantially outperforms the DROR-type detector regardless of varying system parameters.

4.6 Discussion on Implementation

In this section, I briefly review the introduced detectors from a practical point of view and discuss the implementation challenges. As discussed in Chapter 2 in detail, there are basically two approaches to implement bio-nanomachines operating in molecular nanonetworks. The first one is based on the use of synthetic nanomaterials, such as SiNW and graphene, as the building blocks of the nanomachines. For example, a few studies recently proposed the use of SiNW bioFETs, which provide affinity-based detection based on ligand-receptor binding mechanism, as the MC receivers [27, 79, 183]. However, in bioFET-based receivers, the sensory information received from ligand receptors is converted, in a combined manner, into an electrical signal contaminated by various noise sources at the output. Therefore, observing the state of individual receptors is not possible with this technology.

The other approach, which is based on synthetic biology, is to implement transmission and reception within living cells by modifying the natural gene circuits or creating new synthetic ones [28]. The technology is already mature enough to allow performing complex digital computations, e.g., with networks of genetic NAND and NOR gates, as well as analogue computations, such as logarithmically linear addition, ratiometric and

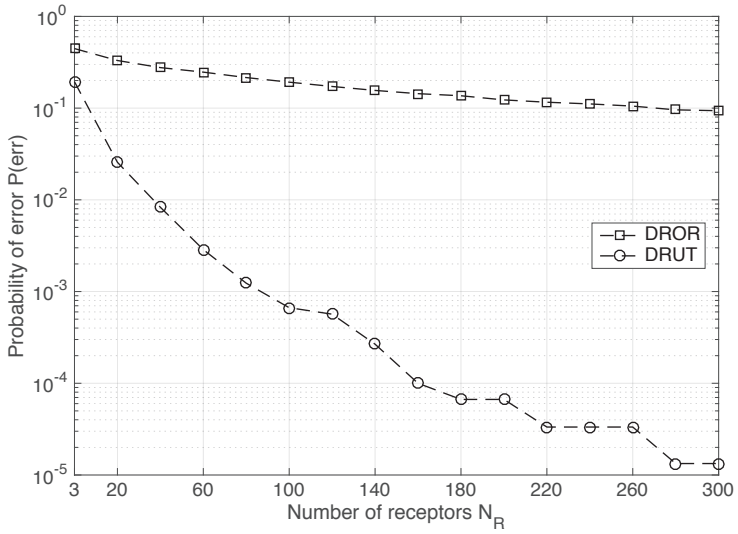

(a)

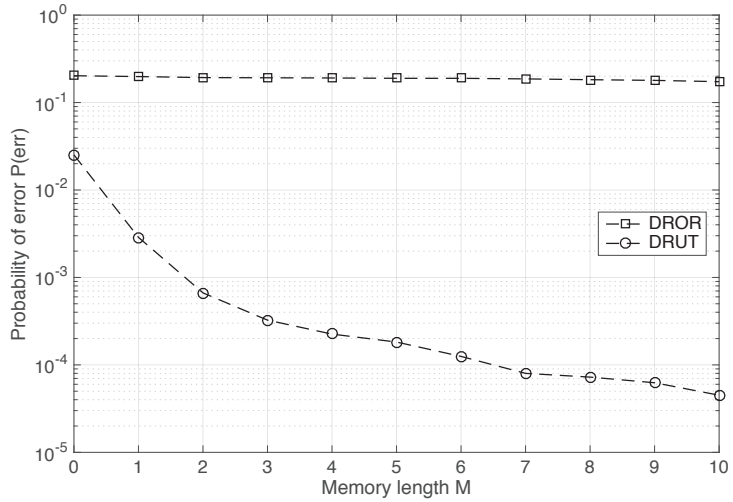

(b)

Fig. 4.6 Bit error probability $P(err)$ with (a) varying number of receptors N_R, and (b) varying receiver memory length M.

power-law computations, in synthetic cells [149]. Synthetic gene networks integrating computation and memory is also proven feasible [150]. More importantly in this context, the technology enables implementing bio-nanomachines capable of observing individual receptors, as naturally done by living cells; thus, stands as a more suitable domain for practically implementing the detectors introduced in this study.

The acquisition of information about the ligand concentration starts with the binding of receptors to ligands. The transduction of the ligand concentration signal to an intracellular molecular signal is realized through downstream signalling networks within the receiver cell. This transduction network outputs a kind of readout molecules inside the cells, which can directly control or modulate a cell activity, or can be an input to another intracellular signalling network, which further processes the data before modulating a cell activity. The latter is the case with the detection mechanisms proposed in this study, as another signalling network will be necessary for decoding the received signals. The state-of-the-art synthetic biology techniques now enable the design of new kinds of receptor-ligand interactions giving rise to new functionalities for receptors and signalling networks [192, 193]. Basically, the conformational changes upon interaction and chemical activation of receptors are the main control parameters for designing receptors with new functionalities [194].

Different network designs can be utilized to implement a cell network, which can achieve the acquisition of the receptor states for both detection schemes. Let us consider the following intracellular reaction network for the DROR scheme, in which the receiver cell needs to sample the instantaneous binding states of the receptors at a given sampling time:

$$S + R^B \xrightarrow{k_{S^*_+}} R^B + S^*, \tag{4.30}$$

$$S^* \xrightarrow{k_{S^*_-}} S. \tag{4.31}$$

Here, R^B, S and S^* denote the bound receptors, readout molecules and activated readout molecules, respectively. Assuming that the reaction rates $k_{S^*_+}$ and $k_{S^*_-}$ are very high compared to the ligand-receptor binding reaction rates, the concentration of activated readout molecules S^* becomes modulated by the instantaneous number of bound receptors. In this way, the intracellular concentration of S^* at the sampling time can be utilized as input to another reaction network within cell to carry out the proposed decoding operation.

The acquisition of unbound time intervals for the DRUT scheme requires more sophisticated reaction networks, as it should include the triggering of the receptors to start reporting the unbound state. The following reaction network can be given as an

example for the signal transduction in this scheme:

$$\varnothing \underset{\mathrm{k_{A-}}}{\overset{\mathrm{k_{A+}}}{\rightleftharpoons}} A, \tag{4.32}$$

$$R_I^B + A \xrightarrow{\mathrm{k_A}} R_A^B + A, \tag{4.33}$$

$$R_I^U + A \xrightarrow{\mathrm{k_A}} R_{A^*}^U + A, \tag{4.34}$$

$$R_{A^*}^U + L \xrightarrow{\mathrm{k_+}} R_A^B, \tag{4.35}$$

$$R_A^B \xrightarrow{\mathrm{k_-}} R_A^U + L, \tag{4.36}$$

$$R_A^U + L \xrightarrow{\mathrm{k_+}} R_I^B, \tag{4.37}$$

$$R_A^U + S \xrightarrow{\mathrm{k_M}} R_A^U + S^*. \tag{4.38}$$

Here, the receptors R have five different states, only one of which is able to react with the readout molecules S. Superscripts B and U denote the bound and unbound states of the receptors, respectively, and subscripts I, A^*, and A denote the inactive, semi-active, and active states of the receptors, respectively. There are also activator molecules A, which are produced with rate k_{A+} when triggered by the receiver at the start time of the sampling for each signalling interval, and degrades with rate k_{A-}. In this network, only the activated unbound receptors R_A^U react with the readout molecules S producing activated readout molecules S^* as the product with rate k_S. Therefore, the concentration of the active readout molecules is modulated by the total unbound time interval T_U, thus they can be used as input to an intracellular decoding network implementing DRUT scheme. The other reactions governing the activation and deactivation of receptors in bound and unbound states, given in (4.33)-(4.37), ensure the proper acquisition of the unbound time data according to the sampling scheme illustrated in Fig. 4.1. Note that the generation and degradation rates of activator molecules k_{A+} and k_{A-} should be high compared to the ligand-receptor binding reaction rates to ensure that the inactivated receptors are not re-activated during the same signalling interval. It is also to be noted that the reaction (4.38) is a quantization operation, which encodes the continuous unbound time information into discrete number of activated readout molecules S^*; therefore, the production rate of S^*, i.e., k_S, determines the extent of the quantization noise, i.e., the higher the rate, the lower the noise.

The detectors investigated in this chapter is based on the likelihood ratio test principle. A comparator gene circuit capable of converting an input analogue signal into a binary signal with an adjustable threshold would be sufficient for the bio-nanomachine to realize any of the detection methods. A recent study has proposed a genetic comparator circuit

integrating analogue and digital computation functionalities, which could serve the needs of the introduced detectors [195]. For DROR and DRUT schemes, the sensory information, which is either the sum of instantaneous receptor occupation states at the sampling time or the total unbound time of receptors, can be directly fed into the analogue input of the comparator in terms of concentration of readout molecules activated by the receptors. The threshold level of the comparator, however, must be set through a series of arithmetic operations on the mean of the ligand concentration at the receiver's vicinity around the sampling time and the previously detected symbols stored in the receiver's memory, see (4.24), (4.28).

The complexity of the required arithmetic operations would add to the detection error, since each computation in a gene network brings its own uncertainty. In addition, for DRUT type detector, the representation of the analogue unbound times with discrete readout molecules would introduce further quantization errors which could propagate to the final readout of the comparator. Fortunately, the quantization errors could be overcome by sufficiently increasing the activation rate of readout molecules by the receptors.

The intrinsic noise in genetic networks, potential errors in the estimation of parameters required for the comparator, and stability issues regarding the memory all add to the overall uncertainty and contribute to the final detection error. However, developing a more comprehensive detection model taking these errors into account is beyond the scope of this dissertation, and thus, remains as a research challenge.

4.7 Conclusion

In this chapter, I investigate the detection problem in diffusion-based MC receivers with ligand receptors. Exploiting the statistical features of the ligand-receptor binding interaction, I propose a novel and easy-to-implement detection method which infers the transmitted symbol from the amount of time the receptors stay in the unbound state. The performance of the proposed detection method is compared to a more conventional detection scheme, which relies on the occupation ratio of the receptors. The results, presented in terms of bit error probability, reveal that the proposed method is substantially more effective in overcoming the saturation problem resulting from the ISI intrinsic to the MC channels.

Chapter 5

Channel Sensing in Molecular Communications with Ligand Receptors

5.1 Introduction

In practice, MC channels, especially in physiologically-relevant environments, can be crowded by many types of molecules that may have similar characteristics rendering their discrimination non-trivial. These molecules can be resulting from natural processes, e.g., intrabody cell signalling, that are generally not relevant to the MC application, leading to natural interference. They can also result from another MC system co-existing in the same medium leading to multi-user interference (MUI) [196]. The knowledge of the channel state information (CSI) in terms of instantaneous concentration of co-existing molecules is crucial for developing reliable detection and modulation methods in the time-varying presence of interferer molecules of similar characteristics with the messenger molecules. It can also enable the application of cognitive medium access (MA) techniques for MC nanonetworks to efficiently allocate the limited molecular resources [197]. Channel estimation techniques are proposed for MC with passive and transparent observers in [198, 199], and channel sensing techniques for co-existing MC nanonetworks that utilize the same type of molecules are considered in [197]. However, simultaneous estimation of concentration of different molecule types has not been investigated in the MC literature before.

This chapter is focused on synthetic biological MC transceivers with ligand receptors on their surface. The receptors constitute the interface between the exterior and interior of

the living cells, interact with the external ligands (i.e., molecules in the MC channel, based on ligand-receptor binding reaction), and transduce the binding events into intracellular signals [188]. The binding rate of ligands to the receptors depend on the transport properties and the concentration of ligands as well as the activation energy of the ligand-receptor binding reaction, whereas the unbinding rate only reflects the affinity between the ligands and the receptors at equilibrium [200]. Ligand receptors, in practice, can provide specificity for the target ligands only to a finite extent, as other types of ligands can also bind the same receptors, though typically having lower affinities [69]. The correlation between unbinding rate and ligand type is exploited in this chapter to develop molecular channel sensing methods.

MC with ligand receptors has been addressed from different aspects. Channel models are developed between point transmitters and reactive receivers with ligand receptors in [71, 72]. Detection techniques are proposed for concentration shift keying (CSK) modulated MC with ligand receptors in [79], based on sampling the instantaneous number of bound receptors. Recently, the continuous history of bound and unbound states has proven to provide more information about the external ligand concentration [77, 201]. In this direction, maximum a posteriori (MAP) detection methods are proposed for MC in [77, 78]. In Chapter 4 of this thesis, receptor unbound time duration statistics is shown to provide a larger dynamic input range for the detector to cope with saturation at high ligand concentrations resulting from intersymbol interference (ISI). Maximum likelihood (ML) estimation of the concentration of two different ligand types based on sampling the receptor bound time durations is studied in [69, 202–204]. These studies also argue practical implementations of the ML estimators exploiting kinetic proofreading (KPR) mechanism, which is an active cellular mechanism that increases specificity, suggested to exist in T-cell receptors that can sense very low concentrations of foreign agents with extreme specificity as part of the immune system [205]. However, none of the previous studies has considered the problem of sensing the concentration of more than two types of ligands at the same time.

In this study, I develop practical channel sensing methods to concurrently estimate the concentrations of different ligand types co-existing in the channel. My work draws on the recent biophysics literature [69, 202], that exploit the receptor cross-talk to sense two types of ligands with a single type of receptors, and generalizes it to the concentration estimation of more than two ligand types for MC applications. The proposed channel sensing methods consist of two estimators. The first one is an unbiased maximum-likelihood (ML) estimator of the total ligand concentration, which uses the amount of time the receptors stay unbound, as proposed in [70, 201]. This estimator exploits the

fact that as the total ligand concentration increases, the receptors bind the ligands more frequently, and thus, the unbound periods of the receptors get shorter. The second estimator is also unbiased, and estimates the concentration ratio of each ligand type from the amount of time the receptors stay bound to a ligand, using the method of moments (MoM). This estimator is based on the fact that the receptors bind more strongly to the ligands of higher affinity, and thus, the duration of bound time periods are correlated with the type of ligands [69]. I also develop a more practical version of the concentration ratio estimator, which is biased, however, requires less number of computations. The product of the total concentration and the ratio estimators provides the instantaneous concentration of each ligand type. The performances of the channel sensing methods are evaluated in terms of normalized mean squared error (NMSE) averaged over all co-existing ligands, for varying number of ligand types in the mixture, varying number of samples, and similarity between the ligand types, and varying concentration distributions of different ligand types within the mixture.

The estimators should operate inside synthetic cells by making use of second messengers, i.e., intracellular signalling molecules, for arithmetic calculations. This requires the transduction of unbound and bound time durations into concentration of second messengers, which are then processed through analogue computing. To this end, I propose a synthetic receptor design with a multitude of internal states, that utilizes a modified version of the conventional KPR mechanism [205]. The proposed receptor is able to be activated by an intracellular activation signal at the start of a sampling period, and encode the observed unbound and bound time durations into the concentration of different types of second messengers. Lastly, I discuss the implementation of the channel sensing methods in synthetic cells, and propose a Chemical Reaction Network (CRN)-based approach to realize the required computations.

The remainder of this chapter is organized as follows. In Section 5.2, I discuss the opportunities of multi-molecular channel sensing in MC focusing on its potential in developing reliable detection methods, adaptive and multi-functional receivers, and medium access techniques. In Section 5.3, I review the fundamental properties of ligand-receptor binding reactions. I present the mathematical framework of the proposed channel sensing methods in Section 5.4. The performance of the techniques is evaluated in Section 5.5. I provide a practical discussion on implementation of the proposed methods in Section 5.6. Lastly, I conclude the chapter in Section 5.7 by discussing open research directions.

5.2 Opportunities of Channel Sensing in MC

Exploiting the cross-talk between different types of ligands for multi-molecular channel sensing with single type of receptors is crucial for improving the adaptivity and reliability of the MC devices, increasing the capacity of the MC channels, and enabling the effective use of limited molecular resources for medium access without requiring substantial amount of additional computational resources and receptors. The proposed channel sensing methods can prove effective especially towards the following directions in the MC research:

- **Development of reliable detection methods for CSK modulated signals based on eliminating the interference of similar ligands released by external sources:** Current studies focusing on CSK-based MC with ligand receptors assume that the receptors are ideal, such that they only react with the ligand type that carries the information [70]. However, in practice, the specificity of receptors is not perfect, and they can react with multiple types of molecules, though with different reaction rates, especially in physiologically relevant conditions. Eliminating the interference by sampling the instantaneous receptor states is not viable, when the channel is time-varying, e.g., the concentration of interferer molecules change between signalling intervals. The channel sensing methods proposed in this study do not require a priori knowledge of the probability distribution of ligand concentrations; therefore, they can enable robust and reliable detection under time-varying conditions.

- **Development of reliable detection methods for molecule shift keying (MoSK) and ratio shift keying (RSK) modulated MC signals:** These modulation techniques rely on the transmission of multiple types of ligands. In MoSK, the information is encoded into the concentration of different ligand types, which are transmitted in separate signalling intervals [20]. On the other hand, in RSK, the information is encoded into the ratio of concentrations of different ligand types transmitted at the same signalling interval. The current studies focusing on both modulation methods assume that there is an ideal receptor for each ligand type, and the cross-talk between different ligand-receptor pairs is neglected [54, 26]. However, this is not the case in practice, as the cross-talk between ligands always exists. The proposed channel sensing methods can be employed to eliminate the cross-talk between different ligand-receptor pairs and increase the capacity of the channel. Additionally, with the use of the proposed methods, both MoSK and RSK modulated MC signals can be accurately detected by utilizing only a single

type of receptor. This can also enable the transmitter to increase the cardinality of the set of transmitted molecule types for boosting the channel capacity, without necessitating the deployment of extra receptors in the receiving side.

- **Development of interference-free molecular division multiple access (MDMA) techniques:** MDMA is based on the idea of using different types of molecules in different MC channels co-existing in the same environment [27, 38]. In this way, multiple nodes can concurrently use the same medium for information transmission; however, the MUI cannot be completely avoided, as the specificity of the receptors is not infinite. Moreover, the number of different ligand types that can be generated and detected by resource-constrained MC devices is limited. Biocompatibility concerns for *in vivo* applications make this limitation more severe [197]. In these circumstances, as similar to the cognitive radio techniques studied for conventional EM communications [206], the channel sensing methods can be opportunistically used to dynamically sense the utilization of different types of carrier molecules in the channel, prior to transmission, to avoid crowding the medium with a particular type of molecule and degrading the communication performance. On the receiver side, the multi-molecule channel sensing methods can provide the receiver with the required adaptivity in detecting different types of molecules transmitted. This also enables the receiving node to simultaneously communicate multiple transmitting nodes through molecular division multiplexing by preventing cross-talk from affecting the reliability of the communication.

- **Multi-functionality:** Lastly, the proposed techniques can enable multi-functional MC devices that can simultaneously perform communication and sensing of multiple types of molecules using the same receptors. This can also help reduce the energy and molecular costs, and simplify the design of biological MC devices for MC nanosensor network applications.

5.3 Statistics of Ligand-Receptor Binding Reactions

Here I provide a brief overview of the statistics of ligand-receptor interactions. More detailed review can be found in Chapter 2 of this thesis. In ligand-receptor binding reaction taking place on the surface of a biological MC device, e.g., engineered bacteria, receptors randomly bind ligands in their vicinity. A receptor can be either in the Bound (B) or Unbound (U) state, with exponential dwell times depending on the binding and unbinding rates of the ligand-receptor pair. The state of a single receptor exposed

to a concentration of ***single type of ligands*** is governed by the following two-state stochastic process,

$$\mathrm{U} \underset{\mathrm{k^-}}{\overset{\mathrm{c_L(t)\ k^+}}{\rightleftharpoons}} \mathrm{B}, \tag{5.1}$$

where $c_L(t)$ denotes the time-varying ligand concentration in the vicinity of receptors, k^+ and k^- are the binding and unbinding rates of the ligand-receptor pair, respectively [187]. Note that the transition rate from unbound to bound state is modulated by ligand concentration $c_L(t)$. In diffusion-based MC, due to the low-pass characteristics of the diffusion channel, the bandwidth of the $c_L(t)$ is typically significantly lower than the characteristic frequency of the binding reaction, i.e., $f_B = c_L(t)k^+ + k^-$; thus, the ligand-receptor reaction is usually assumed to be at equilibrium with a stationary ligand concentration, which is simply denoted by c_L. With this assumption, the process in (5.1) becomes a Continuous Time Markov Process (CTMP). In equilibrium conditions, the probability of observing a receptor in the bound state is given as

$$p_B = \frac{c_L}{c_L + K_D}, \tag{5.2}$$

where $K_D = k^-/k^+$ is the dissociation constant, which gives a measure of the *affinity* between a ligand-receptor pair. If there are multiple receptors that are independently exposed to the same ligand concentration and not interacting with each other, the number of bound receptors becomes a binomial random variable with a success probability of p_B. Hence, the mean and the variance of the number of bound receptors can be written as

$$\begin{aligned} \mathrm{E}[n_B] &= \frac{c_L}{c_L + K_D} N_R, \\ \mathrm{Var}[n_B] &= p_B(1 - p_B) N_R, \end{aligned} \tag{5.3}$$

where N_R is the total number of receptors.

Sampling the number of bound receptors at a given time instant previously proved effective in inferring the concentration of ligands, when the receiver is away from saturation [70], i.e., when $p_B \ll 1$. However, when there are ***multiple types of ligands*** in the channel medium, as shown in Fig. 5.1(a), which can bind the same receptor with different affinities, i.e., with different dissociation constants, the bound state probability of a receptor at equilibrium becomes

$$p_B = \frac{\sum_{i=1}^{M} c_i/K_{D,i}}{1 + \sum_{i=1}^{M} c_i/K_{D,i}}, \tag{5.4}$$

where M is the number of different types of ligands co-existing in the medium.

The expression in (5.4) cannot be used to infer the individual ligand concentrations c_i due to the interchangeability of the summands [69]. Therefore, in the case of a mixture of different ligand types, the required insight into the individual ligand concentrations can only be acquired by examining the continuous history of binding and unbinding events over receptors, which is exemplified in Fig. 5.1(b). In this case, the likelihood of observing a set of N independent binding and unbinding intervals over any set of receptors at equilibrium can be written as

$$\begin{aligned} &\mathrm{p}\left(\{\tau_b, \tau_u\}_N\right) \\ &= \frac{1}{Z}\mathrm{e}^{-\sum_{i=1}^{N}\tau_{u,i}\left(\sum_{j=1}^{M}k_j^+c_j\right)}\prod_{i=1}^{N}\left(\sum_{j=1}^{M}k_j^+c_jk_j^-\mathrm{e}^{-k_j^-\tau_{b,i}}\right), \end{aligned} \tag{5.5}$$

where Z is the probability normalization factor, M is the number of ligand types co-existing in the channel, k_i^+ and k_i^- are the binding and unbinding rates for the i^{th} ligand type, respectively, $\tau_{u,i}$ and $\tau_{b,i}$ are the i^{th} observed unbound and bound time durations, respectively, [69, 70]. Note that an unbound or bound time duration is the duration of a time interval that a receptor continuously stays unbound or bound, respectively. Given that the receptors are independent of each other, and they are exposed to the same ligand concentration assumed to be constant during sampling, ligand-receptor binding reaction becomes a stationary ergodic process. Therefore, the likelihood function (5.5) does not depend on the time instants the ligands bind or unbind, and the indices of bound and unbound time durations do not necessarily imply a receptor-based or chronological order. In other words, the entire set of bound and unbound duration samples $\{\tau_b, \tau_u\}_N$ can be obtained equivalently by observing the time trajectory of only a single receptor or multiple independent receptors.

In the diffusion-limited case, i.e., where the reaction rates are much higher than the characteristic rate of diffusion, the binding rate can be simply given by $k^+ = 4Da$ for circular receptors [69], with D and a being the diffusion constant of molecules and the effective receptor size, respectively. Assuming that the ligands are of similar size, their diffusion coefficients D, which depends on the temperature and viscosity of the fluid medium, and the size of diffusing molecules [188], are approximately equal for all ligand types. In this case, the likelihood function (5.5) can be reduced to

$$\mathrm{p}\left(\{\tau_b, \tau_u\}_N\right) = \frac{1}{Z}e^{-T_u k^+ c_{tot}}(k^+c_{tot})^N\prod_{i=1}^{N}\mathrm{p}\left(\tau_{b,i}\right), \tag{5.6}$$

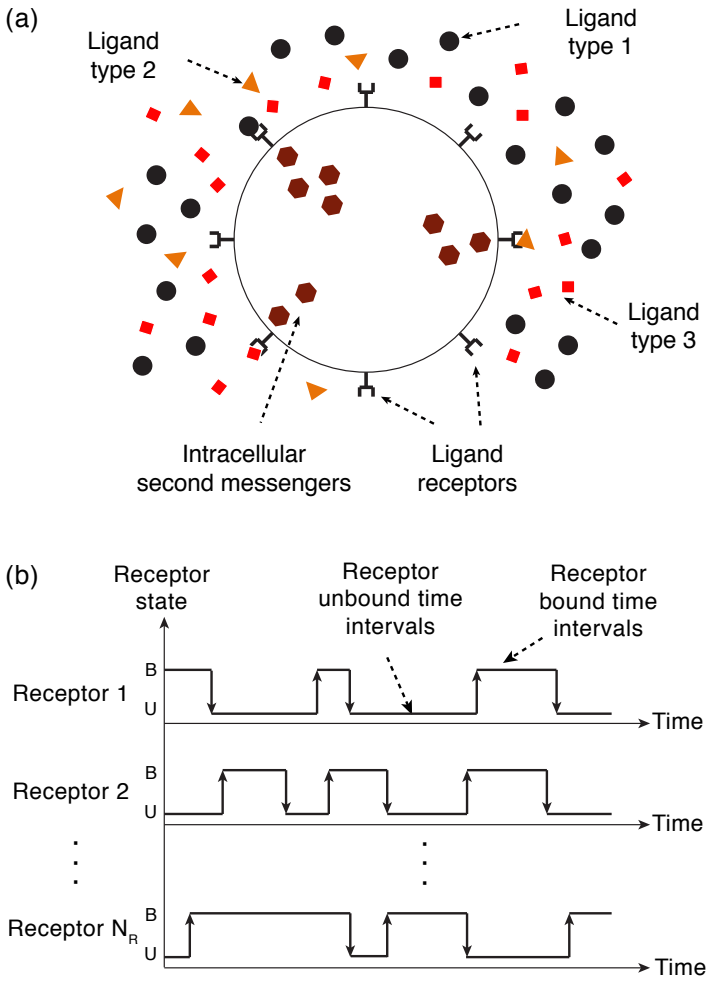

Fig. 5.1 (a) A biological MC device with ligand receptors on its surface exposed to a mixture of different ligand types of different affinities with the receptors. The binding events are transduced into second messengers inside the cell. (b) An example time course of binding and unbinding events occurring on the receptors. Duration of binding events depends on the affinity of the bound ligand with the receptor.

where $T_u = \sum_{i=1}^{N} \tau_{u,i}$ is the total unbound time of all receptors, $c_{tot} = \sum_{i=1}^{M} c_i$ is the total ligand concentration in the vicinity of the receptors, and $\mathrm{p}(\tau_{b,i})$ is the probability of observing a bound time duration, which is given as a *mixture of exponential distributions*, i.e.,

$$\mathrm{p}\left(\tau_{b,i}\right) = \sum_{j=1}^{M} \alpha_j k_j^- \mathrm{e}^{-k_j^- \tau_{b,i}}. \tag{5.7}$$

Here $\alpha_j = c_j / c_{tot}$ is the concentration ratio of the j^{th} ligand type.

The log-likelihood function for an observed set of unbound/bound time durations can be written as the sum of three terms, i.e.,

$$\begin{aligned}\mathcal{L}(\{\tau_b, \tau_u\}_N) &= \ln \mathrm{p}(\{\tau_b, \tau_u\}_N), \\ &= \mathcal{L}_0 + \mathcal{L}\left(T_u|c_{tot}\right) + \mathcal{L}\left(\{\tau_b\}|\boldsymbol{\alpha}\right),\end{aligned} \tag{5.8}$$

where $\mathcal{L}_0$ comprises the terms that do not depend on c_{tot} or $\boldsymbol{\alpha}$, while $\mathcal{L}\left(T_u|c_{tot}\right)$ and $\mathcal{L}\left(\{\tau_b\}|\boldsymbol{\alpha}\right)$ are the functions of the total concentration c_{tot} and the ligand concentration ratios $\boldsymbol{\alpha}$ denoted here as an $(M \times 1)$ vector, respectively. For estimating the individual ligand concentrations, we are only interested in the log-likelihoods that are functions of c_{tot} and $\boldsymbol{\alpha}$ and given as

$$\mathcal{L}\left(T_u|c_{tot}\right) = N \ln(c_{tot}) - k^+ c_{tot} T_u, \tag{5.9}$$

$$\mathcal{L}\left(\{\tau_b\}|\boldsymbol{\alpha}\right) = \sum_{i=1}^{N} \ln \mathrm{p}\left(\tau_{b,i}\right). \tag{5.10}$$

Accordingly, $\mathcal{L}\left(T_u|c_{tot}\right)$ tells us that the total unbound time T_u is informative of the total ligand concentration c_{tot}, whereas $\mathcal{L}\left(\{\tau_b\}|\boldsymbol{\alpha}\right)$ shows that the individual bound time durations $\{\tau_b\}$ are informative of the ligand concentration ratios $\boldsymbol{\alpha}$. Hence, the estimators of individual ligand concentrations introduced in the next section will be based on these two likelihood functions.

5.4 Channel Sensing based on Ligand-Receptor Binding Reaction

5.4.1 System Model

In the considered scenario, the MC receiver is equipped with only a single type of receptors, whereas there are multiple types of ligands in the channel medium. The following assumptions are made regarding the properties of the receiver and ligands.

- There are M different types of ligands in the medium, which have distinct unbinding rates in their reactions with the receptors. It is assumed that the binding rates of ligand types are equal to $k^+ = 4Da$, with the condition of diffusion-limited propagation, as discussed in Section 5.3. This assumption is made for the sake of simplicity of the derivations; however, it does not limit the applicability of the

estimators to other cases, where binding rates may also differ, as investigated in [202] for two types of ligands.

- Receptors are assumed to be independent of each other. All receptors are exposed to the same concentration of ligands. In practice, this may correspond to a scenario where the receptors are free to diffuse in a lipid membrane of a cell. The ligands and receptors are assumed to be homogeneously distributed within this membrane.

- Ligand concentration in the vicinity of receptors is assumed to be stationary during estimation. This assumption is based on the low-pass characteristics of the MC channel, as discussed in the Section 5.3. I also assume the fluctuations in the concentration of ligands resulting from binding reactions are negligible.

- The unbinding rates of co-existing ligands are assumed to be known to the receiver. This may correspond to a scenario, where a receiver is hardwired prior to its utilization for the potential set of ligand types that may exist in an application environment. As we will see in Section 5.5.5, in the case of absence of any ligand type from this set has a slight effect on the overall performance of the estimators. Hence, hardwiring the receiver with a large set of potential ligand types can overcome the limitations of this assumption.

5.4.2 Optimal Estimation of Ligand Concentrations and Cramér-Rao Lower Bound (CRLB)

The likelihood function in (5.8) suggests that we can estimate the concentration of each ligand type by simultaneously inferring the total ligand concentration and concentration ratios of ligand types from the total unbound time T_u and bound time durations $\{\tau_b\}$ of receptors, respectively.

Optimal Estimation of Total Ligand Concentration

An ML estimator of the total ligand concentration c_{tot} can be found by solving $\partial \mathcal{L}\left(T_u|c_{tot}\right)/\partial c_{tot} = 0$ for c_{tot} that maximizes the likelihood. The resulting ML estimator is obtained as $\hat{c}_{tot} = \frac{N}{k^+ T_u}$. Note that T_u, as the sum of N independent exponential random variables ($\tau_{u,i}$'s), is gamma distributed, making its reciprocal $1/T_u$ an inverse gamma-distributed random variable with mean

$$\mathrm{E}[1/T_u] = \frac{k^+ c_{tot}}{N-1}. \tag{5.11}$$

Hence, the mean of the estimator becomes $\mathrm{E}[\hat{c}_{tot}] = (N/k^{+}) \times \mathrm{E}[1/T_u] = c_{tot} \times N/(N-1)$, rendering it biased unless N is very large. Therefore, I prefer here using its unbiased version, which is obtained by modifying only the numerator of the biased estimator as follows

$$\hat{c}_{tot} = \frac{N-1}{k^{+}T_u}, \tag{5.12}$$

which is unbiased for $N > 1$ [70]. Accordingly, the mean squared error (MSE) of this unbiased estimator is given by its variance [70], i.e.,

$$\mathrm{MSE}[\hat{c}_{tot}] = \mathrm{Var}\left[\hat{c}_{tot}\right] = \frac{c_{tot}^2}{N-2} \quad \text{for} \quad N > 2. \tag{5.13}$$

Note that the mean of the total concentration estimator now becomes equal to the actual value of the total ligand concentration, i.e.,

$$\mathrm{E}[\hat{c}_{tot}] = c_{tot}. \tag{5.14}$$

Optimal Estimation of Ligand Concentration Ratios

The ML estimation of the co-existing ligand types' concentration ratios, i.e., $\hat{\boldsymbol{\alpha}}_{\boldsymbol{ML}}$, can be performed in the same manner, by solving $\partial \mathcal{L}\left(\{\tau_b\}|\boldsymbol{\alpha}\right)/\partial \alpha_i = 0$ for the i^{th} ligand, i.e.,

$$0 = \sum_{j=1}^{N} \frac{k_i^{-} \mathrm{e}^{-\left(k_i^{-}\tau_{b,j}\right)}}{\sum_{l=1}^{M} \alpha_l k_l^{-} \mathrm{e}^{-k_l^{-}\tau_{b,j}}} \quad \text{for } i \in \{1, \ldots, M\}. \tag{5.15}$$

The expression in (5.15) does not lend itself to an analytical solution for ML estimate $\hat{\boldsymbol{\alpha}}_{\boldsymbol{ML}}$, and necessitates numerical approaches. In fact, the problem of Bayesian inference from mixture of exponential distributions is generally tackled by computationally expensive iterative algorithms, e.g., expectation-maximization (EM) algorithm [207, 208], which cannot be considered feasible for resource-limited bionanomachines, and thus they are disregarded in this study.

Optimal Estimation of Individual Ligand Concentrations

The optimal ML estimator of the concentration of individual ligand types can be given as the product of the estimators of the total ligand concentration and ligand concentration ratios, i.e.,

$$\hat{\boldsymbol{c}}_{\boldsymbol{ML}} = \hat{c}_{tot}\hat{\boldsymbol{\alpha}}_{\boldsymbol{ML}}. \tag{5.16}$$

The derivation of the variance for this optimal ML estimator is not analytically tractable. Instead, in the following section, I derive a lower bound on its variance through Cramér-Rao formalism.

Error Bound

CRLB gives the minimum variance of any unbiased estimator as the inverse of the Fisher information [209]. The ML estimator of the total ligand concentration, whose variance is given in (5.13), already achieves the CRLB [70]. To obtain the CRLB for the estimator of individual ligand concentrations, we first need to derive the bound for the ML estimator of ligand concentration ratios.

The Fisher information of the concentration ratio vector $\boldsymbol{\alpha}$ is an $(M \times M)$ matrix, which is given by the negative expectation of the Hessian matrix, i.e.,

$$\boldsymbol{I}_{\boldsymbol{\alpha}} = -\mathbf{E}[\boldsymbol{H}_{\boldsymbol{\alpha}}]. \tag{5.17}$$

The elements of the Hessian matrix are given by the second-order partial derivatives of the log-likelihood function that governs the relation between bound time durations and ligand concentration ratios, i.e.,

$$\begin{aligned} \boldsymbol{H}_{\boldsymbol{\alpha}}(i,j) &= \frac{\partial^2}{\partial \alpha_i \partial \alpha_j} \mathcal{L}\left(\{\tau_b\}|\boldsymbol{\alpha}\right) \\ &= -\sum_{l=1}^{N} \frac{k_i^- k_j^-}{\mathrm{p}\left(\tau_{b,l}\right)^2} \mathrm{e}^{-(k_i^- + k_j^-)\tau_{b,l}}. \end{aligned} \tag{5.18}$$

Substituting (5.18) in (5.17), the elements of the Fisher information matrix are obtained as follows

$$\begin{aligned} \boldsymbol{I}_{\boldsymbol{\alpha}}(i,j) &= -\mathrm{E}\left[-\sum_{l=1}^{N} \frac{1}{\mathrm{p}\left(\tau_{b,l}\right)^2} k_i^- k_j^- \mathrm{e}^{-(k_i^- + k_j^-)\tau_{b,l}}\right] \\ &= \sum_{l=1}^{N} \mathrm{E}\left[\frac{1}{\mathrm{p}\left(\tau_{b,l}\right)^2} k_i^- k_j^- \mathrm{e}^{-(k_i^- + k_j^-)\tau_{b,l}}\right] \\ &= N k_i^- k_j^- \int_0^\infty \frac{1}{\mathrm{p}\left(\tau_b'\right)} \mathrm{e}^{-(k_i^- + k_j^-)\tau_b'} d\tau_b'. \end{aligned} \tag{5.19}$$

The CRLB is then given by the inverse of the i^{th} diagonal element of the inverse Fisher information matrix for the estimation of concentration ratio of the i^{th} ligand, i.e.,

$$\mathrm{Var}[\hat{\alpha}_{ML,i}]_{LB} = \boldsymbol{I}_{\boldsymbol{\alpha}}^{-\mathbf{1}}(i,i). \tag{5.20}$$

Given that the ML estimator of total ligand concentration $\hat{c}_{tot}$ already achieves the lower bound, the CRLB for the concentration estimator given in (5.16) can be written as

$$\begin{aligned}\mathbf{Var}[\hat{\boldsymbol{c}}_{\boldsymbol{ML}}]_{\boldsymbol{LB}} =& \mathrm{Var}[\hat{c}_{tot}]\mathbf{Var}[\hat{\boldsymbol{\alpha}}_{\boldsymbol{ML}}]_{\boldsymbol{LB}} + \\ & \mathrm{Var}[\hat{c}_{tot}]\left(\mathbf{E}[\hat{\boldsymbol{\alpha}}_{\boldsymbol{ML}}] \odot \mathbf{E}[\hat{\boldsymbol{\alpha}}_{\boldsymbol{ML}}]\right) + \mathbf{Var}[\hat{\boldsymbol{\alpha}}_{\boldsymbol{ML}}]_{\boldsymbol{LB}}\mathrm{E}[\hat{c}_{tot}]^2,\end{aligned} \tag{5.21}$$

where $\mathbf{E}[\hat{\boldsymbol{\alpha}}_{\boldsymbol{ML}}] = \boldsymbol{\alpha}$; $\mathbf{Var}[\hat{\boldsymbol{\alpha}}_{\boldsymbol{ML}}]_{\boldsymbol{LB}}$ is an $(M\times 1)$ vector with the i^{th} element given by (5.20), and $\odot$ denotes the Hadamard product, i.e., $(\boldsymbol{A} \odot \boldsymbol{B})_{i,j} = (\boldsymbol{A})_{i,j}(\boldsymbol{B})_{i,j}$. Note that since the optimal ML estimator achieving the CRLB is an unbiased estimator, the lower bound on the MSE is equal to the CRLB on the variance, i.e., $\mathbf{MSE}[\hat{\boldsymbol{c}}_{\boldsymbol{ML}}]_{\boldsymbol{LB}} = \mathbf{Var}[\hat{\boldsymbol{c}}_{\boldsymbol{ML}}]_{\boldsymbol{LB}}$.

5.4.3 Suboptimal Estimation of Ligand Concentrations

The optimal ML estimation of the concentration ratios, and thus the individual concentrations of ligands, is not feasible for resource-limited bio-nanomachines, as it requires complex numerical calculations. To overcome this problem, I propose a novel practical method based on method of moments (MoM) to estimate the concentration ratios of ligand types. MoM is a non-optimal estimation method that exploits the theoretical relation between the unknown parameter and the moments of the probability density function (pdf) of the observed parameter [209]. As it is much easier to implement than the optimal estimation methods, it can be considered more suitable for resource-limited biological transceivers.

The proposed estimation method relies on statistically binning the receptor bound times into a number of time intervals determined by the unbinding rates of existing ligands, instead of using the exact bound time durations. Next, I investigate two versions of this estimation method, which provide unbiased and simplified biased estimation of the concentration of each ligand type.

Unbiased Estimation of Ligand Concentrations

The proposed estimation method for ligand concentration ratios is based on counting the number of binding events that fall in specific time intervals. The number of the time intervals is equal to the number of ligand types, as demonstrated in Fig. 5.2. These non-overlapping intervals are defined by time thresholds, which can be taken as proportional to the inverse of the unbinding rates of ligands, i.e.,

$$T_i = \nu/k_i^- \quad \text{for} \quad i \in \{1, \dots M-1\}, \tag{5.22}$$

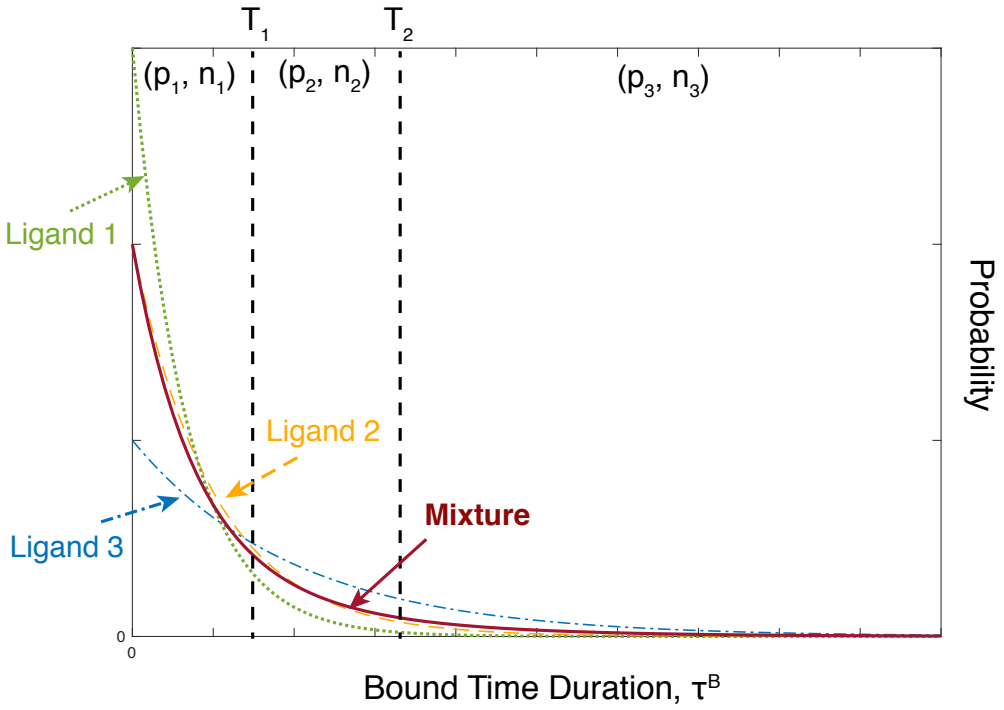

Fig. 5.2 Probability distribution of receptor bound time durations for a mixture of three different types of ligands, which is a mixture of exponential distributions. The regions separated by the time thresholds (T_1 and T_2) are marked with the corresponding probability of observing a binding time duration and the number of binding events in those regions, i.e., p_i, n_i, respectively.

given that all ligand types are sorted in decreasing order of unbinding rate, i.e., increasing order of their affinity with the receptors. Here, $\nu > 0$ is a proportionality constant, which will be optimized in Section 5.5. Later, I will also show that this transduction scheme is suitable for biological MC devices, as it can be implemented by active receptors based on well-known KPR scheme.

The probability of observing a ligand binding event of a duration that falls in a time interval between two time thresholds can be written as

$$\mathrm{p}_l = \int_{T_{l-1}}^{T_l} \mathrm{p}(\tau_b')d\tau_b' = \sum_{i=1}^{M} \alpha_i \left(\mathrm{e}^{-(k_i^- T_{l-1})} - \mathrm{e}^{-(k_i^- T_l)} \right), \tag{5.23}$$

where I set $T_0 = 0$ and $T_M = +\infty$. In matrix notation, the probabilities can be written as

$$\mathbf{p} = \boldsymbol{S}\boldsymbol{\alpha}, \tag{5.24}$$

where $\mathbf{p}$ is an $(M \times 1)$ probability vector with the elements p_l, and $\boldsymbol{S}$ is an $(M \times M)$ matrix with the elements

$$s_{i,j} = \mathrm{e}^{-(k_j^- T_{i-1})} - \mathrm{e}^{-(k_j^- T_i)}. \tag{5.25}$$

The number of binding events that fall in each interval follows binomial distribution with the mean and the variance given by

$$\mathbf{E}[\mathbf{n}] = \mathbf{p}N, \tag{5.26}$$

$$\mathbf{Var}[\mathbf{n}] = (\mathbf{p} \odot (1 - \mathbf{p}))\, N, \tag{5.27}$$

where $\boldsymbol{n}$ is an $(M \times 1)$ vector with the vector elements n_i being the number of binding events whose durations are within the i^{th} time interval defined by T_{i-1} and T_i.

We can now apply the MoM for the estimation of ligand concentration ratios by employing only the first moment. In other words, I match the expected number of binding events in a time interval to the actual number of binding events observed for the same interval, i.e.,

$$\boldsymbol{n} = \hat{\mathbf{p}}N = \boldsymbol{S}\hat{\boldsymbol{\alpha}}N, \tag{5.28}$$

where the hat denotes the estimated parameters. Rearranging the parameters in (5.28), an estimator for the ligand concentration ratio vector is obtained:

$$\hat{\boldsymbol{\alpha}} = \left(\frac{1}{N}\right) \boldsymbol{W}\boldsymbol{n}, \tag{5.29}$$

where $\boldsymbol{W} = \boldsymbol{S}^{-1}$, i.e., the inverse of $\boldsymbol{S}$ matrix, which is also an $(M \times M)$ matrix with elements $w_{i,j}$. Note that the estimated concentration ratio of each ligand type, i.e.,

$$\hat{\alpha}_l = \left(\frac{1}{N}\right) \sum_{i=1}^{M} n_i w_{l,i}, \tag{5.30}$$

becomes the weighted sums of M correlated binomial random variables with the weights $w_{l,i}$.

Combining the ratio estimator with the unbiased estimator of total ligand concentration introduced in Section 5.4.2, one can obtain an estimator for the concentration of each ligand type as follows

$$\hat{\boldsymbol{c}} = \hat{c}_{tot}\hat{\boldsymbol{\alpha}}, \tag{5.31}$$

with

$$\begin{aligned}\hat{c}_l &= \frac{N-1}{N}\frac{1}{k^+T_u}\sum_{i=1}^{M} n_i w_{l,i}, \\ &\approx \frac{1}{k^+T_u}\sum_{i=1}^{M} n_i w_{l,i}, \quad \text{for } N \gg 1.\end{aligned} \tag{5.32}$$

The variance of this estimator can be calculated as follows

$$\begin{aligned}\mathbf{Var}[\hat{\boldsymbol{c}}] = \mathrm{Var}[\hat{c}_{tot}]\mathbf{Var}[\hat{\boldsymbol{\alpha}}] + \mathrm{Var}[\hat{c}_{tot}]\left(\mathbf{E}[\hat{\boldsymbol{\alpha}}] \odot \mathbf{E}[\hat{\boldsymbol{\alpha}}]\right) \\ + \mathbf{Var}[\hat{\boldsymbol{\alpha}}]\mathrm{E}[\hat{c}_{tot}]^2,\end{aligned} \tag{5.33}$$

where the variance and the mean of the unbiased estimator of total concentration $\hat{c}_{tot}$ are given in (5.13) and (5.14), respectively. On the other hand, the variance of the ratio estimator given in (5.30) can be written for the l^{th} ligand as

$$\mathrm{Var}[\hat{\alpha}_l] = \frac{1}{N^2}\sum_{i=1}^{M}\sum_{j=1}^{M} w_{l,i}w_{l,j}\ \mathrm{Cov}[n_i, n_j], \tag{5.34}$$

with the covariance function

$$\mathrm{Cov}[n_i, n_j] = \begin{cases}\mathrm{Var}[n_i], & \text{if } i = j, \\ -p_i p_j N, & \text{otherwise.}\end{cases} \tag{5.35}$$

The expected value of the ratio estimator is equal to the actual value of the concentration ratio vector $\boldsymbol{\alpha}$, i.e.,

$$\mathbf{E}[\hat{\boldsymbol{\alpha}}] = \left(\frac{1}{N}\right)\boldsymbol{W}\mathbf{E}[\boldsymbol{n}] = \boldsymbol{W}\mathbf{p} = \boldsymbol{S}^{-\mathbf{1}}\mathbf{p} = \boldsymbol{\alpha}, \tag{5.36}$$

validating the unbiasedness of the overall concentration estimator, i.e.,

$$\mathbf{E}[\hat{\boldsymbol{c}}] = \mathrm{E}[\hat{c}_{tot}]\mathbf{E}[\hat{\boldsymbol{\alpha}}] = c_{tot}\boldsymbol{\alpha} = \boldsymbol{c}. \tag{5.37}$$

Therefore, resulting MSE for this unbiased concentration estimator becomes equal to its variance, i.e.,

$$\mathbf{MSE}[\hat{\boldsymbol{c}}] = \mathbf{Var}[\hat{\boldsymbol{c}}]. \tag{5.38}$$

Biased Estimation of Ligand Concentrations

I also introduce a biased version of the concentration ratio estimator, which has a simplified design, enabled when the time thresholds given in (5.22) are set sufficiently large. In this case, one can neglect the noisy contributions of the ligand types that have higher unbinding rates than the ligand type that is being estimated. When the thresholds are much larger than the corresponding unbinding rates, i.e., $T_i \gg 1/k_i^-$, $\boldsymbol{S}$ matrix, whose elements are given in (5.25), can be approximated by an upper triangular matrix, i.e.,

$$\boldsymbol{H} = \boldsymbol{S}|_{T_i \gg 1/k_i^-}, \tag{5.39}$$

with the matrix elements given as

$$h_{i,j} = \begin{cases} s_{i,j}, & \text{if } i < j, \\ \mathrm{e}^{-(k_i^- T_{i-1})}, & \text{if } i = j, \\ 0, & \text{otherwise.} \end{cases} \tag{5.40}$$

This approximation results in the following ratio estimator,

$$\hat{\boldsymbol{\alpha}}^* = \left(\frac{1}{N}\right) \boldsymbol{R}\boldsymbol{n}, \tag{5.41}$$

where $\boldsymbol{R} = \boldsymbol{H}^{-1}$, is also an upper triangular matrix. The elements of $\boldsymbol{R}$ can be recursively calculated as follows

$$r_{i,j} = \kappa_j \left(\mathbb{1}_{\{i=j\}} - \sum_{\gamma=1}^{j-i} r_{i+\gamma,j}\ \theta_{i+\gamma,i} \right), \tag{5.42}$$

where $\mathbb{1}_{\{i=j\}}$ is the indicator function which is equal to 1 if $i = j$, and 0 otherwise; $\kappa_j = \mathrm{e}^{k_j^- T_{j-1}}$, and $\theta_{i,j} = \mathrm{e}^{-(k_i^- T_{i-j-1})} - \mathrm{e}^{-(k_i^- T_{i-j})}$. Since $\boldsymbol{R}$ is an upper triangular matrix, the estimator for the concentration ratio of the l^{th} ligand type can be written as the sum of $M - l + 1$ terms, i.e.,

$$\hat{\alpha}_l^* = \frac{1}{N} \sum_{i=0}^{M-l} n_{M-i} r_{l,M-i}. \tag{5.43}$$

This substantially simplifies the ratio estimation of the ligand types with the highest affinities, which, in most cases, are the most relevant ligands for information transfer in MC. Similar to (5.34), the variance of this estimator can be written as

$$\mathrm{Var}[\hat{\alpha}_l^*] = \frac{1}{N^2} \sum_{i=0}^{M-l} \sum_{j=0}^{M-l} r_{l,M-i} r_{l,M-j} \mathrm{Cov}[n_{M-i}, n_{M-j}], \tag{5.44}$$

where $\mathrm{Cov}[n_{M-i}, n_{M-j}]$ can be calculated using (5.35). The mean of this estimator is given as

$$\mathbf{E}[\hat{\boldsymbol{\alpha}}^*] = \left(\frac{1}{N}\right) \boldsymbol{R}\mathbf{E}[\boldsymbol{n}] = \boldsymbol{R}\mathbf{p}. \tag{5.45}$$

As is clear from (5.45), this is a biased estimator, due to the residuals resulting from the approximation of the $\boldsymbol{S}$ matrix with an upper triangular matrix $\boldsymbol{H}$ given in (5.39). The resulting bias can be calculated as the difference between expected value of the estimation and the actual value of the concentration ratios, i.e.,

$$\begin{aligned} \boldsymbol{\Delta}[\hat{\boldsymbol{\alpha}}^*] &= \mathbf{E}[\hat{\boldsymbol{\alpha}}^*] - \boldsymbol{\alpha} \\ &= \boldsymbol{R}\mathbf{p} - \boldsymbol{S}^{-1}\mathbf{p} \\ &= (\boldsymbol{R} - \boldsymbol{W})\,\mathbf{p}. \end{aligned} \tag{5.46}$$

The MSE of this biased ratio estimator can then be written as

$$\mathbf{MSE}[\hat{\boldsymbol{\alpha}}^*] = \mathbf{Var}[\hat{\boldsymbol{\alpha}}^*] + \left(\boldsymbol{\Delta}[\hat{\boldsymbol{\alpha}}^*] \odot \boldsymbol{\Delta}[\hat{\boldsymbol{\alpha}}^*]\right). \tag{5.47}$$

The resulting biased estimator of the concentrations of individual ligand types can be given as

$$\hat{\boldsymbol{c}}^* = \hat{c}_{tot}\hat{\boldsymbol{\alpha}}^*, \tag{5.48}$$

with the matrix elements calculated as

$$\begin{aligned} \hat{c_l}^* &= \frac{N-1}{N}\frac{1}{k^+T_u}\sum_{i=0}^{M-l} n_{M-i}r_{l,M-i}, \\ &\approx \frac{1}{k^+T_u}\sum_{i=0}^{M-l} n_{M-i}r_{l,M-i}, \quad \text{for } N \gg 1, \end{aligned} \tag{5.49}$$

and the corresponding variance is obtained via

$$\mathbf{Var}[\hat{\boldsymbol{c}}^*] = \mathrm{Var}[\hat{c}_{tot}]\mathbf{Var}[\hat{\boldsymbol{\alpha}}^*] + \mathrm{Var}[\hat{c}_{tot}]\left(\mathbf{E}[\hat{\boldsymbol{\alpha}}^*] \odot \mathbf{E}[\hat{\boldsymbol{\alpha}}^*]\right) + \mathbf{Var}[\hat{\boldsymbol{\alpha}}^*]\mathrm{E}[\hat{c}_{tot}]^2. \tag{5.50}$$

The bias of this estimator is given as

$$\begin{aligned} \boldsymbol{\Delta}[\hat{\boldsymbol{c}}^*] &= \mathbf{E}[\hat{\boldsymbol{c}}^*] - \boldsymbol{c} \\ &= c_{tot}\left(\mathbf{E}[\hat{\boldsymbol{\alpha}}^*] - \boldsymbol{\alpha}\right) = c_{tot}\boldsymbol{\Delta}[\hat{\boldsymbol{\alpha}}^*]. \end{aligned} \tag{5.51}$$

Finally, the resulting MSE can be obtained as follows

$$\mathbf{MSE}[\hat{\boldsymbol{c}}^*] = \mathbf{Var}[\hat{\boldsymbol{c}}^*] + (\boldsymbol{\Delta}[\hat{\boldsymbol{c}}^*] \odot \boldsymbol{\Delta}[\hat{\boldsymbol{c}}^*])\,. \tag{5.52}$$

5.5 Performance Evaluation

The performances of the proposed channel sensing methods are evaluated in terms of normalized MSE (NMSE) averaged over all ligands co-existing in the mixture, i.e.,

$$\langle \mathrm{NMSE}[\hat{\boldsymbol{c}}] \rangle = \frac{1}{M} \sum_{i=1}^{M} \mathrm{NMSE}[\hat{c}_i] = \frac{1}{M} \sum_{i=1}^{M} \frac{\mathrm{MSE}[\hat{c}_i]}{c_i^2}. \tag{5.53}$$

The average NMSE can be calculated for the optimal ML estimator $\hat{\boldsymbol{c}}_{\boldsymbol{ML}}$ and the simplified estimator $\hat{\boldsymbol{c}}^*$ in the same way. Note that with the normalization, the analysis is rendered independent of the total ligand concentration c_{tot}. Hence, the performance of the proposed methods in terms of the normalized performance metric only depends on the number of unbound and bound time duration samples, relative affinities of the ligand types with the receptors, number of ligand types, and the ligand concentration ratios.

For the simplicity of the analysis, I assume, without loss of generality, that the unbinding rates of ligand types are indexed in decreasing order, i.e., $k_1^- > k_2^- > ... > k_M^-$, and the following rule is defined to describe the relation between them:

$$k_{M-i}^- = \chi^i k_M^- \quad \text{for } i \in \{1, \ldots, M-1\}, \tag{5.54}$$

where χ is the similarity parameter that provides a measure of pairwise similarity between different ligand types in the mixture. Its effect on the performance of the estimators will be discussed in Section 5.5.2. In the rest of the analysis, I set $\chi = 5$, such that the ratio of the unbinding rates between the two most similar ligands is $\chi = 5$. I also set $k_M^- = 1\mathrm{s}^{-1}$.

The time thresholds, defined in (5.22), are taken as proportional to the inverse of the unbinding rates of the corresponding ligand types, i.e., $T_i = \nu / k_i^-$, where ν is the proportionality constant. For each system setting analysed with sub-optimal unbiased estimator, I also perform the optimization of ν for the minimum average NMSE, i.e.,

$$\nu_{opt} = \arg\min_{\nu > 0} \langle \mathrm{NMSE}[\hat{\boldsymbol{c}}] \rangle, \tag{5.55}$$

Table 5.1 Comparison Matrix for Channel Sensing Methods

	Optimal Estimation $\hat{\boldsymbol{c}}_{ML}$	**Suboptimal Estimation $\hat{\boldsymbol{c}}$**	**Suboptimal Simplified Estimation $\hat{\boldsymbol{c}}^*$**	**Suboptimal ν-Optimized Estimation $\hat{\boldsymbol{c}}_\nu$**
Method	ML	ML + MoM	ML + MoM	ML + MoM
Required Statistics	T_u, $\{\tau_b\}_N$	T_u, n_i for $i \in \{1, \ldots, M\}$	T_u, n_i for $i \in \{1, \ldots, M\}$	T_u, n_i for $i \in \{1, \ldots, M\}$
Biasedness	Unbiased	Unbiased	Biased	Unbiased
Computational Complexity	High, requires iterative methods	Medium, requires weighted sum of M terms and division, for each ligand type	Low, requires weighted sum of (M-i+1) terms and division, for i^{th} ligand type	Medium, requires weighted sum of M terms and division, for each ligand type
MSE	Low (5.21)	Medium (5.38)	High (5.52)	Medium (5.38)

and provide the ν-optimized value of the average NMSE together with the performance of the suboptimal unbiased and simplified biased estimators, and with the corresponding CRLB. The obtained values of ν_{opt} are different for each setting; however, it is found that they concentrate around $\nu_{opt} = 3$ (data not shown). Therefore, in the performance evaluation of the sub-optimal unbiased estimator and in calculating the CRLB, I set $\nu = 3$. For the simplified biased estimator, however, the value of ν is constrained by the fact that the simplification is based on the assumption that $T_i \gg 1/k_i^-$. With this condition, I obtain an upper triangular estimator matrix, which, in turn, simplifies the calculations required for estimation (see (5.39) and (5.40)). In this analysis, I conclude that setting $\nu = 5$ is sufficient for the validity of this assumption. Moreover, throughout the analysis I set the default number of samples and the default number of ligand types in the channel as $N = 10000$ and $M = 5$, respectively.

Given the default system setting above, next I evaluate the sensing performance for varying number, similarity, and ratio distribution of ligand types, and varying number of samples. I will also evaluate the sensing performance in two particular cases, where some of the ligand types considered in the estimator do not actually exist in the channel medium, and new types of ligands that are not hardwired into the estimators are added to the medium. A brief comparison of the investigated channel sensing methods in terms of their requirements, properties and performance is provided in Table 5.1.

5.5.1 Effect of Number of Ligand Types in the Mixture

The first analysis is carried out for varying number of ligand types M. This is a critical parameter that depends on the interference characteristics of the MC channel and the utilized multiple access scheme. The results are provided in Fig. 5.3, for CRLB, sub-optimal unbiased estimator, ν-optimized unbiased estimator, and simplified biased estimator. It is assumed that the concentration ratios of ligand types are equal in all cases, i.e., $\alpha_i = 1/M$ for $i \in \{1, \ldots, M\}$. As expected, the NMSE is increasing with increasing M; however, the channel sensing methods demonstrate acceptable performance even when the channel is crowded by 10 different types of ligands. The results also reveal that the unbiased estimator with $\nu = 3$ and the ν-optimized estimator almost achieve the CRLB, especially when $M < 4$, hence, they can be considered highly efficient. The performance of the simplified estimator follows the same trend; however, the resulting error is almost an order of magnitude larger than the unbiased estimators when M is high.

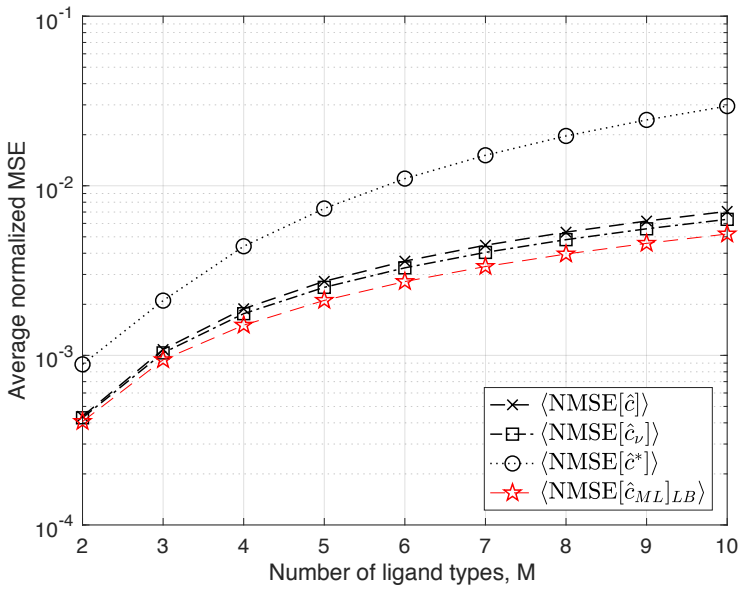

Fig. 5.3 Average NMSE with varying number of ligand types, M, for optimal $\hat{\boldsymbol{c}}_{ML}$, suboptimal unbiased $\hat{\boldsymbol{c}}$, suboptimal biased $\hat{\boldsymbol{c}}^*$, and ν-optimized unbiased $\hat{\boldsymbol{c}}_\nu$ estimators.

5.5.2 Effect of Similarity between Ligand Types

The similarity of the ligands co-existing in the channel has substantial impact on the performance of the channel sensing methods, as demonstrated in Fig. 5.4. An increase in the similarity, reflected by a decreasing χ, reduces the capability of the sensing method to discriminate between different ligand types from the bound time duration data. The results indicate that it is not possible to accurately sense the channel with the unbiased estimators when $\chi < 2$ and $M \geq 5$. Interestingly, however, the simplified biased estimator provides superior performance in this range of similarity, even compared to the CRLB. This implies that neglecting the stochastic contribution of the ligands with lower affinities results in better error performance, when the ligands manifest very similar affinities with the receptors.

5.5.3 Effect of Number of Unbound/Bound Duration Samples

The number of samples affects the performances of both the ratio estimator and the total concentration estimator $\hat{c}_{tot}$. As a result, the overall impact on the estimation of individual concentrations by all types of estimators is remarkable, as demonstrated in Fig. 5.5. The relation between the average NMSE and the number of samples follows the same trend for all estimators, and the unbiased estimator has acceptable accuracy even

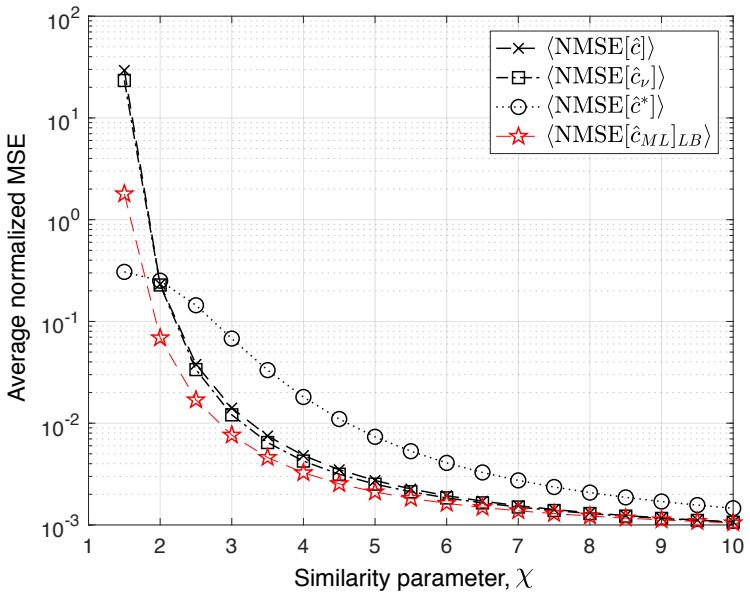

Fig. 5.4 Average NMSE with varying similarity between ligand types, χ, for optimal $\hat{\boldsymbol{c}}_{ML}$, suboptimal unbiased $\hat{\boldsymbol{c}}$, suboptimal biased $\hat{\boldsymbol{c}}^*$, and ν-optimized unbiased $\hat{\boldsymbol{c}}_\nu$ estimators.

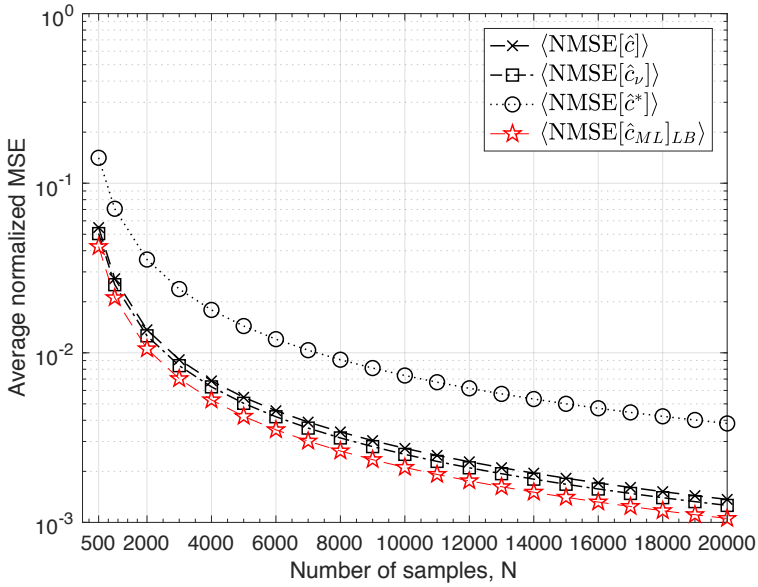

Fig. 5.5 Average NMSE with varying number of unbound and bound time duration samples, N, for optimal $\hat{\boldsymbol{c}}_{ML}$, suboptimal unbiased $\hat{\boldsymbol{c}}$, suboptimal biased $\hat{\boldsymbol{c}}^*$, and ν-optimized unbiased $\hat{\boldsymbol{c}}_\nu$ estimators.

when the number of samples $N = 500$, and $M = 5$. Note that the unbiased estimators, $\hat{\boldsymbol{c}}$ and $\hat{\boldsymbol{c}}_{\boldsymbol{\nu}}$, are highly efficient as they perform very closely to the CRLB.

5.5.4 Effect of Concentration Ratios of Ligands

I also evaluate the sensing performance for the case of heterogeneous distribution of concentration ratios, i.e., $\alpha_i = c_i/c_{tot}$. In particular, the concentration ratio of the ligand type that has the highest affinity with the receptors, i.e., α_M, is varied, while the ratios of the other ligand types are kept uniform, i.e.,

$$\alpha_i = \frac{1-\alpha_M}{M-1} \quad \text{for} \quad i \in \{1, 2, \cdots M-1\}. \tag{5.56}$$

The results are provided in terms of NMSE averaged over all ligand types in Fig. 5.6(a), and in terms of NMSE of concentration estimation of only the highest-affinity ligand in Fig. 5.6(b). Given that there are $M = 5$ different types of ligands in the channel, the average NMSE is minimized when the weights are almost uniformly distributed, i.e., when $\alpha_M \approx 0.2$. Interpreting both results together, we see that while the accuracy of the concentration estimation for the highest-affinity ligand, i.e., c_M, significantly increases for very high values of α_M, the overall performance of the channel sensing deteriorates. In an MC application, it can be expected that the molecules of interest, i.e., information-carrying molecules, would be the ligands that have the highest affinity with the employed receptors. Hence, the results show that the proposed channel sensing methods can be effectively used to eliminate the interference of lower-affinity ligands for improving the detection performance.

5.5.5 Effect of Absence of Ligands

As a particular case, I investigate the estimation performance when the ligands of particular types, which were considered a priori in the implemented estimators, are not actually present in the channel. As discussed in Section 5.4, the proposed estimators should be hardwired in the receiving cell with a set of ligand types potentially existing in the channel before its utilization in an application. Hence, hardwiring the estimator with a large set of ligand types might be necessary for an application medium that could potentially contain varying types of ligands. In these cases, it is likely that some of the considered ligand types are not present in the medium at the time of channel sensing. In order to analyze the effect of absence of any ligand type, it is required to change the previously considered performance metric, i.e., average NMSE, because the concentration of these ligand types is effectively zero, and it is not plausible to normalize the MSE with a zero concentration. Instead, I define a new metric as the total MSE normalized by the

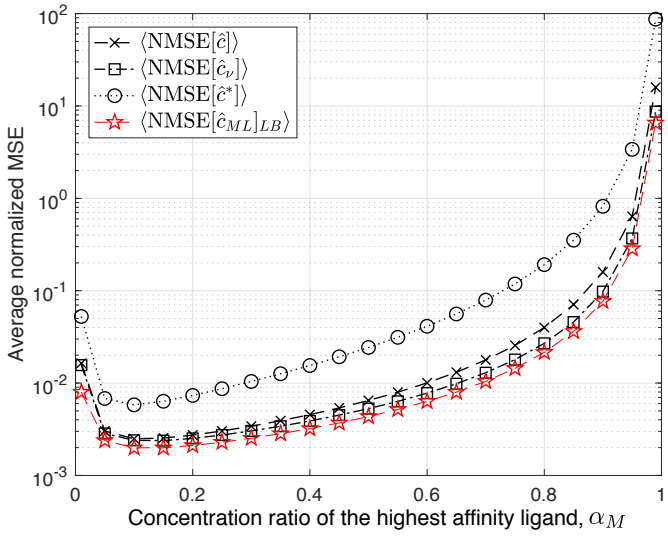

(a)

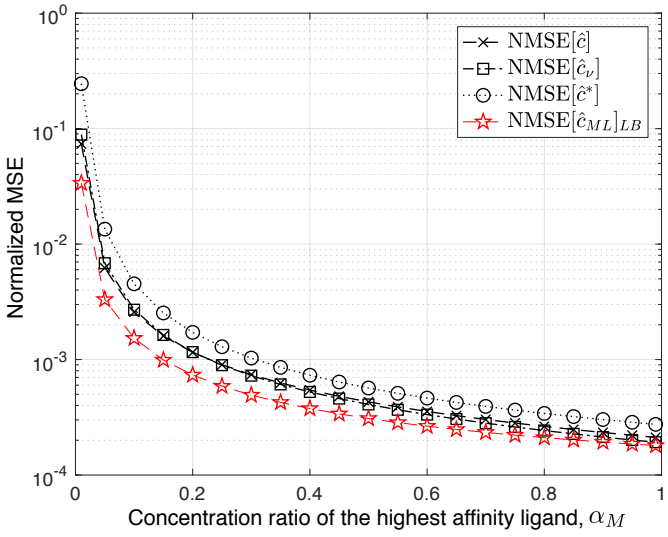

(b)

Fig. 5.6 (a) Average NMSE with varying concentration ratio of the highest-affinity ligand type, α_M, for optimal $\hat{\boldsymbol{c}}_{ML}$, suboptimal unbiased $\hat{\boldsymbol{c}}$, suboptimal biased $\hat{\boldsymbol{c}}^*$, and ν-optimized unbiased $\hat{\boldsymbol{c}}_\nu$ estimators. (b) NMSE in the estimation of concentration of the highest-affinity ligand type, c_M, with varying concentration ratio of the highest-affinity ligand type, α_M, for optimal $\hat{\boldsymbol{c}}_{ML}$, suboptimal unbiased $\hat{\boldsymbol{c}}$, suboptimal biased $\hat{\boldsymbol{c}}^*$, and ν-optimized unbiased $\hat{\boldsymbol{c}}_\nu$ estimators.

square of total concentration, i.e.,

$$\mathrm{MSE}_{tot}[\hat{\boldsymbol{c}}]/c_{tot}^2 = \frac{1}{c_{tot}^2} \sum_{i=1}^{M} \mathrm{MSE}[\hat{c}_i]. \tag{5.57}$$

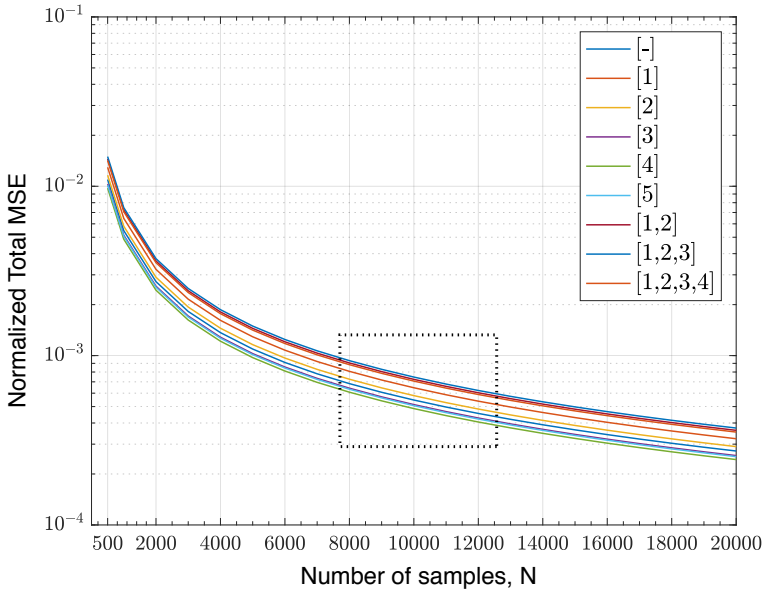

(a)

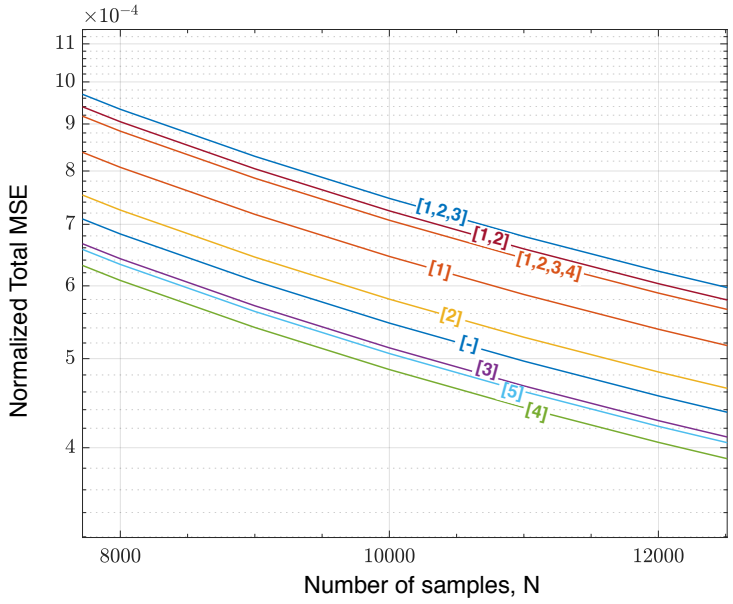

(b)

Fig. 5.7 (a) Total MSE normalized by c_{tot}^2, as a function of varying number of samples N for suboptimal unbiased estimator $\hat{\boldsymbol{c}}$ in the ***absence*** of different types of ligands indicated here by their indices. The region marked by the dashed rectangle is redrawn in (b) for better visualization.

This metric enables a fair assessment of the performance in the absence of ligands.

For the analysis, I consider the default setting with $M = 5$, $\chi = 5$, $k_M^- = 1\text{s}^{-1}$, $\nu = 3$ by leaving the number of samples N as a variable. I investigate the cases when each one of the ligand types is absent, as well as the case when multiple ligands are absent at the same time. In all cases, the concentration ratios of the remaining ligand types are assumed to be equal. The results are shown in Fig. 5.7(a) (with a magnified view provided in Fig. 5.7(b)) for the unbiased estimator $\hat{\boldsymbol{c}}$, and compared to the default case when all types of ligands, that are initially hardwired to the estimator, are present. The numbers in square brackets indicate the index value i of the ligand types varying in their unbinding rates, such that $k_i^- = \chi^{M-i} k_M = 5^{5-i}$ for $i \in \{1, \ldots, 5\}$. As is seen, the estimation performance only slightly changes in different cases, and thus, the proposed estimators can be considered robust against the absence of any ligand types that are hardwired a priori. Although there is not a clear trend in the performance with varying types of ligands that are absent, we can see that while the absence of ligands with higher unbinding rates improve the overall estimation performance, the absence of ligands with higher affinity with receptors degrades the performance compared to the default case.

5.5.6 Effect of Unknown Ligand Types

I also investigate the estimator performance when new types of ligands are introduced to the channel medium. Note that these new ligands are unknown to the estimators. This problem is relevant for communication media with a varying characteristics in terms of interferer molecule types. The objective here is to understand the effect of the unbinding rate and concentration ratio of the new ligand type on the performance of the estimators in estimating the concentration of the known ligands in terms of average NMSE. I derive the average NMSE in the case of new ligands in Appendix A.2, and show that the unbiased estimator becomes biased in this case. The results of the analyses are provided in Fig. 5.8. In addition to the unbiased estimator, which now becomes biased, I also provide results for simplified biased estimator introduced in Section 5.4.3. The default setting is used for existing ligands, i.e., $M = 5$, $k_M^- = 1\text{s}^{-1}$, $\chi = 5$, $\nu = 3$. Note that in this setting the unbinding rates of existing ligands become $k_5^- = 1\text{s}^{-1}$, $k_4^- = 5\text{s}^{-1}$, $k_3^- = 25\text{s}^{-1}$, $k_2^- = 125\text{s}^{-1}$, $k_1^- = 625\text{s}^{-1}$. The concentration of the existing ligands are considered to be equal, such that when a new type of ligand is introduced with a certain concentration ratio α_u, the ratio of the existing ligand types becomes $\alpha_i = (1 - \alpha_u)/M$ for $i \in \{1, \ldots, M\}$.

The first analysis concerns the effect of the concentration ratio of the new ligand type, α_u. The unbinding rate of the new ligand type is taken as $k_u^- = 100\text{s}^{-1}$, such that its affinity with the receptors is close to that of the existing ligands. As is seen in Fig.

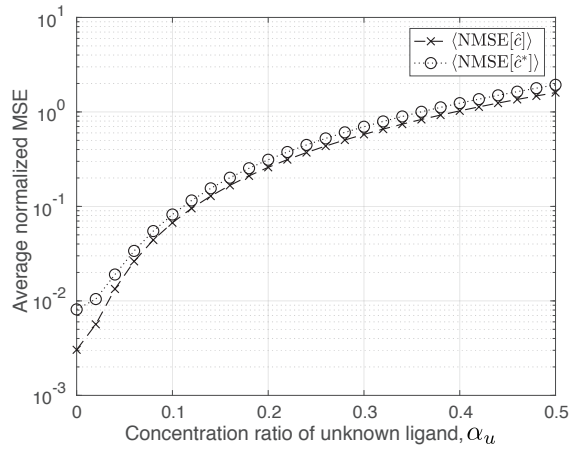

(a)

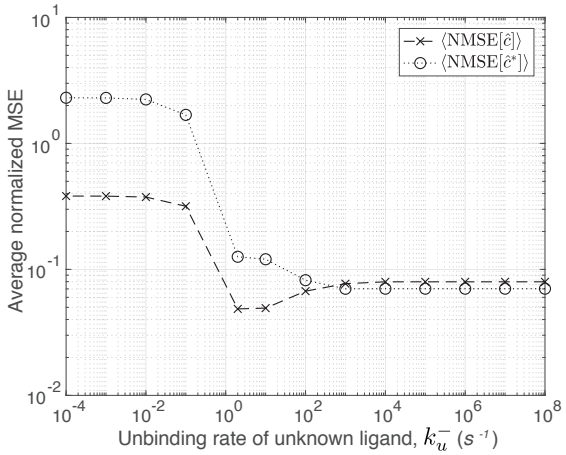

(b)

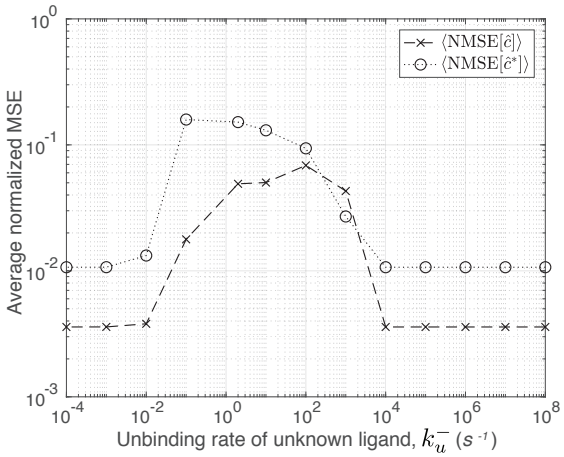

(c)

Fig. 5.8 Average NMSE in the presence of an unknown ligand (a) with varying concentration ratio; (b) with varying unbinding rate; (c) with varying unbinding rate when very short and very long binding events are filtered out.

5.8(a), the ratio of the introduced ligand has a substantial effect on the performance of both estimators, and the estimation becomes highly unreliable when $\alpha_u > 0.2$. In Fig. 5.8(b), I investigate the effect of unbinding rate k_u^- of this new ligand while keeping its concentration ratio fixed at $\alpha_u = 0.1$. As is seen for both types of estimators, the effect of the unknown ligand on the performance is more pronounced when its unbinding rate is lower (i.e., its affinity is higher) than the existing ligands that are known to the estimators.

The detrimental effect of the unknown ligands can be reduced by adjusting the lower and upper time thresholds, i.e., T_0 and T_M defined in (5.22), to filter out the binding

events that last substantially longer or shorter than those resulting from the known ligand types. For this analysis, I set $T_0 = T_1/5 = \nu/(5k_1^-) = [3/(5 \times 625\text{s}^{-1})] = 960\mu\text{s}$ and $T_M = T_{M-1}/5 = \nu/(5k_{M-1}^-) = [3/(5 \times 5\text{s}^{-1})] = 120\text{ms}$, such that the binding events that last shorter than $960\mu\text{s}$ or longer than 120ms are filtered out. The results of this analysis are provided in Fig. 5.8(c) for varying unbinding rate of the new ligand. As compared to the results in Fig. 5.8(b), when the unbinding rate of the new ligand is significantly higher or lower than the unbinding rate of the existing ligands, its detrimental effect is removed. However, when the new ligand has similar characteristics with the existing ligands, the effect cannot be removed.

5.6 Discussion on Implementation

In this section, I investigate the practical aspects of the proposed channel sensing methods. The key element in the channel sensing is the biological receptors, which are the interface between the exterior and interior of a living cell, and transduce the external signals represented by the concentration of ligands into intracellular signals in the form of concentration of second messengers inside a living cell. The transduced signals need to be further processed for the estimation to be achieved.

The proposed estimators, both unbiased and biased, rely on two statistics, i.e., total unbound time T_u, and the number of binding events n_i of durations within $[T_{i-1}, T_i]$ for $i \in \{1, \ldots, M\}$. The first objective here is to provide a practical synthetic receptor design that can transduce both the unbound time and bound time information into the concentration of different intracellular molecules. I then investigate a chemical reaction network (CRN) that can chemically process these intracellular molecules to perform the calculations required for the proposed estimators.

5.6.1 Acquisition of Receptor Unbound/Bound Time Duration Statistics

The proposed estimators require the sampling of only a single pair of unbound and bound time durations from each receptor, as demonstrated in Fig. 5.9(c), because the information of the exact number of independent samples is crucial for the estimation performance. To equate the number of samples and receptors, i.e., $N = N_R$, I first propose a receptor activation mechanism that can be triggered by the receiver cell when it decides to sense the channel. In this scheme, the receptors can be in one of six main states, i.e., inactive unbound/bound, active unbound/bound and intermediate unbound/bound

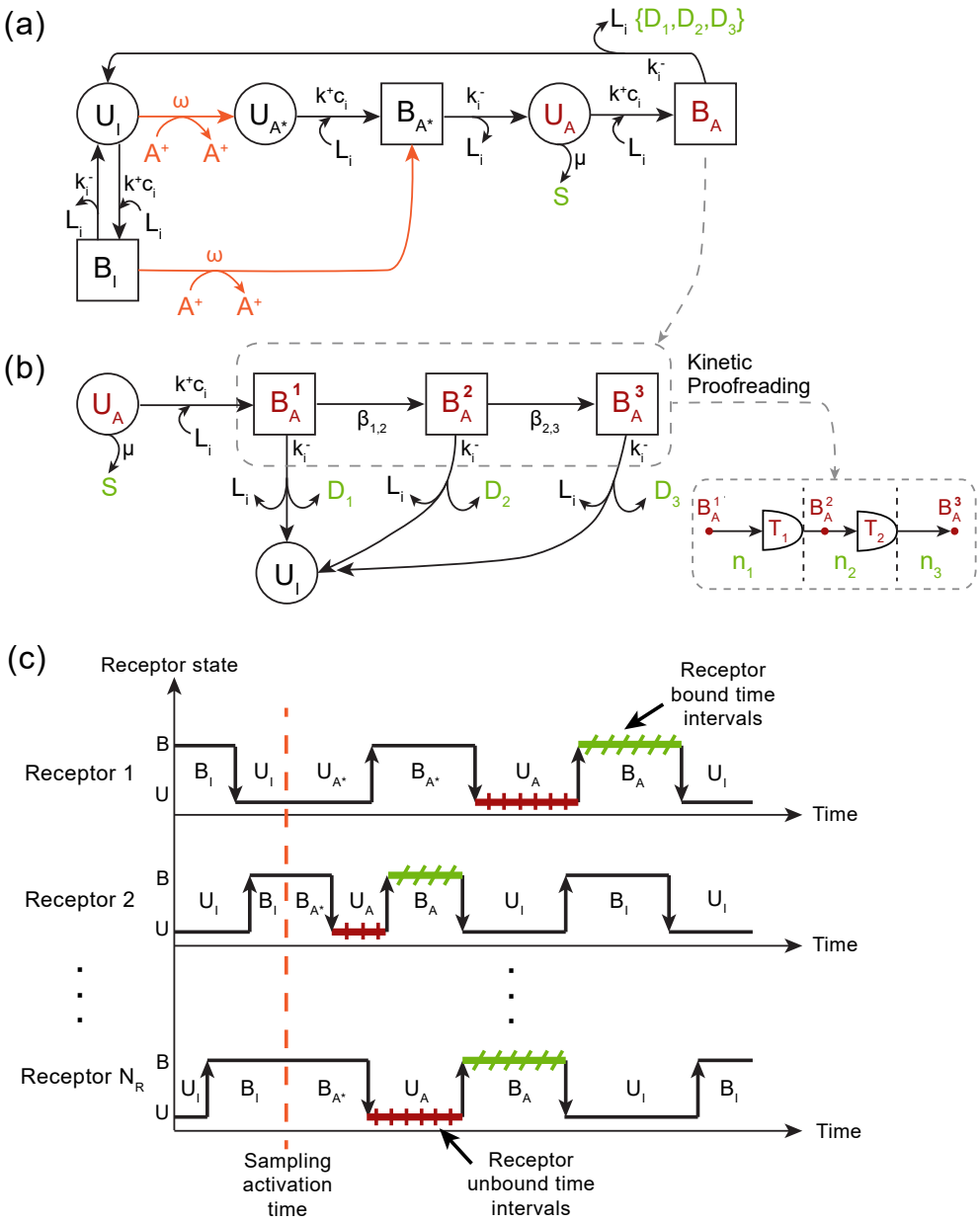

Fig. 5.9 (a) State diagram of the proposed synthetic receptor design that transduces bound and unbound time durations of a receptor into second messengers for intracellular signal processing. The orange line indicates the state transitions initiated by the activation molecules. (b) A closer look into the KPR mechanism with the three KPR substates demonstrated with the corresponding state transition rates. (c) Demonstration of the activation and sampling cycles of the proposed receptors. Dashed orange line marks the reaction time of activation molecules with the receptors.

states, depending on the history of their reactions with ligands and intracellular molecules. The receptors can perform the sampling of the unbound time durations only in the active unbound state, and the bound time durations only in the active bound state through different mechanisms, which will be discussed shortly. Next, the proposed activation mechanism is described along with the sampling of unbound time durations, and then a modified KPR scheme is proposed for the sampling of bound time durations.

Receptor Activation and Transduction of Total Unbound Time Duration

Here a receptor activation mechanism is proposed to control the start time and duration of the channel sensing, such that only one unbound/bound time duration is sampled from each receptor. In this scheme, the sampling process starts with the generation of activation molecules A^+, produced by the cell in an impulsive manner, when the cell decides to sample the receptor states, as demonstrated in Fig. 5.9. The generation of activation signal, thus, occurs in bursts, through the following reaction

$$\varnothing \xrightarrow{\mathrm{s(t)}\ \psi^+} \mathrm{A}^+, \tag{5.58}$$

where the time-varying generation rate is given as $s(t)\psi^+$, with $s(t) \approx \delta(t - t_A)$ being a very short pulse signal centered around the activation time t_A. Shortly after activation, the cell generates deactivation molecules A^-, through the following reaction

$$\varnothing \xrightarrow{\mathrm{d(t)}\ \psi^-} \mathrm{A}^-. \tag{5.59}$$

The reaction rate is given by $d(t)\psi^-$, with $d(t) \approx \delta(t - t_D)$ being again an impulse-like signal centered around the deactivation time t_D. The generated deactivation molecules degrade the existing activation molecules at a rate ρ, i.e.,

$$\mathrm{A}^+ \ + \ \mathrm{A}^- \xrightarrow{\rho} \varnothing, \tag{5.60}$$

such that the duration of the overall sampling process can be controlled. The inactive receptors, i.e., U_I and B_I, transition into their intermediate states, i.e., U_A^* and B_A^*, upon reacting with an activation molecule A^+ at a rate ω, i.e.,

$$\begin{aligned} \mathrm{U_I} \ + \ \mathrm{A}^+ &\xrightarrow{\omega} \mathrm{U_A^*} + \ \mathrm{A}^+ \\ \mathrm{B_I} \ + \ \mathrm{A}^+ &\xrightarrow{\omega} \mathrm{B_A^*} + \ \mathrm{A}^+. \end{aligned} \tag{5.61}$$

The binding of an unbound receptor in the intermediate state U_A^*, transforms it into an intermediate bound receptor B_A^*, i.e.,

$$\mathrm{U_A^* + L_i \xrightarrow{k^+ c_i} B_A^*}, \tag{5.62}$$

where L_i denotes a ligand molecule of i^{th} type. Upon the first unbinding event, a bound receptor in the intermediate state B_A^* goes into the active unbound state U_A, i.e.,

$$\mathrm{B_A^* \xrightarrow{k_i^-} U_A + L_i}. \tag{5.63}$$

In the active unbound state U_A, the receptor produces the secondary messenger molecules S at a constant rate through the following first-order reaction,

$$\mathrm{U_A \xrightarrow{\mu} U_A + S}. \tag{5.64}$$

As a result of this reaction, the steady-state concentration of the produced S molecules becomes proportional to the total unbound time T_u, as we will see in Section 5.6.1.

Upon binding a ligand, the active unbound receptor U_A switches into the first KPR substate of the active bound state B_A^1, i.e.,

$$\mathrm{U_A + L_i \xrightarrow{k^+ c_i} B_A^1}. \tag{5.65}$$

As a result, the modified KPR scheme, consisting of M substates, $\{B_A^1, \ldots, B_A^M\}$, becomes activated.

Some examples are provided in Fig. 5.9(c) for receptor state trajectories governed by the proposed activation mechanism. Receptor 1 is in inactive unbound state when the activation signal is sent. The reaction with activation molecules A^+ turns it into intermediate unbound state U_A^*. Next, with the binding of a ligand, it goes into intermediate bound state. Following the unbinding of the bound ligand, it finally gets activated in the unbound state. During the active unbound state, it generates S molecules following the reaction (5.64). When it binds a ligand again, it switches into active bound state, activating the KPR mechanism. The next unbinding event brings the receptor back into the inactive unbound state. As such one cycle of sampling of unbound and bound time duration is completed. On the other hand, Receptor 2 is in the inactive bound state U_I at the time of activation. Activation reaction switches it into the intermediate bound state B_A^*, during which it is still not able to generate any second messenger. After the first unbinding event it transitions into the active bound state U_A, where it generates S molecules. Upon the next binding, it becomes active in the bound state B_A, and

activates the KPR mechanism. This sampling cycle is also completed with the ensuing unbinding event leading it to the inactive unbound state U_I.

To ensure that the inactivated receptors are not re-activated during the same sampling process for the sake of obtaining only a single pair of unbound and bound duration samples from each receptor, the generation rates of activation and deactivation molecules, i.e., ψ^+ and ψ^-, respectively, as well as the rate of reaction between activation molecules and receptors, i.e., ω, and the rate of deactivation reaction ρ should be very high compared to the ligand-receptor binding/unbinding reaction rates.

Kinetic Proofreading and Transduction of Bound Time Durations

For the sampling of the bound time durations, a modified KPR scheme is proposed. In the KPR mechanism, the active bound receptor sequentially visits its M substates in an irreversible manner during the bound time period by undergoing a series of conformational changes with specific transition rates, as shown in Fig. 5.9(b). In each internal state, the receptor can directly return to the initial inactive unbound state U_I if the bound ligand unbinds from the receptor. In our modified KPR scheme, while returning to the initial unbound state, the receptor releases an intracellular molecule D, type of which is specific to the last occupied KPR substate. As the unbinding rate is different for each ligand type, the last occupied substate is informative of the type of the bound ligand. This information is encoded into the number of D_i molecules generated by all active bound receptors, which becomes proportional to the number of last visits made to the B_A^i substate at steady-state, as discussed in Section 5.6.1.

In order for the proposed KPR scheme to provide the required statistics for the estimation of ligand concentration ratios, the transition rates, β's, between substates should be set in accordance with the time thresholds introduced in (5.22). As such, the resulting number of second messengers, D_i, produced from the internal states B_A^i will approximate the actual number of binding events n_i of durations within corresponding time ranges. Transition rates between the KPR states can be set as a function of time thresholds T_i's, i.e.,

$$\beta_{i,i+1} = \kappa_i / \left(T_i^- - T_{i-1}^- \right) \quad \text{for } i \in \{1, \dots, M-1\}, \tag{5.66}$$

where κ_i's are tuning parameters to adjust the transition rates. In the next section, we will see that setting $\kappa_i = 3/5$ provides a good approximation for the number of binding events falling in each time interval for the unbiased estimator, where $T_i = 3/k_i^-$ for $i \in \{1, \dots, M-1\}$, and $T_0 = 0$.

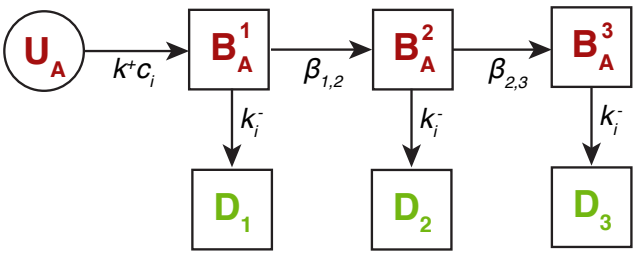

Fig. 5.10 The kinetic scheme of an active receptor given as a Markov Process.

Steady-State Analysis

We can now carry out a steady-state analysis for the transduction of unbound and bound time durations of receptors into second messengers, i.e., S and D molecules. I consider the case when there are $M = 3$ different types of ligands co-existing in the channel, such that each of the receptors has three KPR substates, as shown in Fig. 5.9(a). For the sake of brevity, the analysis omits the activation mechanism, and focuses only on the active receptors. The considered system for steady-state analysis is then a kinetic scheme of Markovian nature, and redrawn in Fig. 5.10, demonstrating possible states of active receptors along with the relevant transition rates.

In order to write the chemical master equation (CME) for this kinetic scheme, at the moment, we can consider the case of single type of ligands. The CME can then be given as a set of differential equations, i.e.,

$$\begin{aligned}
\frac{dP_{U_A|i}}{dt} &= -k^+ c_i P_{U_A|i} \\
\frac{dP_{B_A^1|i}}{dt} &= k^+ c_i P_{U_A|i} - \beta_{1,2} P_{B_A^1|i} - k_i^- P_{B_A^1|i} \\
\frac{dP_{B_A^2|i}}{dt} &= \beta_{1,2} P_{B_A^1|i} - \beta_{2,3} P_{B_A^2|i} - k_i^- P_{B_A^2|i} \\
\frac{dP_{B_A^3|i}}{dt} &= \beta_{2,3} P_{B_A^2|i} - k_i^- P_{B_A^3|i} \\
\frac{dP_{D_j|i}}{dt} &= k_i^- P_{B_A^j|i} \quad \text{for } j \in \{1, \ldots, M\},
\end{aligned} \tag{5.67}$$

where $P_{U_A|i}, P_{B_A^1|i}, P_{B_A^2|i}, P_{B_A^3|i}$ are the time-varying probabilities of an active receptor to be in the unbound state, and in each of the KPR substates, respectively, conditioned on the presence of only the i^{th} type of ligand. D_j's represent virtual states of absorbing nature for an active receptor, and $P_{D_j|i}$ denotes the probability of an active receptor to generate an intracellular D_j molecule and return to the inactive unbound state when

an i^{th} type of ligand is bound. The escape rate from KPR substates is equal to the unbinding rate of the bound ligand, k_i^-.

The steady-state solution of the CME in (5.67) is analytically obtained with the initial conditions $P^0_{U_A|i} = 1$, $P^0_{B^1_A|i} = P^0_{B^2_A|i} = P^0_{B^3_A|i} = P^0_{D_1|i} = P^0_{D_2|i} = P^0_{D_3|i} = 0$, as follows

$$\begin{aligned} P^{ss}_{U_A|i} &= P^{ss}_{B^1_A|i} = P^{ss}_{B^2_A|i} = P^{ss}_{B^3_A|i} = 0, \\ P^{ss}_{D_1|i} &= \frac{k_i^-}{\beta_{1,2} + k_i^-}, \\ P^{ss}_{D_2|i} &= \frac{\beta_{1,2} k_i^-}{\beta_{1,2}\beta_{2,3} + \beta_{1,2} k_i^- + \beta_{2,3} k_i^- + (k_i^-)^2}, \\ P^{ss}_{D_3|i} &= \frac{\beta_{1,2}\beta_{2,3}}{\beta_{1,2}\beta_{2,3} + \beta_{1,2} k_i^- + \beta_{2,3} k_i^- + (k_i^-)^2}. \end{aligned} \tag{5.68}$$

In the presence of three types of ligands, the overall steady-state probabilities can be written as follows

$$\begin{aligned} P^{ss}_{U_A} &= P^{ss}_{B^1_A} = P^{ss}_{B^2_A} = P^{ss}_{B^3_A} = 0, \\ P^{ss}_{D_j} &= \sum_{i=1}^{M=3} \alpha_i P^{ss}_{D_j|i}. \end{aligned} \tag{5.69}$$

Given that all active receptors independently follow the same kinetic scheme, and assuming that each receptor goes through the active state for once during a sampling process, the mean number of generated intracellular D molecules at steady-state can be given as

$$\mathrm{E}[n^{ss}_{D_j}] = N P^{ss}_{D_j}, \quad \text{for } j \in \{1, \ldots, M = 3\}. \tag{5.70}$$

Here I use the previous assumption that number of samples is equal to the number of receptors, i.e., $N = N_R$. Given the statistical independence of receptors, one can also write the variance of number of D molecules as follows

$$\mathrm{Var}[n^{ss}_{D_j}] = N P^{ss}_{D_j}(1 - P^{ss}_{D_j}), \quad \text{for } j \in \{1, \ldots, M = 3\}. \tag{5.71}$$

Assuming that the number of receptors is sufficiently high ($N_R = N = 10000$ in the considered case), we can approximate the random number of produced D molecules at steady-state with a Gaussian distribution, i.e.,

$$n^{ss}_{D_j} \sim \mathcal{N}\left(\mathrm{E}[n^{ss}_{D_j}], \mathrm{Var}[n^{ss}_{D_j}]\right), \quad \text{for } j \in \{1, \ldots, M = 3\}. \tag{5.72}$$

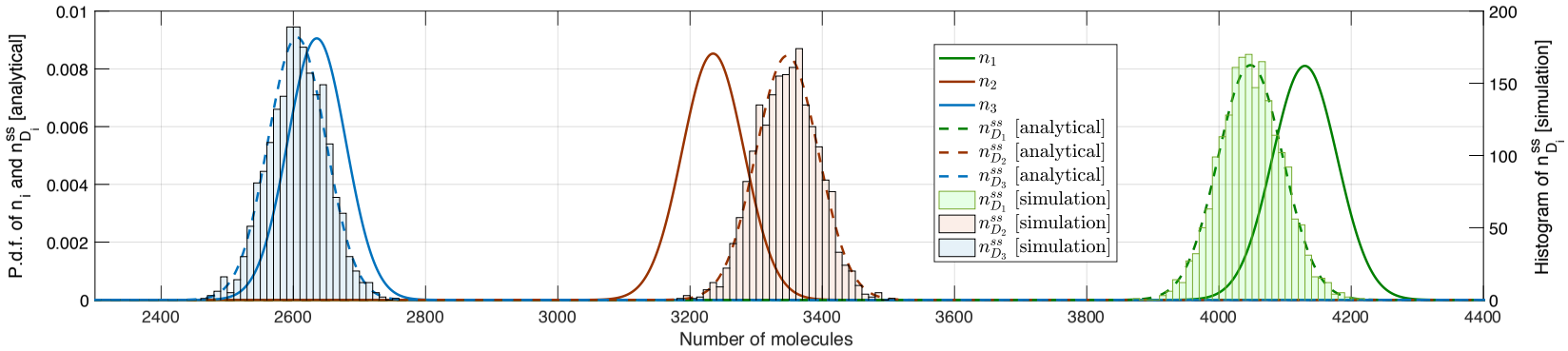

Fig. 5.11 **Solid lines:** Gaussian-approximated probability distribution of number of binding events n_i falling in each time interval defined by the time thresholds T_i's given according to (5.22) with $\nu = 3$. **Dashed lines:** Steady-state probability distribution of number of D molecules $n_{D_j}^{ss}$ for $\kappa = 3/5$, given in (5.72). **Histogram:** Steady-state probability distribution of number of D molecules $n_{D_j}^{ss}$ for $\kappa = 3/5$ obtained through a Monte Carlo simulation of the kinetic scheme demonstrated in Fig. 5.10.

As discussed in Section 5.6.1, the transition rates, β's, between KPR substates should be optimised for obtaining the most accurate representation of actual number of binding events n_i's with D molecules. However, for the sake of brevity of this discussion, I leave the optimization problem as a future research. Here I provide the steady-state probability distribution of number of D molecules $n_{D_j}^{ss}$ for $\kappa = 3/5$ in Fig. 5.11. In the same figure, the results are compared to the histogram of the same statistic obtained through a Monte Carlo simulation of the kinetic scheme demonstrated in Fig. 5.10, and the probability distribution of number of binding events n_i that fall in each time interval defined by the time thresholds T_i's given according to (5.22) with $\nu = 3$. Here, assuming that N is large enough, I also approximate the binomial distribution of n_i with Gaussian distribution, i.e., $n_i \sim \mathcal{N}\left(\mathrm{E}[n_i], \mathrm{Var}[n_i]\right)$, where the mean and variance of n_i are given in (5.26) and (5.27), respectively. As is seen, the analytical results are in very good match with the simulation results. The results also show that the KPR scheme with the selected transition rates can approximate the number of binding events in each time interval. However, the they also imply that the transition rates should be further optimized to obtain better approximation.

The generation of intracellular S molecules encoding the total unbound time duration, on the other hand, is governed by the following rate equations,

$$\begin{aligned} \frac{d\mathrm{E}[n_{U_A}]}{dt} &= N\frac{dP_{U_A}}{dt} = -k^+ c_{tot}\mathrm{E}[n_{U_A}], \\ \frac{d\mathrm{E}[n_S]}{dt} &= \mu\mathrm{E}[n_{U_A}]. \end{aligned} \tag{5.73}$$

In writing (5.73), for mathematical convenience, the receptors are considered as if they independently start in the active unbound state at the same time. This assumption does not degrade the accuracy of the analysis, because the generated S molecules, whose generation rate is dependent on the number of active unbound receptors, are not degraded throughout the entire process (same as D molecules), and we are only concerned about the steady-state statistics of the intracellular molecules, and not interested in their time-varying statistics. Hence, the steady-state solution of (5.73) for the initial conditions $\mathrm{E}[n_{U_A}^0] = N$ and $\mathrm{E}[n_S^0] = 0$, is given as

$$\mathrm{E}[n_{U_A}^{ss}] = 0. \tag{5.74}$$

$$\mathrm{E}[n_S^{ss}] = \frac{\mu N}{k^+ c_{tot}}. \tag{5.75}$$

The produced D and S molecules, whose expected numbers at steady-state are given in (5.70) and (5.75), respectively, will be input to the estimator CRN introduced in the next section.

5.6.2 Estimation with Chemical Reaction Networks

Once the transduction of total unbound time T_u and the number of binding events n_i is completed, the arithmetic operations required for the estimator can be realised through intracellular CRNs that can perform analog computations [149]. Here, I focus on the unbiased estimator; thus, the objective is to implement the following equation with a CRN:

$$\begin{aligned}\hat{c}_l &= \frac{N-1}{N}\frac{1}{k^+T_u}\sum_{i=1}^{M} n_i w_{l,i}, \\ &\approx \frac{1}{k^+T_u}\sum_{i=1}^{M} n_i w_{l,i}, \quad \text{for } N \gg 1.\end{aligned} \tag{5.76}$$

Accordingly, we need to obtain the weighted sum of number of M different types of second messengers D_i's corresponding to the number of binding events that fall in each time interval, divided by the concentration of S molecules encoding the total unbound time duration. This can be achieved through the following CRN, which is designed based on the methodology introduced in [210]:

$$\mathrm{D_i} \xrightarrow{\mathrm{w_{j,i}}} \mathrm{D_i} + \mathrm{Y_j}, \quad \text{for } i,j \in \{1,\ldots,M=3\}, \tag{5.77}$$

$$\mathrm{S} + \mathrm{Y_j} \xrightarrow{\mathrm{k^+}} \mathrm{S}, \quad \text{for } j \in \{1,\ldots,M=3\}. \tag{5.78}$$

In this CRN, while Y molecules are generated by D molecules with different rates set by the matrix $\boldsymbol{W} = \boldsymbol{S}^{-1}$ (see (5.29)), they are consumed by the S molecules that encode the total unbound time duration. The rate equation of the above CRN for the i^{th} ligand can be written as

$$\frac{d\mathrm{E}[n_{Y_i}]}{dt} = \sum_{j=1}^{M} w_{i,j}\mathrm{E}[n_{D_j}] - k^+\mathrm{E}[n_S]\mathrm{E}[n_{Y_i}], \quad \text{for } i \in \{1,\ldots,M=3\}. \tag{5.79}$$

Given the initial condition $\mathrm{E}[n_{Y_i}^0] = 0$, the steady-state solution for $\mathrm{E}[n_{Y_i}]$ is obtained as

$$\mathrm{E}[n_{Y_i}^{ss}] = \frac{1}{k^+ \mathrm{E}[n_S^{ss}]} \sum_{j=1}^{M} w_{i,j} \mathrm{E}[n_{D_j}^{ss}]. \tag{5.80}$$

Recall from (5.11) that $\mathrm{E}[1/T_u] = (k^+ c_{tot})/(N-1) \approx (k^+ c_{tot})/N$ for large N. By combining this with (5.75), we can see that $1/(k^+ \mathrm{E}[n_S^{ss}]) = c_{tot}/(\mu N) \approx \mathrm{E}[1/(\mu k^+ T_u)]$, is on average proportional to the first part of (5.76), i.e., $1/(k^+ T_u)$. The proportionality constant is the rate μ, which is the generation rate of S molecules and can be simply set to $1\mathrm{s}^{-1}$ for a better approximation. Given that the steady-state number of D_i molecules $n_{D_i}^{ss}$ approximates the actual number of binding events n_i, the mean number of Y_i molecules at steady-state given in (5.80) becomes proportional to the concentration estimate of i^{th} type of ligand $\hat{c}_i$ given in (5.76).

Once the estimation through CRN is completed, the produced intracellular molecules, i.e., D, S and Y molecules, should be removed from the cell through a chemical degradation reaction before the cell performs the next round of channel sensing. The rate of the degradation reaction can be set according to the required frequency of channel sensing.

Note that in the analysis of the proposed CRNs, the cross-talk between the internal reaction pathways [211], which may result from the simultaneous reactions of intracellular secondary messengers with similar characteristics is neglected. However, the cross-talk could be a serious limiting factor for the decoding performance especially in the cases where a large set of different secondary messengers needs to be produced by the synthetic receptors to sense a crowded channel. The analysis of the detrimental effects of the cross-talk between the reaction pathways is left for future study.

5.7 Conclusion

In this chapter, I develop channel sensing techniques for MC with ligand receptors for the first time in the literature. In light of the results, I discuss that the proposed technique can be utilized for developing reliable MC detection, modulation, and multiple access methods, as it proved effective in sensing the individual concentrations of multiple ligand types by using only a single type of receptors. The technique is practical and low-complexity, and can be implemented in resource-limited synthetic biological MC devices, e.g., engineered bacteria. In this direction, I also discuss about a synthetic receptor design, built upon the kinetic proofreading mechanism, that can transduce the required statistics of ligand-receptor binding reaction into intracellular signals. Lastly, I discuss about a chemical reaction network that can perform the required arithmetic operations.

This study is not exhaustive, and there remain many challenges and opportunities calling for future research. For example, interesting generalizations can be made by studying non-equilibrium cases where the concentration of ligands are changing more rapidly compared to the binding kinetics. As discussed throughout the chapter, the study can be extended with the applications of the proposed method in developing reliable detection methods for CSK, MoSK and RSK modulated MC signals, and molecular division multiple access techniques.

Chapter 6

Detection with Ligand Receptors under Molecular Interference in Molecular Communications

6.1 Introduction

Of particular interest in MC research has been the detection problem. As discussed in Chapter 2, several detection methods of varying complexity have been developed for different device architectures [19]. Most detection studies consider a particular receiver design that is capable of counting every single molecule inside its virtual reception space [15]. On the other hand, an increasing research interest is being directed towards receivers with ligand receptors, which chemically interact with information molecules through ligand-receptor binding reaction [16, 78, 212]. This receiver architecture is the most physically relevant, as the ligand-receptor interactions are prevalent in biological systems, and thus suitable for synthetic biology-enabled device designs [188]. This additional layer of physical interaction, while adding to the complexity of the overall process, yields interesting statistics that can be exploited in order to develop reliable detection methods.

In existing studies concerning the MC with ligand receptors, receptors are assumed to be ideally selective against the information molecules [19]. On the other hand, in practice, the selectivity of biological ligand receptors are not ideal, and receptors can bind other types of molecules that have a nonzero affinity with the receptors. This molecular interference is inevitable in biologically relevant environments, which are generally crowded with many types of molecules.

In this chapter, I investigate the MC detection problem under molecular interference. I consider an MC system encoding binary information into the concentration of molecules, i.e., utilising binary concentration shift keying (binary CSK). The interference is resulting from a second type of molecules existing in the MC channel, whose number in the receiver's vicinity at the time of sampling follows Poisson distribution. Under these conditions, I investigate the performance of four different detection methods, which exploit different statistics of the ligand-receptor binding reaction.

The first detection method relies on the number of bound receptors at the sampling time, which gives a measure of the total molecular concentration around the receiver. This method is the most widely studied one for MC systems having ligand receptors [213]. The second method uses the maximum likelihood (ML) estimate of the total ligand concentration based on the receptors' unbound time intervals. This method has been previously introduced in Chapter 4 of this thesis to overcome the saturation problem of receptors exposed to a high concentration of molecules [70]. The third method relies on the estimate of the concentration ratio of information molecules based on receptors' bound time intervals. This technique exploits the difference in receptor binding affinities of information and interferer molecules reflected into the mean time duration of receptors in the bound state. The last method combines the estimates of the total ligand concentration and the concentration ratio of information molecules to obtain an estimate of the individual concentration of information molecules, which is then used for detection of molecular messages. This technique utilises both the unbound and bound time intervals of the receptors, as the channel sensing methods proposed in Chapter 5 of this thesis.

I derive the bit error probability (BEP) for each detection method, which is then used for comparing the performances of the introduced detection methods for varying strength of molecular interference, similarity of interferer and information molecules in terms of receptor affinity, number of receptors, and the difference in received concentrations of information molecules for bit-0 and bit-1. I also provide a comprehensive discussion on the implementation of these detection methods. In particular, I propose synthetic receptor designs for the transduction of the required receptor statistics, i.e., number of bound receptors, receptor bound and unbound time intervals, into intracellular molecules. I also propose a chemical reaction network (CRN) for each method that can perform the analog and digital computations required for decoding.

The remainder of this chapter is organised as follows. In Section 6.2, I briefly review the fundamentals of ligand-receptor binding reactions. The considered system is described in Section 6.3 along with the underlying assumptions. I introduce the detection methods

in Section 6.4, where I also derive the BEP for each method. The results of performance evaluation are discussed in Section 6.5. In Section 6.6, I provide a practical discussion on implementation proposing synthetic receptors for signal transduction and CRNs for intracellular calculations. Finally, concluding remarks are given in Section 6.7.

6.2 Statistics of Ligand-Receptor Binding Reactions

The statistics of ligand-receptor binding reactions in the presence of multiple types of ligands has been reviewed in Chapter 5. Here I give a brief overview of the relevant statistics for the case of two types of ligands, i.e., information and interferer molecules, co-existing in the communication channel, which is demonstrated in Fig. 7.17(a). In this case, the bound state probability of a receptor at equilibrium can be written as

$$\mathrm{p}_B = \frac{c_M/K_{D,M} + c_I/K_{D,I}}{1 + c_M/K_{D,M} + c_I/K_{D,I}}, \tag{6.1}$$

where c_M and c_I are the concentrations of information and interferer molecules, whose dissociation constants are denoted by $K_{D,M}$ and $K_{D,I}$, respectively. If the receiver has N independent receptors, the number of bound ones at equilibrium follows binomial distribution with the success probability p_B.

On the other hand, the likelihood of observing a set of N independent binding and unbinding intervals over any set of receptors at equilibrium can be written as

$$\mathrm{p}\left(\{\tau_b, \tau_u\}_N\right) = \frac{1}{Z}\mathrm{e}^{-\sum_{i=1}^{N}\tau_{u,i}\left(k_M^+ c_M + k_I^+ c_I\right)} \times \prod_{i=1}^{N}\left(\sum_{j=\{M,I\}} k_j^+ c_j k_j^- \mathrm{e}^{-k_j^-\tau_{b,i}}\right), \tag{6.2}$$

where Z is the probability normalisation factor, k_i^+ and k_i^- are the binding and unbinding rates for ligand $i \in \{M, I\}$, respectively, and $\tau_{u,i}$ and $\tau_{b,i}$ are the i^{th} observed unbound and bound time durations, respectively [69]. As discussed in Chapter 5, in the diffusion-limited case, the likelihood function (6.2) can be reduced to

$$\mathrm{p}\left(\{\tau_b, \tau_u\}_N\right) = \frac{1}{Z} e^{-T_u k^+ c_{tot}} (k^+ c_{tot})^N \prod_{i=1}^{N} \mathrm{p}\left(\tau_{b,i}\right), \tag{6.3}$$

where $T_u = \sum_{i=1}^{N} \tau_{u,i}$ is the total unbound time of all receptors during the observation period, $c_{tot} = c_M + c_I$ is the total ligand concentration in the vicinity of the receptors, k^+ is the common binding rate of the information and interferer molecules, and $\mathrm{p}(\tau_{b,i})$ is the probability of observing a bound time duration, which is given as the *mixture of two*

exponential distributions, i.e.,

$$\mathrm{p}(\tau_b) = \sum_{i\in\{M,I\}} \alpha_i k_i^- \mathrm{e}^{-k_i^-\tau_b} \tag{6.4}$$

Here $\alpha_j = c_j/c_{tot}$ is the concentration ratio of a particular type of molecule with $j \in \{M, I\}$.

The log-likelihood function for an observed set of unbound/bound time durations can then be written as the sum of three terms, i.e.,

$$\begin{aligned}\mathcal{L}(\{\tau_b, \tau_u\}_N) &= \ln \mathrm{p}(\{\tau_b, \tau_u\}_N), \\ &= \mathcal{L}_0 + \mathcal{L}\left(T_u|c_{tot}\right) + \mathcal{L}\left(\{\tau_b\}|\boldsymbol{\alpha}\right),\end{aligned} \tag{6.5}$$

where $\mathcal{L}_0$ comprises the terms that do not depend on c_{tot} or $\boldsymbol{\alpha} = [\alpha_I, \alpha_M]^T$, while $\mathcal{L}\left(T_u|c_{tot}\right)$ and $\mathcal{L}\left(\{\tau_b\}|\boldsymbol{\alpha}\right)$ are the functions of the total concentration c_{tot} and the ligand concentration ratios $\boldsymbol{\alpha}$, respectively. For detection, we are only interested in the log-likelihoods that are functions of c_{tot} and $\boldsymbol{\alpha}$, i.e.,

$$\mathcal{L}\left(T_u|c_{tot}\right) = N\ln(c_{tot}) - k^+ c_{tot} T_u, \tag{6.6}$$

$$\mathcal{L}\left(\{\tau_b\}|\boldsymbol{\alpha}\right) = \sum_{i=1}^{N} \ln \mathrm{p}\left(\tau_{b,i}\right). \tag{6.7}$$

6.3 Molecular Communication System

I consider an MC system with a receiver equipped with single type of ligand receptors trying to detect a binary message $S \in \{0, 1\}$ encoded by a distant transmitter into the concentration of molecules, i.e., c_M^S, which propagate in the liquid MC channel through free diffusion. The following assumptions define the system:

- Following the convention in MC literature [16], receiver is assumed to have a reception space of a volume V around its lipid membrane, in which receptors along with incoming information and interferer molecules can be assumed to be uniformly distributed at any time instant.

- Receiver is time synchronised with the transmitter, and in the absence of interferer molecules, it has perfect knowledge of the channel state information (CSI) such that it exactly knows the concentration of information molecules in the reception space corresponding to $S = 0$ and $S = 1$ transmissions, i.e., c_M^0 and c_M^1, respectively. This

is justified by the fact that molecular concentration at any point in 3d free diffusion channel is deterministically governed by the Fick's second law of diffusion [15]. On the other hand, in the presence of interferer molecules, receiver only knows the probability distribution of the number of interferer molecules in the reception space. This analysis will not explicitly take the intersymbol interference (ISI) into account for tractability of the derivations; however, I will perform analyses in Section 6.5 for cases when the receptors become saturated as a result of ISI.

- Sampling is performed only once for each receptor in a single signaling interval, such that the number of samples taken for each transmission is equal to the number of receptors, i.e., $N = N_R$. Received molecular signal is taken as steady around the sampling time assuming that the MC system manifests diffusion-limited characteristics, i.e., diffusion dynamics are much slower than the binding kinetics. Receptors are assumed to be operating independently of each other.
- The channel and the reception space of the receiver are crowded with interferer molecules, which can bear significant affinity with the receptors. The number of interferer molecules n_I in the reception space during a sampling period is taken as a Poisson random variable with the mean number μ_I [188]. The binding rates of information and interferer molecules are taken as equal, i.e., $k_M^+ = k_I^+ = k^+$, following the assumption of diffusion-limited binding kinetics, as discussed in Section 5.3. However, the unbinding rates, determined by the affinity with the receptors, are different for information and interferer molecules, and denoted by k_S^- and k_I^-, respectively.

6.4 Detection Methods

Here I introduce four detection methods that use different observable statistics of ligand-receptor binding reaction to decode the incoming messages in the presence of a random number of interferer molecules. These detection methods are based on the instantaneous number of bound receptors, total unbound time of receptors, receptor bound time intervals, and the combination of total unbound time time of receptors and receptor bound time intervals.

6.4.1 Detection based on Number of Bound Receptors (DNBR)

The simplest detection method, which is widely studied in the MC literature, is based on sampling the number of bound receptors, exploiting the relation between the ligand

concentration and the binding probability. As reviewed in Section 6.2, the probability of finding a receptor in the bound state in the presence of interferers is given as

$$\mathrm{p}(B|S,n_I) = \frac{c_M^S/K_{D,M} + c_I/K_{D,I}}{1 + c_M^S/K_{D,M} + c_I/K_{D,I}}, \tag{6.8}$$

where $c_I = n_I/V$. Note that the probability is conditioned on the number of interferer molecules instead of their concentration for mathematical convenience, as the number of interferer molecules are assumed to follow discrete Poisson distribution.

The probability distribution of the number of bound receptors is binomial. Hence, given the number of information and interferer molecules in the reception space, the mean and variance of number of bound receptors at equilibrium can be written as follows

$$\begin{aligned} \mathrm{E}[n_B|S,n_I] &= \mathrm{p}(B|S,n_I)N_R, \\ \mathrm{Var}[n_B|S,n_I] &= \mathrm{p}(B|S,n_I)(1-\mathrm{p}(B|S,n_I))N_R. \end{aligned} \tag{6.9}$$

The mean and variance conditioned only on the number of information molecules thus can be obtained by applying the total law of expectation and variance, i.e.,

$$\begin{aligned} \mathrm{E}[n_B|S] &= \sum_{n=0}^{\infty} \mathrm{E}[n_B|S,n_I=n]\mathrm{p}(n_I=n), \\ \mathrm{Var}[n_B|S] &= \mathrm{E}\Big[\mathrm{Var}[n_B|S,n_I]|S\Big] + \mathrm{Var}\Big[\mathrm{E}[n_B|S,n_I]|S\Big], \end{aligned} \tag{6.10}$$

which do not lend themselves into a more tractable form, and thus the summations should be performed until the results converge. It is shown in Fig. 6.2(a) that the resulting probability distribution can be well approximated with a Gaussian. Hence, we can write

$$\mathrm{p}(n_B|S) \approx \mathcal{N}\Big(\mathrm{E}[n_B|S], \mathrm{Var}[n_B|S]\Big). \tag{6.11}$$

6.4.2 Detection based on Receptor Unbound Time Durations (DRUT)

In this method, the receiver performs the detection based on the estimation of total ligand concentration in the reception space using the total unbound time duration of receptors. Note that this detection method has been first introduced in Chapter 4 to overcome the receptor saturation problem for the case of single type of ligands. Here I derive its statistical properties necessary for the performance evaluation in Section 6.5 under molecular interference.

Exploiting the unbound time durations, an ML estimate of the total molecule concentration can be obtained by using (6.6) as follows

$$\frac{\partial \mathcal{L}\left(T_u|c_{tot}\right)}{\partial c_{tot}}|_{\hat{c}_{tot}} = 0, \tag{6.12}$$

which yields the ML estimator $\hat{c}^*_{tot} = \frac{N}{k^+ T_U}$. However, this is a biased estimator unless N is very large. An unbiased version of this estimator can be obtained with a slight modification as follows

$$\hat{c}_{tot} = \frac{N-1}{k^+ T_u}, \tag{6.13}$$

whose mean and variance are given by

$$\mathrm{E}[\hat{c}_{tot}|S, n_I] = c_{tot}, \tag{6.14}$$

$$\mathrm{Var}[\hat{c}_{tot}|S, n_I] = \frac{c^2_{tot}}{N_R - 2}. \tag{6.15}$$

Using the law of total expectation and variance, the mean and variance of this estimator conditioned only on the number of information molecules can be written as

$$\begin{aligned} \mathrm{E}[\hat{c}_{tot}|S] &= \mathrm{E}\Big[\mathrm{E}[\hat{c}_{tot}|S, n_I]|S\Big] \\ &= \mathrm{E}\Big[c^S_M + n_I/V|S\Big] \\ &= c^S_M + \mu_I/V, \end{aligned} \tag{6.16}$$

$$\begin{aligned} \mathrm{Var}[\hat{c}_{tot}|S] &= \mathrm{E}\Big[\mathrm{Var}[\hat{c}_{tot}|S, n_I]|S\Big] + \mathrm{Var}\Big[\mathrm{E}[\hat{c}_{tot}|S, n_I]|S\Big] \\ &= \sum_{n=0}^{\infty} \frac{(c^S_M + n/V)^2}{(N-2)} \mathrm{p}(n_I = n) + \mathrm{Var}\left[c^S_M + n_I/V|S\right] \\ &\approx \frac{1}{(N-2)\sqrt{2\pi\mu_I}} \int_{-\infty}^{\infty} (c^S_M + n/V)^2 \mathrm{e}^{-\frac{(n-\mu_I)^2}{2\mu_I}} dn + \frac{\mu_I}{V^2} \\ &\approx \frac{(c^S_M + \mu_I/V)^2}{N-2} + \frac{\mu_I(N-1)}{V^2(N-2)}, \end{aligned} \tag{6.17}$$

where the Gaussian approximation is used for the Poisson distribution. As demonstrated in Fig. 6.2(b), the probability distribution of the total concentration estimator can also be approximated with a Gaussian, i.e.,

$$\mathrm{p}(\hat{c}_{tot}|S) \approx \mathcal{N}\Big(\mathrm{E}[\hat{c}_{tot}|S], \mathrm{Var}[\hat{c}_{tot}|S]\Big). \tag{6.18}$$

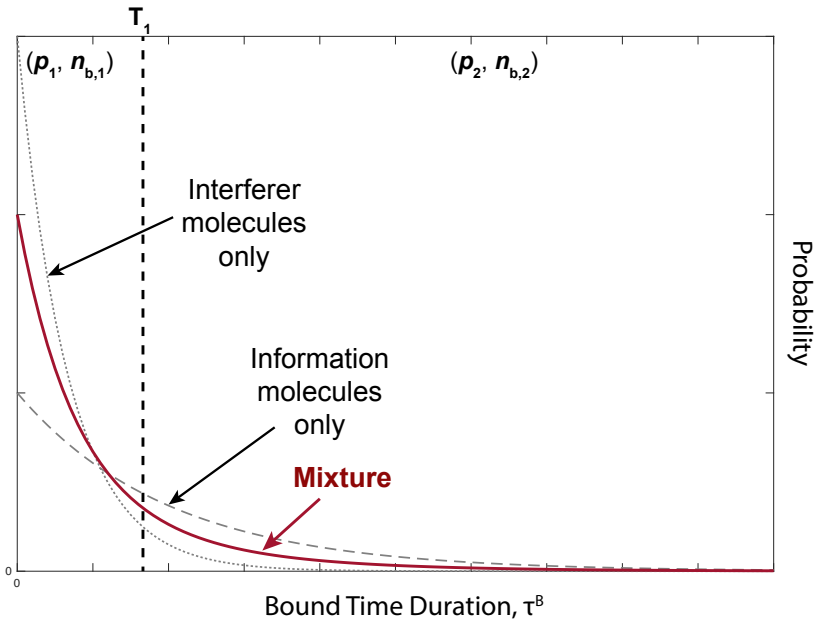

Fig. 6.1 Probability distributions of the bound time durations corresponding to interferer molecules, information molecules, and the mixture of them. The dashed line indicates the time threshold (see (6.20)) that helps discriminate between information and interferer molecules by separating the longer binding events from the shorter ones.

6.4.3 Detection based on Receptor Bound Time Durations (DRBT)

The concentration ratio of information molecules α_M in the reception space is also expected to be different for bit-0 and bit-1 transmissions, and thus can be used for discriminating between the two symbols. We can obtain the ML estimation of the concentration ratio, i.e., $\hat{\boldsymbol{\alpha}}_{\boldsymbol{ML}}$, by solving $\partial \mathcal{L}\left(\{\tau_b\}|\boldsymbol{\alpha}\right)/\partial \alpha_M^S|_{\hat{\alpha}_M^S} = 0$ for the information molecules, i.e.,

$$0 = \sum_{i=1}^{N} \frac{k_M^- \mathrm{e}^{-\left(k_M^- \tau_{b,i}\right)}}{\alpha_M^S k_M^- \mathrm{e}^{-k_M^- \tau_{b,i}} + (1-\alpha_M^S) k_I^- \mathrm{e}^{-k_I^- \tau_{b,i}}}. \tag{6.19}$$

However, the expression in (6.19) does not have any analytical solution for ML estimate $\hat{\boldsymbol{\alpha}}_{\boldsymbol{ML}}$, and requires numerical approaches, which are not feasible for resource-limited bionanomachines [19]. Instead, in Chapter 5, I proposed a feasible near-optimal estimation method for concentration ratios based on counting the number of binding events that fall in specific time intervals. In this estimation scheme, the time domain is divided

into time intervals as many as the number of molecule types existing in the channel, as demonstrated in Fig. 6.1. In the presence of one type of interferer, we have two time intervals. These non-overlapping intervals are defined by a time threshold, which can be taken as proportional to the inverse of the unbinding rate of the molecule type with the lower binding affinity, i.e.,

$$T_1 = \nu / k_I^- \tag{6.20}$$

Here, $\nu > 0$ is a proportionality constant. In this study, it is set to $\nu = 3$, which is shown in Chapter 5 to yield near-optimal results in terms of estimation error. In the same chapter, I also show that this transduction scheme is suitable for biological MC devices, as it can be implemented by active receptors based on well-known KPR scheme.

The probability of observing a ligand binding event with the binding duration falling in a time interval can be written as

$$\mathrm{p}_l = \int_{T_{l-1}}^{T_l} \mathrm{p}(\tau_b') d\tau_b' = \alpha_M^S \left(\mathrm{e}^{-(k_M^- T_{l-1})} - \mathrm{e}^{-(k_M^- T_l)} \right) + \alpha_I \left(\mathrm{e}^{-(k_I^- T_{l-1})} - \mathrm{e}^{-(k_I^- T_l)} \right), \tag{6.21}$$

where $\mathrm{p}(\tau_b)$ is given in (6.4). Here I take $T_0 = 0$ and $T_2 = +\infty$. In matrix notation, the probabilities can be written as

$$\mathbf{p} = \boldsymbol{Q} \boldsymbol{\alpha}, \tag{6.22}$$

where $\mathbf{p} = [\mathrm{p}_1, \mathrm{p}_2]^T$, $\boldsymbol{\alpha} = [\alpha_I, \alpha_M^S]^T$, and $\boldsymbol{Q}$ is an (2×2) matrix with the elements

$$\boldsymbol{Q} = \begin{bmatrix} 1 - \mathrm{e}^{-(k_I^- T_1)} & 1 - \mathrm{e}^{-(k_M^- T_1)} \\ \mathrm{e}^{-(k_I^- T_1)} & \mathrm{e}^{-(k_M^- T_1)} \end{bmatrix}$$

The number of binding events that fall in each interval follows binomial distribution with the mean and the variance given by

$$\mathbf{E}[\boldsymbol{n_b} | S, n_I] = \mathbf{p} N, \tag{6.23}$$

$$\mathbf{Var}[\boldsymbol{n_b} | S, n_I] = (\mathbf{p} \odot (1 - \mathbf{p})) N, \tag{6.24}$$

where $\boldsymbol{n_b}$ is an (2×1) vector with the vector elements $n_{b,i}$ being the number of binding events whose durations are within the i^{th} time interval defined by T_{i-1} and T_i.

Applying the Method of Moments (MoM) for the estimation of ligand concentration ratios by employing only the first moment yields an estimator in terms of number of

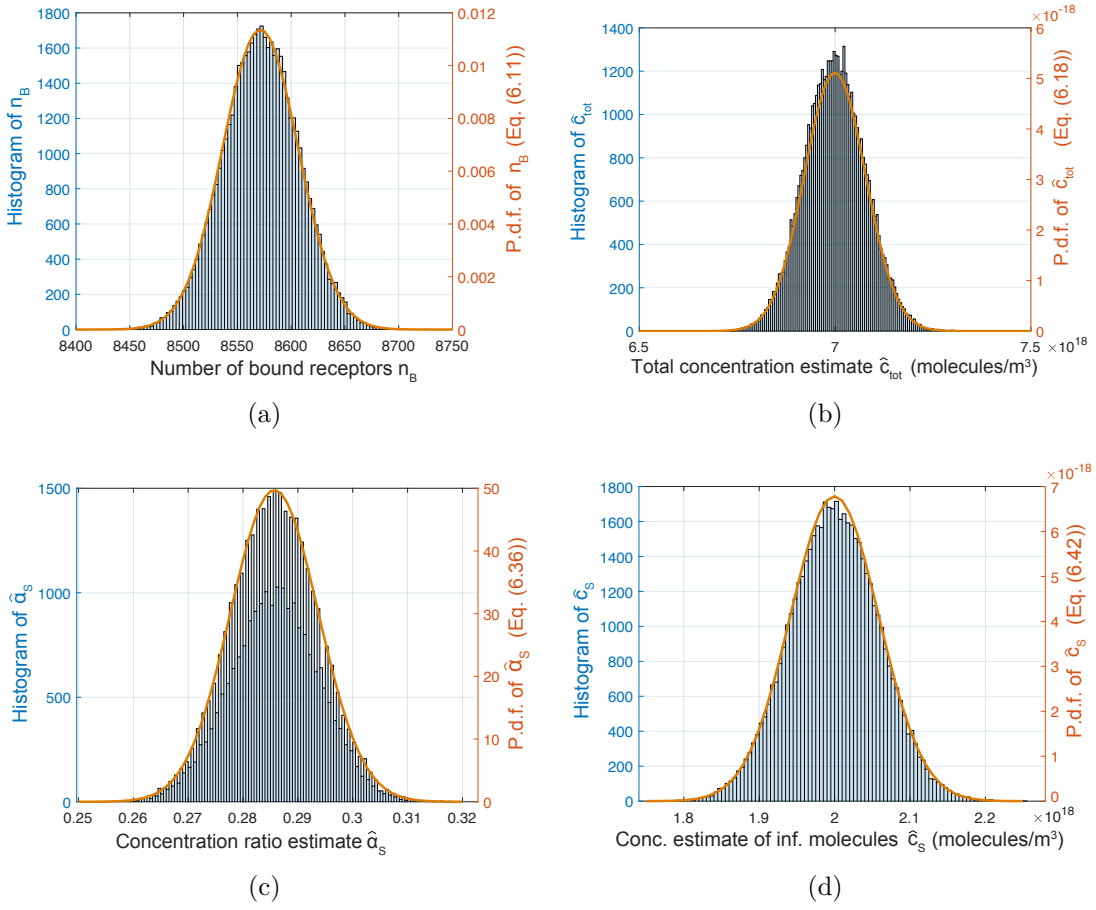

Fig. 6.2 Gaussian approximation of decision statistics. Histograms are obtained via Monte Carlo simulations (50000 iterations) of stochastic ligand-receptor binding process under interference. Simulation parameters are set to the default values that are used in performance evaluation (see Table 6.2). Here it is assumed that bit-0 is transmitted, and thus, I use $c_0 = 4 \times K_{D,S}$.

binding events [214], i.e.,

$$\hat{\boldsymbol{\alpha}} = \left(\frac{1}{N}\right) \boldsymbol{W} \boldsymbol{n_b}, \tag{6.25}$$

where $\boldsymbol{W} = \boldsymbol{Q}^{-1}$, i.e., the inverse of $\boldsymbol{Q}$ matrix, which is also a (2×2) matrix with elements $w_{i,j}$. Note that the estimated concentration ratio of information molecules becomes

$$\hat{\alpha}_M^S = \left(n_{b,1} w_{2,1} + n_{b,2} w_{2,2}\right) / N. \tag{6.26}$$

The variance of this ratio estimator can be written as

$$\mathrm{Var}[\hat{\alpha}_M^S|S,n_I] = \frac{1}{N^2}\sum_{i=1}^{2}\sum_{j=1}^{2} w_{2,i}w_{2,j}\ \mathrm{Cov}[n_{b,i},n_{b,j}|S,n_I], \tag{6.27}$$

with the covariance function

$$\mathrm{Cov}[n_{b,i},n_{b,j}|S,n_I] = \begin{cases} \mathrm{Var}[n_{b,i}|S,n_I], & \text{if } i=j, \\ -p_i p_j N, & \text{otherwise.} \end{cases} \tag{6.28}$$

After some trivial manipulations, one can rewrite (6.27) in closed form as

$$\mathrm{Var}[\hat{\alpha}_M^S|S,n_I] = \frac{1}{N}\frac{\Gamma_1(n_I/V)^2+\Gamma_2(n_I/V)+\Gamma_3}{(c_M^S+n_I/V)^2}, \tag{6.29}$$

where, Γ_1, Γ_2 and Γ_3 are given as follows

$$\Gamma_1 = w_{2,1}^2 s_{1,1} - w_{2,1}^2 s_{1,1}^2 - 2w_{2,1}w_{2,2}s_{1,1}s_{2,1} + w_{2,2}^2 s_{2,1} - w_{2,2}^2 s_{2,1}^2 \tag{6.30}$$

$$\begin{aligned}\Gamma_2 =& c_M^S\Big(w_{2,1}^2 s_{1,2} + w_{2,1}^2 s_{1,1} - w_{2,1}^2 s_{1,1}s_{1,2} - w_{2,1}^2 s_{1,1}s_{1,2} - 2w_{2,1}w_{2,2}s_{1,1}s_{2,2} \\ & - 2w_{2,1}w_{2,2}s_{1,2}s_{2,1} + w_{2,2}^2 s_{2,2} + w_{2,2}^2 s_{2,1} + w_{2,2}^2 s_{2,1}s_{2,2} - w_{2,2}^2 s_{2,1}s_{2,2}\Big)\end{aligned} \tag{6.31}$$

$$\Gamma_3 = (c_M^S)^2\Big(w_{2,1}^2 s_{1,2} - w_{2,1}^2 s_{1,2}^2 - 2w_{2,1}w_{2,2}s_{1,2}s_{2,2} + w_{2,2}^2 s_{2,2} - w_{2,2}^2 s_{2,2}^2\Big) \tag{6.32}$$

The expected value of the ratio estimator is equal to the actual value of the concentration ratio vector $\boldsymbol{\alpha}$, i.e.,

$$\begin{aligned}\mathbf{E}[\hat{\boldsymbol{\alpha}}|S,n_I] &= \left(\frac{1}{N}\right)\boldsymbol{W}\mathbf{E}[\boldsymbol{n_b}|S,n_I] \\ &= \boldsymbol{W}\mathbf{p} \\ &= \boldsymbol{Q^{-1}}\mathbf{p} \\ &= \boldsymbol{\alpha}.\end{aligned} \tag{6.33}$$

Using the law of total expectation and variance, we can write

$$\begin{aligned} \mathrm{E}[\hat{\alpha}_M^S|S] &= \mathrm{E}\Big[\mathrm{E}[\hat{\alpha}_M^S|S, n_I]|S\Big] \\ &= \mathrm{E}\Big[c_M^S/(c_M^S + n_I/V)|S\Big] \\ &= \sum_{n=0}^{\infty} \frac{c_M^S}{c_M^S + n/V} \mathrm{p}(n_I = n), \end{aligned} \tag{6.34}$$

$$\begin{aligned} \mathrm{Var}[\hat{\alpha}_M^S|S] &= \mathrm{E}\Big[\mathrm{Var}[\hat{\alpha}_M^S|S, n_I]|S\Big] + \mathrm{Var}\Big[\mathrm{E}[\hat{\alpha}_M^S|S, n_I]|S\Big] \\ &= \sum_{n=0}^{\infty} \frac{1}{N} \frac{\Gamma_1 (n_I/V)^2 + \Gamma_2 (n_I/V) + \Gamma_3 + N (c_M^S)^2}{(c_M^S + n_I/V)^2} \mathrm{p}(n_I = n) \\ &\quad - \left(\sum_{n=0}^{\infty} \frac{c_M^S}{c_M^S + n/V} \mathrm{p}(n_I = n) \right)^2 . \end{aligned} \tag{6.35}$$

It is shown in Fig. 6.2(c) that the distribution of the ratio estimator for information molecules can be approximated with a Gaussian, as follows

$$\mathrm{p}(\hat{\alpha}_M^S|S) \approx \mathcal{N}\Big(\mathrm{E}[\hat{\alpha}_M^S|S], \mathrm{Var}[\hat{\alpha}_M^S|S]\Big). \tag{6.36}$$

6.4.4 Detection based on Receptor Unbound and Bound Time Durations (DRUBT)

Combining the ratio estimator with the unbiased estimator of total ligand concentration, we can obtain an estimator for the individual concentration of information molecules as follows

$$\begin{aligned} \hat{c}_M^S &= \hat{c}_{tot} \times \hat{\alpha}_M^S, \\ &= \frac{N-1}{N} \frac{1}{k^+ T_u} \left(n_{b,1} w_{2,1} + n_{b,2} w_{2,2} \right), \\ &\approx \frac{1}{k^+ T_u} \left(n_{b,1} w_{2,1} + n_{b,2} w_{2,2} \right), \quad \text{for } N \gg 1. \end{aligned} \tag{6.37}$$

The mean of this concentration estimator conditioned on the number of information and interferer molecules can be calculated as follows

$$\begin{aligned}\mathrm{E}[\hat{c}_M^S|S,n_I] &= \mathrm{E}[\hat{c}_{tot}|S,n_I]\mathrm{E}[\hat{\alpha}_M^S|S,n_I] \\ &= c_{tot}\alpha_M^S \\ &= c_M^S,\end{aligned} \tag{6.38}$$

by exploiting the conditional independence of $\hat{c}_{tot}$ and $\hat{\alpha}_S$. The variance of this estimator can be obtained as follows

$$\begin{aligned}\mathrm{Var}[\hat{c}_M^S|S,n_I] &= \mathrm{Var}[\hat{c}_{tot}|S,n_I]\mathrm{Var}[\hat{\alpha}_M^S|S,n_I] + \mathrm{Var}[\hat{c}_{tot}|S,n_I]\mathrm{E}[\hat{\alpha}_M^S|S,n_I]^2 \\ &\quad + \mathrm{Var}[\hat{\alpha}_M^S|S,n_I]\mathrm{E}[\hat{c}_{tot}|S,n_I]^2 \\ &\approx \frac{1}{N}\left(\Gamma_1(n_I/V)^2 + \Gamma_2(n_I/V) + \Gamma_3 + \left(c_M^S\right)^2\right) \qquad \text{for } N \gg 1.\end{aligned} \tag{6.39}$$

Employing the law of total expectation and variance, we then obtain

$$\mathrm{E}[\hat{c}_M^S|S] = \mathrm{E}\Big[\mathrm{E}[\hat{c}_M^S|S,n_I]|S\Big] = \mathrm{E}[c_M^S|S] = c_M^S, \tag{6.40}$$

$$\begin{aligned}\mathrm{Var}[\hat{c}_M^S|S] &= \mathrm{E}\Big[\mathrm{Var}[\hat{c}_M^S|S,n_I]|S\Big] + \mathrm{Var}\Big[\mathrm{E}[\hat{c}_M^S|S,n_I]|S\Big] \\ &= \frac{1}{N}\sum_{n=0}^{\infty}(\Gamma_1(n/V)^2 + \Gamma_2(n/V) + \Gamma_3 + \left(c_M^S\right)^2)\mathrm{p}(n_I = n) \\ &\approx \frac{1}{N\sqrt{2\pi\mu_I}} \times \int_{-\infty}^{\infty}\left(\Gamma_1\left(\frac{n}{V}\right)^2 + \Gamma_2\left(\frac{n}{V}\right) + \Gamma_3 + (c_M^S)^2\right)\mathrm{e}^{-\frac{(n-\mu_I)^2}{2\mu_I}}dn \\ &\approx \frac{1}{N}\left(\Gamma_1\left(\frac{\mu_I}{V}\right)^2 + (\Gamma_1+\Gamma_2)\frac{\mu_I}{V} + \Gamma_3 + (c_M^S)^2\right).\end{aligned} \tag{6.41}$$

Note that in (6.41), I approximate the Poisson distribution of the number of interferer molecules with a Gaussian distribution.

I demonstrate in Fig. 6.2(d) that the p.d.f. of the concentration estimator can also be approximated with a Gaussian, i.e.,

$$\mathrm{p}(\hat{c}_M^S|S) \approx \mathcal{N}\Big(\mathrm{E}[\hat{c}_M^S|S], \mathrm{Var}[\hat{c}_M^S|S]\Big). \tag{6.42}$$

Table 6.1 Comparison of Detection Methods

Detection Method	Sampled Receptor Statistics	Decision Statistics	Complexity	Probability Distribution
DNBR	Number of bound receptors	Number of bound receptors	Low	(6.11)
DRUT	Total receptor unbound time	Total molecular concentration	Moderate	(6.18)
DRBT	Number of binding events of durations in specific time intervals	Concentration ratio of information molecules	High	(6.36)
DRUBT	Total receptor unbound time + Number of binding events of durations in specific time intervals	Total molecular concentration + Concentration ratio of information molecules	Very high	(6.42)

6.4.5 Decision Rule

In previous sections, I derive the likelihood of four different statistics given the number of information molecules in the reception space. A summary comparison of these detection methods is provided in Table 6.1.

Considering that the system employs binary CSK, the decision rule can simply be written as

$$\hat{S} = \underset{S\in\{0,1\}}{\arg\max}\, \mathrm{p}(\kappa|S), \tag{6.43}$$

where $\kappa \in \{n_B, \hat{c}_{tot}, \hat{\alpha}_M^S, \hat{c}_M^S\}$ is the received signal statistics corresponding to the introduced detection methods. The rule can be further simplified by defining a decision threshold, i.e.,

$$\kappa \underset{H_0}{\overset{H_1}{\gtrless}} \lambda_\kappa. \tag{6.44}$$

For Gaussian signals, the optimal decision threshold yielding the minimum error probability can be calculated as follows

$$\begin{aligned}\lambda_\kappa =& \gamma_\kappa^{-1}\Bigg(\mathrm{Var}[\kappa|n_1]\mathrm{E}[\kappa|n_0] - \mathrm{Var}[\kappa|n_0]\mathrm{E}[\kappa|n_1] + \mathrm{Std}[\kappa|n_1]\mathrm{Std}[\kappa|n_0] \\ &\times \sqrt{(\mathrm{E}[\kappa|n_1] - \mathrm{E}[\kappa|n_0])^2 + 2\gamma_\kappa \ln\frac{\mathrm{Std}[\kappa|n_1]}{\mathrm{Std}[\kappa|n_0]}}\Bigg),\end{aligned} \tag{6.45}$$

where $\gamma_\kappa = \text{Var}[\kappa|n_1] - \text{Var}[\kappa|n_0]$, and $\text{Std}[.] = \sqrt{\text{Var}[.]}$ denotes standard deviation [215]. Given the decision thresholds, the BEP for detection method can be obtained as

$$\begin{aligned} \text{p}_\kappa(e) &= \frac{1}{2}\Big[\text{p}_\kappa(\hat{S}=1|S=0) + \text{p}_\kappa(\hat{S}=0|S=1)\Big] \\ &= \frac{1}{4}\left[\text{erfc}\left(\frac{\lambda_\kappa - \text{E}[\kappa|n_0]}{\sqrt{2\text{Var}[\kappa|n_0]}}\right) + \text{erfc}\left(\frac{\text{E}[\kappa|n_1] - \lambda_\kappa}{\sqrt{2\text{Var}[\kappa|n_1]}}\right)\right]. \end{aligned} \tag{6.46}$$

6.5 Performance Evaluation

In this section, the performances of the introduced detection methods are evaluated in terms of BEP, which is calculated according to (6.46). The default values of the system parameters used in the analysis are given in Table 6.2, with reaction rates taken from the previous literature [16, 188, 212].

Throughout the analysis, the amount of interferer molecules in the reception space is expressed in terms of their concentration; however, the following convention is adopted to convert the concentration into the number of molecules when dealing with discrete Poisson distribution in the computations:

$$\mu_{n_I} = \lfloor \mu_{c_I} V \rfloor. \tag{6.47}$$

Several analyses are performed to evaluate the effect of the expected number of interferer molecules, the ratio between the affinities of information and interferer molecules with the receptors, the ratio between bit-0 and bit-1 concentration levels, and the number of receptors. In the presentation of the results, I also provide the saturation level of the receiver in terms of binding probability corresponding to bit-0 (s=0) and bit-1 (s=1) transmissions.

Table 6.2 Default Values of System Parameters

Binding rate for both types of molecules (k^+)	2×10^{-17} m^3/s
Unbinding rate for information molecules (k_M^-)	10 s^{-1}
Affinity ratio (η)	0.2
Conc. of information molecules for $S=0$ (c_M^0)	$4 \times K_{D,M}$
Conc. of information molecules for $S=1$ (c_M^1)	$5 \times K_{D,M}$
Mean concentration of interferer molecules (μ_{c_I})	$2 \times K_{D,I}$
Number of receptors on the receiver surface (N_R)	10000
Volume of the reception space (V)	4000 μm^3

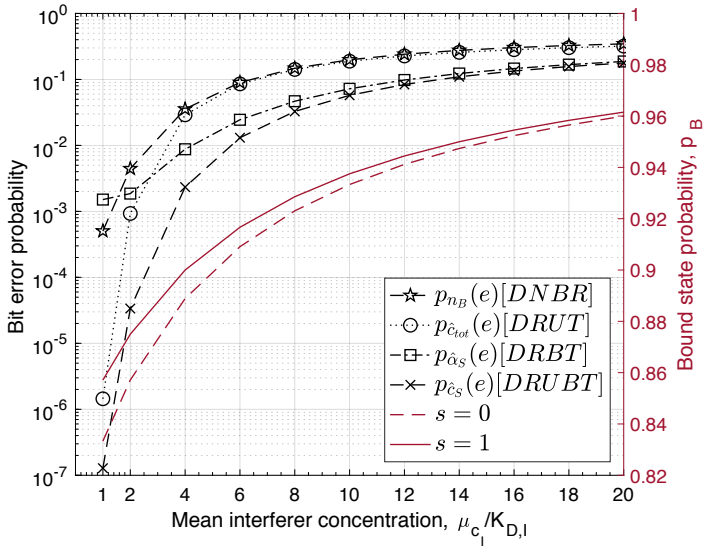

(a)

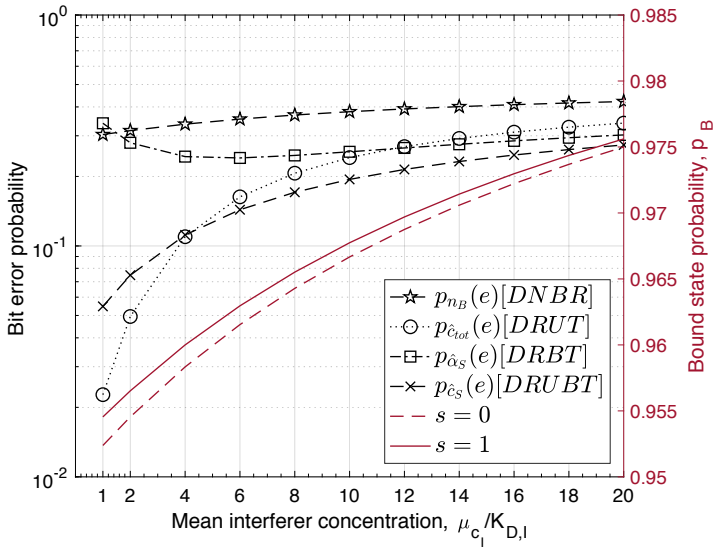

(b)

Fig. 6.3 Bit error probability as a function of mean interferer concentration μ_{C_I}/K_{D_I} for (a) non-saturation and (b) saturation conditions of the receiver.

6.5.1 Effect of Interferer Concentration

The first analysis concerns the strength of molecular interference. I analyse the effect of expected number of interferer molecules in the reception space for two different scenarios regarding the saturation level of the receptors. In the first scenario, it is considered that the receiver is reasonably away from saturation by setting the received concentration of

information molecules for bit-0 and bit-1 as $c_M^0 = 4K_{D,M}$ and $c_M^1 = 5K_{D,M}$, respectively. The results, demonstrated in Fig. 6.3(a), show that DRUBT outperforms the other detection methods in the simulated range of interference. On the other hand, DRUT, while performing poorly under high interference, substantially outperforms DNBR and DRBT when the interference level is relatively low. In the same region, the performance improvement obtained by DRUBT is more pronounced. It is also worth noting that DRNB, which is the simplest detection method, performs better than DRBT at the lowest level of interference.

In the second case, the receptors are driven into saturation by setting the received concentrations as $c_M^0 = 19K_{D,M}$ and $c_M^1 = 20K_{D,M}$. In these conditions, the BEP for all detection methods is significantly higher than the non-saturation case as shown in Fig. 6.3(b). Yet the performance improvement obtained with DRUBT is notable. This time, however, at low interference levels, DRUT, which was previously proposed for overcoming the receptor saturation problem in Chapter 4, outperforms DRUBT. Also, in the case of receptor saturation, the performance of DRBT is worsened as the mean interference level decreases below $\mu_{c_I} = 4K_{D,I}$, in contrast to the common trend observed in other detection methods. This is because the difference between the mean of ratio estimates conditioned on bit-0 and bit-1, i.e., $\mathrm{E}[\hat{\alpha}_M^S|S=0]$ and $\mathrm{E}[\hat{\alpha}_M^S|S=1]$, is a concave function of mean interferer concentration, which is maximised around $\mu_{c_I} = 4K_{D,I}$. On the other hand, the corresponding variances of the ratio estimates monotonically increases with the decreasing interference level. This hampers the receiver's ability to discriminate between two symbols. The poor performance of the ratio estimation in this range also affects the performance of DRUBT. As a result, at very low interference levels, DRUBT is outperformed by DRUT.

6.5.2 Effect of Similarity between Information and Interferer Molecules

The affinity ratio $\eta = k_M^-/k_I^-$ between information and interferer molecules determines how similar they are in terms of binding affinity with receptors. The effect of affinity ratio on the detection performance is analysed in two parts corresponding to the scenarios when $\eta < 1$ and $\eta > 1$. In both analyses, I keep the unbinding rate of information molecules constant and equal to its default value $k_M^- = 10s^{-1}$, and thus, the unbinding rate of interferer molecules k_I^- is changed with the varying affinity ratio. I also keep mean concentration of interferer molecules in the reception space constant and equal to $\mu_{c_I} = 10K_{D,M} = 5\mu m^{-3}$.

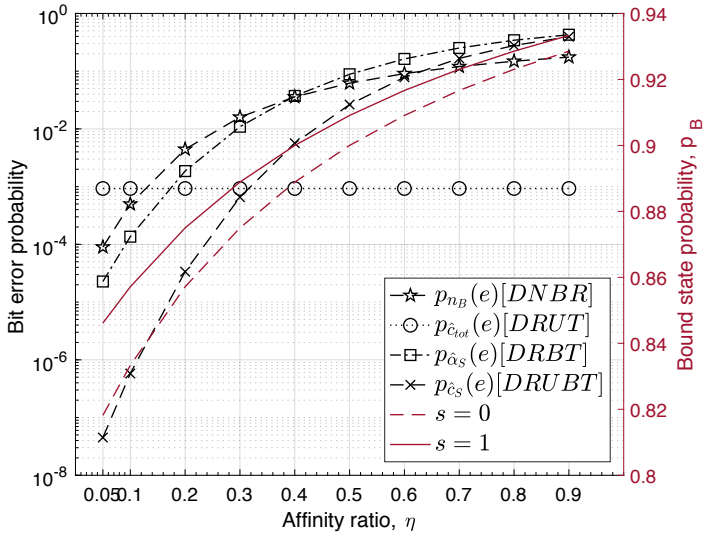

(a)

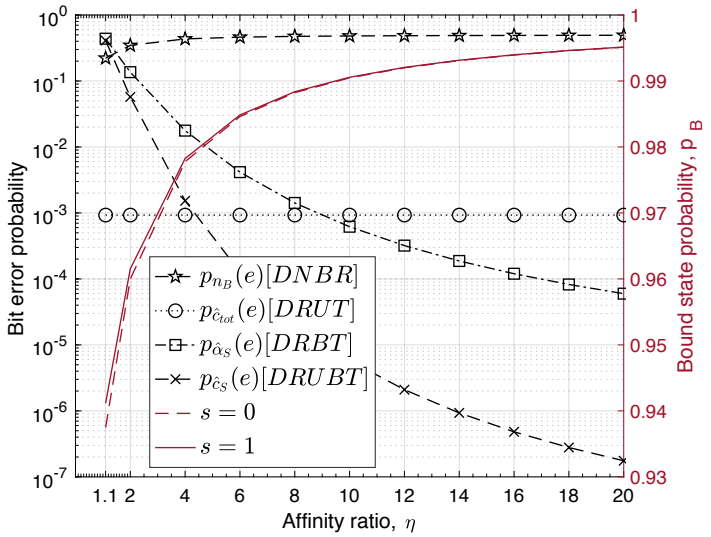

(b)

Fig. 6.4 Bit error probability as a function of affinity ratio $\eta = k_S^-/k_I^-$ for the cases (a) when information molecules have more binding affinity, i.e., $\eta < 1$, and (b) when interferer molecules have more binding affinity, i.e., $\eta > 1$.

In the first scenario, information molecules have more binding affinity than the interferers, e.g., $\eta < 1$. As is seen from the results provided in Fig. 6.4(a), when the two types of molecules become similar, the error probability substantially increases for all detection methods except DRUT. The performance of DRUT is not affected by the binding affinity, as the total unbound time of receptors, which DRUT relies on, are

independent of the unbinding rate of ligand-receptor pairs, and only depends on the binding rate and molecular concentration. On the other hand, DRUBT performs best when the information and interferer molecules differ greatly in terms of binding affinity. In the case of high similarity, the ratio estimator DRBT is the worst performer, as it becomes unable to discriminate the two types of molecules based on their bound time durations. The same reasoning applies to the performance of DRUBT in this region, which also partly relies on concentration ratio estimation.

In the second analysis, I consider the case when the information molecules have lower binding affinity than the interferers. In this case, we can expect that the most of the receptors are occupied by the interferer molecules. As shown in Fig. 6.4(b), DNBR, the simplest detection method, performs particularly poorly for $\eta > 1$. As the affinity ratio increases, the advantage of those detection methods relying on the difference between unbinding rates become more pronounced. While DRUBT significantly outperforms other methods in this case, the performance of DRUT, which is more practical than DRUBT, is notable.

6.5.3 Effect of Bit-0/Bit-1 Concentration Ratio

I also analyse the effect of the distance between bit-0 and bit-1 in terms of received concentration. In the case of high ISI in the MC channel, it is probable that a high concentration of information molecules from previous transmissions remains in the reception space. As a result, the ratio between the distinct concentration levels corresponding to bit-0 and bit-1 transmissions can approach to 1, making the discrimination between them difficult. Here the ratio of bit-0 and bit-1 concentration is varied from 0.1 to 0.99. The results are provided in Fig. 6.5(a) (with a magnified view provided in Fig. 6.5(b)). As the concentration ratio approaches 1, all the detection methods fail to provide an acceptable error performance. On the other hand, DRUBT performs significantly better than any of the other detection methods tested. It is also to be noted that the performance of DRUT becomes the worst among all, when the concentration levels are well-separated, e.g., in the case of very low ISI. In this range, DNBR, which is the simplest detection method, performs very well. This indicates that even in the presence of interferer molecules, the instantaneous number of bound receptors can provide sufficient statistics for detection as long as the concentration levels for bit-0 and bit-1 are well-separated, and the interferer concentration is at a moderate level.

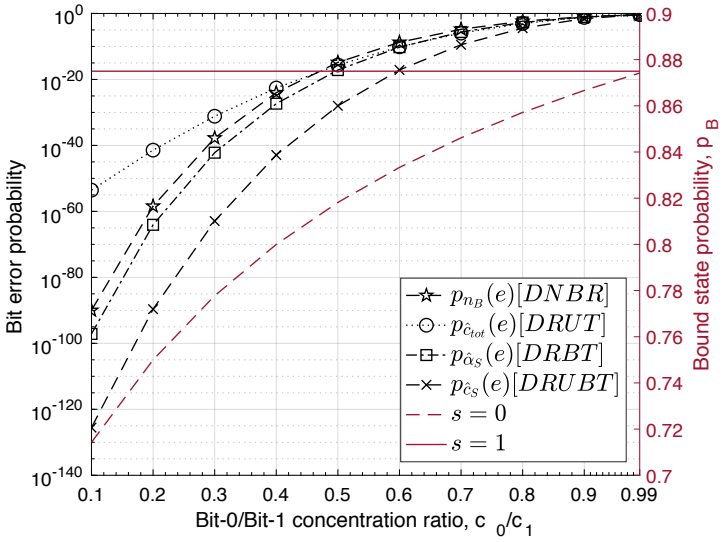

(a)

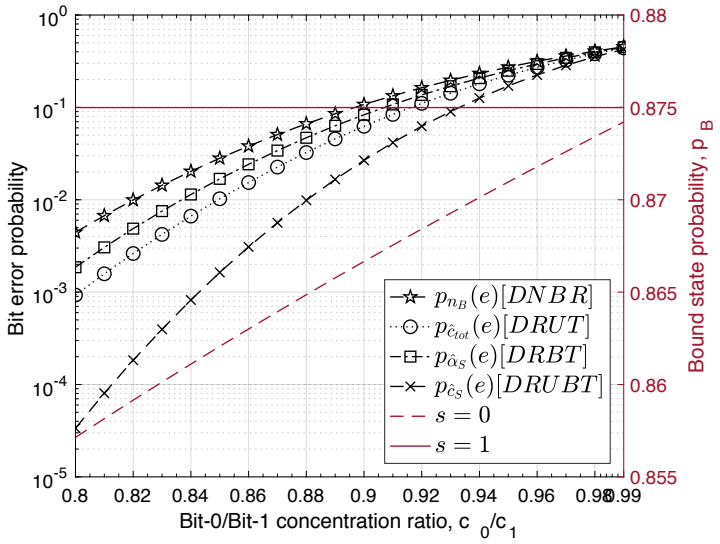

(b)

Fig. 6.5 (a) Bit error probability with varying ratio of the received concentrations corresponding to bit-0 and bit-1 transmissions, i.e., c_0/c_1. A magnified view is provided in (b).

6.5.4 Effect of Number of Receptors

The number of receptors determines the number of independent samples taken for detection. For example, in DNBR, the instantaneous number of bound receptors is the sum of N_R random variables independently following Bernoulli distribution. In

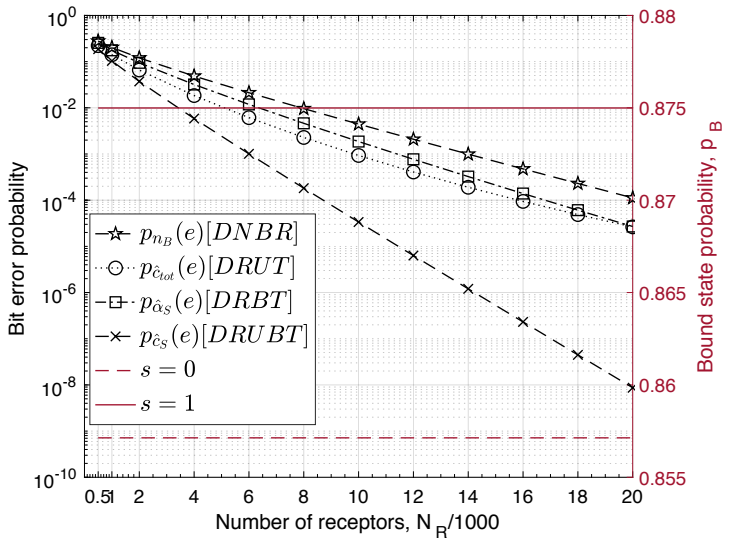

Fig. 6.6 Bit error probability as a function of number of receptors.

DRUT and DRUBT, the total unbound time T_u is the sum of N_R unbound time intervals which independently follow exponential distributions. In DRBT and DRUBT, each of the independent receptors is assumed to sample only one binding event, leading to the observation of N_R independent binding events. All detection methods show similar, almost log-linear, performance trends with the increasing number of receptors. The most significant performance improvement is observed with DRUBT as it relies on both unbound time and bound time statistics taken independently from all receptors.

6.6 Discussion on Implementation

The introduced detection methods are practical in the sense that they can be implemented by synthetic receptors and CRNs in biological MC receivers. In this section, I discuss four different receptor designs that can transduce the required receptor statistics, i.e., number of bound receptors, total unbound time, number of binding events of durations within specific intervals, into the concentration of intracellular molecules, i.e., secondary messengers. The receptor designs incorporate an activation mechanism, which was previously introduced in Chapter 5 of this thesis, to control the start time and duration of sampling. I also discuss potential CRNs, which can chemically process the generated secondary messengers in order to perform the analogue and digital computations required for the detection.

Activation Mechanism

In order to control the start time and duration of the sampling of receptor statistics, the receptor designs should have an activation mechanism that allows the receptors to generate secondary messengers only when they are in an active state. In Chapter 5, I proposed an activation mechanism that enables the sampling of the required statistics from independent receptors only once during each sampling period. The synthetic receptor designs, which will be introduced next, incorporate this mechanism. In this scheme, the cell generates activator molecules A^+, which can rapidly diffuse and interact with only inactive receptors with the reaction rate ω, and convert them into active or intermediate states depending on the receptor design. The generation of activation molecules is governed by the following reaction

$$\varnothing \xrightarrow{\mathrm{s(t)}\ \psi^+} \mathrm{A}^+, \tag{6.48}$$

where $s(t)\psi^+$ is the time-varying generation rate of A^+ molecules, and $s(t) \approx \delta(t - t_A)$ is a very short pulse signal centred around the activation time t_A. The generation of A^+ molecules is followed by the generation of deactivation molecules A^-, i.e.,

$$\varnothing \xrightarrow{\mathrm{d(t)}\ \psi^-} \mathrm{A}^-. \tag{6.49}$$

The generation rate of deactivation molecules is given by $d(t)\psi^-$. Here $d(t) \approx \delta(t - t_D)$ is an impulse-like signal centred around the deactivation time t_D. The activation molecules are degraded by the deactivation molecules with the reaction rate ρ, i.e.,

$$\mathrm{A}^+ \ + \ \mathrm{A}^- \xrightarrow{\rho} \varnothing, \tag{6.50}$$

In this way, the duration of the overall sampling process is controlled by the receiver cell. Note that the reaction rates governing the activation mechanism, i.e., ψ^+, ψ^-, ω, ρ, should be very high compared to the ligand-receptor binding/unbinding reaction rates to prevent the inactivated receptors from being re-activated in the same sampling process.

Implementation of DNBR

In DNRB, we need the representation of the number of bound receptors at the sampling time in terms of the concentration of intracellular molecules. A potential synthetic receptor design is provided in Fig. 6.7(a). In this design, the receptor has three states, unbound state U, inactive bound state B_I, and active bound state B_A. The receiver

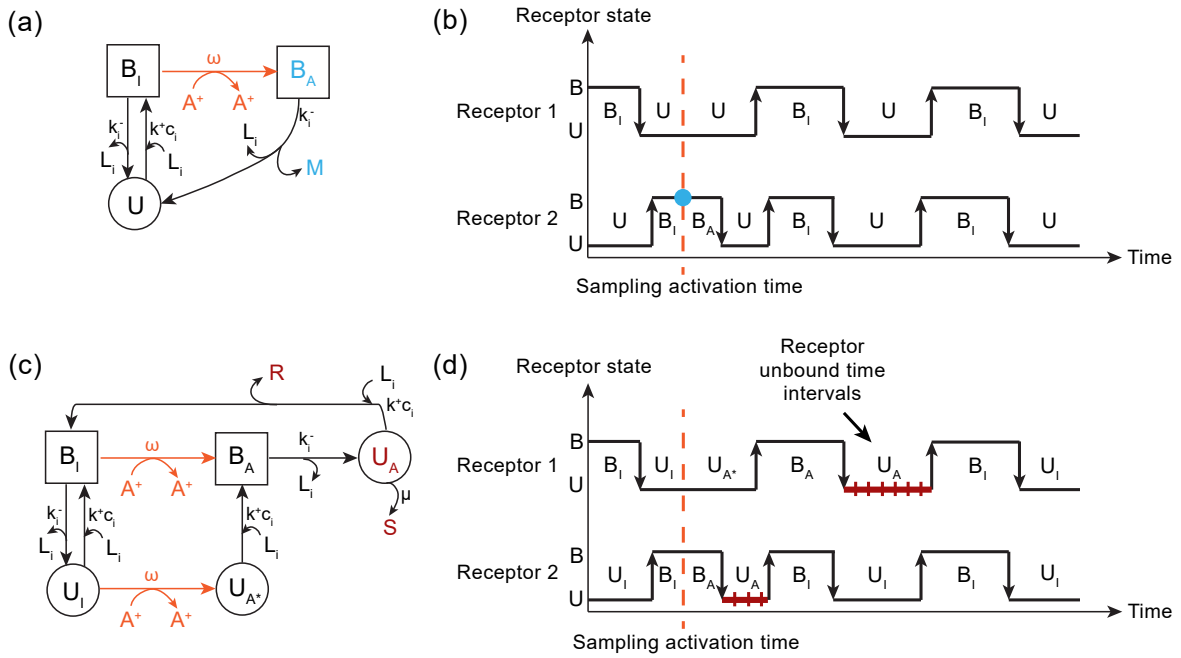

Fig. 6.7 (a) Receptor design for DNBR. (b) Sampling of the number of bound receptors. (c) Receptor design for DRUT. (d) Sampling of the receptor unbound time intervals.

cell releases intracellular activation molecules at the time of sampling. The released activation molecules A^+ only react with B_I, and convert them to B_A. The active bound receptors release an intracellular molecule M upon unbinding from a ligand and returns to the unbound state. Therefore, the number of M molecules encodes the number of bound receptors at the sampling time. This intracellular signal can be amplified, if the design allows the active receptor molecules to release multiple M molecules.

The next process is to compare the intracellular concentration of M molecules to a threshold encoded by a different secondary messenger. A simple comparator can be implemented through the following reaction

$$\mathrm{M} + \mathrm{X} \xrightarrow{\xi} \varnothing, \tag{6.51}$$

where X molecules encode the threshold given in (6.44). If M molecules remain inside the cell after this reaction, the receiver decides bit-1, otherwise it decides bit-0. Note that in the case of amplification of intracellular concentration of M molecules, the threshold signal should be also amplified proportionally.

Implementation of DRUT

DRUT requires the transduction of the total unbound time of receptors into the concentration of second messengers. I propose a synthetic receptor design with an activation mechanism demonstrated in Fig. 6.7(c), to guarantee that only one unbound time information is acquired from each independent receptor. In this design, the receptor has 5 states: inactive unbound (U_I), intermediate unbound (U_A^*), active unbound (U_A), inactive bound (B_I), and active bound (B_A) states. At the sampling time, the receiver releases activation molecules, which can rapidly diffuse and react with only the receptors at U_I and B_I states. If the receptor is already unbound at the time of activation, it waits until the next complete unbound period for providing the information on the unbound time duration. Therefore, it first goes into the intermediate state U_A^*, which is followed by B_A and U_A states. If it is bound when activated, the next unbinding event transitions it into the active unbound state U_A. Receptors at U_A states release intracellular molecules S at a fixed rate, and upon the first binding event, they transition into inactive bound state B_I releasing a single molecule of a different type R to encode the number of independent samples taken.

The resulting concentration of intracellular S molecules encodes the total unbound time of receptors over a single period of sampling. These second messengers along with R molecules can go through a chemical reaction network (CRN) to implement the total concentration estimator, given in Eq. (6.13). An example CRN would be as follows:

$$\mathrm{R} \xrightarrow{1} \mathrm{R} + \mathrm{Y}, \tag{6.52}$$

$$\mathrm{S} + \mathrm{Y} \xrightarrow{\mathrm{k}^+} \mathrm{S}. \tag{6.53}$$

In this CRN, I introduce another type of intracellular molecule Y, which is produced by R molecules at the unit rate, while consumed by S molecules at the common binding rate of ligands k^+. The rate equation of this CRN can be written as

$$\frac{d\mathrm{E}[n_Y]}{dt} = \mathrm{E}[n_R] - k^+\mathrm{E}[n_S]\mathrm{E}[n_Y], \tag{6.54}$$

where n_Y, n_R, and n_S are the number of Y, R, and S molecules, respectively. Given the initial condition $\mathrm{E}[n_Y^0] = 0$, the steady-state solution for $\mathrm{E}[n_Y]$ can be obtained as

$$\mathrm{E}[n_Y^{ss}] = \frac{\mathrm{E}[n_R^{ss}]}{k^+\mathrm{E}[n_S^{ss}]}, \tag{6.55}$$

Given that n_R^{ss} and n_S^{ss} encode the number of independent receptors and the total unbound time, the resulting number of Y molecules at steady-state, n_Y^{ss}, approximates the total concentration estimator $\hat{c}_{tot} = \frac{N-1}{k^+ T_u}$.

For the decision, the comparator reaction utilised in DNBR can also be implemented here, i.e.,

$$\mathrm{Y} \; + \; \mathrm{X} \xrightarrow{\xi} \varnothing, \tag{6.56}$$

where the number of X molecules encodes the optimal threshold value. If Y molecules remain in the cell as a result of this reaction, the receiver decides bit-1, otherwise it decides bit-0.

Implementation of DRBT

To implement DRBT, we need to convert the number of binding events of durations within specific time intervals to the concentration of intracellular molecules. Following my proposal in Chapter 5, a synthetic receptor design is introduced with an activation mechanism and a modified KPR mechanism, as demonstrated in Fig. 6.8(a). The activation mechanism is similar to those introduced for DNBR and DRUT, and ensures that only one binding time information is received from each independent receptor, as shown in Fig. 6.8(b). In this design, when an active unbound receptor U_A binds a ligand, it goes into the active bound state B_A where the KPR mechanism is activated.

The KPR mechanism, in this case, consists of two substates, B_A^1 and B_A^2, with a unidirectional state transition rate β, which can be set as a function of the time threshold T_1 as follows

$$\beta = \kappa / T_1, \tag{6.57}$$

where κ's is a tuning parameter to adjust the transition rates. My previous analysis in Chapter 5 showed that $\kappa = 3/5$ provides reasonable accuracy in representing the number of binding events, $n_{b,1}$ and $n_{b,2}$, with second messengers via this stochastic KPR mechanism.

The receptor is allowed to return to the inactive unbound state U_I any time upon unbinding from the bound ligand. While returning to U_I, the receptor releases a single R molecule encoding the number of independent samples, and one of the intracellular molecules D_1 or D_2, depending on the last visited KPR substate. In this way, the KPR mechanism allows to discriminate the long binding events, which are more likely to be resulting from the molecules with higher affinity, from the short binding events through

encoding the number of corresponding binding events into the number of D_1 and D_2 molecules. A steady-state analysis of a similar KPR mechanism is provided in Chapter 5.

The generated intracellular molecules R, D_1 and D_2 go into a CRN for realizing the ratio estimator $\hat{\alpha}_S$, given in (6.26). An example CRN can be given as follows

$$\mathrm{D_1} \xrightarrow{\mathrm{w_{2,1}}} \mathrm{D_1} + \ \mathrm{Y}, \tag{6.58}$$

$$\mathrm{D_2} \xrightarrow{\mathrm{w_{2,2}}} \mathrm{D_2} + \ \mathrm{Y}, \tag{6.59}$$

$$\mathrm{R} + \mathrm{Y} \xrightarrow{1} \mathrm{R}. \tag{6.60}$$

In this CRN, the intracellular molecules Y are produced by D_1 and D_2 with the reactions rates $w_{2,1}$ and $w_{2,2}$, respectively. They are consumed by R molecules at the unit rate. The rate equation of this CRN can be written as

$$\frac{d\mathrm{E}[n_Y]}{dt} = w_{2,1}\mathrm{E}[n_{D_1}] + w_{2,2}\mathrm{E}[n_{D_2}] - \mathrm{E}[n_R]\mathrm{E}[n_Y]. \tag{6.61}$$

Given the initial condition $\mathrm{E}[n_Y^0] = 0$, the steady-state solution for $\mathrm{E}[n_Y]$ can be obtained as

$$\mathrm{E}[n_Y^{ss}] = \frac{w_{2,1}\mathrm{E}[n_{D_1}^{ss}] + w_{2,2}\mathrm{E}[n_{D_2}^{ss}]}{E[n_R^{ss}]}. \tag{6.62}$$

Given that $n_{D_1}^{ss}$ and $n_{D_2}^{ss}$ encode $n_{b,1}$ and $n_{b,2}$, respectively, and n_R^{ss} encodes number of independent samples, the number of Y molecules at steady-state, n_Y^{ss}, approximates $\hat{\alpha}_M^S = \left(n_{b,1}w_{2,1} + n_{b,2}w_{2,2}\right)/N$.

The comparator reaction for the decision on the received bit can be realised in a similar way as DNBR and DRUT, i.e.,

$$\mathrm{Y} \ + \ \mathrm{X} \xrightarrow{\xi} \varnothing, \tag{6.63}$$

where the number of X molecules encodes the optimal threshold given in (6.46). If Y molecules remain in the cell as a result of this reaction, the receiver decides bit-1, otherwise bit-0 is decided.

Implementation of DRUBT

DRUBT requires both the transduction of the total unbound time and the number of binding events of durations within specific time intervals. Hence, a combination of receptor designs introduced for DRUT and DRBT would realise the necessary conversions. The

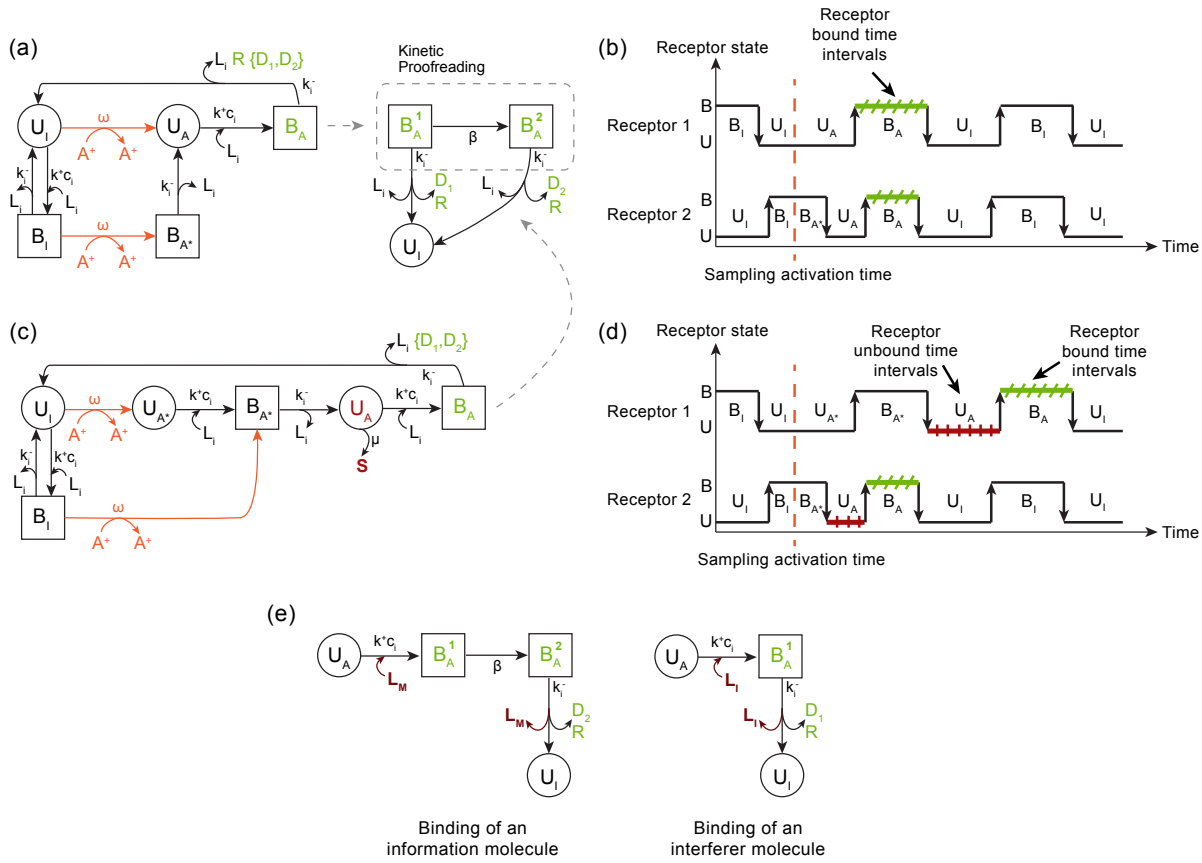

Fig. 6.8 (a) Receptor design for DRBT. (b) Sampling of the number of binding events of durations within specific time intervals. (c) Receptor design for DRUBT. (d) Sampling of the receptor unbound time intervals and the number of binding events of durations within specific time intervals. (e) Typical pathways in the kinetic proofreading mechanism of the DRBT and DRUBT receptors when information and interferer molecules bind an active unbound receptor.

synthetic receptor design given in Fig. 6.8(c) ensures that only a single pair of complete unbound and bound time information is sampled from each independent receptor. Note that the receptor is not required to generate R molecules, as in this case, the CRN does not need the information of the number of receptors.

Given that the number of generated S, D_1 and D_2 molecules encodes T_U, $n_{b,1}$ and $n_{b,2}$, respectively, the CRN for the concentration estimator $\hat{c}_S$, given in (6.37), can be implemented as follows

$$\mathrm{D}_1 \xrightarrow{\mathrm{w}_{2,1}} \mathrm{D}_1 + \mathrm{Y}, \tag{6.64}$$

$$\mathrm{D}_2 \xrightarrow{\mathrm{w}_{2,2}} \mathrm{D}_2 + \mathrm{Y}, \tag{6.65}$$

$$\mathrm{S} + \mathrm{Y} \xrightarrow{\mathrm{k}^+} \mathrm{S}. \tag{6.66}$$

The rate equation of this CRN can be written as

$$\frac{d\mathrm{E}[n_Y]}{dt} = w_{2,1}\mathrm{E}[n_{D_1}] + w_{2,2}\mathrm{E}[n_{D_2}] - k^{+}\mathrm{E}[n_S]\mathrm{E}[n_Y]. \tag{6.67}$$

Given the initial condition $\mathrm{E}[n_Y^0] = 0$, the steady-state solution for $\mathrm{E}[n_Y]$ can be obtained as

$$\mathrm{E}[n_Y^{ss}] = \frac{w_{2,1}\mathrm{E}[n_{D_1}^{ss}] + w_{2,2}\mathrm{E}[n_{D_2}^{ss}]}{k^{+}E[n_S^{ss}]}. \tag{6.68}$$

As is obvious, the number of Y molecules at steady-state n_Y^{ss} approximates $\hat{c}_M^S = \frac{1}{k^{+}T_u}\left(n_{b,1}w_{2,1} + n_{b,2}w_{2,2}\right)$ for $N \gg 1$.

The following comparator can be applied here as well for the decision

$$\mathrm{Y} \;+\; \mathrm{X} \xrightarrow{\xi} \varnothing, \tag{6.69}$$

where the number of X molecules encodes the optimal threshold value given in (6.46). If eventually Y molecules outnumber X molecules, the receiver decides bit-1, otherwise it decides bit-0.

6.7 Conclusion

In this chapter, I investigate the performance of four different MC detection methods in the presence of interference resulting from molecules having similar binding affinity as the information-carrying molecules. The detection methods are based on different statistics of the ligand-binding reaction that reveal information about the concentration and binding affinity of the molecules, e.g., instantaneous number of bound receptors, duration of receptors' bound and unbound time intervals. The methods vary in complexity; however, they are all practical in the sense that they can be implemented by synthetic receptors and simple chemical reaction networks in biological MC devices. The analyses show that the effect of molecular interference on the detection performance can be substantially reduced by using the combination of unbound and bound time durations of receptors instead of relying on the number of bound receptors, which was the prevalent approach in the previous literature.

Chapter 7

Graphene-based Molecular Communication Receiver

7.1 Introduction

As discussed earlier in Chapter 2, the lack of practical micro/nanoscale MC devices and MC testbeds has limited the research in this emerging field only to theoretical studies that usually rely on unrealistic assumptions about the device designs, nano-bio-physical interactions at the device-channel interfaces, and the resulting constraints [19]. As the first step to overcome this challenge, in this work, I report on the first implementation of a micro/nanoscale MC receiver based on graphene field-effect transistor-based DNA biosensors (graphene bioFETs), and its ICT tests in a custom-designed microfluidic MC system. The main objective of this work is to provide an experimental testbed at physically relevant dimensions for nanonetworks, which can be used to reveal and study the effects of intricate biochemical and physical processes on the MC performance and develop practical and realistic communication methods, including new MC detection techniques.

Graphene, with its exceptional electrical, chemical and mechanical properties, such as high carrier mobility at room temperature, one atomic layer thickness and two dimensional geometry exposing all its atoms to the sensing environment, provides very high sensitivity towards biochemical molecules especially in a bioFET configuration [4, 86, 115]. Owing to these properties, graphene has been extensively studied for selective sensing of a wide range of biomolecules ranging from carbohydrates [216] to proteins [217] and oligonucleotides [89, 97]. Meeting the fundamental requirements of an MC receiver, such as the capability of label-free and reversible detection and high sensitivity, graphene bioFET stands as an ideal candidate for the implementation of

the MC receiver. Flexibility and nanoscale 2d geometry of graphene are particularly favourable for the integration of graphene-based MC receiver into functional nanoscale devices.

Functionalisation of graphene with biomolecular probes can provide the selectivity against target analytes, required for avoiding biochemical interference for MC applications in physiologically relevant environments. In this work, graphene is functionalised with single-stranded DNA (ssDNA) probes (pDNAs) which undergo reversible hybridisation reaction with the complementary target DNAs (tDNAs). The reason for selecting DNA as the recognition element is that DNA can be easily customized with different base sequences of different lengths, and can be designed to bind not only complementary DNAs but also peptides, proteins, carbohydrates and small molecules [218]. As a result, the implemented device can serve as a model system to provide insight into a broad range of MC systems relying on detection of molecular messages through affinity-based ligand-receptor interactions [16, 19]. Moreover, integration of the fabricated MC receiver into a pressure-regulated microfluidic testbed provides control over the fluid flow rate, and enables flexibility and practicality in testing different channel geometries, which can mimic the most promising application environments of the MC inside human body, e.g., circulatory system [29, 219].

In the remainder of this chapter, I elaborate on the fabrication process of single layer graphene (SLG) bioFET-based MC receiver and its integration into a microfluidic testbed. The optical and electrical characterisation of the device is performed at each step of functionalisation. Sensing response characteristics are revealed to determine the affinity between the complementary tDNA-pDNA pair. Selectivity of the device against complementary tDNAs is examined through real-time sensing response to non-complementary target DNAs (ntDNAs). Note that this thesis does not contribute new knowledge to the design, fabrication and characterisation of the graphene bioFET-based biosensors. However, the work until this point serves to lay the groundwork for the implementation and accurate evaluation of the graphene bioFET-based DNA biosensors as MC receiver. Following the fabrication and sensitivity/selectivity analysis, I provide an MC detection performance analysis based on the transmission of pseudo-random binary data encoded into the concentration of tDNAs. The time-varying response of the MC receiver is fitted by the microfluidic MC model developed in Chapter 3. This analysis provides important insights particularly into the infamous ISI problem of MC resulting from the slow kinetics of ligand-receptor binding reactions. Similar to the existing approaches in the MC literature [72, 220], a concentration difference-based

detection method is utilised to overcome the ISI effects by obviating the need for channel state information (CSI).

7.2 Fabrication of MC Receiver

MC receiver is fabricated in three consecutive steps. First, a graphene field-effect transistor (GFET) with chemical vapour deposition (CVD)-grown SLG is fabricated on Si/SiO_2 substrate through optical lithography techniques. Then, a polydimethylsiloxane (PDMS)-based microfluidic channel is produced to encapsulate the GFET for bio-functionalisation, and real-time microfluidic sensing and communication experiments. Finally, for selectivity of the MC receiver against information-carrying target DNAs, bio-functionalisation of the GFET channels with probe DNA molecules is performed inside the microfluidic channel connected to a pressure-regulated microfluidic setup.

7.2.1 Fabrication of GFET

MC receiver is fabricated with a CVD-grown SLG polycrystalline domain on an n-type Si/SiO_2 substrate (525 μm with 90 nm thermal oxide layer, obtained from Mi-Net Technology Ltd). The CVD-grown SLG on Cu with PMMA coating (60 nm, 495K, A2) is obtained from Graphenea Inc.

Wet Transfer of CVD graphene on Si/SiO_2 Substrate: The Cu layer of the PMMA/SLG/Cu stack should be removed before transfer onto Si/SiO_2 substrate. The Cu side is partially covered with a graphitic film, which may result in poor Cu etching performance. This backside graphene on Cu is etched away with O_2 plasma at 3 W for 30 seconds in a low-power Reactive Ion Etcher (RIE) in NanoEtch (Moorfield Nanotechnology Ltd). After this step, Cu is etched by placing the PMMA/SLG/Cu stack on the surface of a solution of ammonium persulphate (APS) (1.8 g of APS in 150 ml DI water (18.2 MΩ·cm)).

The Si/SiO_2 substrate is cleaned before the transfer by means of sonication for 10 minutes in acetone followed by immersion in isopropyl alcohol (IPA) for 5 minutes and drying with nitrogen (N_2). Once the Cu is entirely dissolved, the floating PMMA/SLG stack is transferred onto the surface of DI water in a beaker by a glass slide to dilute the APS residuals, and then, the stack is fished onto the Si/SiO_2 substrate. The resulting sample (PMMA/SLG/SiO_2/Si) is left vertically to dry overnight, and then annealed over a hot plate at 150 °C for 2 hours. The sample is then transferred into a beaker with

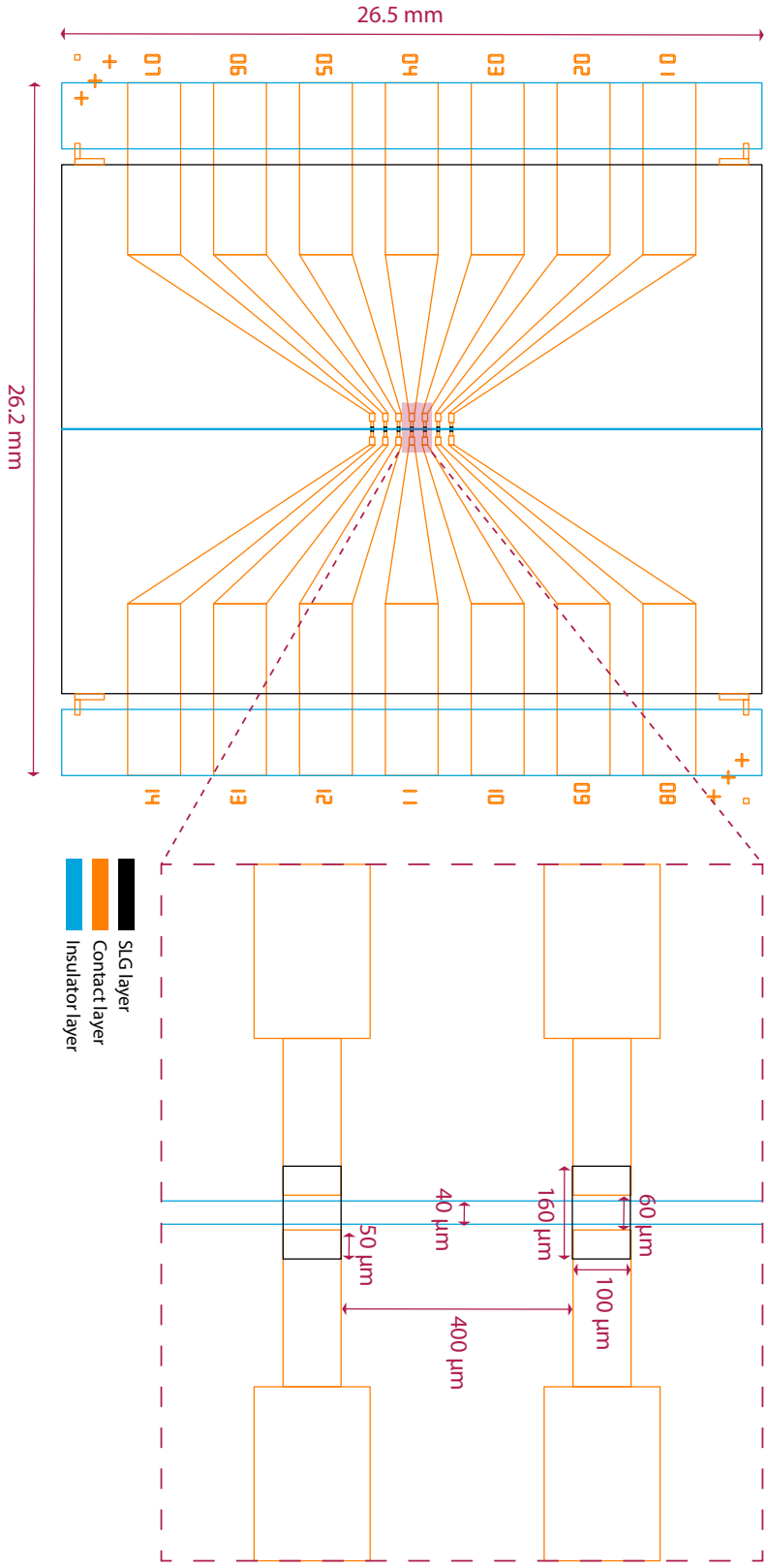

Fig. 7.1 Computer-aided design for optical lithography of MC receiver.

acetone for PMMA removal for 2 hours, and then immersed in IPA for 5 minutes and dried with N_2, leaving only the SLG film on the Si/SiO_2 substrate (Fig. 7.2(a)).

Patterning of SLG Channels: MC receiver is designed to contain 7 GFETs having isolated source and drain contacts but being exposed to a common electrolyte gate. The individual SLG channels are patterned via optical lithography with a laser writer according to the design shown in Fig. 7.1. Prior to all laser writing processes in this work, the sample is spin-coated with a photoresist (AZ-5214E from Microchemicals GmbH) at 4000 rpm for 60 seconds (Fig. 7.2(b)), and baked at 110 °C for 50 seconds on a hot plate. The photoresist layer is exposed by direct laser writing (wavelength-405 nm 169 mJ/cm^2) via laser writer (LW-405B+ from Microtech Srl), and the pattern is successively developed in diluted developer solution (1:4, AZ-351B/DI Water) for 35-45 seconds followed by brief immersion of the sample in DI-water for 2 seconds and drying with N_2 (Fig. 7.2(c)). The patterning of the individual SLG channels is completed with RIE removing the undesired areas of SLG film, which are not covered with the photoresist layer, via O_2 plasma at 3 W for 60 seconds (Fig. 7.2(d)). Finally, to remove the photoresist layer, the sample is successively immersed in acetone and IPA for 20

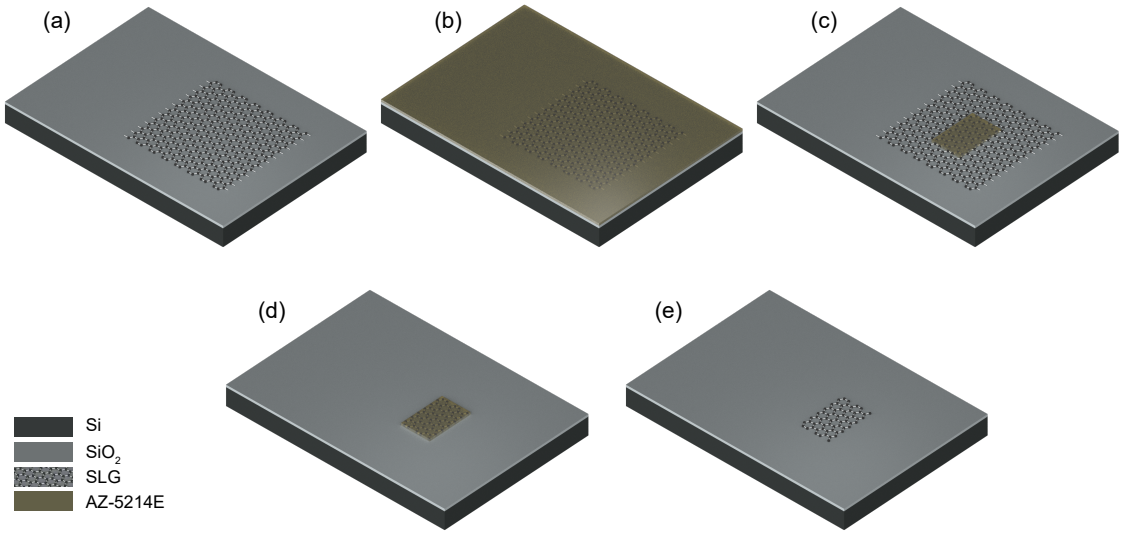

Fig. 7.2 Process flow for the patterning of SLG channels. (a) SLG transferred on Si/SiO_2 substrate. (b) Coating of sample with photoresist layer. (c) SLG channel pattern defined by optical lithography. (d) SLG channel pattern after RIE etching. (e) Removal of residual photoresist layer from SLG surface, and the resulting SLG channel on the substrate.

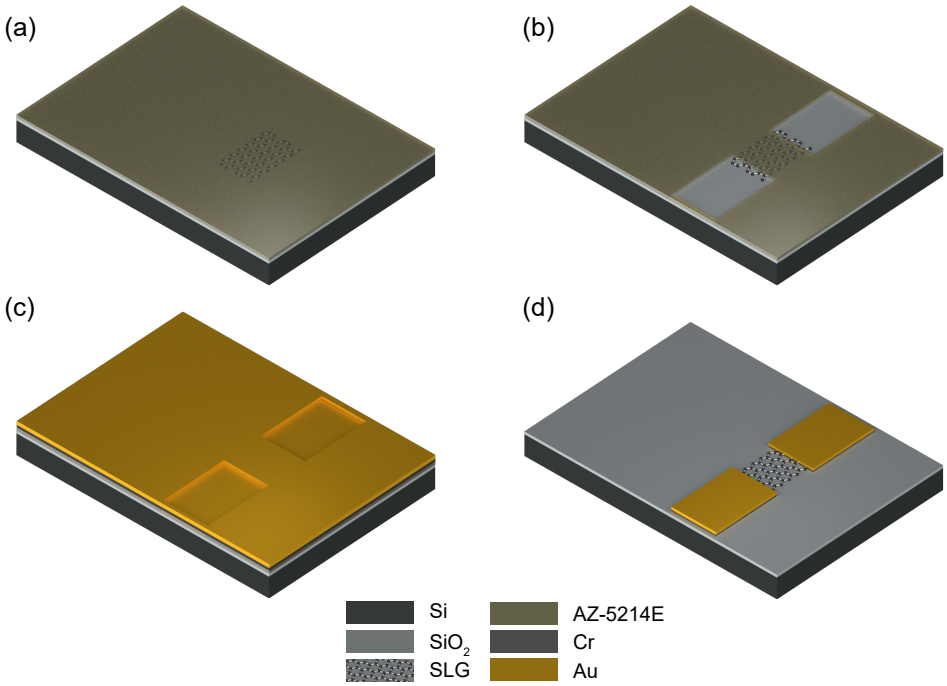

Fig. 7.3 Process flow for the deposition of contacts. (a) Coating of sample with photoresist layer. (b) Contact pattern defined by optical lithography. (c) Deposition of Cr and Au metal films through thermal evaporation. (d) Patterned contacts after lift-off process.

minutes and 5 minutes, respectively, and dried with N_2, leaving the patterned SLG film on the substrate (Fig. 7.2(e)).

Deposition of Contacts: In the following step, metal contact areas (source and drain) are defined on the sample through another optical lithography process (Figs. 7.3(a)-(b)). Depositions of 5 nm Cr and 50 nm Au are performed successively over the sample covered with the patterned photoresist layer by thermal evaporation at 10^{-6} mbar (using MiniLab 060 from Moorfield Nanotechnology Ltd) (Fig. 7.3(c)). Once the metals are deposited uniformly, the sample is dipped in acetone for 2 hours for lift-off process, during which the metals over the photoresist layer are removed leaving only the patterned contacts (Fig. 7.3(d)).

Deposition of Insulator: Finally, the drain and source contact areas, which might be exposed to the electrolyte during microfluidic experiments, are insulated to prevent any parasitic current between metal contacts through the electrolyte. For this, a thin layer of Al_2O_3 (20 nm) is uniformly deposited over the sample through atomic layer deposition (ALD) in TFS200 (manufactured by Beneq) (Fig. 7.4(a)). This step is followed by

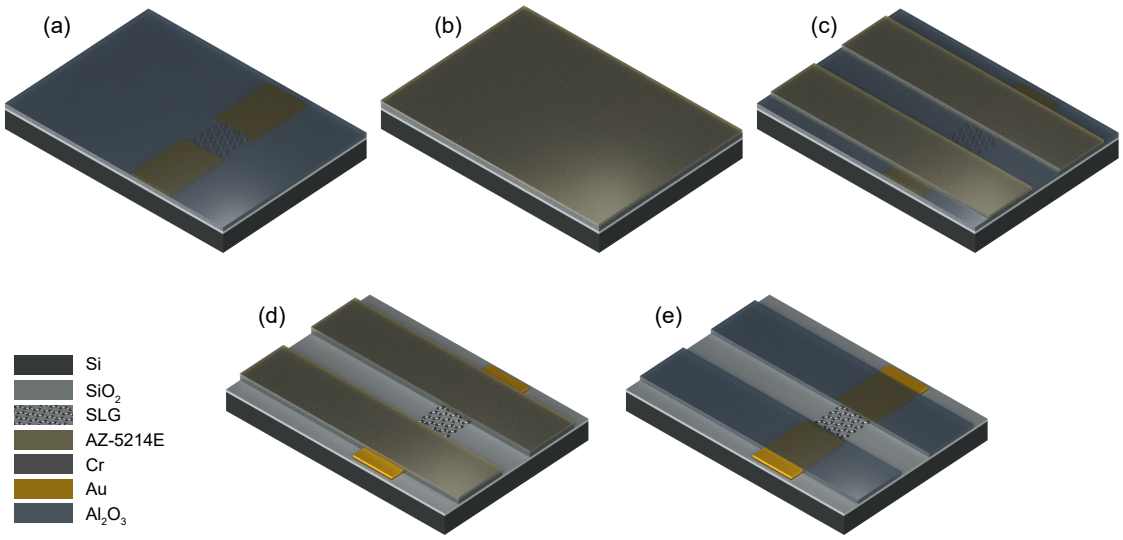

Fig. 7.4 Process flow for the deposition of insulator. (a) Uniform Al_2O_3 film over the sample after ALD. (b) Coating of sample with photoresist layer. (c) Insulator pattern defined by optical lithography. (d) Exposed SLG channel and contacts after wet etching of Al_2O_3. (e) Patterned Al_2O_3 film after removal of excess photoresist.

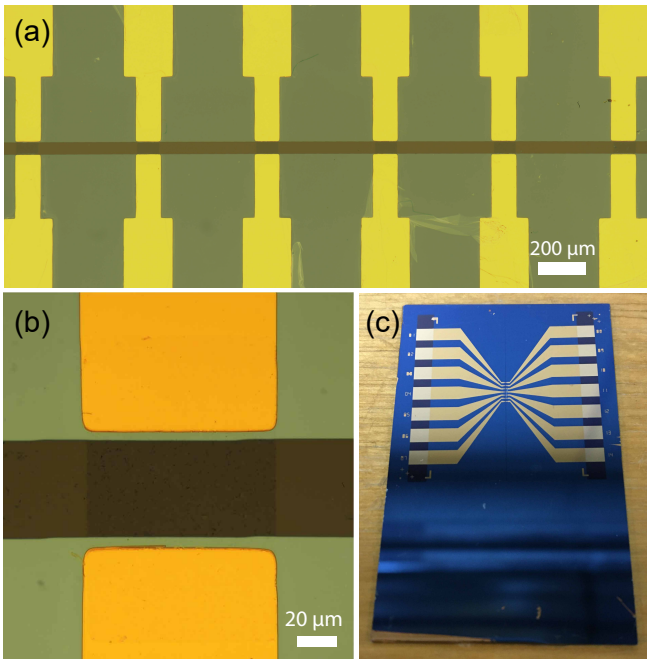

Fig. 7.5 (a) Optical micrograph of the fabricated GFET channels after Al_2O_3 etching process (only six of the seven channels are visible). (b) A closer look into one of the GFET channels. (c) Overall view of the fabricated 7-channel GFET before the bonding of microfluidic PDMS layer.

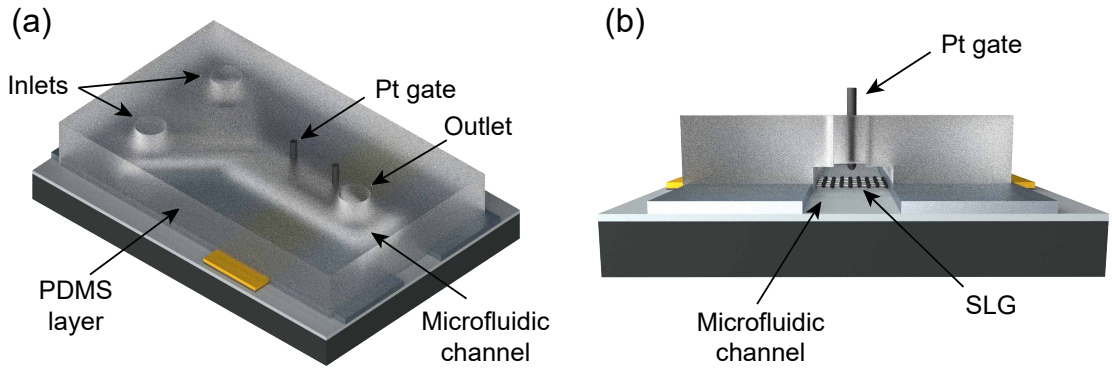

Fig. 7.6 (a) Microfluidic PDMS layer bonded to the GFET surface after the inlets and outlet are defined, and the Pt gate electrode is placed on top. (b) Cross-sectional view of the MC receiver after PDMS layer bonding.

another optical lithography process, which defines the windows over Al_2O_3 to expose only the SLG channels to the electrolyte, and to expose the source and drain contact pads, which remain outside of the microfluidic channel for electrical measurements (Figs. 7.4(b)-(c)). The exposed areas of Al_2O_3 are then wet-etched in Phosphoric Acid (85% wt. in H_2O obtained from Sigma-Aldrich) at 60 °C for 1 minute (Fig. 7.4(d)). For removing any excess photoresist, the sample is dipped in acetone for 20 minutes and IPA for 5 minutes followed by drying with N_2, leaving the patterned Al_2O_3 film on top (Fig. 7.4(e)).

The optical images of the fabricated GFET are shown in Fig. 7.5.

7.2.2 Fabrication of Microfluidic Channels and Device Integration

Fabricated GFET is encapsulated with a PDMS microfluidic channel, as demonstrated in Fig. 7.6. To this end, a 3d-printed mould is designed to define the geometry of the rectangular fluidic channel within the PDMS layer, as shown in Fig. 7.7(a). The microfluidic channel has a width of 4×10^3 μm and a height of 1.5×10^3 μm. At one end, the channel bifurcates for connection with the two channel inlets, which are designated for connection to the fluid reservoirs containing the buffer and information-carrying tDNA solutions during the communication experiments.

PDMS prepolymer is prepared using a 10:1 mixture of PDMS base monomer (Sylgard 184 Silicone Elastomer) and PDMS curing agent (obtained from Dow Corning Corporation). Air bubbles inside the PDMS are removed by degassing in a desiccator for 1

hour. The degassed mixture is poured onto the 3d-printed mould and left for curing overnight at room temperature. The cured PDMS is then carefully peeled off from its mould (Fig. 7.7(b)). The inlet and outlet holes are punched through the PDMS layer for microfluidic connections by a biopsy punch (1.25 mm radius). A platinum (Pt) wire having a diameter of 0.5 mm acting as the common solution gate is then mounted to the top of the PDMS channel right above the SLG channels (Figs. 7.6 and 7.7(c)). The length of the Pt wire inside the channel is set to 1 cm.

In the next step, the patterned PDMS with the Pt solution gate is bonded to the surface of the MC receiver, ensuring that the graphene channels are well-aligned with the microfluidic channel and not placed under the PDMS walls. The most common method for bonding PDMS on SiO_2 and glass substrates is based on the O_2 plasma activation of the PDMS surface and the target substrate. This requires the surfaces of both the PDMS and the target substrate to be smooth. In my case, however, the exposed graphene channels on the target SiO_2 substrate prevents the application of the O_2 plasma, as this would cause the removal of graphene channels through plasma etching. Moreover, the plasma activation of only the PDMS surface is not sufficient because curing in the 3d-printed moulds made of Polylactic acid (PLA) results in PDMS layers with a rough surface (Fig. 7.7(c)) rendering O_2 plasma activation ineffective in bonding. Therefore, I apply an alternative method, which was first introduced in [221] for bonding porous membranes into PDMS devices. In this method, a thin layer of PDMS prepolymer, which is in liquid form, is coated on the bonding surface of the cured PDMS layer. Then, the PDMS is carefully placed on the sample, which is cleaned off any dust with N_2 prior to bonding. After placement, it takes approximately 1 minute for the PDMS prepolymer to spread uniformly and cover the entire area between the PDMS and substrate except for the empty area defining the microfluidic channel. Once a uniform PDMS prepolymer layer is observed, the temperature of the hot plate is increased to 150 °C, and the prepolymer, serving as mortar, is quickly cured, resulting in a strong bonding. This method has consistently yielded leakage-free PDMS-substrate bonding during the fabrication process.

After bonding process, the inlet and outlet tubes are placed on the predefined inlet/outlet holes, as shown in Fig. 7.8(b). Here, Teflon PTFE tubing (1/16" OD x 1/32" ID, obtained from Darwin Microfluidics) is preferred because of its higher chemical stability compared to Tygon tubing, which reacts with DMF used in the functionalisation process. The placement of the inlet and outlet tubes is followed by the application of PDMS prepolymer around the connection points of inlet, outlet and Pt gate over the cured PDMS layer for the complete sealing of the device.

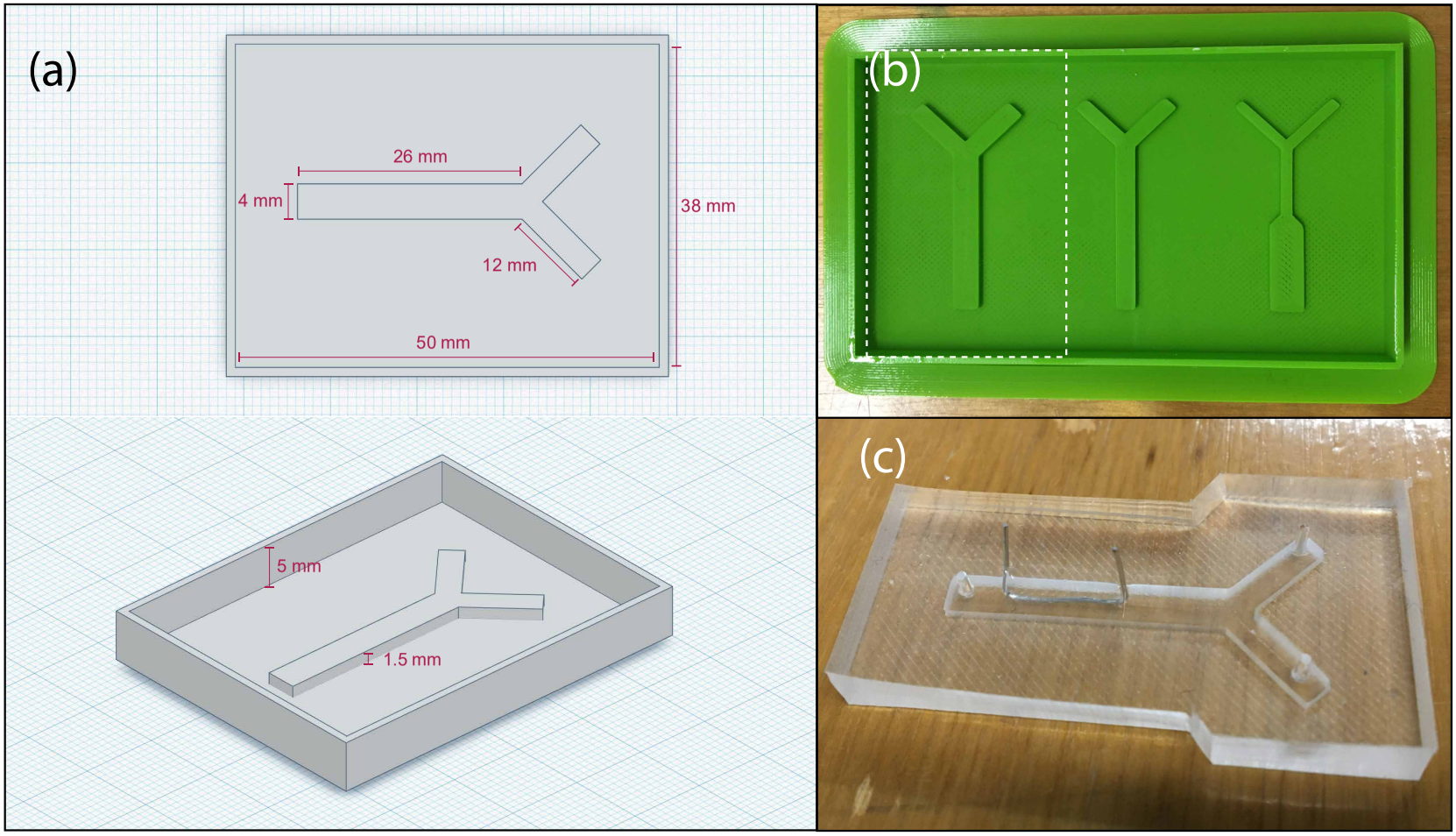

Fig. 7.7 (a) Computer-aided design for 3d printing of PDMS mould. (b) 3d-printed PDMS mould. (c) PDMS microfluidic channel with the Pt wire mounted on top as the gate electrode.

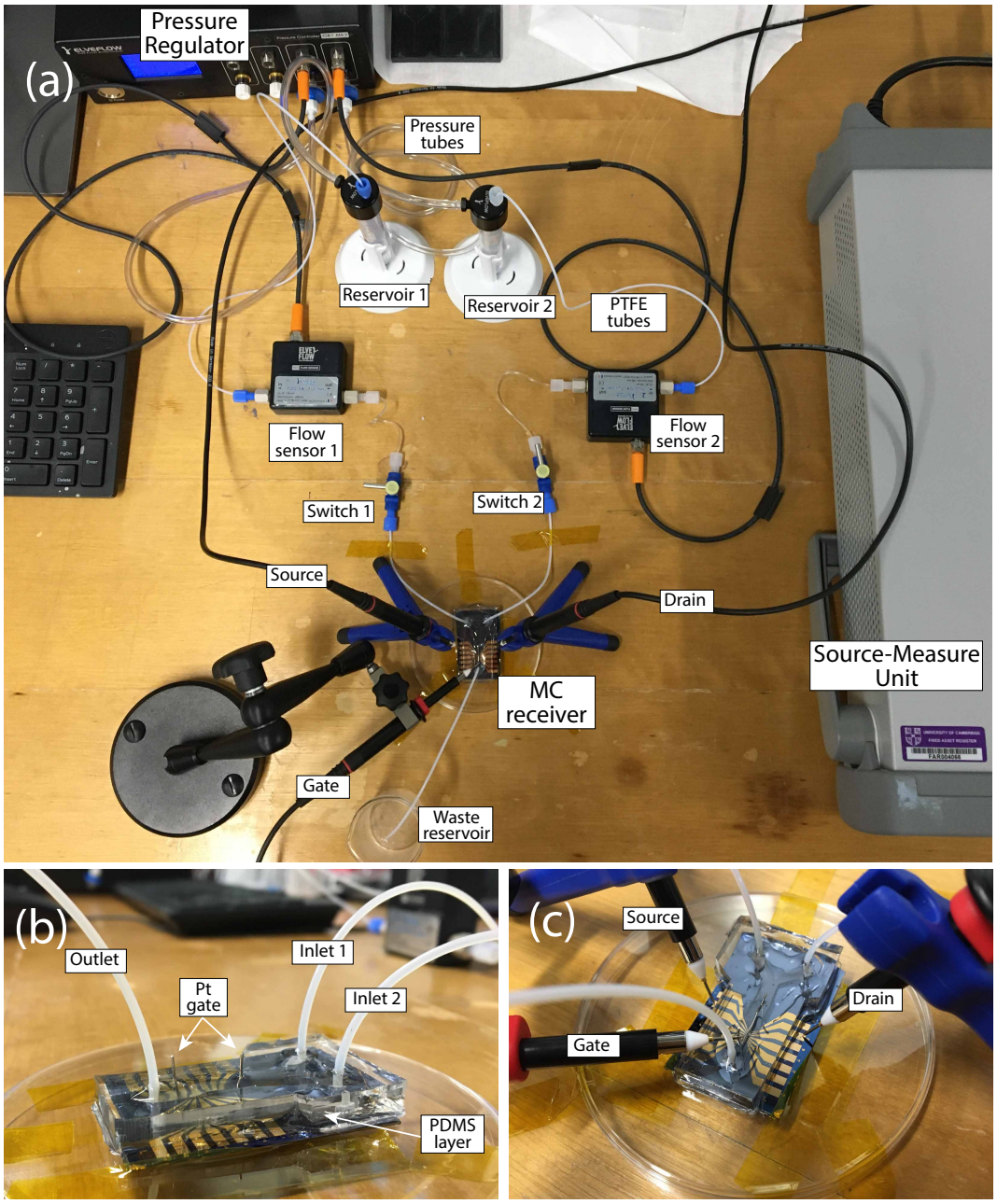

Fig. 7.8 (a) Microfluidic measurement setup consisting of a 4-channel pressure regulator, a high-precision SMU, electrical probes and microfluidic accessories. (b) A closer look into the fabricated graphene-based MC receiver connected to the microfluidic setup. (c) Probe connections for electrical tests of the device.

The dimensions of the microfluidic channel together with the fluid flow rate and fluid properties determine the Reynolds number, which is a dimensionless variable indicating the fluid flow regime in the channel [176]. Reynolds number is the ratio of the inertial

forces to the viscous forces, and can be given by

$$\mathrm{Re} = \frac{\rho u D_H}{\mu}, \tag{7.1}$$

where ρ is the fluid density, u is the linear flow velocity of the fluid, μ is the viscosity of the fluid, and D_H is the hydraulic diameter, which can be obtained for rectangular channels as follows

$$D_H = \frac{4A_{ch}}{P}. \tag{7.2}$$

Here $A_{ch} = w_{ch} \times h_{ch}$ is the cross-sectional area of the channel, and $P = 2(w_{ch} + h_{ch})$ is the cross-sectional channel perimeter. In the sensing and communication experiments of this work, water-based solutions are flowed at a constant volumetric flow rate $u_V = 80$ μl/min. The linear flow velocity can then be obtained as $u = u_V/A_{ch} = 220$ μm/s. By using $\rho \approx 1000$ kg·m^{-3} and $\mu \approx 0.001002$ Pa·s for water, we can obtain the Reynolds number for the microfluidic MC system as $\mathrm{Re} = 0.4839$, indicating a strong laminar flow regime, where viscous forces overcome the inertial forces resulting in non-crossing, parallel streamlines [176].

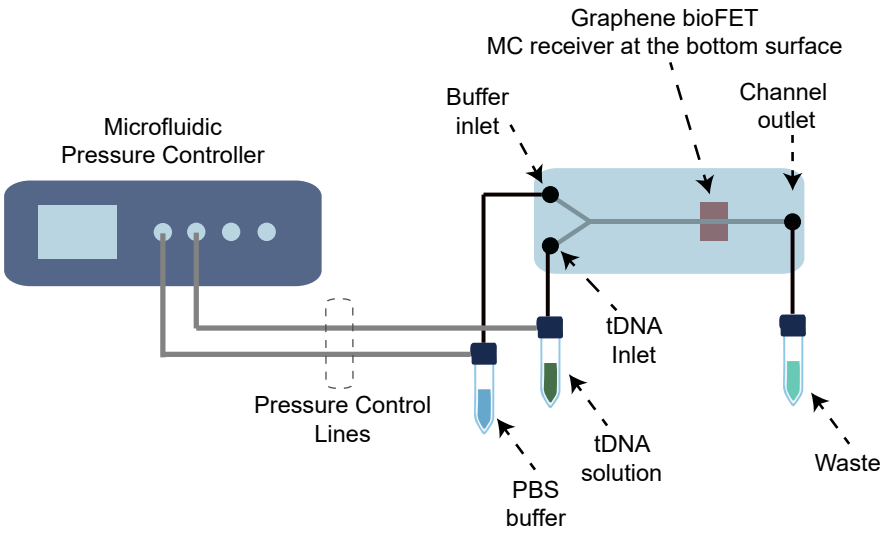

Fig. 7.9 Conceptual drawing of the microfluidic measurement setup with the practical implementation shown in Fig. 7.8

Microfluidic Setup

For functionalisation and electrical characterisation in the next steps, the device was connected to a microfluidic test setup, as shown in Fig. 7.8. The setup consists of a pressure regulator (OB1 MK3 - Microfluidic flow control system, obtained from Elveflow) with four pressure outlets, two of which are connected to fluid reservoirs through the pressure inlets. The fluid outlets of the fluid reservoirs are connected to the device through PTFE tubing.

Throughout the bio-functionalisation, sensing and communication experiments, microfluidic flow sensors are partly utilised for feedback-controlled modulation of the inlet pressure, and mechanical flow switches are used in cases where immediate stop/start of the microfluidic flow is required.

7.2.3 Functionalisation of GFET

Due to its one atomic thickness and 2d structure, the electronic properties of the pristine SLG is highly sensitive to the biochemical environment in the vicinity of its surface. Therefore, it suffers from low-level selectivity. On the other hand, in order to suppress the interference from other biochemical processes in physiologically relevant applications of the MC receiver, selectivity against information-carrying molecules is a must. Selectivity of the graphene can be realised through bio-functionalisation with recognition elements such as DNA and antibodies. As ssDNAs are preferred as target information-carrying molecules, i.e., tDNAs, in this work, the fabricated GFET is functionalised with probe DNAs (pDNAs), which are complementary to tDNAs.

For increasing the strength of the probe DNA immobilisation, and reducing the effect of nonspecific binding, the pristine SLG channels are first functionalised with 1-Pyrenebutyric acid N-hydroxysuccinimide ester (PBASE, obtained from Cambridge Bioscience Ltd), which has been widely utilised in the literature as linker molecules between graphene surface and DNA molecules [89, 97, 147, 222]. PBASE is an aromatic molecule having an aromatic pyrenyl group and an amine-reactive succinimide group (Fig. 7.10(a)). PBASE exhibits a strong affinity towards SLG as its aromatic pyrenyl group interacts with the basal plane of graphene through π-π interactions resulting in a strong noncovalent binding (Fig. 7.10(b)). The noncovalent attachment of the PBASE does not alter the inherent electronic structure and physical properties of the graphene [223]. For the functionalisation of the SLG with PBASE molecules, 10 mM solution of PBASE in N,N-Dimethylformamide (DMF, anhydrous, 99.8%, obtained from Sigma-Aldrich) is prepared in a glass bottle, and sonicated for 30 seconds for mixing. The prepared

PBASE/DMF solution is flowed through the microfluidic channel until the entire channel is filled with the solution. Then the flow is stopped, and the SLG channels are exposed to steady PBASE/DMF solution for 2 hours. After functionalisation with PBASE, unbound PBASE molecules are removed from the channel with pure DMF, followed by rinsing with phosphate buffered saline (PBS, pH 7.4).

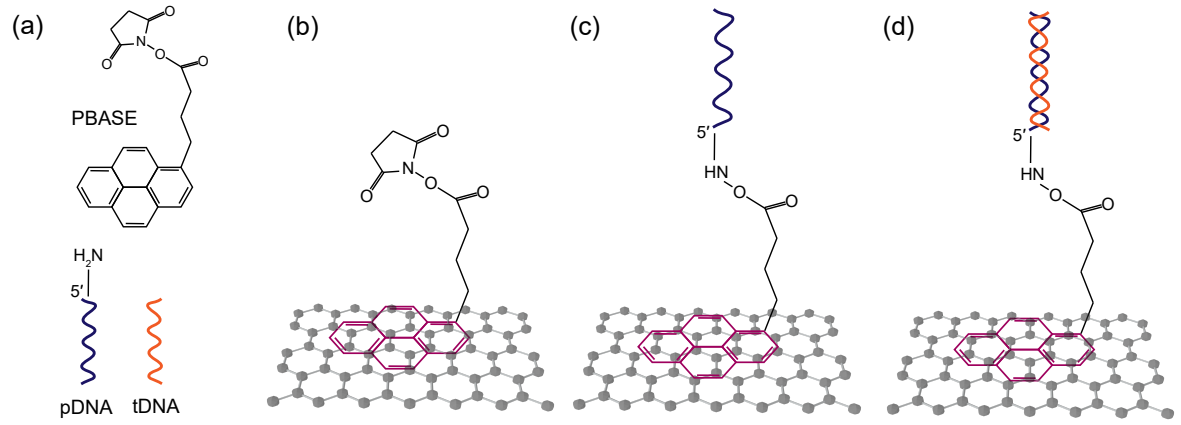

Fig. 7.10 (a) Molecular structure of PBASE, and conceptual drawing of probe DNA (pDNA) and complementary target DNA (tDNA). (b) Noncovalent binding of PBASE to graphene via $\pi - \pi$ interaction. (c) Immobilisation of pDNA via conjugation reaction with the succinimide group of PBASE. (d) pDNA-tDNA hybridisation.

The next step is the immobilisation of 18-mer 5'-amine-modified probe DNAs, which have the base sequence H_2N-$(CH_2)_6$-5'-AGG ACT TCA CCG TAT TGC-3'. The DNAs are custom designed and obtained from Sigma Aldrich. 2 μM of probe DNAs, prepared in PBS, is flowed through the microfluidic channel over the SLG channels. The device is left for immobilisation with probe DNAs overnight at 4 °C inside a wet chamber following the recipe given in [97]. The amine group of the pDNA reacts with the succinimide group of PBASE through conjugation reaction (Fig. 7.10(c)). The excess pDNA is then removed from the channel with PBS rinsing. Note that although the ssDNAs and the double-stranded DNAs (dsDNAs) shown in Figs. 7.10(c)-(d) are depicted as vertically aligned over the linker molecules, the orientation of DNAs tethered to surfaces through their single end can be influenced by the electrical potential of the surface, electrolyte flow conditions, the length of the DNAs, temperature, pH, ionic strength of the electrolyte, and the existence of the linker molecules. It is shown through molecular dynamics simulations that under zero potential of the surface and in the absence of the solution gate potential and the linker molecules, the flexible nature of the ssDNAs results in tilted and near-parallel orientation on the surface [224]. On the other hand, dsDNAs attain

more vertical alignment under zero potential due to their higher rigidity [224]. However, to the best of author's knowledge, the effect of the solution gate potential and the linker molecules has not been studied in the literature.

After pDNA immobilisation, the passivation of the unbound PBASE molecules is necessary to prevent nonspecific binding of target DNAs (tDNAs). This is performed by flowing 100 mM ethanolamine ($NH_2CH_2CH_2OH$) solution prepared in DI water through the microfluidic channel. Ethanolamine reacts with amine-reactive succinimide group of unbound PBASE molecules. With the passivation of PBASE, the device becomes ready for sensing and communication experiments with tDNAs.

7.3 Characterisation of MC Receiver

The fabricated MC receiver is characterised by optical and electrical means.

7.3.1 Optical Characterisation

The optical characterisation of the MC receiver is performed at each step of functionalisation by means of Raman spectroscopy, which is a powerful characterisation tool providing a wide range of information about the quality of graphene, number of layers, doping level, and type of defects [225]. In this work, all spectra are measured using a Renishaw InVia integrated with a 50× objective at 514 nm wavelength. The laser power is fixed below 1 mW to prevent any heating damage on the sample. The results are shown in Fig. 7.11.

Raman spectrum of the wet-transferred CVD-grown SLG on Si/SiO_2 substrate shows the characteristic 2D and G peaks of pristine graphene at Pos(2D) $\approx$ 2690 cm^{-1} , Pos(G) $\approx$ 1588 cm^{-1}, respectively. Single-Lorentzian shape of the 2D peak confirms the single layer nature of the CVD-grown graphene [226]. Then, the PBS electrolyte is drop-cast on the transferred SLG. Raman spectrum is taken after the drop-cast PBS is dried under N_2. No major change is observed compared to the Raman spectrum of the SLG, confirming that the PBS electrolyte does not cause any defect or doping. On the other hand, after functionalisation with PBASE, a new peak at $\sim$1621.5 cm^{-1} is observed, which can be attributed to the pyrene group resonance [89]. The other peak at $\sim$1344 cm^{-1} indicates the D mode, which requires defects to be activated. The presence of D peak, which is consistent with the previous reports [89, 97], shows that the noncovalent functionalisation of PBASE introduces moderate level of defects on the SLG surface. This was previously assigned to the disorders caused by the orbital hybridisation of the PBASE molecules with the graphene plane [89].

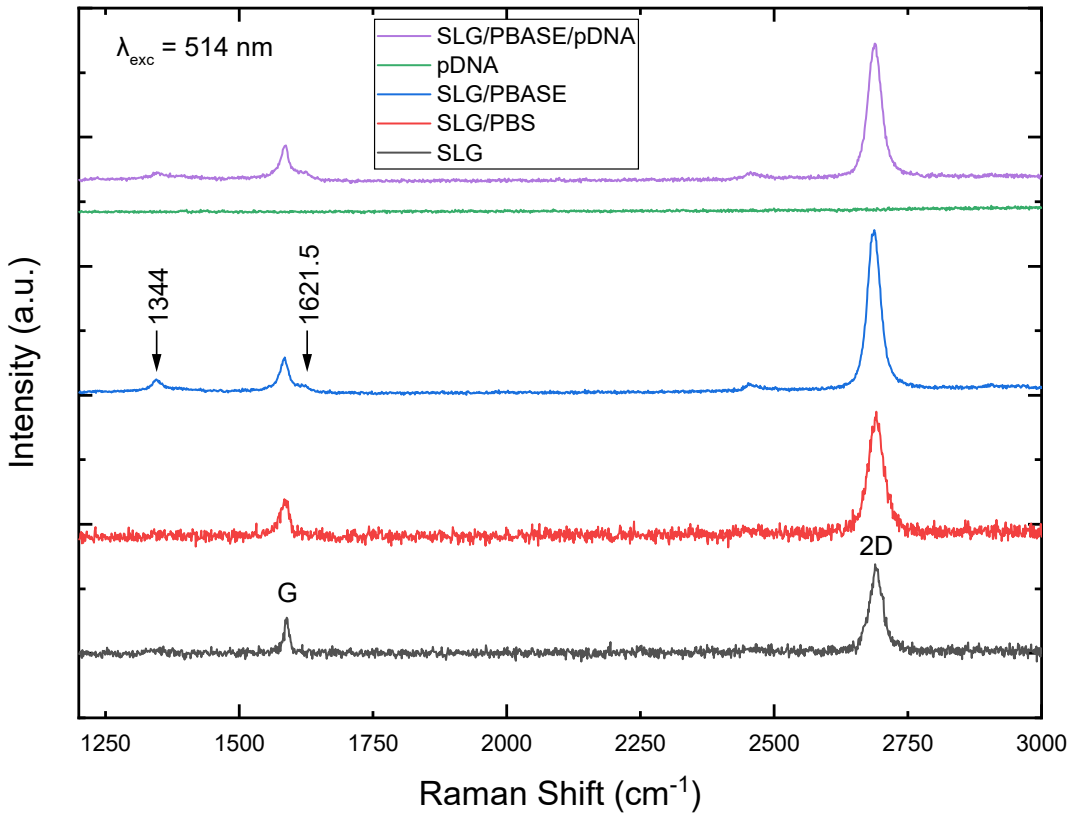

Fig. 7.11 Raman spectra at 514 nm for the SLG on Si/SiO_2 substrate (black), after the application of the PBS electrolyte and drying (red), after the functionalisation with the PBASE linker (blue), and after the immobilisation of the pDNAs (purple). Raman spectrum of the pDNA molecules drop-cast on Si/SiO_2 substrate is also shown (green). All spectra except the one for pDNA on Si/SiO_2 (green) are normalised to the intensity of the G peak, I(G).

After the immobilisation of the pDNA molecules by the conjugation reaction with the PBASE linkers, no new peak is observed. This result is confirmed by the Raman spectrum of the pDNA molecules directly drop-cast on the Si/SiO_2 substrate, which also shows no spectral peak. Further investigation performed by measuring the absorbance spectrum of the pDNA molecules (shown in Fig. 7.12), reveals that the absorbance of the DNA molecules at wavelengths greater than 300 nm is very weak. This is consistent with the previous reports showing that the DNA absorbance is peaked around 260 nm [227]. Therefore, we can conclude that the immobilised pDNA molecules are not excited enough at 514 nm radiation, resulting in no discernible peak in the Raman spectra. Proper Raman characterisation of the pDNA immobilisation requires excitation at wavelengths shorter than 300 nm, which could not be realised during this PhD work. However,

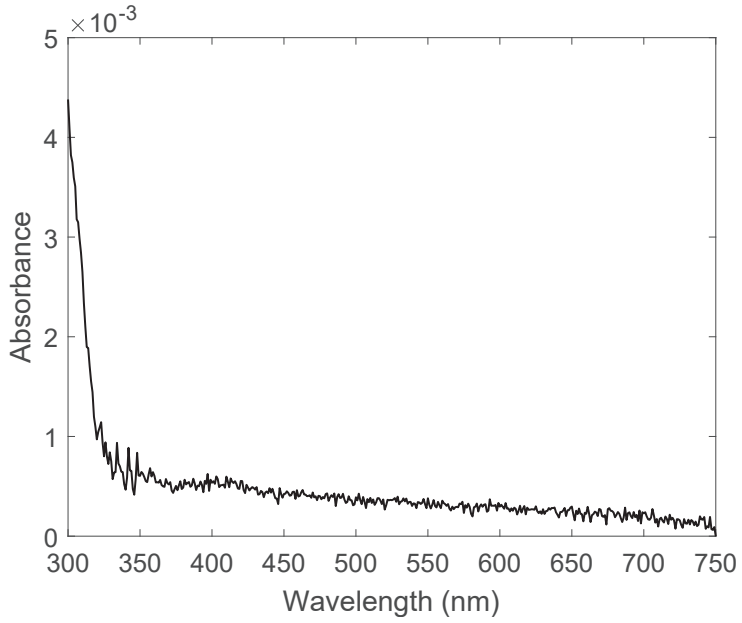

Fig. 7.12 Absorbance spectrum of pDNA molecules, taken with 3 μM pDNA solution in PBS. The spectrum is shown after subtraction of the absorbance spectrum of PBS.

further measurements at this range of excitation wavelengths are ongoing. On the other hand, the electrical characterisation provided in the next section already confirms the immobilisation of the pDNA molecules.

7.3.2 Electrical Characterisation

For the electrical characterisation of the fabricated devices, direct-current (DC) measurements are taken using a high-precision source measure unit (SMU, Keysight B2902A), which is connected to the device electrodes via high-impedance passive probes, as shown in Fig. 7.8.

On the other hand, the mobility of the GFET channels is measured before functionalisation in a back-gate configuration using EverBeing probe station. Based on the linear approximation of the transfer curve, the mobility is calculated as (240.62 ± 23.47) $\mathrm{cm}^2/\mathrm{V{\cdot}s}$.

Transfer Characteristics

After each step of functionalisation, transfer characteristics of the devices are obtained with a constant drain-to-source bias $V_{ds} = 100$ mV, and a solution gate potential V_g varying between -0.2 V and 1.2 V. The sweep rate of V_g is set to 140 mV/s. All data are

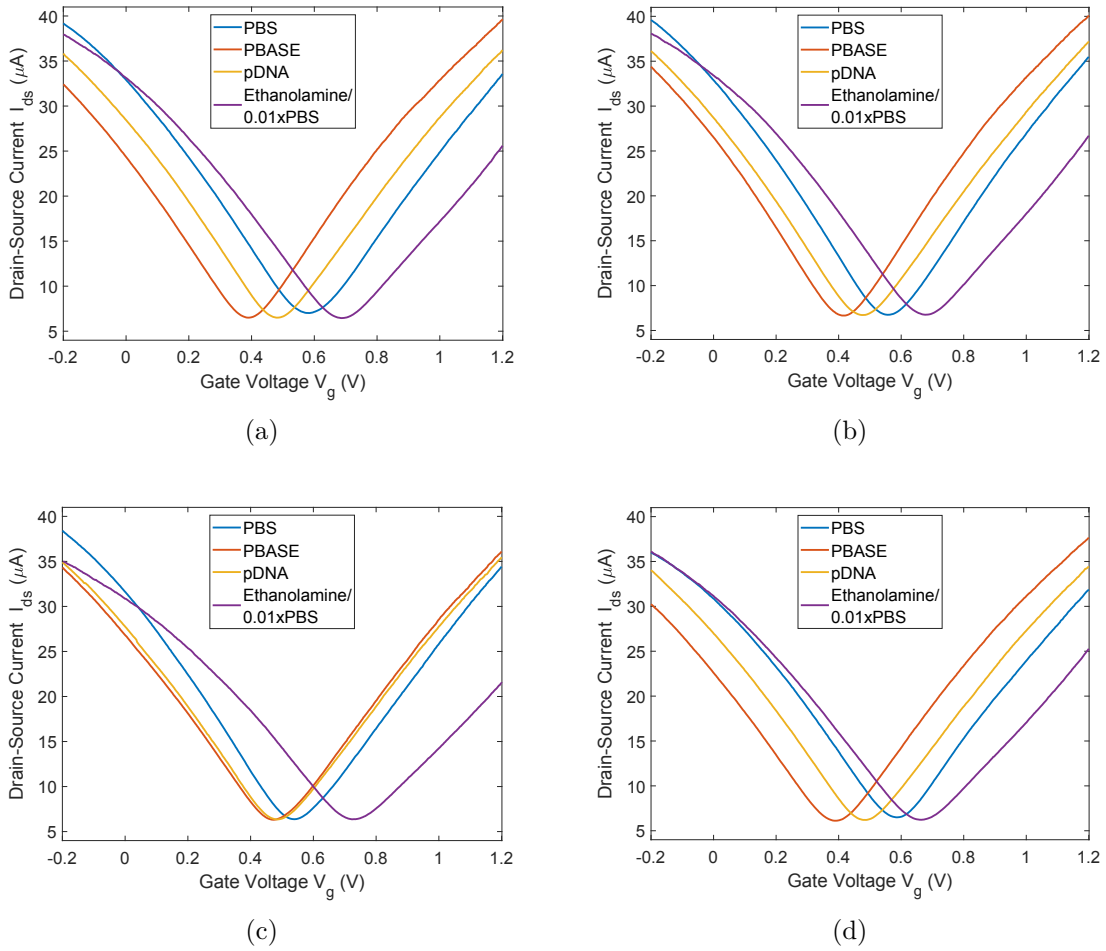

Fig. 7.13 Transfer characteristics of four channels at different steps of functionalisation in terms of drain-source current I_{ds} as a function of varying gate voltage V_g with sweep rate 140 mV/s. In all measurements drain-source voltage is held constant at $V_{ds} = 0.1$ V.

obtained after removal of excessive functional molecules from the microfluidic channel and the SLG surfaces by rinsing with PBS. This ensures that no change occurs in transfer characteristics due to ongoing chemical reactions. The PBS (pH 7.4) is used as the electrolyte in all measurements of transfer characteristics.

The measurements are taken from four of the SLG channels in the MC receiver, and results are provided in Fig. 7.13. Hysteresis was negligible for all channels (see Fig. 7.14), thus, only the forward sweep of V_g is demonstrated. First measurement is taken with only the PBS electrolyte inside the microfluidic channel prior to the functionalisation process. The p-type behaviour and ambipolar characteristics of the SLG-based devices are revealed with the charge neutrality point (CNP), i.e., the gate voltage of the minimum

conductance, observed at ∼0.57 V on average over four channels with a standard deviation of ∼0.02 V. Upon functionalisation with PBASE linker, a negative shift of the CNP by 150 ± 61 mV is observed, indicating n-type doping. The negative shift of the CNP after the PBASE functionalisation was previously attributed to the dominance of the n-type doping effect of DMF in competition with the p-type doping effect of the PBASE molecules over long incubation times [223, 228]. Note that the large standard deviation of the CNP shift is mostly resulting from the atypical behaviour observed in the third GFET channel, the transfer characteristics of which are demonstrated in Fig. 7.13(c). In this channel, only 67 mV-shift in CNP is observed with the functionalisation of PBASE. The significantly smaller shift compared to other channels, which manifest consistent transfer characteristics, can be indicative of the poor functionalisation of the PBASE linkers on this particular GFET channel. The poor functionalisation can be due to the residual polymers or insulator material on the graphene surface remaining from the fabrication process and preventing the non-covalent attachment of the PBASE molecules.

On the other hand, the immobilisation of pDNAs resulted in a positive shift of the CNP in consistence with the previous literature [89]. DNA molecules are negatively charged at pH 7.4, attracting hole carriers to the graphene surface, thus, contributing to the p-type doping [89]. The shift of the CNP is observed as 66 ± 41 mV over the four channels. Again, the large standard deviation can be attributed to the third channel given in Fig. 7.13(c), where the CNP shift is only 11 mV. This is again indicative of the poor functionalisation of the PBASE molecules, which in turn results in a very low concentration of immobilised pDNAs. Other channels, on the other hand, show similar CNP shifts, indicating more consistent immobilisation of DNAs.

The last measurements are taken after the passivation of excess PBASE linkers with the ethanolamine, and the introduction of the 0.01xPBS to the microfluidic channel to be used for the following sensing and communication experiments. 0.01xPBS is the 100-fold diluted version of PBS with DI water (18.2 MΩ·cm). While the ethanolamine does not possess any charge, the observed positive shift of the CNP is consistent with the previous literature reporting increased p-type doping with decreasing ionic concentration of the buffer solution [229]. Also note that in all of the measured GFET channels, a mobility reduction is observed upon passivation with ethanolamine in 0.01xPBS. The reason for switching to the diluted version of PBS for sensing and communication experiments is to decrease the effect of the Debye screening for enhancing the sensitivity of the device for the hybridisation events on the SLG surface. Note that in all measurements, leakage current I_{gs} has been detected to be under 15 nA, and therefore, its effect on the transfer

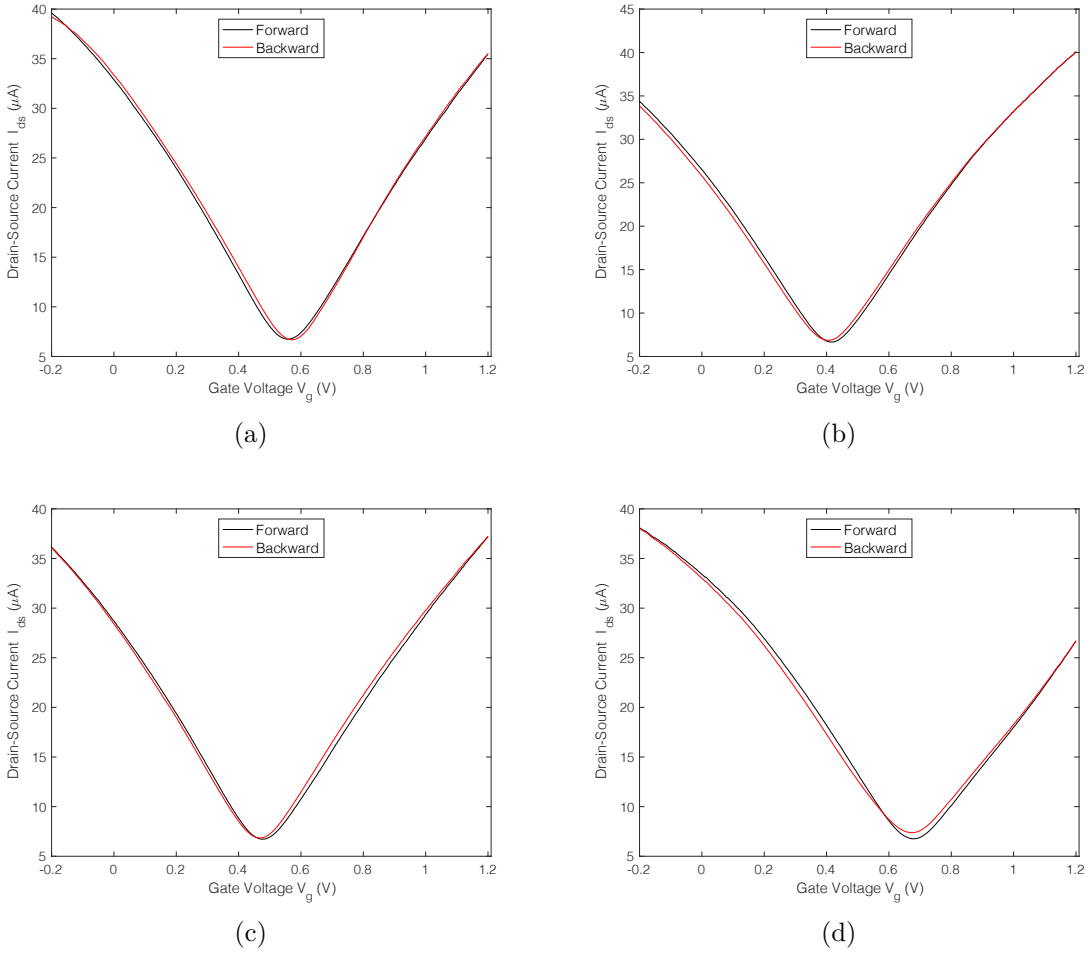

Fig. 7.14 Transfer characteristics of four channels at different steps of functionalisation in terms of drain-source current I_{ds} as a function of varying gate voltage V_g with sweep rate 140 mV/s. In all measurements drain-source voltage is held constant at $V_{ds} = 0.1$ V.

curve characteristics is negligible. The leakage current measurements are reported in Fig. 7.15.

With the help of the transfer characteristics, we can deepen our analysis by determining the surface density of the immobilised pDNAs. To this end, we need to first determine the electrolyte gate capacitance, which can be approximated by the overall capacitance of three parallel plate capacitors connected in series:

$$C_G = \left(\frac{1}{C_{Gr}} + \frac{1}{C_{Pt}} + \frac{1}{C_Q} \right)^{-1}, \tag{7.3}$$

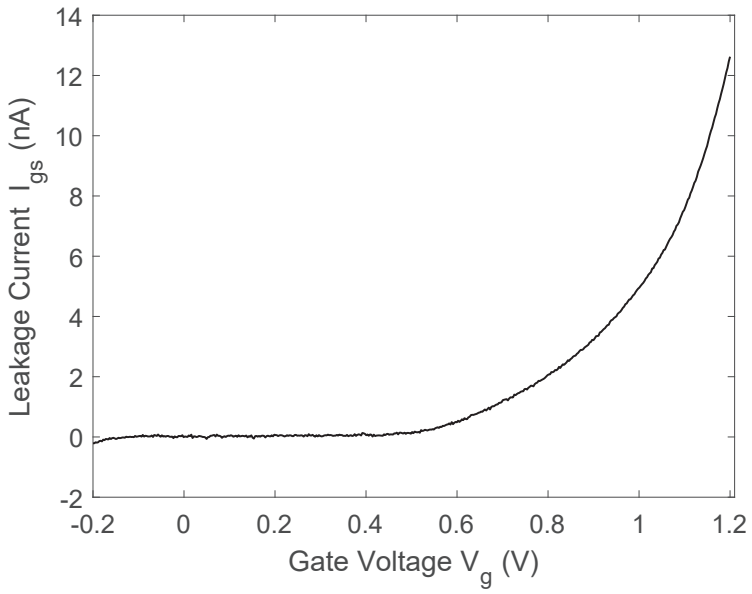

Fig. 7.15 Leakage current analysis of the MC receiver: Gate-source current I_{gs} with varying gate voltage V_g.

where C_{Gr} is the EDLC between the graphene and the electrolyte, C_{Pt} is the EDLC between Pt gate electrode and electrolyte, and C_Q is the quantum capacitance of graphene [89]. The EDLC of graphene to electrolyte can be calculated as $C_{Gr} = A_{Gr}\epsilon_r\epsilon_0/\lambda_D$, with $A_{Gr} = 40\ \mu\text{m}\times 100\ \mu\text{m} = 4\times 10^3\ \mu\text{m}^2$ being the area of graphene surface exposed to electrolyte, ϵ_0 is the vacuum permittivity, and ϵ_r is the relative permittivity of PBS electrolyte, which is only slightly lower than the one of water, thus, taken as $\epsilon_r \approx 80$ [89, 230]. Lastly, λ_D is the Debye length which gives the thickness of the EDLC, and it can be approximated in aqueous solutions as $\lambda_D \approx 0.3/\sqrt{\rho_{ion}}$ in nm, with ρ_{ion} being the ionic density in M [231]. For 1xPBS buffer, the ionic density is ~150 mM, thus, $\lambda_D \approx 0.77$ nm. The resulting EDLC for graphene is $C_{Gr} \approx 3.68$ nF. The EDLC between the Pt electrode and the electrolyte can be obtained similarly as $C_{Pt} = A_{Pt}\epsilon_r\epsilon_0/\lambda_D$. However, since the surface area of the Pt wire inside the electrolyte ($A_{Pt} = l_{Pt}d_{Pt}\pi/2 = 1$ cm$\times$0.5 mm$\times\pi/2 = 7.85\times 10^6\ \mu\text{m}^2$, calculated as the area of an half sphere of 1cm-length and 0.5mm-diameter) is significantly larger than the graphene surface area ($A_{gr} = 4\times 10^3\ \mu\text{m}^2$), C_{Pt} can be neglected. Lastly, the quantum capacitance of graphene per unit area has been reported as $c_q \approx 2\ \mu\text{F}\cdot\text{cm}^{-2}$ [89, 232], which gives $C_Q = c_q \times A_{gr} = 8\times 10^{-2}$ nF. The overall gate capacitance given by (7.3) then becomes $C_G \approx 7.83\times 10^{-2}$ nF.

The effective electric charge of a single immobilised 18-mer pDNA screened by the EDL can be written as

$$q_{pDNA} = 18 \times q_e \times e^{-r/\lambda_D}, \tag{7.4}$$

where q_e is the elementary charge, r is the effective length of the pDNA taken as the half of its length, i.e., $r = 18(\text{basepairs}) \times 0.34(\text{nm/basepair}) \times 1/2 = 3.06$ nm, by assuming a vertical orientation for the single-stranded pDNAs following the analysis in [89], where similar solution gate potentials and the same type of linker molecules are used.

Finally, the surface density of the immobilised pDNAs can be written as a function of the average shift in V_{CNP} upon pDNA functionalisation:

$$n_{pDNA} = \frac{\Delta V_{CNP} C_G}{q_{pDNA} A_{gr}}, \tag{7.5}$$

which gives $n_{pDNA} \approx 2 \times 10^3$ μm^{-2}. A similar surface density ($\sim 1.14 \times 10^3$ μm^{-2}) for pDNA was previously reported in [89].

Sensing Response

For determining the sensing characteristics of the MC receiver, complementary 18-mer target DNA (tDNA: 5'-GCA ATA CGG TGA AGT CCT-3', obtained from Sigma Aldrich) is prepared in 0.01xPBS solution. tDNAs of varying concentrations (50 nM, 100 nM, ... 10 μM) are successively flowed through the microfluidic channel in the order of increasing concentration, and I_{ds} is recorded in real time with $V_{ds} = 100$ mV and $V_g = 0$ V. During the experiment, the volumetric flow rate is held constant at $u_V = 80$ μl/min. The results of the measurements are provided in Fig. 7.16(a), where a decrease in the drain-source current is observed with increasing tDNA concentration, implying n-type doping effect in contrast to the p-type doping of pDNAs. The n-type doping effect upon target DNA hybridisation or probe DNA immobilisation was previously reported in [97, 123, 142, 147, 148, 228], where the effect is mainly attributed to the partial interaction of the DNAs with the graphene surface through $\pi - \pi$ stacking of the nucleobase aromatic rings resulting in direct electron transfer to graphene instead of electrostatic gating. The electron transfer from DNA upon immobilisation was also reported for CNT transistors [233]. Moreover, it is known that DNA molecules immobilised on a surface with their single end can be stretched in parallel to the surface under lateral flow [234], and the extent of this conformational change can be increased by a positive surface potential attracting the negatively charged DNA molecules to the surface [148, 224]. Note that

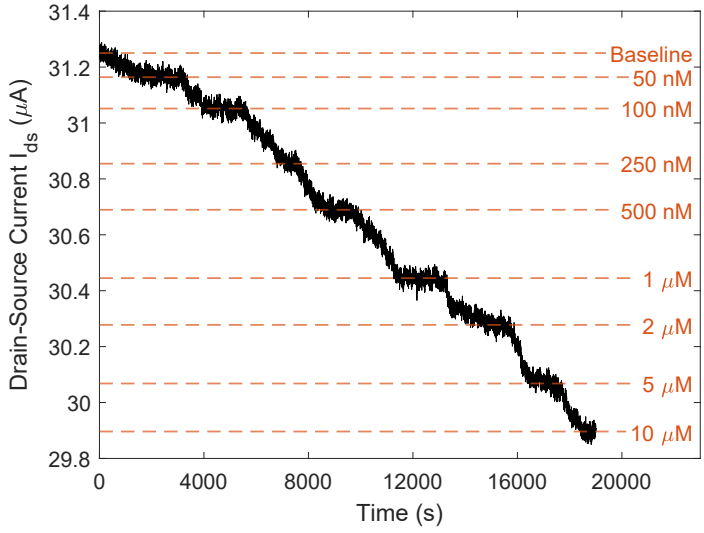

(a)

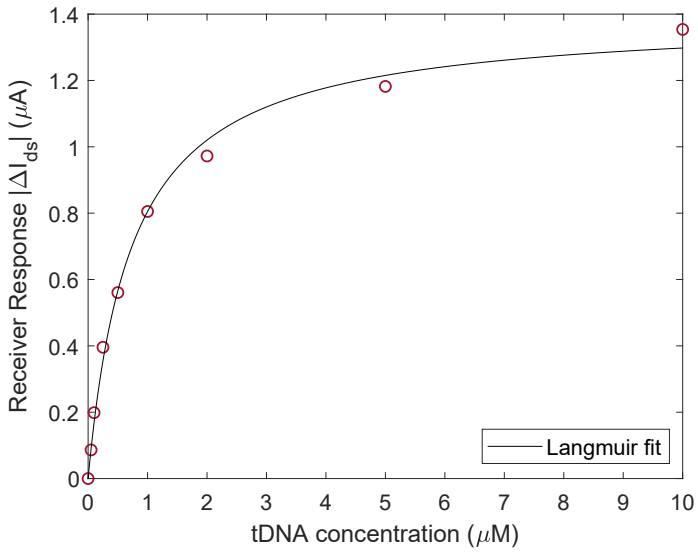

(b)

Fig. 7.16 (a) Real-time sensing response of the MC receiver in terms of drain-source current I_{ds} with varying concentration of complementary target DNAs (tDNAs). (b) Equilibrium sensing response fitted by the Langmuir adsorption isotherm. Resulting dissociation constant for pDNA-tDNA hybridisation is $K_D = 730$ nM.

in my case, the graphene surface is continuously exposed to a positive drain-source bias during the sensing measurements. Therefore, I speculate that the conformational change resulting from microfluidic flow, hybridisation, and the positive surface charge of graphene brings the hybridised DNA molecules closer to the graphene surface, causing

their partial interaction and electron transfer. Also, compared to the measurements taken with the single-stranded pDNAs under no-flow conditions, the ionic strength of the electrolyte (0.01×PBS), in which the sensing experiments are performed, is significantly lower (compared to 1×PBS), such that the attractive electrostatic force caused by the positive surface potential extends more into the electrolyte without being significantly screened [235]. Given that the hybridised dsDNAs carry twice the amount of negative charge of the ssDNAs, it can be considered that the hybridised pDNA-tDNA pairs, in my case, are more strongly attracted to the graphene surface compared to pDNAs [236]. The stronger electrostatic attraction combined with the stretching effect of lateral microfluidic flow supports my argument. However, this requires further confirmation, potentially through molecular dynamics simulations of both ssDNAs and hybridised dsDNAs under similar conditions to understand the effect of lateral flow, surface potential, solution-gate potential, and the linker molecules.

Each working concentration of tDNAs were propagated in the channel until I_{ds} reaches a plateau. The value of I_{ds} at these plateaus are used to construct the sensing response graph of the MC receiver, which is provided in Fig. 7.16(b). The response curve is fitted by the Langmuir adsorption isotherm, i.e.,

$$\Delta I_{ds}/\Delta I_{ds,sat} = \frac{1}{1 + K_D/C_{tDNA}}, \tag{7.6}$$

where $\Delta I_{ds,sat}$ is the receiver response in saturation, which occurs when all the probe DNAs are hybridised. K_D is the dissociation constant of pDNA-tDNA hybridisation, and C_{tDNA} is the applied concentration of tDNAs. The curve fitting gives the dissociation constant as $K_D = 730$ nM for the DNA hybridisation on the fabricated MC receiver, and the receiver response at saturation as $\Delta I_{ds,sat} = 1.393$ μA.

Specificity

The specificity of the MC receiver against the complementary tDNAs is evaluated by comparing the receiver's response to different ssDNAs, which are not complementary to the pDNAs. The ultimate specificity can be determined with the application of an ssDNA having only one single base-pair mismatch. For this, I use 18-mer ntDNA_1 with the base sequence 5'-GCA ATA CGG CGA AGT CCT-3', which has the mismatch in its 10^{th} base pair, where T to C mutation occurs. Another test is performed with the application of 18-mer ntDNA_2 (5'-GCA CGT CGG CGT CGT CAT-3'), which has 7 base-pair mismatches. Complementary tDNA is also applied for comparison. All DNAs are dissolved in 0.01xPBS with 1 μM working concentration. The measurement results

Table 7.1 Kinetic constants of DNA hybridisation measured by MC receiver

DNA	**Sequence**	**Binding rate k^+ ($\mathbf{M^{-1}s^{-1}}$)**	**Unbinding rate k^- ($\times$ 10^{-4} $\mathbf{s^{-1}}$)**	**Dissociation constant K_D ($\times$ 10^{-6} M)**
tDNA	5'-GCA ATA CGG TGA AGT CCT-3'	1814.9	13.538	0.746
ntDNA$_1$	5'-GCA ATA CGG CGA AGT CCT-3'	355.3	12.454	3.506
ntDNA$_2$	5'-GCA CGT CGG CGT CGT CAT-3'	48.9	13.110	26.829

before and after a moving mean filter of 21-second window length is applied are provided in Fig. 7.17(a).

The response curve of the MC receiver for different DNAs is fitted by the Langmuir model of adsorption to determine the kinetic rates of the DNA hybridisation for the three DNA sequences. The solution of the Langmuir model gives the time-varying response of the MC receiver during the association and dissociation phases of DNA hybridisation [89] as follows

$$\Delta I_{ds}(t) = \Delta I_{ds,eq}\left(1 - e^{-(k^+ c_{in} + k^-)t}\right), \text{for} \quad 0 \leq t \leq t_d, \tag{7.7}$$

$$\Delta I_{ds}(t) = \Delta I_{ds}(t_d) e^{-k^- t}, \text{for} \quad t > t_d, \tag{7.8}$$

where, c_{in} is the input concentration, which is set to $c_{in} = 1$ μM for all DNAs. t_d denotes the time of dissociation, and $\Delta I_{ds,eq}$ is the asymptotic value of the sensing response, which occurs when the hybridisation reaches equilibrium. The variables to be fitted are the binding rate k^+, unbinding rate k^-, and $\Delta I_{ds,eq}$. The fitted response is plotted in Fig. 7.17(b), and the resulting kinetic rates are provided in Table 7.1, which shows that the binding rate of the target DNAs substantially decreases with increasing number of base-pair mismatches.

The nonlinear curve fitting gives the dissociation constant of the tDNA as $K_D(\text{tDNA}) = k^-(\text{tDNA})/k^+(\text{tDNA}) \approx 746$ nM, which is very close to the value obtained by the fitting of the sensor response, i.e., 730 nM. On the other hand I obtain higher dissociation constants for non-complementary DNAs, i.e., $K_D(\text{ntDNA}_1) = 3.506$ μM and $K_D(\text{ntDNA}_2) = 26.829$ μM, indicating the specificity of the MC receiver against the complementary tDNAs.

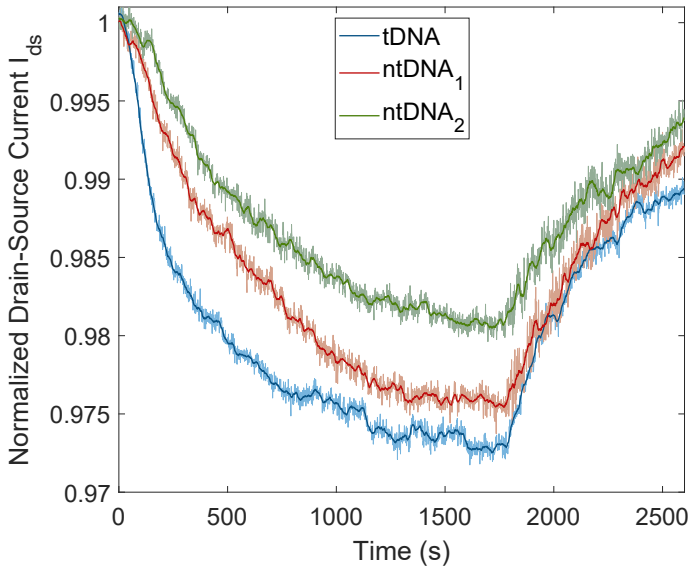

(a)

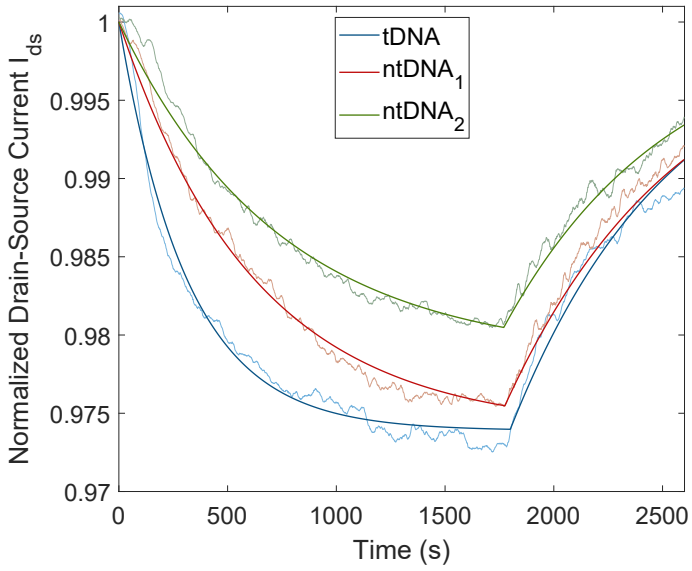

(b)

Fig. 7.17 Specificity analysis of the MC receiver. (a) Real-time sensing response for complementary tDNA, non-complementary ntDNA$_1$ with single base-pair mismatch, and non-complementary ntDNA$_2$ with 7 base-pair mismatches (see Table 7.1). At $t \approx 1800$ s, the DNA solutions are replaced with 0.01xPBS solution to allow dissociation of the hybridised DNAs. (b) Real-time sensing response fitted by the Langmuir adsorption/desorption model, equations (7.7)-(7.8).

7.4 Communication Performance

Time-varying communication experiments are performed in the microfluidic testbed to reveal the detection performance of the MC receiver. For these experiments, both inlets are utilised as shown in Fig. 7.8. One of the inlets is connected to the reservoir containing the 0.01xPBS buffer solution, and the other one is connected to the reservoir containing the tDNA solution in 0.01xPBS buffer. Manually controlled mechanical switches are utilised as they proved more effective in stopping the fluid flow into the channel than the digital control due to the fact that the pressure controller can drift out of calibration as the experiments progress. Accordingly, for the transmission of tDNAs, the buffer flow is rapidly stopped through the mechanical switch along the buffer line, and the tDNA line is opened at the same time. When the transmission ends, flow in the tDNA line is stopped, and the buffer flow is simultaneously started again by means of mechanical switching.

Time-varying Response

To determine the time-varying response of the receiver, varying length pulses of 1μM tDNAs are flowed through the microfluidic channel. The results of three independent measurements taken from the same channel are provided in Fig. 7.18(a) and Fig. 7.18(b) for 30-second and 60-second pulses, respectively. As with the previous cases, a 21-second-length moving mean filter is applied for each measurement.

The time-varying response of the MC receiver to finite-length concentration pulses can be described by the analytical microfluidic MC model developed in Chapter 3. This approximate model gives the receiver response in terms of number of bound receptors, i.e.,

$$\begin{aligned} N_R(t) =& N_{R,eq}\left(1-\frac{\mathcal{W}_0\left[\alpha^*\exp\left(\alpha^*-\beta^*(t-t_a)\right)\right]}{\alpha^*}\right)\Big(\Theta\left[t-t_a\right]-\Theta\left[t-t_d-\epsilon\right]\Big) \\ &-\gamma^*\mathcal{W}_0\left[-\frac{N_{R,0}}{\gamma^*}\exp\left(\frac{-k^+N_{R,0}-k_T^*k^-(t-t_d)}{k^+\gamma^*}\right)\right]\Theta\left[t-t_d-\epsilon\right], \end{aligned} \tag{7.9}$$

where t_a and t_d denote the start times of association (i.e., pDNA-tDNA hybridisation in this case) and dissociation phases, respectively, $N_R(t)$ is the number of bound receptors at time t, $N_{R,eq}$ is the number of bound receptors at equilibrium, $N_{R,0} = N_R(t_d)$ is the number of bound receptors when the dissociation starts. Here $\mathcal{W}_0[.]$ denotes the principal branch of the Lambert $\mathcal{W}$ function, and $\Theta[.]$ denotes Heaviside step function

with $\Theta[0] = 1$. The parameters α^*, β^* and γ^* are given in (3.37)-(3.39) as functions of $N_{R,max}$, which is the upper limit of the receiver response in terms of bound number of receptors. In theory, $N_{R,max}$ can be taken as equal to the total number of receptors. Lastly, the transport parameter k_T^* incorporating the effect of the microfluidic channel geometry and flow velocity on the molecular transport dynamics is given in (3.44).

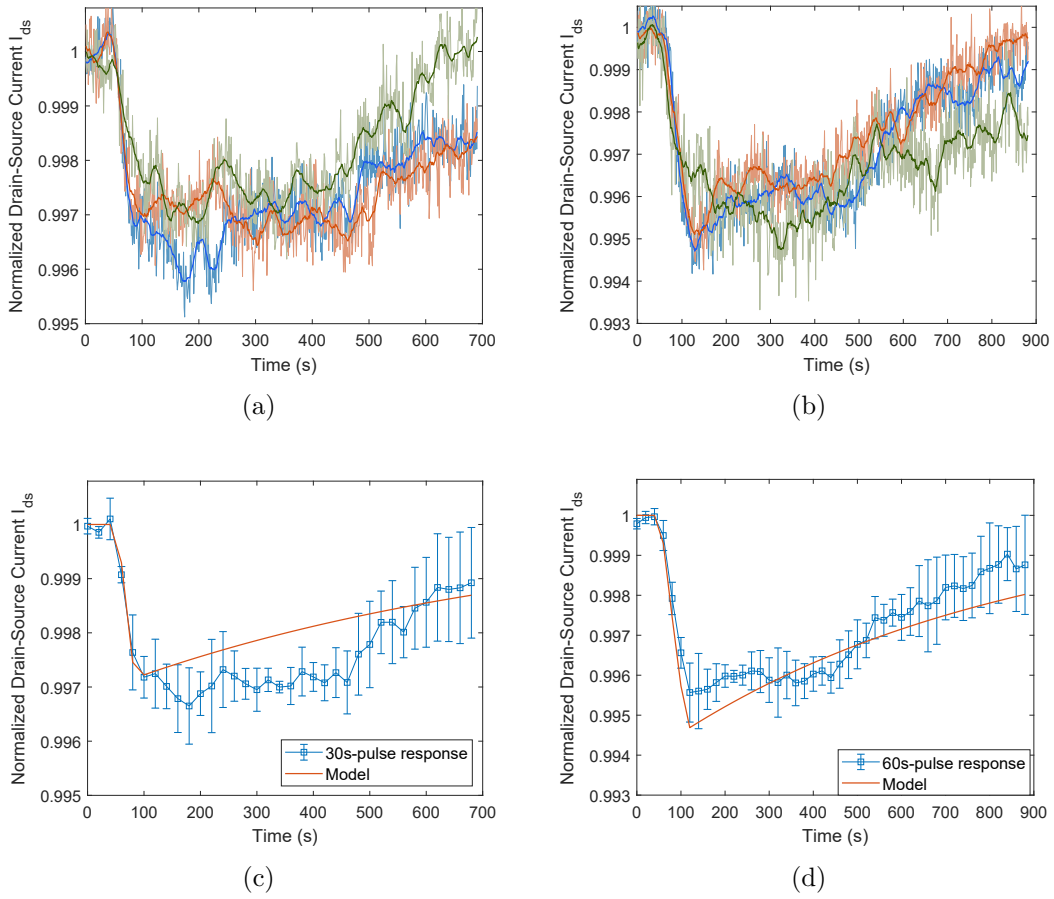

Fig. 7.18 Normalised pulse response of the MC receiver in terms of drain-source current I_{ds} with constant operating voltages set to $V_g = 0$ V and $V_{ds} = 0.1$ V. (a, b) Three independent measurements taken from the same channel for 30-second-long and 60-second-long 1 μM tDNA pulses, respectively. (c, d) Pulse responses fitted by the normalised output of the transformed model given in (7.13).

To use this model for fitting the electrical measurements obtained by the graphene-based MC receiver, we need to transform the variables in (7.9) to obtain a function of ΔI_{ds}. The number of bound receptors is proportional to the change in the drain-source

current through the following relation:

$$N_R(t) = \Delta I_{ds}(t)/Q_{tDNA}, \tag{7.10}$$

with $Q_{tDNA} = g_m \frac{q_{tDNA}}{C_G}$. Here, $g_m = \partial I_{ds}/\partial V_g$ is the transconductance of the device, q_{tDNA} is the effective charge of a single tDNA molecule, and $C_{G,0.01\text{xPBS}}$ is the total gate capacitance in 0.01xPBS buffer. Gate capacitance is obtained as $C_{G,0.01\text{xPBS}} = 6.58 \times 10^{-2}$ nF using (7.3) with the new Debye length in diluted PBS electrolyte, i.e., $\lambda_{D,0.01\text{xPBS}} = 7.75$ nm. The effective charge of a single tDNA is obtained similarly using (7.4) with $\lambda_{D,0.01\text{xPBS}}$. The transconductance of the device $g_m = \partial I_{ds}/\partial V_g$ before the communication experiments can be calculated by a linear approximation of the $V_g - I_{ds}$ curve around $V_g = 0$ V bias. Averaging over the transfer curves of the four graphene channels obtained at the last step of functionalisation in 0.01xPBS, shown in Fig. 7.13, I obtain $g_m \approx -28.0 \pm 2.9$ μA/V. Similarly, the following transformation is made:

$$N_{R,eq} = \Delta I_{ds,eq}/Q_{tDNA}. \tag{7.11}$$

Here, $\Delta I_{ds,eq}$ is the response of the receiver to 1 μM tDNA at equilibrium, and obtained from the sensing response given in Fig. 7.16 as $\Delta I_{ds,eq} = -0.805$ μA. Note that $N_{R,max}$ can also be calculated as a function of $\Delta I_{ds,eq}$ as follows

$$\begin{aligned} N_{R,max} &= ((c_{avg} + K_D)/c_{avg}) \times N_{R,eq} \\ &= ((c_{avg} + K_D)/c_{avg}) \times \Delta I_{ds,eq}/Q_{tDNA}, \end{aligned} \tag{7.12}$$

with the average tDNA concentration passing over the receiver surface c_{avg} given in (3.33), and the dissociation constant K_D for pDNA-tDNA pair given in Table 7.1. Accordingly, (7.9) can be rewritten by substituting (7.10), (7.11), and (7.12) into (7.9) as follows

$$\begin{aligned} \Delta I_{ds}(t) =& \Delta I_{ds,eq} \left(1 - \frac{\mathcal{W}_0\left[\alpha^* \exp\left(\alpha^* - \beta^*(t - t_a)\right)\right]}{\alpha^*}\right) \Big(\Theta\left[t - t_a\right] - \Theta\left[t - t_d - \epsilon\right]\Big) \\ &- \gamma^* Q \mathcal{W}_0\left[-\frac{\Delta I_{ds}(t_d)}{\gamma^* Q} \exp\left(\frac{-k^+ \Delta I_{ds}(t_d)/Q - k_T^* k^- (t - t_d)}{k^+ \gamma^*}\right)\right] \Theta\left[t - t_d - \epsilon\right], \end{aligned} \tag{7.13}$$

with the transformed parameters given as

$$\alpha^* = \frac{k^+ c_{avg} \Delta I_{ds,eq}/Q}{k^- \Delta I_{ds,eq}/Q + k_T^* c_{avg}}, \tag{7.14}$$

$$\beta^* = \frac{k^+ c_{avg} + k^-}{1 + \frac{k^- \Delta I_{ds,eq}/Q}{k_T^* c_{avg}}}, \tag{7.15}$$

$$\gamma^* = \frac{(c_{avg} + K_D)\Delta I_{ds,eq}/Q}{c_{avg}} + \frac{k_T^*}{k^+}. \tag{7.16}$$

The model developed in Chapter 3 includes many other input parameters concerning the microfluidic channel geometry and molecular transport dynamics. The linear flow velocity is already obtained as $u = 220$ μm/s by transforming the volumetric flow rate $u_V = 80$ μl/min. Diffusion coefficient of tDNAs is taken as $D_0 = 100$ μm^2/s, which is in the range of previously reported values for ssDNAs of similar lengths [237, 238].

For comparison to the empirical MC signals, the model response is normalised by the mean empirical baseline current ($I_{ds,baseline} = 31.25$ μA, as plotted in Fig. 7.16(a)), i.e.,

$$\hat{I}_{ds}(t) = (I_{ds,baseline} + \Delta I_{ds}(t))/I_{ds,baseline}. \tag{7.17}$$

The normalised output of the transformed model for pulse lengths $T_p = 30$ s and $T_p = 60$ s is shown in Fig. 7.18(c) and Fig. 7.18(d), respectively, presented in comparison to the mean of three independent measurements taken for each pulse length. The error bars represent the standard deviation of the measurements. We can observe that the approximate model is highly accurate in calculating the propagation delay and I_{ds} during the association phase. Although its accuracy is lower during the dissociation phase, it well captures the pulse amplitude and the pulse width, which are the two important parameters in evaluating the performance of a communication system. The same model will be applied in the next section for binary data transmission.

Data Transmission

To reveal the detection performance of the MC receiver, 20-bit-long pseudorandom binary information encoded into the concentration of tDNAs is transmitted through the microfluidic channel and detected by the fabricated MC receiver located at the bottom of the channel. Here bit-1 is represented by a 30-second pulse of 1 μM tDNA at the beginning of a bit interval, and bit-0 is represented by no pulse transmission during the entire bit interval, i.e., the buffer line stays connected into the microfluidic channel. The results are provided for bit intervals of 60-, 120-, and 360-second length in Fig. 7.19. As expected, the slow rate of dissociation of the bound tDNAs from the immobilised pDNAs results in a significant amount of intersymbol interference (ISI), which can potentially complicate the decoding at the receiver. The ISI is more pronounced for shorter bit intervals, i.e., higher transmission rates, such that the baseline could not find enough

time to recover. On the other hand, for 360-second-long bit interval (Fig. 7.19(c)), ISI is significantly lower and I_{ds} is able to return to the baseline.

Another important observation is that the propagation delay t_{delay} between the transmission time of the bit-1 and the receiver response is ∼55 seconds in each test, and the delay remains almost constant during the entire data transmission period. This implies that the application of a constant delay shift in the receiver response can be sufficient for the synchronisation of the receiver with the transmitter during the decoding process.

As the receiver response is away from saturation in the performed tests, we can assume that the response is linear and time-invariant (LTI). Based on this assumption, we can reconstruct the received signal by applying the superposition principle of LTI systems in the approximate model developed in Chapter 3. Accordingly, using (7.13), the received signal can be written as

$$R(t) = \sum_{i=1}^{L} s[i] \Delta I_{ds} \left(t - t_{transmit} - (i-1)T_b\right), \tag{7.18}$$

where $L = 20$ is the number of transmitted bits, $t_{transmit}$ is the start time of transmission, T_b is the bit interval, and $s[i] \in \{0, 1\}$ is the i^{th} transmitted bit. Similar to (7.17), the model response is normalised by the mean empirical baseline current ($I_{ds,baseline} = 31.25$ μA), i.e.,

$$\hat{I}_{ds}(t) = (I_{ds,baseline} + R(t))/I_{ds,baseline}. \tag{7.19}$$

The normalised model response is plotted in Fig. 7.19 over the empirical MC signal for varying bit intervals. We can see that the approximate model is very accurate in capturing the transmission delay and the overall trend of I_{ds}, although it is not able to exactly reconstruct the original signal. The deviations can largely be attributed to the LTI approximation in writing (7.18), which neglects the effect of previously transmitted bits on the received signal corresponding to the current bit.

Based on the observation of constant delay during data transmission, the delay-shifted version of the bit intervals is indicated with dashed lines in Fig. 7.20 with the transmitted bits written inside each bit interval. As the envisioned MC applications demand low-complexity communication techniques due to the resource and size limitations of the communicating nanodevices, constant threshold detection has been favoured in the literature. In this scheme, the received signal is sampled at a predefined sampling time instant, and its amplitude is compared to a threshold value for deciding between

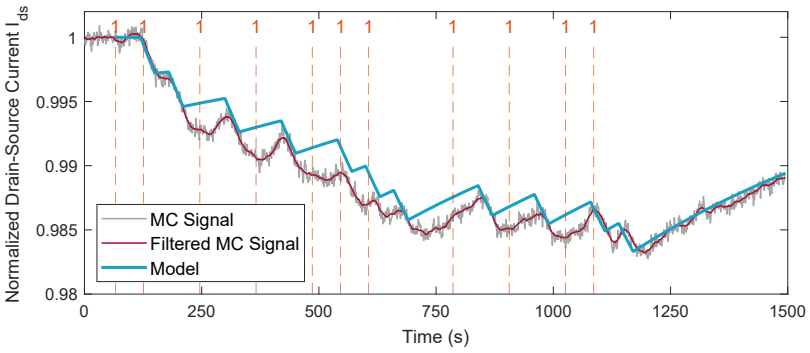

(a)

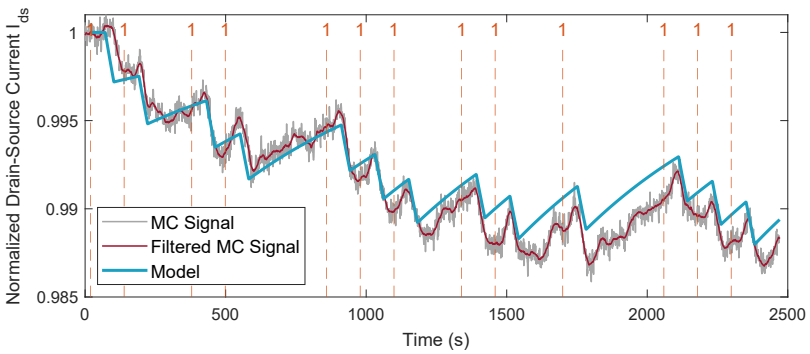

(b)

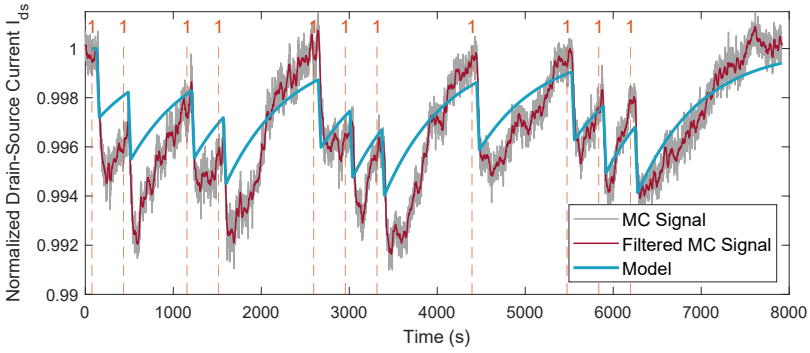

(c)

Fig. 7.19 Normalised receiver response for binary data transmission with fixed pulse length $T_p = 30$ s and varying bit intervals: (a) $T_s = 60$ s, (b) $T_s = 120$ s, (c) $T_s = 360$ s. The grey lines denote the received MC signals normalised by the baseline current, and the solid red lines are their low-pass filtered version by a moving average filter of 21-second length in MATLAB. Solid blue lines represent the normalised output of the model given in (7.17). Dashed orange lines indicate the time instants when bit-1 is transmitted, i.e., when the mechanical switch in the tDNA line is opened for 30 seconds.

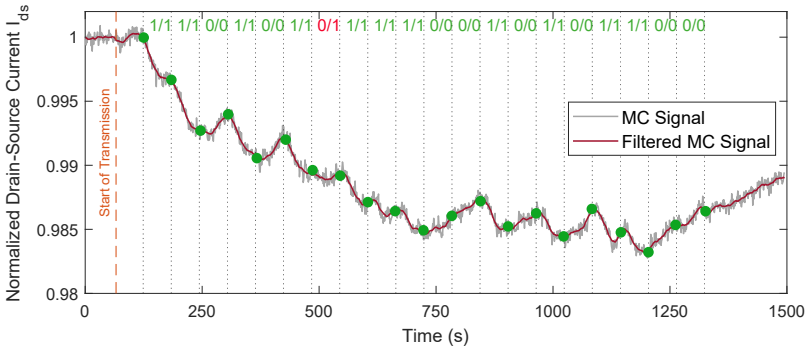

(a)

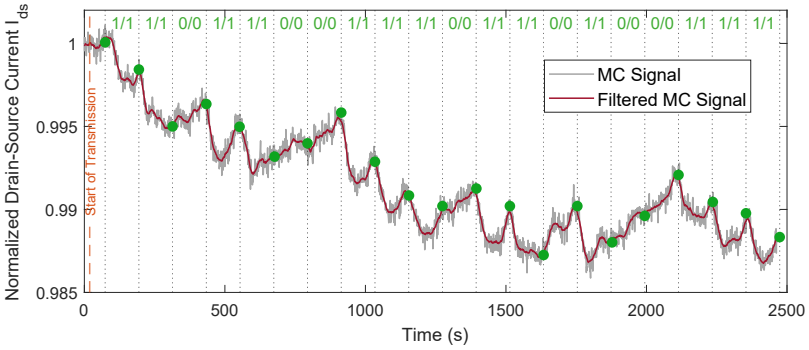

(b)

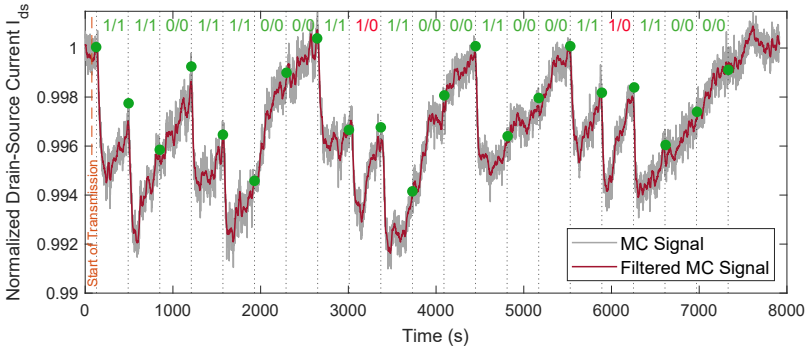

(c)

Fig. 7.20 Delay-shifted version of the receiver response for binary data transmission for varying bit intervals: (a) $T_s = 60$ s, (b) $T_s = 120$ s, (c) $T_s = 360$ s. Dashed orange line denotes the start time of the data transmission, and grey dashed lines demarcate the individual bit intervals. Green dots on the received MC signal indicates the sampled current values for difference-based detection method with the decoding rule formulated in (7.20). Transmitted/decoded bits are noted above each bit interval, with the red-coloured ones denoting the erroneously decoded bits.

bit-0 and bit-1. However, the high ISI of the MC channel, and the resulting drift of baseline, observed in these experiments, render the constant threshold detection methods ineffective, especially at high communication rates. Therefore, in line with some of the previous work in the MC literature concerning ligand-receptor binding systems, I utilise a simple difference-based detection method, which decodes the information based on the difference in I_{ds} measurements taken at the start and end points of a bit interval. Recall that the receiver is synchronised with the transmitter through the application of a constant delay shift at the receiver side. The sampling time points are demonstrated in Fig. 7.20 with green dots. Accordingly, the decoded bits can be written as follows

$$\hat{s}[i] = \sum_{i=1}^{L} s[i] \mathbb{1}\Big[r[i+1] - r[i] < 0\Big], \tag{7.20}$$

where $\hat{s}[i]$ is the decoded bit, and $r[i] = I_{ds}(t - t_{transmit} - t_{delay} - (i-1)T_s)$ is the discrete time sample of I_{ds} at decision points, and $\mathbb{1}\big[.\big]$ is the indicator function, which outputs 1 if the inside expression is true.

Applying the difference-based detection method on the unfiltered MC signal yielded 5% bit error rate (BER). I observed 1 bit error for 60 s bit interval, and 2 bit errors for 360 s bit intervals. The decoding of the unfiltered MC signal of 120 s bit interval yielded no error. The erroneous transmissions are indicated in Fig. 7.20. On the other hand, the difference-based detection applied on the low-pass filtered MC signal correctly decoded all the transmitted bits.

7.5 Conclusion

This proof-of-concept study reports the very first fabrication and characterisation of a micro/nanoscale graphene bioFET-based MC receiver. The ICT tests of the MC receiver is performed in a custom-designed micro/nanoscale MC system using a PDMS-based microfluidic channel as the controllable propagation medium, and a pressure-regulated flow control system for transmitting binary data encoded into the concentration of target DNA molecules. The time-varying hybridisation of the information-carrying target DNAs with the probe DNAs immobilised on the SLG surface of the MC receiver is selectively transduced into a change in drain-source current over the SLG channel. In light of the experimental sensing results, this transduction mechanism is speculated to be related to both electrostatic gating and direct electron transfer. The ICT performance of the MC receiver is evaluated by binary data transmissions at different bit intervals. The response of the MC receiver is well-fitted by the analytical microfluidic MC model developed

in Chapter 3. The slow hybridisation kinetics of DNA molecules is revealed to cause significant ISI. A simple difference-based detection method is shown to overcome the ISI to a significant extent, and provide reliable detection performance. The fabricated graphene-based micro/nanoscale MC receiver and the overall microfluidic MC system can be used as an experimental testbed for probing intricate dynamics of MC, and developing novel communication techniques, transceiver architectures, and applications for MC.

Chapter 8

Conclusions and Future Work

8.1 Conclusions

In this dissertation, I address the interdisciplinary problems concerning the design, modelling and fabrication of MC receivers. I develop an analytical model for the microfluidic MC systems with surface-based receivers, fabricate the first experimental testbed of a microfluidic MC system with a graphene bioFET-based DNA sensor as the micro/nanoscale MC receiver. I develop several low-complexity and reliable MC detection methods for engineered bacteria-based biological MC receivers with synthetic ligand receptors.

Microfluidic MC systems are promising for groundbreaking applications within the IoNT framework, such as *in vivo* continuous health monitoring, organs-on-chips and artificial synapses, where the complex interplay between convection, diffusion and reaction plays a crucial role in molecular information transfer. To reveal the effects of this interplay on the communication performance one must resort to computationally-expensive and time-consuming numerical methods, e.g., finite element analysis. In this dissertation, I develop the first analytical model of nonlinear convection-diffusion-reaction systems as an ICT optimisation framework for a microfluidic MC system with surface receiver equipped with ligand receptors. The model provides closed-form analytical expressions for the expected time course of the received MC signal, and the ICT metrics, such as received pulse width, pulse delay and pulse amplitude.

Since MC is inherently a biological phenomenon, there emerged another approach for realising MC systems for IoNT applications, which suggests the use of synthetic biology-enabled engineered cells as nanoscale all-biological transceivers. In this dissertation, I also focus my attention toward this approach by addressing the detection problem for biological MC receivers with ligand receptors, which have been largely neglected in

the literature with the overly simplified assumption of passive and absorbing receivers, leading to a discrepancy between the developed MC methods and the limitations of the practical systems. While the consideration of ligand receptors, which stochastically bind ligands, as the interface between the MC channel and receiver complicates the MC detection problem, it provides a more physically-relevant framework, and at the same time, unveils a whole new set of observable parameters over the receptor binding states that are informative of the transmitted molecular messages. In this direction, I first propose an ML detection method, which infers the transmitted symbols from the amount of time the receptors stay unbound. For the first time in the MC literature, I address the receptor saturation problem, and show that detection based on receptor unbound times is quite reliable in the saturation regime of the receiver, in sharp contrast to the other detection methods relying on sampling the instantaneous number of bound receptors.

MC channel is in practice, e.g., in physiologically relevant conditions, crowded with a variety of molecules interfering with the interactions of the information-carrying ligands with receptors complicating their detection. In this dissertation, I develop a practical channel sensing method to concurrently estimate the concentrations of different ligand types co-existing in the channel. The proposed method provides the required dynamic channel information, i.e., the instantaneous concentration of each ligand type. Exploiting the crosstalk between different types of ligands for channel sensing with single type of receptors is important for improving the adaptivity and reliability of the MC devices, increasing the capacity of the MC channels, and enabling the effective use of molecular spectrum for multiple access in dense nanonetworks without requiring substantial amount of additional computational resources and receptors. In this direction, I also proposed a synthetic receptor design with a multitude of internal states, that utilises a modified version of the conventional Kinetic Proofreading (KPR) mechanism implemented by the T-cells in our immune system. I designed customised chemical reaction networks for the arithmetic operations required for decoding with intracellular molecules.

Based on the developed detection and channel sensing methods with ligand receptors, I address the molecular interference problem for the first time in the MC literature. Considering a channel comprising interferer molecules of different types, but having non-negligible affinity with the receptors, I investigate the performance of four different MC detection methods which exploit different statistics of the ligand-binding reaction that reveal information about the concentration and binding affinity of the molecules, e.g., instantaneous number of bound receptors, duration of receptors' bound and unbound time intervals. The analyses reveal that the combination of unbound and bound time duration statistics of receptor-ligand reactions can substantially reduce the detrimental

effect of the molecular interference on the detection performance. The practicality of the methods has been justified by the designed synthetic receptors and chemical reaction networks.

A major challenge in MC research is the lack of any experimentally validated micro/nanoscale MC system with practical MC transceivers. This issue is pressing, as the literature is overwhelmed with theoretical studies tailoring conventional ICT-inspired methods/protocols to MC based on unrealistic assumptions isolating the MC channel from the processes regarding the transceiving operations. To address this challenge, in this thesis, I report on the first fabrication and characterization of a micro/nanoscale selective and sensitive MC receiver built on graphene bioFET-based DNA sensor. The detection performance of the receiver is tested with a custom-designed PDMS-based microfluidic testbed. The transmission of a binary information encoded into the concentration of target DNA molecules is performed at different transmission rates. The received signals are shown to be in good agreement with the approximate analytical model developed for microfluidic MC systems. These first results point out the need for further research on optimisation of functionalisation processes and system design from ICT perspective.

The practical receiver architectures and detection methods developed during this PhD thesis work will help overcome the major bottleneck resulting from the long-standing discrepancy between theory and practice in MC, which has, so far, severely impeded the innovation in this field linked with groundbreaking applications of huge societal and economic impact.

8.2 Future Work

The results obtained in this PhD research have pointed out many critical research directions that should be taken to realise the IoNT applications.

A considerable amount of effort should be devoted to optimise the practical biosensor-based MC receivers from ICT perspective in light of experimental results that can be obtained with the fabricated microfluidic MC testbed. For this aim, stochastic ICT models capturing the noise characteristics of the receiver including the inherent 1/f noise and binding noise resulting from ligand-receptor interactions need to be developed. Frequency-domain modelling of the MC receiver response can shed light on new detection techniques for biosensor-based receivers to reliably detect molecular messengers in the presence of interferers, device and channel noise.

The results obtained with the fabricated MC receiver demonstrate the need for improving the LoD, sensitivity and specificity. From fabrication point of view, using

CVD-grown single crystal graphene domains as the transducer channel could improve the LoD and sensitivity by increasing the mobility of the graphene channel and eliminating the grain boundaries, which otherwise increase the background noise of the ionic electrolyte buffer. Optimisation of the functionalisation process of PBASE linkers and DNA probes on the graphene surface can improve the LoD and sensitivity by improving the coverage of probe DNAs on the graphene surface. This could also improve the specificity by preventing the non-specific adsorption of non-complementary DNAs onto the graphene surface. Optimisation of the GFET fabrication process can also significantly improve the sensitivity by reducing defects and impurities resulting from the wet transfer process, polymer residuals and contamination. Other 2d nanomaterials, such as TMDs and black phosphorus, which are shown to manifest superior FET sensing performance in terms of sensitivity, could also be targeted for MC receivers.

There are also many rooms for optimisation concerning the microfluidic channel. The dimensions of the microfluidic channel determine the fluid flow regime inside the channel. The fabricated MC was tested at very low Reynolds number, i.e., Re < 1, indicating laminar flow regime. Turbulent flow regime with higher flow rates could also be addressed to determine whether it increases the transport rate of molecules, which, in turn, could affect the sensitivity of the receiver depending on the binding kinetics at the receiver surface. Different channel geometries could also yield different waveforms for propagating MC signals in the channel. This would in turn change the received pulse characteristics. In this way, the received pulse shape could be optimised in order to increase the SNR and reduce the ISI.

In testing the MC receiver with target DNA molecules, the diluted version of the electrolyte buffer, i.e., 0.01xPBS, is used to reduce the effect of Debye screening. However, physiological conditions, where most of the envisioned MC applications are targeted, imply much higher ionic concentrations, which may substantially degrade the detection performance in practice. To overcome the limitation of Debye screening, biasing the source-drain potential with high-frequency alternating current (AC) voltage instead of DC can be targeted. It is shown that the effect of Debye screening on bound ligands becomes linear rather than exponential under AC bias, significantly extending the range of sensing, i.e., Debye length.

One of the most important conclusions that can be drawn from this research is that the slow binding kinetics of DNA result in considerable ISI, which necessitates long bit intervals, e.g., $T_s \approx 60$ seconds, limiting the communication rate below 0.02 bps for binary CSK modulation, as shown in Chapter 7. Using probe-target pairs with lower affinity could help increase the dissociation rate; however, this strategy would compromise on the

sensitivity of the device. Therefore, the trade-off between sensitivity and communication rate should be optimised for different applications.

Regarding the design of detection methods for biological receivers, which is addressed in Chapter 4-6, more research is needed to understand the fundamental limits of sensing the external molecular concentrations, particularly when the concentrations are time-varying. Understanding how natural cells communicate and process information in such a robust, reliable, and ridiculously energy-efficient way by investigating the stochastic thermodynamics of cellular information processing, signal inference, adaptivity, learning and storage, could shed light on the design principles of novel genetic circuits for transceiving molecular signals. With this understanding, practical implementation of the communication functionalities, such as these detection algorithms, medium access control, channel coding, in engineered cells can be targeted for future IoNT applications.

Finally, devising physical interfaces between the networks of biological machines and macroscale conventional networks should be addressed. The emerging field of optogenetics provides tools for external control on the biological cells through the use of light-sensitive proteins. Moreover, fluorescent proteins, as being widely utilized in many bio-imaging techniques, stand as invaluable tools for reporting the nanoscale phenomena to the macroscale observers. Therefore, engineering cells with capabilities of expressing light-sensitive proteins and fluorescent proteins, could provide a full-duplex interface between macro and nanoscale molecular networks that can be incorporated into the IoNT framework. Enabled by these interfaces, novel IoNT applications ranging from molecular information processing to distributed cooperative sensing and actuating for diagnosing and treating human diseases with single molecule precision can be developed.

Bibliography

[1] A. C. Neto, F. Guinea, N. M. Peres, K. S. Novoselov, and A. K. Geim, "The electronic properties of graphene," *Reviews of Modern Physics*, vol. 81, no. 1, p. 109, 2009.

[2] E. Dinc, M. Kuscu, B. A. Bilgin, and O. B. Akan, "Internet of Everything (IoE) - from molecules to the universe," in *Harnessing the Internet of Everything (IoE) for Accelerated Innovation Opportunities*. IGI, 2018.

[3] I. F. Akyildiz and J. M. Jornet, "The internet of nano-things," *IEEE Wireless Communications*, vol. 17, no. 6, 2010.

[4] A. C. Ferrari, F. Bonaccorso, V. Fal'Ko, K. S. Novoselov, S. Roche, P. Bøggild, S. Borini, F. H. Koppens, V. Palermo, N. Pugno *et al.*, "Science and technology roadmap for graphene, related two-dimensional crystals, and hybrid systems," *Nanoscale*, vol. 7, no. 11, pp. 4598–4810, 2015.

[5] I. Akyildiz, M. Pierobon, S. Balasubramaniam, and Y. Koucheryavy, "The Internet of Bio-Nano Things," *IEEE Communications Magazine*, vol. 53, no. 3, pp. 32–40, 2015.

[6] M. Kuscu and O. B. Akan, "The internet of molecular things based on fret," *IEEE Internet of Things Journal*, vol. 3, no. 1, pp. 4–17, 2016.

[7] O. B. Akan, H. Ramezani, T. Khan, N. A. Abbasi, and M. Kuscu, "Fundamentals of molecular information and communication science," *Proceedings of the IEEE*, vol. 105, no. 2, pp. 306–318, 2017.

[8] L. Felicetti, M. Femminella, G. Reali, and P. Liò, "Applications of molecular communications to medicine: A survey," *Nano Communication Networks*, vol. 7, pp. 27–45, 2016.

[9] D. Malak and O. Akan, "Communication theoretical understanding of intra-body nervous nanonetworks," *IEEE Communications Magazine*, vol. 52, no. 4, pp. 129–135, 2014.

[10] N. Farsad, W. Guo, and A. W. Eckford, "Tabletop molecular communication: Text messages through chemical signals," *PloS One*, vol. 8, no. 12, p. e82935, 2013.

[11] N. Farsad, D. Pan, and A. Goldsmith, "A novel experimental platform for in-vessel multi-chemical molecular communications," in *GLOBECOM 2017-2017 IEEE Global Communications Conference*. IEEE, 2017, pp. 1–6.

[12] H. Unterweger, J. Kirchner, W. Wicke, A. Ahmadzadeh, D. Ahmed, V. Jamali, C. Alexiou, G. Fischer, and R. Schober, "Experimental molecular communication testbed based on magnetic nanoparticles in duct flow," in *2018 IEEE 19th International Workshop on Signal Processing Advances in Wireless Communications (SPAWC)*. IEEE, 2018, pp. 1–5.

[13] M. Moore, A. Enomoto, T. Nakano, R. Egashira, T. Suda, A. Kayasuga, H. Kojima, H. Sakakibara, and K. Oiwa, "A design of a molecular communication system for nanomachines using molecular motors," in *Pervasive Computing and Communications Workshops, 2006. PerCom Workshops 2006. Fourth Annual IEEE International Conference on*. IEEE, 2006, pp. 6–pp.

[14] D. Kilinc and O. B. Akan, "An information theoretical analysis of nanoscale molecular gap junction communication channel between cardiomyocytes," *IEEE Transactions on Nanotechnology*, vol. 12, no. 2, pp. 129–136, 2013.

[15] M. Pierobon, I. F. Akyildiz *et al.*, "Diffusion-based noise analysis for molecular communication in nanonetworks," *IEEE Transactions on Signal Processing*, vol. 59, no. 6, pp. 2532–2547, 2011.

[16] M. Pierobon and I. F. Akyildiz, "Noise analysis in ligand-binding reception for molecular communication in nanonetworks," *IEEE Transactions on Signal Processing*, vol. 59, no. 9, pp. 4168–4182, 2011.

[17] ——, "Intersymbol and co-channel interference in diffusion-based molecular communication," in *Communications (ICC), 2012 IEEE International Conference on*. IEEE, 2012, pp. 6126–6131.

[18] B. D. Unluturk, D. Malak, and O. B. Akan, "Rate-delay tradeoff with network coding in molecular nanonetworks," *IEEE Transactions on Nanotechnology*, vol. 12, no. 2, pp. 120–128, 2013.

[19] M. Kuscu, E. Dinc, B. A. Bilgin, H. Ramezani, and O. B. Akan, "Transmitter and receiver architectures for molecular communications: A survey on physical design with modulation, coding, and detection techniques," *Proceedings of the IEEE*, vol. 107, no. 7, pp. 1302–1341, 2019.

[20] M. S. Kuran, H. B. Yilmaz, T. Tugcu, and I. F. Akyildiz, "Modulation techniques for communication via diffusion in nanonetworks," in *Communications (ICC), 2011 IEEE International Conference on*. IEEE, 2011, pp. 1–5.

[21] M. U. Mahfuz, D. Makrakis, and H. T. Mouftah, "On the characterization of binary concentration-encoded molecular communication in nanonetworks," *Nano Communication Networks*, vol. 1, no. 4, pp. 289–300, 2010.

[22] M. Ş. Kuran, H. B. Yilmaz, T. Tugcu, and I. F. Akyildiz, "Interference effects on modulation techniques in diffusion based nanonetworks," *Nano Communication Networks*, vol. 3, no. 1, pp. 65–73, 2012.

[23] H. Arjmandi, A. Gohari, M. N. Kenari, and F. Bateni, "Diffusion-based nanonetworking: A new modulation technique and performance analysis," *IEEE Communications Letters*, vol. 17, no. 4, pp. 645–648, 2013.

[24] B. Atakan, S. Galmes, and O. B. Akan, "Nanoscale communication with molecular arrays in nanonetworks," *IEEE Transactions on NanoBioscience*, vol. 11, no. 2, pp. 149–160, 2012.

[25] N. Garralda, I. Llatser, A. Cabellos-Aparicio, E. Alarcón, and M. Pierobon, "Diffusion-based physical channel identification in molecular nanonetworks," *Nano Communication Networks*, vol. 2, no. 4, pp. 196–204, 2011.

[26] N.-R. Kim and C.-B. Chae, "Novel modulation techniques using isomers as messenger molecules for nano communication networks via diffusion," *IEEE Journal on Selected Areas in Communications*, vol. 31, no. 12, pp. 847–856, 2013.

[27] M. Kuscu and O. B. Akan, "On the physical design of molecular communication receiver based on nanoscale biosensors," *IEEE Sensors Journal*, vol. 16, no. 8, pp. 2228–2243, 2016.

[28] B. D. Unluturk, A. O. Bicen, and I. F. Akyildiz, "Genetically engineered bacteria-based biotransceivers for molecular communication," *IEEE Transactions on Communications*, vol. 63, no. 4, pp. 1271–1281, 2015.

[29] D. Malak and O. B. Akan, "Molecular communication nanonetworks inside human body," *Nano Communication Networks*, vol. 3, no. 1, pp. 19–35, 2012.

[30] I. F. Akyildiz, M. Pierobon, and S. Balasubramaniam, "Moving forward with molecular communication: From theory to human health applications," *Proceedings of the IEEE*, vol. 107, no. 5, pp. 858–865, 2019.

[31] B. Atakan, O. B. Akan, and S. Balasubramaniam, "Body area nanonetworks with molecular communications in nanomedicine," *IEEE Communications Magazine*, vol. 50, no. 1, 2012.

[32] M. Femminella, G. Reali, and A. V. Vasilakos, "A molecular communications model for drug delivery," *IEEE Transactions on Nanobioscience*, vol. 14, no. 8, pp. 935–945, 2015.

[33] I. F. Akyildiz, J. Chen, M. Ghovanloo, U. Guler, T. Ozkaya-Ahmadov, M. Pierobon, A. F. Sarioglu, and B. D. Unluturk, "Microbiome-gut-brain axis as a biomolecular communication network for the internet of bio-nanothings," *IEEE Access*, vol. 7, pp. 136 161–136 175, 2019.

[34] G. L. Adonias, A. Yastrebova, M. T. Barros, Y. Koucheryavy, F. Cleary, and S. Balasubramaniam, "Utilizing neurons for digital logic circuits: A molecular communications analysis," *IEEE Transactions on NanoBioscience*, vol. 19, no. 2, pp. 224–236, 2020.

[35] J. D. Caplin, N. G. Granados, M. R. James, R. Montazami, and N. Hashemi, "Microfluidic organ-on-a-chip technology for advancement of drug development and toxicology," *Advanced Healthcare Materials*, vol. 4, no. 10, pp. 1426–1450, 2015.

[36] N. Farsad, A. W. Eckford, S. Hiyama, and Y. Moritani, "On-chip molecular communication: Analysis and design," *IEEE Transactions on NanoBioscience*, vol. 11, no. 3, pp. 304–314, 2012.

[37] N. Islam, S. Pal, S. Balasubramaniam, and S. Misra, "Energy-aware tracking of mobile targets by bacterial nanonetworks," *IEEE Transactions on Mobile Computing*, 2020.

[38] L. P. Giné and I. F. Akyildiz, "Molecular communication options for long range nanonetworks," *Computer Networks*, vol. 53, no. 16, pp. 2753–2766, 2009.

[39] S. L. Shipman, J. Nivala, J. D. Macklis, and G. M. Church, "Crispr–cas encoding of a digital movie into the genomes of a population of living bacteria," *Nature*, vol. 547, no. 7663, pp. 345–349, 2017.

[40] J. Gorecki, K. Gizynski, J. Guzowski, J. Gorecka, P. Garstecki, G. Gruenert, and P. Dittrich, "Chemical computing with reaction–diffusion processes," *Philosophical Transactions of the Royal Society A: Mathematical, Physical and Engineering Sciences*, vol. 373, no. 2046, p. 20140219, 2015.

[41] A. Adamatzky, B. D. L. Costello, and T. Asai, *Reaction-diffusion computers*. Elsevier, 2005.

[42] W. Haselmayr, A. Springer, G. Fischer, C. Alexiou, H. Boche, P. A. Hoeher, F. Dressler, and R. Schober, "Integration of molecular communications into future generation wireless networks," *1st 6G Wireless Summit. IEEE, Levi, Finland*, 2019.

[43] H. B. Yilmaz, A. C. Heren, T. Tugcu, and C. B. Chae, "Three-dimensional channel characteristics for molecular communications with an absorbing receiver," *IEEE Communications Letters*, vol. 18, no. 6, pp. 929–932, 2014.

[44] A. Noel, K. C. Cheung, and R. Schober, "Improving receiver performance of diffusive molecular communication with enzymes," *IEEE Transactions on NanoBioscience*, vol. 13, no. 1, pp. 31–43, 2014.

[45] ——, "A unifying model for external noise sources and isi in diffusive molecular communication," *IEEE Journal on Selected Areas in Communications*, vol. 32, no. 12, pp. 2330–2343, 2014.

[46] D. Kilinc and O. B. Akan, "Receiver design for molecular communication," *IEEE Journal on Selected Areas in Communications*, vol. 31, no. 12, pp. 705–714, 2013.

[47] L.-S. Meng, P.-C. Yeh, K.-C. Chen, and I. F. Akyildiz, "On receiver design for diffusion-based molecular communication," *IEEE Transactions on Signal Processing*, vol. 62, no. 22, pp. 6032–6044, 2014.

[48] V. Jamali, A. Ahmadzadeh, and R. Schober, "On the design of matched filters for molecule counting receivers," *IEEE Communications Letters*, vol. 21, no. 8, pp. 1711–1714, 2017.

[49] A. Noel, K. C. Cheung, and R. Schober, "Optimal receiver design for diffusive molecular communication with flow and additive noise," *IEEE Transactions on Nanobioscience*, vol. 13, no. 3, pp. 350–362, 2014.

[50] A. Shahbazi and A. Jamshidi, "Adaptive weighted signal detection for nanoscale molecular communications," in *The International Zurich Seminar on Information and Communication (IZS 2018) Proceedings*. ETH Zurich, 2018, pp. 149–152.

[51] P. He, Y. Mao, Q. Liu, and K. Yang, "Improving reliability performance of diffusion-based molecular communication with adaptive threshold variation algorithm," *International Journal of Communication Systems*, vol. 29, no. 18, pp. 2669–2680, 2016.

[52] G. H. Alshammri, M. S. Alzaidi, W. K. Ahmed, and V. B. Lawrence, "Low-complexity memory-assisted adaptive-threshold detection scheme for on-off-keying diffusion-based molecular communications," in *Sarnoff Symposium, 2017 IEEE 38th*. IEEE, 2017, pp. 1–6.

[53] M. Damrath and P. A. Hoeher, "Low-complexity adaptive threshold detection for molecular communication," *IEEE Transactions on Nanobioscience*, vol. 15, no. 3, pp. 200–208, 2016.

[54] H. ShahMohammadian, G. G. Messier, and S. Magierowski, "Optimum receiver for molecule shift keying modulation in diffusion-based molecular communication channels," *Nano Communication Networks*, vol. 3, no. 3, pp. 183–195, 2012.

[55] M. U. Mahfuz, D. Makrakis, and H. T. Mouftah, "A comprehensive analysis of strength-based optimum signal detection in concentration-encoded molecular communication with spike transmission," *IEEE Transactions on Nanobioscience*, vol. 14, no. 1, pp. 67–83, 2015.

[56] ——, "A comprehensive study of sampling-based optimum signal detection in concentration-encoded molecular communication," *IEEE Transactions on Nanobioscience*, vol. 13, no. 3, pp. 208–222, 2014.

[57] H. Yan, G. Chang, Z. Ma, and L. Lin, "Derivative-based signal detection for high data rate molecular communication system," *IEEE Communications Letters*, vol. 22, no. 9, pp. 1782–1785, 2018.

[58] B. Li, M. Sun, S. Wang, W. Guo, and C. Zhao, "Low-complexity noncoherent signal detection for nanoscale molecular communications," *IEEE Transactions on Nanobioscience*, vol. 15, no. 1, pp. 3–10, 2016.

[59] ——, "Local convexity inspired low-complexity noncoherent signal detector for nanoscale molecular communications," *IEEE Transactions on Communications*, vol. 64, no. 5, pp. 2079–2091, 2016.

[60] V. Jamali, N. Farsad, R. Schober, and A. Goldsmith, "Non-coherent detection for diffusive molecular communication systems," *IEEE Transactions on Communications*, 2018.

[61] V. Jamali, A. Ahmadzadeh, N. Farsad, and R. Schober, "Constant-composition codes for maximum likelihood detection without csi in diffusive molecular communications," *IEEE Transactions on Communications*, vol. 66, no. 5, pp. 1981–1995, 2018.

[62] A. Noel and A. W. Eckford, "Asynchronous peak detection for demodulation in molecular communication," in *Communications (ICC), 2017 IEEE International Conference on*. IEEE, 2017, pp. 1–6.

[63] G. Chang, L. Lin, and H. Yan, "Adaptive detection and isi mitigation for mobile molecular communication," *IEEE Transactions on Nanobioscience*, vol. 17, no. 1, pp. 21–35, 2018.

[64] A. Ahmadzadeh, V. Jamali, and R. Schober, "Stochastic channel modeling for diffusive mobile molecular communication systems," *arXiv preprint arXiv:1709.06785*, 2017.

[65] Y. Murin, N. Farsad, M. Chowdhury, and A. Goldsmith, "Time-slotted transmission over molecular timing channels," *Nano Communication Networks*, vol. 12, pp. 12–24, 2017.

[66] ——, "Optimal detection for diffusion-based molecular timing channels," *arXiv preprint arXiv:1709.02977*, 2017.

[67] ——, "Exploiting diversity in one-shot molecular timing channels via order statistics," *IEEE Transactions on Molecular, Biological and Multi-Scale Communications*, vol. 4, no. 1, pp. 14–26, 2018.

[68] B. C. Akdeniz, A. E. Pusane, and T. Tugcu, "Optimal reception delay in diffusion-based molecular communication," *IEEE Communications Letters*, vol. 22, no. 1, pp. 57–60, 2018.

[69] T. Mora, "Physical limit to concentration sensing amid spurious ligands," *Physical Review Letters*, vol. 115, no. 3, p. 038102, 2015.

[70] M. Kuscu and O. B. Akan, "Maximum likelihood detection with ligand receptors for diffusion-based molecular communications in Internet of Bio-Nano Things," *IEEE Transactions on Nanobioscience*, vol. 17, no. 1, pp. 44–54, 2018.

[71] A. Ahmadzadeh, H. Arjmandi, A. Burkovski, and R. Schober, "Comprehensive reactive receiver modeling for diffusive molecular communication systems: Reversible binding, molecule degradation, and finite number of receptors," *IEEE Transactions on Nanobioscience*, vol. 15, no. 7, pp. 713–727, 2016.

[72] Y. Deng, A. Noel, M. Elkashlan, A. Nallanathan, and K. C. Cheung, "Modeling and simulation of molecular communication systems with a reversible adsorption receiver," *IEEE Transactions on Molecular, Biological and Multi-Scale Communications*, vol. 1, no. 4, pp. 347–362, 2015.

[73] H. ShahMohammadian, G. G. Messier, and S. Magierowski, "Modelling the reception process in diffusion-based molecular communication channels," in *Communications Workshops (ICC), 2013 IEEE International Conference on*. IEEE, 2013, pp. 782–786.

[74] C. T. Chou, "Extended master equation models for molecular communication networks," *IEEE Transactions on Nanobioscience*, vol. 12, no. 2, pp. 79–92, 2013.

[75] G. Aminian, M. Farahnak-Ghazani, M. Mirmohseni, M. Nasiri-Kenari, and F. Fekri, "On the capacity of point-to-point and multiple-access molecular communications with ligand-receptors." *IEEE Transactions on Molecular, Biological and Multi-Scale Communications*, vol. 1, no. 4, pp. 331–346, 2015.

[76] M. U. Mahfuz, D. Makrakis, and H. T. Mouftah, "Strength-based optimum signal detection in concentration-encoded pulse-transmitted ook molecular communication with stochastic ligand-receptor binding," *Simulation Modelling Practice and Theory*, vol. 42, pp. 189–209, 2014.

[77] C. T. Chou, "A markovian approach to the optimal demodulation of diffusion-based molecular communication networks," *IEEE Transactions on Communications*, vol. 63, no. 10, pp. 3728–3743, 2015.

[78] ——, "Maximum a-posteriori decoding for diffusion-based molecular communication using analog filters," *IEEE Transactions on Nanotechnology*, vol. 14, no. 6, pp. 1054–1067, 2015.

[79] M. Kuscu and O. B. Akan, "Modeling and analysis of sinw fet-based molecular communication receiver," *IEEE Transactions on Communications*, vol. 64, no. 9, pp. 3708–3721, 2016.

[80] F. W. Scheller, U. Wollenberger, A. Warsinke, and F. Lisdat, "Research and development in biosensors," *Current Opinion in Biotechnology*, vol. 12, no. 1, pp. 35–40, 2001.

[81] S. M. Borisov and O. S. Wolfbeis, "Optical biosensors," *Chemical Reviews*, vol. 108, no. 2, pp. 423–461, 2008.

[82] J. Arlett, E. Myers, and M. Roukes, "Comparative advantages of mechanical biosensors," *Nature Nanotechnology*, vol. 6, no. 4, p. 203, 2011.

[83] J. Tamayo, P. M. Kosaka, J. J. Ruz, Á. San Paulo, and M. Calleja, "Biosensors based on nanomechanical systems," *Chemical Society Reviews*, vol. 42, no. 3, pp. 1287–1311, 2013.

[84] J. Wang, "Electrochemical glucose biosensors," *Chemical Reviews*, vol. 108, no. 2, pp. 814–825, 2008.

[85] K. R. Rogers, "Principles of affinity-based biosensors," *Molecular Biotechnology*, vol. 14, no. 2, pp. 109–129, 2000.

[86] Y. Huang, X. Dong, Y. Shi, C. M. Li, L.-J. Li, and P. Chen, "Nanoelectronic biosensors based on CVD grown graphene," *Nanoscale*, vol. 2, no. 8, pp. 1485–1488, 2010.

[87] A. Poghossian and M. J. Schöning, "Label-free sensing of biomolecules with field-effect devices for clinical applications," *Electroanalysis*, vol. 26, no. 6, pp. 1197–1213, 2014.

[88] J. Shan, J. Li, X. Chu, M. Xu, F. Jin, X. Wang, L. Ma, X. Fang, Z. Wei, and X. Wang, "High sensitivity glucose detection at extremely low concentrations using a mos 2-based field-effect transistor," *RSC Advances*, vol. 8, no. 15, pp. 7942–7948, 2018.

[89] S. Xu, J. Zhan, B. Man, S. Jiang, W. Yue, S. Gao, C. Guo, H. Liu, Z. Li, J. Wang *et al.*, "Real-time reliable determination of binding kinetics of DNA hybridization using a multi-channel graphene biosensor," *Nature Communications*, vol. 8, p. 14902, 2017.

[90] W. Fu, L. Feng, G. Panaitov, D. Kireev, D. Mayer, A. Offenhäusser, and H.-J. Krause, "Biosensing near the neutrality point of graphene," *Science Advances*, vol. 3, no. 10, p. e1701247, 2017.

[91] J. Liu, J. Goud, P. M. Raj, M. Iyer, Z. Wang, and R. R. Tummala, "Label-free protein detection by zno nanowire based bio-sensors," in *Electronic Components and Technology Conference, 2007. ECTC'07. Proceedings. 57th.* IEEE, 2007, pp. 1971–1976.

[92] F. Patolsky, G. Zheng, and C. M. Lieber, "Nanowire-based biosensors," *Analytical Chemistry*, vol. 78, no. 13, pp. 4260–4269, 2006.

[93] J. P. Kim, B. Y. Lee, J. Lee, S. Hong, and S. J. Sim, "Enhancement of sensitivity and specificity by surface modification of carbon nanotubes in diagnosis of prostate cancer based on carbon nanotube field effect transistors," *Biosensors and Bioelectronics*, vol. 24, no. 11, pp. 3372–3378, 2009.

[94] B. Kim, H. S. Song, H. J. Jin, E. J. Park, S. H. Lee, B. Y. Lee, T. H. Park, and S. Hong, "Highly selective and sensitive detection of neurotransmitters using receptor-modified single-walled carbon nanotube sensors," *Nanotechnology*, vol. 24, no. 28, p. 285501, 2013.

[95] Y.-S. Lo, D. H. Nam, H.-M. So, H. Chang, J.-J. Kim, Y. H. Kim, and J.-O. Lee, "Oriented immobilization of antibody fragments on ni-decorated single-walled carbon nanotube devices," *ACS Nano*, vol. 3, no. 11, pp. 3649–3655, 2009.

[96] G.-J. Zhang, M. J. Huang, Z. H. H. Luo, G. K. I. Tay, E.-J. A. Lim, E. T. Liu, and J. S. Thomsen, "Highly sensitive and reversible silicon nanowire biosensor to study nuclear hormone receptor protein and response element DNA interactions," *Biosensors and Bioelectronics*, vol. 26, no. 2, pp. 365–370, 2010.

[97] R. Campos, J. Borme, J. R. Guerreiro, G. Machado Jr, M. F. Cerqueira, D. Y. Petrovykh, and P. Alpuim, "Attomolar label-free detection of dna hybridization with electrolyte-gated graphene field-effect transistors," *ACS Sensors*, vol. 4, no. 2, pp. 286–293, 2019.

[98] Y. Ohno, K. Maehashi, and K. Matsumoto, "Label-free biosensors based on aptamer-modified graphene field-effect transistors," *Journal of the American Chemical Society*, vol. 132, no. 51, pp. 18 012–18 013, 2010.

[99] J. Liu, X. Chen, Q. Wang, M. Xiao, D. Zhong, W. Sun, G. Zhang, and Z. Zhang, "Ultrasensitive monolayer MoS2 field-effect transistor based DNA sensors for screening of down syndrome," *Nano Letters*, vol. 19, no. 3, pp. 1437–1444, 2019.

[100] H. S. Song, H. J. Jin, S. R. Ahn, D. Kim, S. H. Lee, U.-K. Kim, C. T. Simons, S. Hong, and T. H. Park, "Bioelectronic tongue using heterodimeric human taste receptor for the discrimination of sweeteners with human-like performance," *ACS Nano*, vol. 8, no. 10, pp. 9781–9789, 2014.

[101] C.-M. Lim, J. Y. Kwon, and W.-J. Cho, "Field-effect transistor biosensor platform fused with Drosophila odorant-binding proteins for instant ethanol detection," *ACS Applied Materials & Interfaces*, vol. 9, no. 16, pp. 14 051–14 057, 2017.

[102] S. Eissa and M. Zourob, "In vitro selection of DNA aptamers targeting β-lactoglobulin and their integration in graphene-based biosensor for the detection of milk allergen," *Biosensors and Bioelectronics*, vol. 91, pp. 169–174, 2017.

[103] A. Ganguly, C.-P. Chen, Y.-T. Lai, C.-C. Kuo, C.-W. Hsu, K.-H. Chen, and L.-C. Chen, "Functionalized gan nanowire-based electrode for direct label-free voltammetric detection of DNA hybridization," *Journal of Materials Chemistry*, vol. 19, no. 7, pp. 928–933, 2009.

[104] W. Yang, K. R. Ratinac, S. P. Ringer, P. Thordarson, J. J. Gooding, and F. Braet, "Carbon nanomaterials in biosensors: should you use nanotubes or graphene?" *Angewandte Chemie International Edition*, vol. 49, no. 12, pp. 2114–2138, 2010.

[105] D. Sarkar, W. Liu, X. Xie, A. C. Anselmo, S. Mitragotri, and K. Banerjee, "MoS2 field-effect transistor for next-generation label-free biosensors," *ACS Nano*, vol. 8, no. 4, pp. 3992–4003, 2014.

[106] L. Torsi, M. Magliulo, K. Manoli, and G. Palazzo, "Organic field-effect transistor sensors: a tutorial review," *Chemical Society Reviews*, vol. 42, no. 22, pp. 8612–8628, 2013.

[107] M. Curreli, R. Zhang, F. N. Ishikawa, H.-K. Chang, R. J. Cote, C. Zhou, and M. E. Thompson, "Real-time, label-free detection of biological entities using nanowire-based fets," *IEEE Transactions on Nanotechnoly*, vol. 7, no. 6, pp. 651–667, 2008.

[108] S. U. Senveli and O. Tigli, "Biosensors in the small scale: methods and technology trends," *IET Nanobiotechnology*, vol. 7, no. 1, pp. 7–21, 2013.

[109] D. P. Tran, M. A. Winter, B. Wolfrum, R. Stockmann, C.-T. Yang, M. Pourhassan-Moghaddam, A. Offenhausser, and B. Thierry, "Toward intraoperative detection of disseminated tumor cells in lymph nodes with silicon nanowire field effect transistors," *ACS Nano*, vol. 10, no. 2, pp. 2357–2364, 2016.

[110] X. Duan, Y. Li, N. K. Rajan, D. A. Routenberg, Y. Modis, and M. A. Reed, "Quantification of the affinities and kinetics of protein interactions using silicon nanowire biosensors," *Nature Nanotechnology*, vol. 7, no. 6, p. 401, 2012.

[111] A. Gao, N. Lu, P. Dai, T. Li, H. Pei, X. Gao, Y. Gong, Y. Wang, and C. Fan, "Silicon-nanowire-based cmos-compatible field-effect transistor nanosensors for ultrasensitive electrical detection of nucleic acids," *Nano Letters*, vol. 11, no. 9, pp. 3974–3978, 2011.

[112] F. Shen, M. Tan, Z. Wang, M. Yao, Z. Xu, Y. Wu, J. Wang, X. Guo, and T. Zhu, "Integrating silicon nanowire field effect transistor, microfluidics and air sampling techniques for real-time monitoring biological aerosols," *Environmental Science & Technology*, vol. 45, no. 17, pp. 7473–7480, 2011.

[113] Y. Pei-Wen, H. Che-Wei, H. Yu-Jie, C. Min-Cheng, L. Hsin-Hao, L. Shey-Shi, and L. Chih-Ting, "A device design of an integrated cmos poly-silicon biosensor-on-chip to enhance performance of biomolecular analytes in serum samples," *Biosensors and Bioelectronics*, vol. 61, pp. 112–118, 2014.

[114] K.-I. Chen, B.-R. Li, and Y.-T. Chen, "Silicon nanowire field-effect transistor-based biosensors for biomedical diagnosis and cellular recording investigation," *Nano Today*, vol. 6, no. 2, pp. 131–154, 2011.

[115] B. Zhan, C. Li, J. Yang, G. Jenkins, W. Huang, and X. Dong, "Graphene field-effect transistor and its application for electronic sensing," *Small*, vol. 10, no. 20, pp. 4042–4065, 2014.

[116] G.-J. Zhang and Y. Ning, "Silicon nanowire biosensor and its applications in disease diagnostics: a review," *Analytica Chimica Acta*, vol. 749, pp. 1–15, 2012.

[117] R. G. Hobbs, N. Petkov, and J. D. Holmes, "Semiconductor nanowire fabrication by bottom-up and top-down paradigms," *Chemistry of Materials*, vol. 24, no. 11, pp. 1975–1991, 2012.

[118] D. Tran, T. Pham, B. Wolfrum, A. Offenhäusser, and B. Thierry, "Cmos-compatible silicon nanowire field-effect transistor biosensor: Technology development toward commercialization," *Materials*, vol. 11, no. 5, p. 785, 2018.

[119] K. Maehashi and K. Matsumoto, "Label-free electrical detection using carbon nanotube-based biosensors," *Sensors*, vol. 9, no. 7, pp. 5368–5378, 2009.

[120] S. J. Park, O. S. Kwon, S. H. Lee, H. S. Song, T. H. Park, and J. Jang, "Ultrasensitive flexible graphene based field-effect transistor (fet)-type bioelectronic nose," *Nano Letters*, vol. 12, no. 10, pp. 5082–5090, 2012.

[121] J. Ping, R. Vishnubhotla, A. Vrudhula, and A. C. Johnson, "Scalable production of high-sensitivity, label-free DNA biosensors based on back-gated graphene field effect transistors," *ACS Nano*, vol. 10, no. 9, pp. 8700–8704, 2016.

[122] N. Gao, T. Gao, X. Yang, X. Dai, W. Zhou, A. Zhang, and C. M. Lieber, "Specific detection of biomolecules in physiological solutions using graphene transistor biosensors," *Proceedings of the National Academy of Sciences*, vol. 113, no. 51, pp. 14 633–14 638, 2016.

[123] A. K. Manoharan, S. Chinnathambi, R. Jayavel, and N. Hanagata, "Simplified detection of the hybridized DNA using a graphene field effect transistor," *Science and Technology of Advanced Materials*, vol. 18, no. 1, pp. 43–50, 2017.

[124] G. Wu, Z. Dai, X. Tang, Z. Lin, P. K. Lo, M. Meyyappan, and K. W. C. Lai, "Graphene field-effect transistors for the sensitive and selective detection of escherichia coli using pyrene-tagged DNA aptamer," *Advanced Healthcare Materials*, vol. 6, no. 19, p. 1700736, 2017.

[125] S. Viswanathan, T. N. Narayanan, K. Aran, K. D. Fink, J. Paredes, P. M. Ajayan, S. Filipek, P. Miszta, H. C. Tekin, F. Inci *et al.*, "Graphene–protein field effect biosensors: glucose sensing," *Materials Today*, vol. 18, no. 9, pp. 513–522, 2015.

[126] M. Khalid, O. Amin, S. Ahmed, and M.-S. Alouini, "System modeling of virus transmission and detection in molecular communication channels," in *2018 IEEE International Conference on Communications (ICC)*. IEEE, 2018, pp. 1–6.

[127] A. K. Geim and P. Kim, "Carbon wonderland," *Scientific American*, vol. 298, no. 4, pp. 90–97, 2008.

[128] A. K. Geim and K. S. Novoselov, "The rise of graphene," *Nature Materials*, vol. 6, no. 3, pp. 183–191, 2007.

[129] J.-H. Chen, C. Jang, S. Xiao, M. Ishigami, and M. S. Fuhrer, "Intrinsic and extrinsic performance limits of graphene devices on sio 2," *Nature nanotechnology*, vol. 3, no. 4, p. 206, 2008.

[130] D. De Fazio, D. G. Purdie, A. K. Ott, P. Braeuninger-Weimer, T. Khodkov, S. Goossens, T. Taniguchi, K. Watanabe, P. Livreri, F. H. Koppens *et al.*, "High-mobility, wet-transferred graphene grown by chemical vapor deposition," *ACS Nano*, vol. 13, no. 8, pp. 8926–8935, 2019.

[131] D. Purdie, N. Pugno, T. Taniguchi, K. Watanabe, A. Ferrari, and A. Lombardo, "Cleaning interfaces in layered materials heterostructures," *Nature Communications*, vol. 9, no. 1, pp. 1–12, 2018.

[132] A. K. Geim, "Graphene: status and prospects," *Science*, vol. 324, no. 5934, pp. 1530–1534, 2009.

[133] F. Bonaccorso, A. Lombardo, T. Hasan, Z. Sun, L. Colombo, and A. C. Ferrari, "Production and processing of graphene and 2d crystals," *Materials Today*, vol. 15, no. 12, pp. 564–589, 2012.

[134] X. Li, W. Cai, J. An, S. Kim, J. Nah, D. Yang, R. Piner, A. Velamakanni, I. Jung, E. Tutuc *et al.*, "Large-area synthesis of high-quality and uniform graphene films on copper foils," *Science*, vol. 324, no. 5932, pp. 1312–1314, 2009.

[135] S. Bae, H. Kim, Y. Lee, X. Xu, J.-S. Park, Y. Zheng, J. Balakrishnan, T. Lei, H. R. Kim, Y. I. Song *et al.*, "Roll-to-roll production of 30-inch graphene films for transparent electrodes," *Nature Nanotechnology*, vol. 5, no. 8, p. 574, 2010.

[136] H. Zhou, W. J. Yu, L. Liu, R. Cheng, Y. Chen, X. Huang, Y. Liu, Y. Wang, Y. Huang, and X. Duan, "Chemical vapour deposition growth of large single crystals of monolayer and bilayer graphene," *Nature Communications*, vol. 4, no. 1, pp. 1–8, 2013.

[137] D. De Fazio, "Graphene, layered materials and hybrid structures for advanced photodetectors," Ph.D. dissertation, University of Cambridge, 2018.

[138] W. Fu, L. Jiang, E. P. van Geest, L. M. Lima, and G. F. Schneider, "Sensing at the surface of graphene field-effect transistors," *Advanced Materials*, vol. 29, no. 6, p. 1603610, 2017.

[139] D. K. H. Tsang, T. J. Lieberthal, C. Watts, I. E. Dunlop, S. Ramadan, E. Armando, and N. Klein, "chemically functionalised graphene fet biosensor for the label-free sensing of exosomes," *Scientific Reports*, vol. 9, no. 1, pp. 1–10, 2019.

[140] I. Heller, S. Chatoor, J. Mannik, M. A. Zevenbergen, J. B. Oostinga, A. F. Morpurgo, C. Dekker, and S. G. Lemay, "Charge noise in graphene transistors," *Nano Letters*, vol. 10, no. 5, pp. 1563–1567, 2010.

[141] F. Yan, M. Zhang, and J. Li, "Solution-gated graphene transistors for chemical and biological sensors," *Advanced Healthcare Materials*, vol. 3, no. 3, pp. 313–331, 2014.

[142] X. Dong, Y. Shi, W. Huang, P. Chen, and L.-J. Li, "Electrical detection of dna hybridization with single-base specificity using transistors based on cvd-grown graphene sheets," *Advanced Materials*, vol. 22, no. 14, pp. 1649–1653, 2010.

[143] J. Lin, D. Teweldebrhan, K. Ashraf, G. Liu, X. Jing, Z. Yan, R. Li, M. Ozkan, R. K. Lake, A. A. Balandin *et al.*, "Gating of single-layer graphene with single-stranded deoxyribonucleic acids," *Small*, vol. 6, no. 10, pp. 1150–1155, 2010.

[144] Y. Ohno, S. Okamoto, K. Maehashi, and K. Matsumoto, "Direct electrical detection of dna hybridization based on electrolyte-gated graphene field-effect transistor," *Japanese Journal of Applied Physics*, vol. 52, no. 11R, p. 110107, 2013.

[145] S.-R. Guo, J. Lin, M. Penchev, E. Yengel, M. Ghazinejad, C. S. Ozkan, and M. Ozkan, "Label free dna detection using large area graphene based field effect transistor biosensors," *Journal of Nanoscience and Nanotechnology*, vol. 11, no. 6, pp. 5258–5263, 2011.

[146] M. T. Hwang, M. Heiranian, Y. Kim, S. You, J. Leem, A. Taqieddin, V. Faramarzi, Y. Jing, I. Park, A. M. Van Der Zande *et al.*, "Ultrasensitive detection of nucleic acids using deformed graphene channel field effect biosensors," *Nature Communications*, vol. 11, no. 1, pp. 1–11, 2020.

[147] W. Yue, C. Tang, C. Wang, C. Bai, S. Liu, X. Xie, H. Hua, Z. Zhang, and D. Li, "An electricity-fluorescence double-checking biosensor based on graphene for detection of binding kinetics of dna hybridization," *RSC Advances*, vol. 7, no. 70, pp. 44 559–44 567, 2017.

[148] G. Xu, J. Abbott, L. Qin, K. Y. Yeung, Y. Song, H. Yoon, J. Kong, and D. Ham, "Electrophoretic and field-effect graphene for all-electrical dna array technology," *Nature Communications*, vol. 5, p. 4866, 2014.

[149] R. Daniel, J. R. Rubens, R. Sarpeshkar, and T. K. Lu, "Synthetic analog computation in living cells," *Nature*, vol. 497, no. 7451, p. 619, 2013.

[150] O. Purcell and T. K. Lu, "Synthetic analog and digital circuits for cellular computation and memory," *Current Opinion in Biotechnology*, vol. 29, pp. 146–155, 2014.

[151] S. Balasubramaniam, N. Lyamin, D. Kleyko, M. Skurnik, A. Vinel, and Y. Koucheryavy, "Exploiting bacterial properties for multi-hop nanonetworks," *IEEE Communications Magazine*, vol. 52, no. 7, pp. 184–191, 2014.

[152] M. Gregori and I. F. Akyildiz, "A new nanonetwork architecture using flagellated bacteria and catalytic nanomotors," *IEEE Journal on Selected Areas in Communications*, vol. 28, no. 4, 2010.

[153] V. Petrov, D. Moltchanov, S. Balasubramaniam, and Y. Koucheryavy, "Incorporating bacterial properties for plasmid delivery in nano sensor networks," *IEEE Transactions on Nanotechnology*, vol. 14, no. 4, pp. 751–760, 2015.

[154] M. Pierobon, "A molecular communication system model based on biological circuits," in *Proceedings of ACM The First Annual International Conference on Nanoscale Computing and Communication*. ACM, 2014, p. 2.

[155] ——, "A systems-theoretic model of a biological circuit for molecular communication in nanonetworks," *Nano Communication Networks*, vol. 5, no. 1-2, pp. 25–34, 2014.

[156] A. Marcone, M. Pierobon, and M. Magarini, "A biological circuit design for modulated parity-check encoding in molecular communication," in *Communications (ICC), 2017 IEEE International Conference on*. IEEE, 2017, pp. 1–7.

[157] ——, "A parity check analog decoder for molecular communication based on biological circuits," in *INFOCOM 2017-IEEE Conference on Computer Communications, IEEE*. IEEE, 2017, pp. 1–9.

[158] M. Laddomada and M. Pierobon, "A biochemical filter for frequency-based signal reception in molecular communication," in *Global Communications Conference (GLOBECOM), 2015 IEEE*. IEEE, 2015, pp. 1–6.

[159] N.-R. Kim, N. Farsad, C.-B. Chae, and A. W. Eckford, "A universal channel model for molecular communication systems with metal-oxide detectors," in *Communications (ICC), 2015 IEEE International Conference on*. IEEE, 2015, pp. 1054–1059.

[160] B.-H. Koo, C. Lee, H. B. Yilmaz, N. Farsad, A. Eckford, and C.-B. Chae, "Molecular mimo: From theory to prototype," *IEEE Journal on Selected Areas in Communications*, vol. 34, no. 3, pp. 600–614, 2016.

[161] W. Wicke, A. Ahmadzadeh, V. Jamali, H. Unterweger, C. Alexiou, and R. Schober, "Magnetic nanoparticle-based molecular communication in microfluidic environments," *IEEE Transactions on Nanobioscience*, vol. 18, no. 2, pp. 156–169, 2019.

[162] N. Malmstadt, P. Yager, A. S. Hoffman, and P. S. Stayton, "A smart microfluidic affinity chromatography matrix composed of poly (n-isopropylacrylamide)-coated beads," *Analytical Chemistry*, vol. 75, no. 13, pp. 2943–2949, 2003.

[163] X. D. Hoa, A. Kirk, and M. Tabrizian, "Towards integrated and sensitive surface plasmon resonance biosensors: a review of recent progress," *Biosensors and Bioelectronics*, vol. 23, no. 2, pp. 151–160, 2007.

[164] D.-S. Wang and S.-K. Fan, "Microfluidic surface plasmon resonance sensors: From principles to point-of-care applications," *Sensors*, vol. 16, no. 8, p. 1175, 2016.

[165] K. Choi, J.-Y. Kim, J.-H. Ahn, J.-M. Choi, M. Im, and Y.-K. Choi, "Integration of field effect transistor-based biosensors with a digital microfluidic device for a lab-on-a-chip application," *Lab on a Chip*, vol. 12, no. 8, pp. 1533–1539, 2012.

[166] T. Gervais and K. F. Jensen, "Mass transport and surface reactions in microfluidic systems," *Chemical Engineering Science*, vol. 61, no. 4, pp. 1102–1121, 2006.

[167] T. M. Squires, R. J. Messinger, and S. R. Manalis, "Making it stick: convection, reaction and diffusion in surface-based biosensors," *Nature Biotechnology*, vol. 26, no. 4, p. 417, 2008.

[168] A. O. Bicen and I. F. Akyildiz, "End-to-end propagation noise and memory analysis for molecular communication over microfluidic channels," *IEEE Transactions on Communications*, vol. 62, no. 7, pp. 2432–2443, 2014.

[169] ——, "Interference modeling and capacity analysis for microfluidic molecular communication channels," *IEEE Transactions on Nanotechnology*, vol. 14, no. 3, pp. 570–579, 2015.

[170] A. O. Bicen, C. M. Austin, I. F. Akyildiz, and C. R. Forest, "Efficient sampling of bacterial signal transduction for detection of pulse-amplitude modulated molecular signals," *IEEE Transactions on Biomedical Circuits and Systems*, vol. 9, no. 4, pp. 505–517, 2015.

[171] E. De Leo, L. Donvito, L. Galluccio, A. Lombardo, G. Morabito, and L. M. Zanoli, "Communications and switching in microfluidic systems: Pure hydrodynamic control for networking labs-on-a-chip," *IEEE Transactions on Communications*, vol. 61, no. 11, pp. 4663–4677, 2013.

[172] E. De Leo, L. Galluccio, A. Lombardo, and G. Morabito, "Networked labs-on-a-chip (nloc): Introducing networking technologies in microfluidic systems," *Nano Communication Networks*, vol. 3, no. 4, pp. 217–228, 2012.

[173] B. A. Bilgin and O. B. Akan, "A fast algorithm for analysis of molecular communication in artificial synapse," *IEEE Transactions on Nanobioscience*, vol. 16, no. 6, pp. 408–417, 2017.

[174] T. Khan, B. A. Bilgin, and O. B. Akan, "Diffusion-based model for synaptic molecular communication channel," *IEEE Transactions on Nanobioscience*, vol. 16, no. 4, pp. 299–308, 2017.

[175] R. Hansen, H. Bruus, T. H. Callisen, and O. Hassager, "Transient convection, diffusion, and adsorption in surface-based biosensors," *Langmuir*, vol. 28, no. 19, pp. 7557–7563, 2012.

[176] A. O. Bicen and I. F. Akyildiz, "System-theoretic analysis and least-squares design of microfluidic channels for flow-induced molecular communication," *IEEE Transactions on Signal Processing*, vol. 61, no. 20, pp. 5000–5013, 2013.

[177] B. Goldstein, D. Coombs, X. He, A. R. Pineda, and C. Wofsy, "The influence of transport on the kinetics of binding to surface receptors: application to cells and biacore," *Journal of Molecular Recognition*, vol. 12, no. 5, pp. 293–299, 1999.

[178] K. Sigmundsson, G. Másson, R. Rice, N. Beauchemin, and B. Öbrink, "Determination of active concentrations and association and dissociation rate constants of interacting biomolecules: an analytical solution to the theory for kinetic and mass transport limitations in biosensor technology and its experimental verification," *Biochemistry*, vol. 41, no. 26, pp. 8263–8276, 2002.

[179] D. G. Myszka, X. He, M. Dembo, T. A. Morton, and B. Goldstein, "Extending the range of rate constants available from biacore: interpreting mass transport-influenced binding data," *Biophysical Journal*, vol. 75, no. 2, pp. 583–594, 1998.

[180] M. Goličnik, "On the lambert w function and its utility in biochemical kinetics," *Biochemical Engineering Journal*, vol. 63, pp. 116–123, 2012.

[181] M. Karsenty, S. Rubin, and M. Bercovici, "Acceleration of surface-based hybridization reactions using isotachophoretic focusing," *Analytical Chemistry*, vol. 86, no. 6, pp. 3028–3036, 2014.

[182] I. Llatser, E. Alarcón, and M. Pierobony, "Diffusion-based channel characterization in molecular nanonetworks," in *Computer Communications Workshops (INFOCOM WKSHPS), 2011 IEEE Conference on*. IEEE, 2011, pp. 467–472.

[183] M. Kuscu and O. B. Akan, "Modeling and analysis of sinw biofet as molecular antenna for bio-cyber interfaces towards the Internet of Bio-Nanothings," in *Internet of Things (WF-IoT), 2015 IEEE 2nd World Forum on*. IEEE, 2015, pp. 669–674.

[184] ——, "On the capacity of diffusion-based molecular communications with sinw fet-based receiver," in *Engineering in Medicine and Biology Society (EMBC), 2016 IEEE 38th Annual International Conference of the*. IEEE, 2016, pp. 3043–3047.

[185] G. Zheng, X. P. Gao, and C. M. Lieber, "Frequency domain detection of biomolecules using silicon nanowire biosensors," *Nano Letters*, vol. 10, no. 8, pp. 3179–3183, 2010.

[186] H. C. Berg and E. M. Purcell, "Physics of chemoreception," *Biophysical Journal*, vol. 20, no. 2, pp. 193–219, 1977.

[187] A. M. Berezhkovskii and A. Szabo, "Effect of ligand diffusion on occupancy fluctuations of cell-surface receptors," *The Journal of Chemical Physics*, vol. 139, no. 12, p. 09B610_1, 2013.

[188] W. Bialek, *Biophysics: searching for principles*. Princeton University Press, 2012.

[189] P. R. ten Wolde, N. B. Becker, T. E. Ouldridge, and A. Mugler, "Fundamental limits to cellular sensing," *Journal of Statistical Physics*, vol. 162, no. 5, pp. 1395–1424, 2016.

[190] R. Mosayebi, H. Arjmandi, A. Gohari, M. Nasiri-Kenari, and U. Mitra, "Receivers for diffusion-based molecular communication: Exploiting memory and sampling rate," *IEEE Journal on Selected Areas in Communications*, vol. 32, no. 12, pp. 2368–2380, 2014.

[191] V. Singh, M. Tchernookov, and I. Nemenman, "Effects of receptor correlations on molecular information transmission," *Physical Review E*, vol. 94, no. 2, p. 022425, 2016.

[192] L. L. Looger, M. A. Dwyer, J. J. Smith, and H. W. Hellinga, "Computational design of receptor and sensor proteins with novel functions," *Nature*, vol. 423, no. 6936, p. 185, 2003.

[193] E. Andrianantoandro, S. Basu, D. K. Karig, and R. Weiss, "Synthetic biology: new engineering rules for an emerging discipline," *Molecular Systems Biology*, vol. 2, no. 1, 2006.

[194] C. Hoffmann, A. Zurn, M. Bunemann, and M. Lohse, "Conformational changes in g-protein-coupled receptors—the quest for functionally selective conformations is open," *British Journal of Pharmacology*, vol. 153, no. S1, pp. S358–S366, 2008.

[195] J. R. Rubens, G. Selvaggio, and T. K. Lu, "Synthetic mixed-signal computation in living cells," *Nature Communications*, vol. 7, p. 11658, 2016.

[196] E. Dinc and O. B. Akan, "Theoretical limits on multiuser molecular communication in internet of nano-bio things," *IEEE Transactions on Nanobioscience*, vol. 16, no. 4, pp. 266–270, 2017.

[197] A. Alizadeh, H. R. Bahrami, M. Maleki, N. H. Tran, and P. Mohseni, "On the coexistence of nano networks: Sensing techniques for molecular communications," *IEEE Transactions on Molecular, Biological and Multi-Scale Communications*, 2018.

[198] V. Jamali, A. Ahmadzadeh, C. Jardin, H. Sticht, and R. Schober, "Channel estimation for diffusive molecular communications," *IEEE Transactions on Communications*, vol. 64, no. 10, pp. 4238–4252, 2016.

[199] A. Noel, K. C. Cheung, and R. Schober, "Joint channel parameter estimation via diffusive molecular communication," *IEEE Transactions on Molecular, Biological and Multi-Scale Communications*, vol. 1, no. 1, pp. 4–17, 2015.

[200] A. C. Pan, D. W. Borhani, R. O. Dror, and D. E. Shaw, "Molecular determinants of drug–receptor binding kinetics," *Drug Discovery Today*, vol. 18, no. 13-14, pp. 667–673, 2013.

[201] R. G. Endres and N. S. Wingreen, "Maximum likelihood and the single receptor," *Physical Review Letters*, vol. 103, no. 15, p. 158101, 2009.

[202] V. Singh and I. Nemenman, "Simple biochemical networks allow accurate sensing of multiple ligands with a single receptor," *PLoS Computational Biology*, vol. 13, no. 4, p. e1005490, 2017.

[203] J.-B. Lalanne and P. François, "Chemodetection in fluctuating environments: Receptor coupling, buffering, and antagonism," *Proceedings of the National Academy of Sciences*, vol. 112, no. 6, pp. 1898–1903, 2015.

[204] E. D. Siggia and M. Vergassola, "Decisions on the fly in cellular sensory systems," *Proceedings of the National Academy of Sciences*, vol. 110, no. 39, pp. E3704–E3712, 2013.

[205] T. W. Mckeithan, "Kinetic proofreading in t-cell receptor signal transduction," *Proceedings of the National Academy of Sciences*, vol. 92, no. 11, pp. 5042–5046, 1995.

[206] O. B. Akan, O. B. Karli, and O. Ergul, "Cognitive radio sensor networks," *IEEE Network*, vol. 23, no. 4, 2009.

[207] V. Hasselblad, "Estimation of finite mixtures of distributions from the exponential family," *Journal of the American Statistical Association*, vol. 64, no. 328, pp. 1459–1471, 1969.

[208] N. P. Jewell, "Mixtures of exponential distributions," *The Annals of Statistics*, pp. 479–484, 1982.

[209] S. M. Kay, *Fundamentals of statistical signal processing: Estimation theory*. Englewood Cliffs NJ USA: Prentice-Hall, 1993.

[210] C. T. Chou, "Chemical reaction networks for maximum likelihood estimation of the concentration of signalling molecules," in *Proceedings of the 4th ACM International Conference on Nanoscale Computing and Communication*. ACM, 2017, p. 4.

[211] M. Bouvier, "Cross-talk between second messengers," *Annals of the New York Academy of Sciences*, vol. 594, no. 1, pp. 120–129, 1990.

[212] M. Kuscu and O. B. Akan, "Modeling convection-diffusion-reaction systems for microfluidic molecular communications with surface-based receivers in Internet of Bio-Nano Things," *PloS One*, vol. 13, no. 2, p. e0192202, 2018.

[213] A. Einolghozati, M. Sardari, and F. Fekri, "Capacity of diffusion-based molecular communication with ligand receptors," in *Information Theory Workshop (ITW), 2011 IEEE*. IEEE, 2011, pp. 85–89.

[214] M. Kuscu and O. B. Akan, "Channel sensing in molecular communications with single type of ligand receptors," *IEEE Transactions on Communications*, vol. 67, no. 10, pp. 6868–6884, 2019.

[215] A. Singhal, R. K. Mallik, and B. Lall, "Performance analysis of amplitude modulation schemes for diffusion-based molecular communication," *IEEE Transactions on Wireless Communications*, vol. 14, no. 10, pp. 5681–5691, 2015.

[216] Y. H. Kwak, D. S. Choi, Y. N. Kim, H. Kim, D. H. Yoon, S.-S. Ahn, J.-W. Yang, W. S. Yang, and S. Seo, "Flexible glucose sensor using cvd-grown graphene-based field effect transistor," *Biosensors and Bioelectronics*, vol. 37, no. 1, pp. 82–87, 2012.

[217] Y. Ohno, K. Maehashi, Y. Yamashiro, and K. Matsumoto, "Electrolyte-gated graphene field-effect transistors for detecting ph and protein adsorption," *Nano Letters*, vol. 9, no. 9, pp. 3318–3322, 2009.

[218] N. S. Green and M. L. Norton, "Interactions of dna with graphene and sensing applications of graphene field-effect transistor devices: A review," *Analytica Chimica Acta*, vol. 853, pp. 127–142, 2015.

[219] Y. Chahibi and I. F. Akyildiz, "Molecular communication noise and capacity analysis for particulate drug delivery systems," *IEEE Transactions on Communications*, vol. 62, no. 11, pp. 3891–3903, 2014.

[220] B. Li, M. Sun, S. Wang, W. Guo, and C. Zhao, "Low-complexity noncoherent signal detection for nanoscale molecular communications," *IEEE Transactions on Nanobioscience*, vol. 15, no. 1, pp. 3–10, 2015.

[221] B.-h. Chueh, D. Huh, C. R. Kyrtsos, T. Houssin, N. Futai, and S. Takayama, "Leakage-free bonding of porous membranes into layered microfluidic array systems," *Analytical Chemistry*, vol. 79, no. 9, pp. 3504–3508, 2007.

[222] M. T. Hwang, P. B. Landon, J. Lee, D. Choi, A. H. Mo, G. Glinsky, and R. Lal, "Highly specific snp detection using 2d graphene electronics and dna strand displacement," *Proceedings of the National Academy of Sciences*, vol. 113, no. 26, pp. 7088–7093, 2016.

[223] G. Wu, X. Tang, M. Meyyappan, and K. W. C. Lai, "Doping effects of surface functionalization on graphene with aromatic molecule and organic solvents," *Applied Surface Science*, vol. 425, pp. 713–721, 2017.

[224] M. Kabeláč, O. Kroutil, M. Předota, F. Lankaš, and M. Šíp, "Influence of a charged graphene surface on the orientation and conformation of covalently attached oligonucleotides: a molecular dynamics study," *Physical Chemistry Chemical Physics*, vol. 14, no. 12, pp. 4217–4229, 2012.

[225] A. C. Ferrari and D. M. Basko, "Raman spectroscopy as a versatile tool for studying the properties of graphene," *Nature Nanotechnology*, vol. 8, no. 4, p. 235, 2013.

[226] A. C. Ferrari, J. Meyer, V. Scardaci, C. Casiraghi, M. Lazzeri, F. Mauri, S. Piscanec, D. Jiang, K. Novoselov, S. Roth *et al.*, "Raman spectrum of graphene and graphene layers," *Physical Review Letters*, vol. 97, no. 18, p. 187401, 2006.

[227] J. C. Sutherland and K. P. Griffin, "Absorption spectrum of dna for wavelengths greater than 300 nm," *Radiation Research*, vol. 86, no. 3, pp. 399–410, 1981.

[228] S. Ghosh, N. I. Khan, J. G. Tsavalas, and E. Song, "selective detection of lysozyme biomarker utilizing large area chemical vapor deposition-grown graphene-based field-effect transistor," *Frontiers in Bioengineering and Biotechnology*, vol. 6, p. 29, 2018.

[229] T.-Y. Chen, P. T. K. Loan, C.-L. Hsu, Y.-H. Lee, J. T.-W. Wang, K.-H. Wei, C.-T. Lin, and L.-J. Li, "Label-free detection of dna hybridization using transistors based on cvd grown graphene," *Biosensors and Bioelectronics*, vol. 41, pp. 103–109, 2013.

[230] Y. Zheng, J. Nguyen, C. Wang, and Y. Sun, "Electrical measurement of red blood cell deformability on a microfluidic device," *Lab on a Chip*, vol. 13, no. 16, pp. 3275–3283, 2013.

[231] B. R. Goldsmith, L. Locascio, Y. Gao, M. Lerner, A. Walker, J. Lerner, J. Kyaw, A. Shue, S. Afsahi, D. Pan *et al.*, "Digital biosensing by foundry-fabricated graphene sensors," *Scientific Reports*, vol. 9, no. 1, pp. 1–10, 2019.

[232] I. Meric, M. Y. Han, A. F. Young, B. Ozyilmaz, P. Kim, and K. L. Shepard, "Current saturation in zero-bandgap, top-gated graphene field-effect transistors," *Nature Nanotechnology*, vol. 3, no. 11, p. 654, 2008.

[233] A. Star, E. Tu, J. Niemann, J.-C. P. Gabriel, C. S. Joiner, and C. Valcke, "Label-free detection of dna hybridization using carbon nanotube network field-effect transistors," *Proceedings of the National Academy of Sciences*, vol. 103, no. 4, pp. 921–926, 2006.

[234] J. van Mameren, E. J. Peterman, and G. J. Wuite, "See me, feel me: methods to concurrently visualize and manipulate single dna molecules and associated proteins," *Nucleic Acids Research*, vol. 36, no. 13, pp. 4381–4389, 2008.

[235] W. Kaiser and U. Rant, "Conformations of end-tethered dna molecules on gold surfaces: influences of applied electric potential, electrolyte screening, and temperature," *Journal of the American Chemical Society*, vol. 132, no. 23, pp. 7935–7945, 2010.

[236] U. Rant, K. Arinaga, S. Fujita, N. Yokoyama, G. Abstreiter, and M. Tornow, "Dynamic electrical switching of dna layers on a metal surface," *Nano Letters*, vol. 4, no. 12, pp. 2441–2445, 2004.

[237] E. Stellwagen and N. C. Stellwagen, "Determining the electrophoretic mobility and translational diffusion coefficients of dna molecules in free solution," *Electrophoresis*, vol. 23, no. 16, pp. 2794–2803, 2002.

[238] A. E. Nkodo, J. M. Garnier, B. Tinland, H. Ren, C. Desruisseaux, L. C. McCormick, G. Drouin, and G. W. Slater, "Diffusion coefficient of dna molecules during free solution electrophoresis," *Electrophoresis*, vol. 22, no. 12, pp. 2424–2432, 2001.

Appendix A

Clarifications and Derivation Details

A.1 Constraints on Signalling Interval for MC Detection Based on Receptor Unbound Time (DRUT)

As discussed in Section 4.2 (Chapter 4), there is a trade-off between the time necessary for the receiver to acquire enough data and the accuracy of the estimation. Although ERUT scheme provides much better estimate of the ligand concentration than the EROR scheme, it takes the receiver longer to collect the necessary information, i.e., receptor unbound times, from the receptors. As given in (4.8), in the worst case scenario, the average time required to sample a receptor unbound time from each receptor can be expressed by

$$\mu_{\tau_s} = 2\mu_{\tau_u} + \mu_{\tau_b} = 2/(k_+ c) + 1/k_-, \tag{A.1}$$

which shows that the decision can get longer as the ligand concentration at the receiver gets smaller. This poses a challenge for the MC detection problem, as the receiver needs to collect samples and carry out the decoding before another message of transmitter arrives. This could be a problem especially when the transmitter sends successive bit-0's, which in turn makes the ligand concentration at the receiver very low. Therefore, I find it crucial to put a constraint on the signalling interval T_s, to specify a range for system parameters, for which one can safely assume that the receiver finds enough time to sample the total unbound time of N_R receptors in DRUT scheme. To this aim, I consider the worst-case scenario as being the successive transmission of 10 bit-0's, since the probability for the transmitter to successively send bit-0's for more than 10 times

gets too small (i.e., $\leq (1-p_1)^{11}$) for $p_1 = 0.5$, such that it can be neglected. Accordingly, the constraint is written as follows

$$T_s > 2\mu_{\tau_u} + \mu_{\tau_b}, > \frac{2}{k_+ p_1 Q \sum_{i=H}^{\infty} h(t_s + iT_s)} + \frac{1}{k_-}, \tag{A.2}$$

where $H = 10$ is the number of successive bit-0's that have been sent. This constraint is typically satisfied when the receiver is expected to operate near saturation, as the receptor unbound times get shorter; however, other system parameters, such as the unbinding rate k_- and the distance represented in the channel impulse response $h(t)$, can also affect the validity of the constraint. The range of parameter values, for which I evaluate the performance of the detection schemes in Section 4.5, readily satisfies this condition, as the operating conditions are set to make the receiver operate near saturation.

A.2 Introducing Unknown Ligand Types for MC Channel Sensing

In the proposed suboptimal estimators in Chapter 5, the time thresholds, T_i's, and the corresponding $\boldsymbol{S}$ and $\boldsymbol{H}$ matrices, given in (5.25) and (5.39), respectively, are constructed assuming that there are M types of ligands with the unbinding rates known to the receiver. Here, I investigate the case when L different types of additional ligands with unbinding rates unknown to the receiver are introduced to the channel. I will derive the MSE for the suboptimal unbiased concentration estimator introduced in Section 5.4.3. The derivation of the biased estimator, investigated in Section 5.4.3, can be done in a similar way. We will see that in the case of unknown ligands, the unbiased estimator becomes biased.

Since the receiver assumes that there are M different types of ligands, the time domain is divided into M different regions. When there are L additional ligand types, the probability of a binding duration to fall in a specific time interval can be rewritten in vector form as follows

$$\mathbf{p} = \mathbf{E}[\boldsymbol{n}]/N = \boldsymbol{S_r}\boldsymbol{\alpha_r}, \tag{A.3}$$

where $\mathbf{p}$ is $(M \times 1)$ probability vector, and $\boldsymbol{\alpha_r}$ is an $([M+L] \times 1)$ vector of concentration ratios of all ligand types including the additional ones. Note that $\boldsymbol{\alpha}_{\boldsymbol{r}}^T = [\boldsymbol{\alpha}^T \alpha_{M+1} \dots \alpha_{M+L}]$, with $\boldsymbol{\alpha}$ is the $(M \times 1)$ vector of concentration ratios of known ligand types. Here, $\boldsymbol{S_r}$ is

an $(M \times [M+L])$ matrix, whose elements are given by

$$\boldsymbol{S_r}(i,j) = \mathrm{e}^{-(k_j^- T_{i-1})} - \mathrm{e}^{-(k_j^- T_i)} \quad \text{for } i \in \{1,\dots,M\},\ j \in \{1,\dots,M+L\}. \tag{A.4}$$

Using the knowledge of only M ligand types, the receiver utilizes the concentration ratio estimator given in (5.29), as follows

$$\hat{\boldsymbol{\alpha}} = \left(\frac{1}{N}\right) \boldsymbol{W}\boldsymbol{n}, \tag{A.5}$$

where $\boldsymbol{W} = \boldsymbol{S}^{-1}$ is the inverse of $\boldsymbol{S}$ matrix, that is given in (5.25). The mean of the ratio estimator then becomes

$$\mathbf{E}[\hat{\boldsymbol{\alpha}}] = \left(\frac{1}{N}\right) \boldsymbol{W}\mathbf{E}[\boldsymbol{n}] = \boldsymbol{W}\mathbf{p} = \boldsymbol{S}^{-1}\boldsymbol{S_r}\boldsymbol{\alpha_r}. \tag{A.6}$$

The bias of the ratio estimator can then be written as:

$$\boldsymbol{\Delta}[\hat{\boldsymbol{\alpha}}] = \mathbf{E}[\hat{\boldsymbol{\alpha}}] - \boldsymbol{\alpha} = \boldsymbol{S}^{-1}\boldsymbol{S_r}\boldsymbol{\alpha_r} - \boldsymbol{\alpha}. \tag{A.7}$$

The concentration estimator for individual ligand types is given as $\hat{\boldsymbol{c}} = \hat{\boldsymbol{\alpha}}\hat{c}_{tot}$. Note that the ML estimator of total ligand concentration, $\hat{c}_{tot}$, is unbiased. Therefore, the bias of the concentration estimator can be computed as follows

$$\boldsymbol{\Delta}[\hat{\boldsymbol{c}}] = \boldsymbol{\Delta}[\hat{\boldsymbol{\alpha}}]c_{tot}, \tag{A.8}$$

where the total ligand concentration is now given as $c_{tot} = \sum_{i=1}^{M+L} c_i$. Recall from (5.33) that the variance of the concentration estimator is written as

$$\mathbf{Var}[\hat{\boldsymbol{c}}] = \mathrm{Var}[\hat{c}_{tot}]\mathbf{Var}[\hat{\boldsymbol{\alpha}}] + \mathrm{Var}[\hat{c}_{tot}]\left(\mathbf{E}[\hat{\boldsymbol{\alpha}}] \odot \mathbf{E}[\hat{\boldsymbol{\alpha}}]\right) + \mathbf{Var}[\hat{\boldsymbol{\alpha}}]\mathrm{E}[\hat{c}_{tot}]^2. \tag{A.9}$$

Here, $\mathrm{Var}[\hat{c}_{tot}] = \frac{c_{tot}^2}{N-2}$ for $N > 2$ and $\mathrm{E}[\hat{c}_{tot}] = c_{tot}$. The variance of the ratio estimator, $\mathbf{Var}[\hat{\boldsymbol{\alpha}}]$, can be calculated by using (5.34) and (5.35), with the new probability vector $\mathbf{p}$, given in (A.3). Finally, the MSE of the concentration estimator in case of additional unknown ligands can be written as

$$\mathbf{MSE}[\hat{\boldsymbol{c}}] = \mathbf{Var}[\hat{\boldsymbol{c}}] + \left(\boldsymbol{\Delta}[\hat{\boldsymbol{c}}] \odot \boldsymbol{\Delta}[\hat{\boldsymbol{c}}]\right). \tag{A.10}$$